



**Deliverable 2.17: Integrated reactive transport
models for assessing the chemical evolution at the
disposal cell scale**

Work Package 2

EURAD Deliverable 2.17 – Integrated reactive transport models for assessing the chemical evolution at the disposal cell scale

The project leading to this application has received funding from the European Union's Horizon 2020 research and innovation programme under grant agreement No 847593.



Document information

Project Acronym	EURAD
Project Title	European Joint Programme on Radioactive Waste Management
Project Type	European Joint Programme (EJP)
EC grant agreement No.	847593
Project starting / end date	1st June 2019 – 30 May 2024
Work Package No.	2
Work Package Title	Assessment of the geochemical evolution of ILW and HLW disposal cells
Work Package Acronym	ACED
Deliverable No.	2.17
Deliverable Title	Integrated reactive transport models for assessing the chemical evolution at the disposal cell scale
Lead Beneficiary	Mines Paris
Contractual Delivery Date	
Actual Delivery Date	22-05-2024
Type	Report
Dissemination level	
Authors	Laurent De Windt (Mines Paris), Javier Samper (UDC), Benoit Cochepin (Andra), Vanessa Montoya (SCK CEN), Enrique García (ENRESA), Jaime Garibay-Rodriguez (UFZ), Alba Mon (UDC), Luis Montenegro (UDC), Aurora Samper (UDC), Louis Raimbault (Mines Paris), Edouard Veilly (IRSN)

To be cited as:

De Windt L., Samper J., Cochepin B., Montoya V., Garcia E., Garibay-Rodrigues, J., Mon A., Montenegro L., Samper A., Raimbault L., Veilly E. (2024): Integrated reactive transport models for assessing the chemical evolution at the disposal cell scale. Final version as of 21-05-2024 of deliverable D2.17 of the HORIZON 2020 project EURAD. EC Grant agreement no: 847593.

Disclaimer

All information in this document is provided "as is" and no guarantee or warranty is given that the information is fit for any particular purpose. The user, therefore, uses the information at its sole risk and liability. For the avoidance of all doubts, the European Commission has no liability in respect of this document, which is merely representing the authors' view.

Acknowledgement

This document is a deliverable of the European Joint Programme on Radioactive Waste Management (EURAD). EURAD has received funding from the European Union's Horizon 2020 research and innovation programme under grant agreement No 847593.

EURAD Deliverable 2.17 – Integrated reactive transport models for assessing the chemical evolution at the disposal cell scale

Status of deliverable		
	By	Date
Delivered (Lead Beneficiary)	Laurent De Windt (Mines Paris), et al.	
Verified (WP Leader)	Diederik Jacques (SCK CEN)	July 2023
Reviewed (Reviewers)	Hans Meeussen (NRG) J. Griffioen (TNO) L. Vondrovic (SURA) R. Plukinie (FTMC)	March 2024
Revised & Verified	Diederik Jacques	May 2024
Approved (PMO)	Tara Beattie	May 2024
Submitted to EC (Coordinator)	Andra (Coordinator)	May 2024

Executive Summary

HLW disposal cell in granite

A reactive transport model of the geochemical evolution of a HLW disposal cell in granite has been performed. Model predictions have been carried out for a base run and several sensitivity cases and variants. The base run considers the vitrified waste (40 cm in diameter), the carbon-steel canister (5 cm thick), a 75 cm thick saturated FEBEX bentonite buffer and the Spanish Reference granitic rock. The model is non-isothermal, accounts for the thermal transient stage and assumes generalized carbon steel corrosion under anaerobic conditions. The model considers three periods. Period I corresponds to the initial oxic transient stage. Period II starts when the bentonite barrier is fully saturated and anoxic conditions are prevailing. Canister corrosion, the interactions of corrosion products and the bentonite and the interactions of bentonite and granite take place in Period II. Period II is assumed to last 25,000 years which coincides with the time at which the remaining thickness of the overpack is 1.5 cm. The corrosion rate is equal to 1.41 m/y and is such that 3.5 cm of canister corrode after 25,000 years. The canister is fully corroded at $t = 35,300$ years. Period III starts after canister failure and accounts for glass alteration and the interactions of glass with corrosion products and uncorroded iron. The model accounts for Periods II and III. This approach is consistent with that used for the HLW disposal cell in clay.

The concentration of dissolved Cl^- in the bentonite in Period II decreases with time due to Cl^- diffusion from the bentonite into the granite because the initial concentration of Cl^- in the granite porewater is much smaller than the initial concentration in the bentonite. The profiles of the Cl^- concentration show very small gradients because the solute flux from the bentonite into the granite is not controlled by solute diffusion through the bentonite, but by solute advection and diffusion in the granite. Canister corrosion causes an increase in pH. The computed pH at the end of Period II (25,000 years) is equal to 9.25 in the canister and ranges from 9.25 to 7.82 in the bentonite. The concentration of dissolved Fe^{2+} increases in the first 1,000 years and later decreases. Magnetite precipitates mostly in the canister in Period II. Magnetite precipitation proceeds as long as the canister is corroding. The thickness of magnetite precipitation band in the bentonite at $t = 25,000$ years is about 1 cm. Siderite precipitates at both sides of the canister/bentonite interface. The precipitation front penetrates more than 1 cm into the bentonite. Greenalite is the main corrosion product in the bentonite in Period II. Smectite dissolution triggers the precipitation of a small amount of Mg-saponite in the bentonite at 25,000 years. Calcite precipitates in the canister near the bentonite/canister interface, the bentonite and the granite. Model results show that dissolved Fe enters the exchange complex and sorbs on strong and weak #1 sorption sites of the bentonite near the canister interface at 25,000 years. The base run does not consider the porosity feedback effect (PFE) on chemical and transport parameters. The porosity in the canister decreases mostly due to magnetite precipitation. Clogging is predicted to occur after 10,000 years. The porosity of the bentonite at a point 1 cm away from the canister interface decreases due to the precipitation of calcite, siderite and greenalite.

Glass dissolution in Period III leads to an increase of pH with time in the glass. The concentration of dissolved silica increases in the inner part of the glass until $t = 30,000$ years while it decreases in the outer part of the glass due to the out diffusion of dissolved silica into the canister and the bentonite. This diffusive flux causes the precipitation of greenalite at the glass-canister and canister-bentonite interfaces. The pH at 50,000 years ranges from 7.93 to 7.89 in the glass, from 7.89 to 8.66 in the canister and from 7.87 to 8.6 in the bentonite. The concentration of dissolved Cl^- keeps decreasing from 25,000 to 50,000 years, reaching a uniform concentration equal to $6.9 \cdot 10^{-4}$ M at 50,000 years. Magnetite precipitates in the canister while there is carbon steel to corrode. Once the canister is fully corroded, magnetite redissolves near the glass/canister interface and greenalite precipitates. Greenalite precipitates in the canister and the bentonite, especially at the glass/canister interface. Siderite precipitates at the canister/bentonite interface. Smectite dissolution triggers the precipitation of a small amount of Mg-saponite. Calcite re-dissolves in the canister and the bentonite/canister interface at 50,000 years. The porosity in the glass increases due to glass dissolution while it decreases in the canister where pore clogging is predicted at 10,000 years due to calcite, magnetite, siderite and

EURAD Deliverable 2.17 – Integrated reactive transport models for assessing the chemical evolution at the disposal cell scale

greenalite precipitation. The porosity in the bentonite at 1 cm from the canister interface decreased with time due to the precipitation of calcite, siderite and greenalite, kept decreasing until $t = 28,000$ years, when reached clogging due to the precipitation of siderite and calcite and later increases slightly up to 0.05.

The results of the sensitivity runs and variants show that the glass dissolution front is sensitive to a decrease of threshold silica concentration, C_{Si}^* , from 10^{-3} to $5 \cdot 10^{-4}$ mol/L. Model results are sensitive to consider MX80 bentonite; specially computed pH is larger in Variant 1 and siderite and greenalite precipitation and ISG and smectite dissolution in Variant 1 are smaller than those in the base run. Predictions are not sensitive to an increase of Cl^- concentration in the granite water and neither green rust nor akaganeite precipitate. The larger the granite flux, the larger the decrease of solute concentrations in the bentonite. The precipitation of corrosion products is slightly sensitive to the increase in granite flux. Model results are not sensitive to the chemical composition of the Czech granite porewater.

HLW disposal cell in clay

The Belgium, Dutch and French concepts are based on the geologic disposal of vitrified high-level waste (HLW) in a deep clay formation. The first two ones rely on supercontainers containing HLW and carbon steel overpack encased in a concrete buffer to keep steel passivation. In the French concept, the annular gap between a carbon steel sleeve and host rock is filled with a low-pH/bentonite grout that imposes a corrosion-limiting environment during the operating period but has to be neutralized over the very first thousand of years of storage. Despite their own particularities, some common features were identified and a generic configuration with variants was modelled. Reactive transport modelling with HYTEC was developed to assess the chemical evolution of the full system including the “vitrified waste – steel overpack – concrete buffer – clay host rock”. Full water saturation and isothermal condition at $25^\circ C$ were considered. The ThermoChimie database was used to calculate a very large set of chemical reactions at thermodynamic equilibrium. Kinetic pH-dependent rate laws were set for the dissolution of the host-rock clay phases, the generalized corrosion of carbon steel and the dissolution of the international simple glass (ISG).

The modelling of the full system showed that the driving force was the chemical destabilization of the cement phases of the concrete buffer by the clay rock. This perturbation (decalcification, sulphate attack, carbonation) slowly propagated by diffusion towards the steel overpack with a decreasing pH in the whole concrete buffer. The chemical alteration was more important in the concrete than in the clay. Therefore, the durability of the cement buffer would strongly affect the duration of the containment properties of the multi-barrier system as a whole. As long as the high-pH buffering capacity lasted, steel corrosion was minimized and magnetite was the main corrosion product. The loss of such high-pH conditions led to the speed-up of the corrosion with Fe(II)-silicate formation. The overpack breaching led to the income of aqueous solution in contact with the IS glass. The important formation of Fe-silicates corrosion products at the glass/overpack interface sustained glass dissolution. The full depletion of Fe(0) corresponded to a strong decrease in the dissolution of glass that shifted to the low residual rate mode. Diffusion-driven transfer led to a protective effect of the inner zone of the fractured glass by the external ones.

Variant cases and sensitivity analysis were performed in complement to the base case. HYTEC led to a similar sequence of chemical alteration whatever the buffer thickness (5 to 100 cm) but the degradation fronts were spatially larger and required more time for a complete degradation while the buffer thickness increased. The lifetime of the buffer varied from 1,250 years to more than 100,000 years. There was a clear possibility of clogging at the cement/clay interface as well as in the steel overpack by the formation of corrosion products. The low-pH/bentonite grout was subjected to hydrolysis and magnesium attack. Due to the small buffer thickness (5 cm), there was no significant difference on the long term with respect to the effect of the buffer nature on the corrosion of steel and the dissolution of the IS glass.

EURAD Deliverable 2.17 – Integrated reactive transport models for assessing the chemical evolution at the disposal cell scale

The transient thermal and hydric stage has been investigated with the reactive transport code iCP on a subsystem consisting of magnetite (corroded steel) – CEM I concrete buffer – CO_x rock. The evolution of temperature in space and time modified the effective diffusion coefficient and the solubility of the minerals for about 1,000 years. In that case (and under water saturated conditions), temperature increase significantly reduced the lifetime for the smallest thickness but did have a moderate effect in the other cases. The thermal transient stage has also an influence on the stability of (S,Al)-bearing minerals. Ettringite and monocarboaluminate are progressively dissolved but secondary ettringite precipitated once the temperature decreases back.

The partial water saturation modified the effective diffusion coefficients according to a Millington and Quirk type model. The influence of the desaturation tends to slow down the decalcification sequence opposite to the effect of temperature. These iCP calculations demonstrated that neglecting the thermal and hydric transient stages in the HYTEC modelling was a reasonable approximation for the 30 – 100 cm buffer thickness but should be considered for the 5 cm cases.

ILW disposal cell in clay

The studied disposal system is based on a multi-barrier system including the waste matrix (in the primary coli or drum), the disposal container, the mortar backfill in the emplacement tunnel and the clay host rock (Callovo Oxfordian). Reinforced of the tunnels walls with a shotcrete is also part of the concept. It is assumed that the disposal cell contains a number of stacked waste containers (with organic or metallic waste). In addition, a backfilling material between the waste containers is considered and in the case of the organic waste, 6 different waste packages are also inside the containers. The dimensions of the multibarrier system are 11 x 13 m without including the host rock and the excavation disturbed zone (EDZ). Hydration models for the four different CEM I cementitious materials (i.e. functional concrete walls of the containers, backfill mortar between the waste containers, vault backfill mortar and shotcrete liner) have been performed to determine the initial hydrated cement phases in the reactive transport model. All the materials have been conceptualized as homogeneous porous media. Diffusion is the main transport mechanism and no temperature effects has been considered. Aqueous complexation reactions, mineral dissolution/precipitation reactions, cation exchange and surface complexation reactions are part of the model. When considering changes of porosity due to precipitation/dissolution of minerals, standard molar volumes are used. All this information is contained in the same chemical thermodynamic database, CEMDATA v18.1. Additional thermodynamic data for some clay minerals not found in CEMDATA is retrieved and adapted to match the same master species of CEMDATA from the latest version of the ThermoChimie database. Simulations are for 100 000 years and are performed with the T-H-M-C code OpenGeoSys v.6. Four different cases have been considered, i) fully water saturated media, ii) 50% water saturation, iii) 10% water saturation, iv) no change of porosity. A summary of the relevant output variables are given.

ILW disposal cell in granite

The same multibarrier system considered for the ILW disposal cell in clay is used here except the host rock. In this case the Spanish granitic rock is considered and an EDZ is not present. Advective flow from the host rock is considered and no temperature effects has been considered. Aqueous complexation reactions, mineral dissolution/precipitation reactions, cation exchange and surface complexation reactions are part of the model. When considering changes of porosity due to precipitation/dissolution of minerals, standard molar volumes are used. All this information is contained in the same chemical thermodynamic database, CEMDATA v18.1. Simulations are for 100 000 years and are performed with the T-H-M-C code OpenGeoSys v.6. Two different cases have been considered, i) diffusive transport in the vertical direction, ii) diffusive transport in the x direction. Comparison of results with a without porosity feedback from reactions are also part of the assessment. A summary of the relevant output variables are given.

Table of content

Executive Summary.....	5
Table of content.....	9
List of figures	13
List of Tables	19
Abbreviations	21
1. Introduction.....	23
1.1 Reactive transport modelling of the multiple barrier system	23
1.2 Aims and structure of this deliverable	23
2. Modelling of a full HLW disposal cell in granite.....	25
2.1 Description of the disposal cell concept	25
2.2 Conceptual model.....	28
2.2.1 Narrative evolution.....	28
2.2.2 Sensitivity cases and variants	28
2.2.3 Hydrodynamic processes	31
2.2.4 Thermal processes	31
2.2.5 Chemical processes	32
2.3 Numerical model.....	38
2.3.1 Grid and simulated time.....	38
2.3.2 Flow and transport parameters.....	39
2.3.3 Chemical parameters.....	39
2.3.4 Parameters for the sensitivity cases and variants	41
2.4 Computer code	44
2.5 Differences between D2.16 and D2.17	45
2.5.1 Conceptual model.....	45
2.5.2 Numerical model.....	45
2.5.3 Computer codes	45
2.5.4 Sensitivity cases	45
2.6 Calculated results of the base case.....	46
2.6.1 Model results for Period II: canister corrosion	47
2.6.2 Calculated results at Period III: glass dissolution	57
2.7 Model results for variants and sensitivity cases	66
2.7.1 Sensitivity Case 1	66
2.7.2 Sensitivity Case 2	66
2.7.3 Variant 1	66

EURAD Deliverable 2.17 – Integrated reactive transport models for assessing the chemical evolution at the disposal cell scale

2.7.4	Variant 2	72
2.7.5	Variant 3	76
2.8	Summary and Conclusions.....	77
3.	Modelling of a full HLW disposal cell in clay.....	81
3.1	Disposal cell configuration.....	81
3.1.1	European HLW disposal concepts in clay	81
3.1.2	The generic configuration of the HLW cell	81
3.1.3	Variants of the HLW cell configuration	83
3.2	Conceptual model and evolution scenarios.....	85
3.2.1	Successive periods considered in the evolution of the HLW cell	85
3.2.2	Base case and variants of the HLW cell modelling	86
3.3	Computer code and thermodynamic database	87
3.3.1	The reactive transport code HYTEC.....	87
3.3.2	Thermodynamic database	87
3.4	Numerical model parameters	88
3.4.1	Grid, boundary/initial conditions and simulated times	88
3.4.2	Clay rock parameters.....	89
3.4.3	CEM I concrete (buffer) parameters	91
3.4.4	Low-pH cement/bentonite grout (buffer) parameters	92
3.4.5	Low carbon steel parameters	93
3.4.6	Vitrified waste parameters	95
3.5	Differences between D2.16 and D2.17	96
3.5.1	Conceptual model.....	96
3.5.2	Numerical model.....	97
3.5.3	Sensitivity cases	97
3.6	Modelling results of the Base Case – 30 cm CEM I buffer.....	97
3.6.1	Near field perturbation of the clay.....	100
3.6.2	Degradation of the cementitious buffer.....	104
3.6.3	Corrosion of the steel waste overpack	107
3.6.4	Dissolution of the international standard glass (ISG)	112
3.6.5	Evolution of the aqueous chemistry.....	114
3.7	Modelling results of the Variant Cases	115
3.7.1	CEM I buffer thickness of 5 cm and 100 cm.....	115
3.7.2	Low-pH cement/bentonite grout	119
3.7.3	Complementary sensitivity simulations.....	120
3.8	Conclusions and perspectives.....	121

4.	Modelling of the transient stage effects on the cement buffer in a HLW cell in clay	123
4.1	Cell configuration, conceptual model and narrative evolution	123
4.2	Mathematical model	124
4.3	Parameter values in iCP	124
4.3.1	Clay host rock	124
4.3.2	CEM I-based concrete (buffer)	127
4.3.3	Low carbon steel.....	129
4.4	Numerical model.....	130
4.5	Results of iCP simulations: assessing the influence of thermal and saturation transients on the chemical degradation of concrete materials.....	130
4.5.1	Results of the base case with iCP: constant temperature and constant saturation	130
4.5.2	Consequences of the thermal transient stage on the concrete degradation	132
4.5.3	Consequences of the thermal and partial desaturation transients	134
4.6	Conclusions and implications for the modelling of the full HLW cell in clay	136
5.	Modelling of a full ILW disposal cell in clay	137
5.1	Simulation in one dimension.....	139
5.1.1	Model discretization	139
5.1.2	Case 1a: fully-water saturated media	140
5.1.3	Case 1b: 50% water saturation	141
5.1.4	Case 1c: 10% saturation	142
5.1.5	Case 1d: constant porosity	144
5.2	Simulations in two-dimensions	145
5.3	Summary and conclusions	154
6.	ILW disposal cell in granite.....	156
6.1	Simulations in one dimension	157
6.1.1	Model discretization	157
6.1.2	Case 1a: diffusive transport in the Y direction	158
6.1.3	Case 1b: diffusive transport in the X direction	163
6.2	Simulations in two dimensions	167
6.3	Summary and conclusions	176
7.	References	177

EURAD Deliverable 2.17 – Integrated reactive transport models for assessing the chemical evolution at the disposal cell scale

List of figures

<i>Figure 2-1. Layout of the representative HLW disposal cell concept in a granitic host rock which includes: vitrified waste (40 cm diameter), steel canister (5 cm thick), FEBEX bentonite (75 cm thickness) and Spanish Reference Granite.</i>	26
<i>Figure 2-2. Underground installations of a radioactive waste repository in granite according to the spent-fuel Spanish Reference Concept (ENRESA, 2001).</i>	26
<i>Figure 2-3. Longitudinal section of a disposal drift in the spent fuel Spanish repository concept in granite (ENRESA, 2001).</i>	27
<i>Figure 2-4. Dimensions of a disposal cell in the spent fuel Spanish repository concept in granite (ENRESA, 2001).</i>	27
<i>Figure 2-5. Geometric configurations of the variants considered for the HLW disposal cell in granite. Variant 1 considers MX bentonite (35 cm thick). Variant 2 considers an excavation damaged zone (EDZ) of 1 m thickness. Variant 3 considers the Czech reference crystalline rock.</i>	30
<i>Figure 2-6. Calculated time evolution of the temperature in a HLW disposal cell in granite after 100 years of storage (wet bentonite) and 170 years of storage (dry bentonite) at the canister-bentonite and the bentonite-granite interfaces (Neeft, 2020a; personal communication).</i>	31
<i>Figure 2-7. Time evolution of the temperatures at the canister/bentonite and bentonite/granite interfaces. These temperatures were prescribed in the reactive transport model of the HLW disposal cell in granite.</i>	32
<i>Figure 2-8. Glass dissolution rate for different values of pH.</i>	37
<i>Figure 2-9. Scheme of the finite element mesh used in the model of the HLW disposal cell in granite.</i>	38
<i>Figure 2-10. Spatial distribution of the computed mineral volume fractions at selected times of Period II and Period III. The left axis is a ampliation from 0.5 to 1.</i>	47
<i>Figure 2-11. Spatial distribution of the computed pH at selected times of Period II.</i>	50
<i>Figure 2-12. Spatial distribution of the computed concentration of dissolved Fe at selected times of Period II.</i>	50
<i>Figure 2-13. Spatial distribution of the computed volume fraction of magnetite at selected times of Period II. The bottom plot shows an enlargement around the canister ($1 < r < 4$ dm).</i>	51
<i>Figure 2-14. Spatial distribution of the computed volume fraction of siderite at selected times of Period II. The bottom plot shows an enlargement around the canister ($1 < r < 4$ dm).</i>	51
<i>Figure 2-15. Spatial distribution of the computed volume fraction of greenalite at selected times of Period II. The bottom plot shows an enlargement around the canister ($1 < r < 4$ dm).</i>	52
<i>Figure 2-16. Spatial distribution of the computed volume fraction of smectite at selected times of Period II.</i>	52
<i>Figure 2-17. Spatial distribution of the computed volume fraction of calcite at selected times of Period II.</i>	53
<i>Figure 2-18. Time evolution of the porosity during Period II due to changes in mineral dissolution/precipitation in the glass ($r = 12.5$ cm), the canister ($r = 22$ cm) and the bentonite ($r = 26.5$ cm).</i>	53
<i>Figure 2-19. Spatial distribution of the computed concentration of dissolved Cl at selected times of Period II.</i>	54

EURAD Deliverable 2.17 – Integrated reactive transport models for assessing the chemical evolution at the disposal cell scale

Figure 2-20. Spatial distribution of the computed concentration of dissolved aluminum at selected times of Period II. 54

Figure 2-21. Spatial distribution of the computed concentration of exchanged cations at the end of Period II ($t = 25,000$ years). 55

Figure 2-22. Spatial distribution of the computed concentration of surface complexes at strong (upper plot), weak #1 (intermediate plot) and weak #2 (bottom plot) sites at the end of Period II ($t = 25,000$ years)..... 56

Figure 2-23. Spatial distribution of the computed volume fraction of ISG at selected times of Period III. 58

Figure 2-24. Spatial distribution of the computed pH at selected times of Period III. 58

Figure 2-25. Spatial distribution of the computed concentration of dissolved silica at selected times of Period III. 59

Figure 2-26. Spatial distribution of the computed volume fraction of magnetite at selected times of Period III. The bottom plot shows an enlargement around the canister ($1 < r < 4$ dm). 59

Figure 2-27. Spatial distribution of the computed volume fraction of greenalite at selected times of Period III..... 60

Figure 2-28. Spatial distribution of the computed volume fraction of siderite at selected times of Period III..... 60

Figure 2-29. Spatial distribution of the computed volume fraction of smectite at selected times of Period III..... 61

Figure 2-30. Spatial distribution of the computed volume fraction of Mg-saponite at selected times of Period III. 61

Figure 2-31. Spatial distribution of the computed volume fraction of calcite at selected times of Period III..... 62

Figure 2-32. Time evolution of the porosity changes caused by mineral dissolution/precipitation during Periods II and III in the glass ($r = 12.5$ cm), the canister ($r = 22$ cm) and the bentonite ($r = 26.5$ cm). 62

Figure 2-33. Spatial distribution of the computed concentration of dissolved Cl^- at selected times of Period III. 63

Figure 2-34. Spatial distribution of the computed concentration of dissolved Fe^{2+} at selected times of Period III. 63

Figure 2-35. Spatial distribution of the computed concentration of exchanged cations at the end of Period III ($t = 50,000$ years). 64

Figure 2-36. Spatial distribution of the computed concentration of surface complexes at the strong (upper plot), weak #1 (intermediate plot) and weak #2 (bottom plot) sites at the end of Period III ($t = 50,000$ years)..... 65

Figure 2-37. Time evolution of the computed concentration of dissolved Cl^- in the bentonite ($r = 7.535$ dm) for the base case and the Sensitivity Case 2. 66

Figure 2-38. Finite element mesh used in Variant 1 which considers MX-80 bentonite with a thickness of 35 cm instead of FEBEX bentonite. 67

Figure 2-39. Spatial distribution of the computed pH at 25,000 years and at 50,000 years for the base case (FEBEX bentonite) and Variant 1 (MX80 bentonite). Results are presented for the glass, canister and bentonite FEBEX (7.5 dm) and MX80 (3.5 dm)..... 68

Figure 2-40. Spatial distribution of the computed dissolved Fe^{+2} at 25,000 years and at 50,000 years for the base case (FEBEX bentonite) and Variant 1 (MX80 bentonite). Results are presented for the glass, canister and bentonite FEBEX (7.5 dm) and MX80 (3.5 dm)..... 68

Figure 2-41. Spatial distribution of the computed magnetite volume fraction at 25,000 years and at 50,000 years for the base case (FEBEX bentonite) and Variant 1 (MX80 bentonite). Results are presented for the glass, canister and bentonite FEBEX (7.5 dm) and MX80 (3.5 dm)..... 69

Figure 2-42. Spatial distribution of the computed siderite volume fraction at 50,000 years for the base case (FEBEX bentonite) and Variant 1 (MX80 bentonite). Results are presented for the glass, canister and bentonite FEBEX (7.5 dm) and MX80 (3.5 dm)..... 69

Figure 2-43. Spatial distribution of the computed greenalite volume fraction at 50,000 years for the base case (FEBEX bentonite) and Variant 1 (MX80 bentonite). Results are presented for the glass, canister and bentonite FEBEX (7.5 dm) and MX80 (3.5 dm)..... 70

Figure 2-44. Spatial distribution of the computed ISG volume fraction at 50,000 years for the base case (FEBEX bentonite) and Variant 1 (MX80 bentonite). Results are presented for the glass, canister and bentonite FEBEX (7.5 dm) and MX80 (3.5 dm)..... 70

Figure 2-45. Spatial distribution of the computed smectite volume fraction at 50,000 years for the base case (FEBEX bentonite) and Variant 1 (MX80 bentonite). Results are presented for the glass, canister and bentonite FEBEX (7.5 dm) and MX80 (3.5 dm)..... 71

Figure 2-46. Time evolution of the porosity changes caused by mineral dissolution/precipitation during Periods II and III in the glass ($r = 12.5$ cm), the canister ($r = 22$ cm) and the bentonite ($r = 26.5$ cm) for the base case (FEBEX bentonite) and the Varian 1 (MX80 bentonite)..... 71

Figure 2-47. Spatial distribution of the computed pH at 25,000 years (top) and at 50,000 years (bottom) for the base case ($Q = 0.1$ L/y) and Variant 2 ($Q = 1$ L/y and $Q = 4.7$ L/y). 73

Figure 2-48. Time evolution of the computed concentrations of dissolved Cl^- and Fe in the bentonite near the canister interface ($r = 26$ cm) for the base case ($Q = 0.1$ L/y) and Variant 2 ($Q = 1$ L/y and $Q = 4.7$ L/y)..... 74

Figure 2-49. Time evolution of the computed concentration of dissolved Cl^- and Fe in the bentonite near the granite interface ($r = 75$ cm) for the base case ($Q = 0.1$ L/y) and Variant 2 ($Q = 1$ L/y and $Q = 4.7$ L/y)..... 74

Figure 2-50. Time evolution of the computed volume fraction of magnetite and siderite in the canister ($r = 22$ cm) for the base case ($Q = 0.1$ L/y) and Variant 2 ($Q = 1$ L/y and $Q = 4.7$ L/y). 75

Figure 2-51. Time evolution of the computed volume fraction of greenalite and siderite in the bentonite near the canister interface ($r = 26$ cm) for the base case ($Q = 0.1$ L/y) and Variant 2 ($Q = 1$ L/y and $Q = 4.7$ L/y)..... 75

Figure 2-52. Spatial distribution of the computed pH for the base run and Variant 3. 76

Figure 2-53. Time evolution of the computed concentrations of dissolved Cl^- and Fe^{2+} siderite in the bentonite near the canister interface ($r = 2.605$ dm) for the base case and Variant 3. 76

Figure 3-1. Initial geometry of the generic configuration of the HLW disposal cell in a clay host rock. 82

Figure 3-2. Variants in terms of buffer thickness of generic HLW disposal cell towards the French liner concept or the Belgian/Dutch super container concept; another variant of the liner concept considers a low-pH cement/bentonite grout instead of the CEM I based buffer..... 84

Figure 3-3. Successive periods considered in reactive transport modelling (RTM) and evolution of temperature in the disposal cell; the effect of hydrogen production on water saturation was not taken into account (although indirectly in Chap 4). Only, periods II and III were considered in the present reactive transport modelling. It is worth noting that the safety function of the cement buffer with respect

EURAD Deliverable 2.17 – Integrated reactive transport models for assessing the chemical evolution at the disposal cell scale

to the steel overpack breaching significantly differs between the Belgian/Dutch and the French disposal concepts. 85

Figure 3-4. Key parameters used for the sensitivity analysis of the reactive transport modelling of the HLW cell, in particular for the durability of steel overpack and dissolution of the nuclear glass. 87

Figure 3-5. The HYTEC modelling was set in 1D-radial (axis-symmetric) geometry with boundary conditions located in the far-field of the clay host rock. 89

Figure 3-6. (a) Long-term generalized corrosion rates of carbon steel under anaerobic conditions selected for the reactive transport modelling at 25°C at neutral and high pH values where aerobic rates are also given for comparison). (b) Relationships that could be used to simulate the evolution from hyperalkaline pH values to more neutral values during the alteration of the cement-based buffer (relative rate = 1 corresponds to the anaerobic corrosion rate at neutral pH). 94

Figure 3-7. Base Case – 30 cm CEM I buffer. HYTEC modelling of the chemical evolution of the HLW cell with time with a selection of the key “disruptive” processes. Base Case – 30 cm CEM I buffer. . 100

Figure 3-8. Base Case – 30 cm CEM I buffer. HYTEC modelling of the progressive and moderate alteration of the solid phases of the host-rock. 103

Figure 3-9. Base Case – 30 cm CEM I buffer. HYTEC modelling of evolution with time of the cationic exchangeable occupancy of the host-rock. 104

Figure 3-10. Base Case – 30 cm CEM I buffer. HYTEC modelling of the progressive and significant decalcification of the cement phase in the concrete buffer. 107

Figure 3-11. Base Case – 30 cm CEM I buffer. HYTEC modelling of the progression of a moderate sulphate attack of the cement phase in the concrete buffer. 107

Figure 3-12. Base Case – 30 cm CEM I buffer. HYTEC modelling of the evolution of the generalized corrosion rate of Fe(0) with time, i.e. with the degree of chemical alteration of the CEM I buffer, close to the steel/concrete interface. 110

Figure 3-13. Pourbaix diagrams of the oxyhydroxide-silicate iron system iron calculated with CHESS/HYTEC at 25°C; activity $Fe^{2+} = 1 \times 10^{-5}$, activity $Ca^{2+} = 4 \times 10^{-3}$, total $H_4SiO_4 = 2 \times 10^{-4}$; in red highly alkaline conditions, in blue weakly alkaline conditions. 110

Figure 3-14. Base Case – 30 cm CEM I buffer. HYTEC modelling of steel generalized corrosion and formation of the two main corrosion products magnetite and greenalite. 111

Figure 3-15. Base Case – 30 cm CEM I buffer. HYTEC modelling of the partial dissolution of the international simple glass. 114

Figure 3-16. Base Case – 30 cm CEM I buffer. HYTEC modelling of the distribution of the IS glass mass initially and after 30,000 y, as well as of the relative kinetic rate of IS glass dissolution. 114

Figure 3-17. Base Case – 30 cm CEM I buffer. HYTEC modelling of evolution of some key aqueous parameters in the full HLW cell. 115

Figure 3-18. Variant Case – 5 cm CEM I buffer. HYTEC modelling of the chemical alteration of the concrete buffer and host-rock. 116

Figure 3-19. Variant Case – 100 cm CEM I buffer. HYTEC modelling of the chemical alteration of the concrete buffer and host-rock at 50,000 years. 117

Figure 3-20. Variant Case – 5 cm CEM I buffer. HYTEC modelling of the steel generalized corrosion and IS glass dissolution. 118

Figure 3-21. Variant Case – 100 cm CEM I buffer. HYTEC modelling of the chemical evolution of all HLW components at 50,000 years. 119

EURAD Deliverable 2.17 – Integrated reactive transport models for assessing the chemical evolution at the disposal cell scale

Figure 3-22. Variant Case – 5 cm low-pH grout. HYTEC modelling of the chemical alteration of the low-pH grout and host-rock. 120

Figure 3-23. Variant Case – 5 cm low-pH grout. HYTEC modelling of the steel corrosion and IS glass dissolution..... 120

Figure 4-1. Temperature time series simulated a generic HLW cell in clay surrounded by a cement grout buffer of 5 cm thick and after 120 years of storage (communication with E. NEEFT, COVRA). 127

Figure 4-2. Decalcification and pH evolution in the concrete material for the base case simulated with iCP (T = 25°C and full water saturation). Temporal evolution in the first cell next to the liner (left) and spatial profile at t = 200 y (right). Concrete thickness = 5 cm. 131

Figure 4-3. Decalcification and pH evolution in the concrete material for the base case simulated with iCP (T=25°C and full water saturation). Temporal evolution in the first cell next to the liner (left) and spatial profile at t = 3,000 y (right). Concrete thickness = 30 cm. 131

Figure 4-4. Temporal sequence of the other minerals in the first cell of the concrete material next to the liner. Concrete thickness of 5 cm (left) and 30 cm (right) for the base case with iCP..... 132

Figure 4-5. Decalcification sequence and pH evolution in the concrete material for the base case (left) and the case considering the thermal transient (right). Concrete thickness = 5 cm. 133

Figure 4-6. Decalcification sequence and pH evolution in the concrete material for the base case (left) and the case considering the thermal transient (right). Concrete thickness = 30 cm. 133

Figure 4-7. Temporal evolution of (S,Al)-bearing minerals during the thermal transient in the concrete material. Concrete thickness = 5 cm. 134

Figure 4-8. Comparison of the decalcification sequences between the base case (full line) and the case considering both the thermal transient and the partial desaturation (dotted line). Temporal evolution in the first cell next to the liner for concrete thicknesses of 5 cm (left) and 30 cm (right). 134

Figure 4-9. Comparison of the pH evolution between the base case (full line) and the case considering both the thermal transient and the partial desaturation (dotted line). Temporal evolution in the first cell next to the liner for concrete thicknesses of 5 cm (left) and 30 cm (right). 135

Figure 5-1. – Schematic representations of the generic disposal cell considered for intermediate radioactive waste in clay..... 137

Figure 5-2. Location of the 1D model 138

Figure 5-3. 1D configuration of the EBS materials and the host rock for the ILW cell in clay..... 139

Figure 5-4. Mineral changes at 100,000 years of the ILW disposal cell in clay assuming full-water saturation (Case 1a). 140

Figure 5-5. Mineral changes at 100 000 years of the ILW disposal cell in clay assuming simplified 50 % saturation conditions in the system. 142

Figure 5-6. Mineral changes of the ILW in contact with clay after 100 000 years assuming 10% water saturation. 143

Figure 5-7. Comparison of final porosity profiles of the ILW in clay of the full, 50%, and 10% water saturation cases. 143

Figure 5-8. Mineral changes at 100,000 years for the ILW disposal cell in clay without considering feedback between the chemical reactions and the porosity..... 144

Figure 5-9. Comparison of the reactions of calcite and M-S-H between enabling porosity feedback and constant porosity for the ILW disposal cell in clay. 145

Figure 5-10. Mesh discretization of the 2D ILW disposal cell in clay. 146

EURAD Deliverable 2.17 – Integrated reactive transport models for assessing the chemical evolution at the disposal cell scale

Figure 5-11. Illustration of the evolution of the volume fraction of calcite in the 2D ILW cell in clay...	147
Figure 5-12. Dolomite volume fraction evolution in the 2D ILW cell in clay.	148
Figure 5-13. Evolution of the portlandite volume fraction in the 2D ILW cell in clay.	149
Figure 5-14. CSHQ-JenD volume fraction evolution in the 2D ILW cell in clay.	150
Figure 5-15. Volume fraction evolution of ettringite in the 2D ILW cell in clay.	151
Figure 5-16. pH evolution in the 2D ILW cell in clay.....	152
Figure 5-17. Porosity evolution in the 2D ILW cell in clay.	153
Figure 5-18. Comparison of the main minerals between the 2D and 1D disposal ILW disposal cell in clay.	154
Figure 6-1. 1D abstractions of the ILW disposal cell in granite.	158
Figure 6-2. Mineral changes of the 1D ILW in granite at 0, 1e4, 5e4, and 1e5 years in the Y direction.	159
Figure 6-3. Changes in minerals over time at different observation points for the 1D ILW disposal cell in granite in the Y-direction.....	161
Figure 6-4. Changes in porosity over time at different observation points for the 1D ILW disposal cell in granite in the Y-direction.....	161
Figure 6-5. Concentration of species over time at different observation points for the 1D ILW cell in granite in the Y-direction.....	162
Figure 6-6. pH changes over time for the 1D ILW cell in granite in the Y-direction.	163
Figure 6-7. Mineral changes of the 1D ILW disposal cell in granite at 0, 1e4, 5e4, and 1e5 years in the X-direction.....	164
Figure 6-8. Mineral changes over time at different observation points for the 1D ILW cell in granite in the X-direction.....	165
Figure 6-9. Changes in porosity over time at different observation points for the 1D ILW disposal cell in granite in the X-direction.....	166
Figure 6-10. The concentration of species over time at different observation points for the 1D ILW cell in granite in the X-direction.	166
Figure 6-11. pH changes over time for the 1D ILW cell in granite in the X-direction.	167
Figure 6-12. 2D mesh discretization of the ILW cell in granite.	168
Figure 6-13. Volume fraction evolution of CSHQ-JenD in the 2D ILW cell in granite.	169
Figure 6-14. Evolution of the volume fraction of CSHQ-TobH in the 2D ILW cell in granite.	170
Figure 6-15. Volume fraction evolution of calcite in the 2D ILW cell in granite.	171
Figure 6-16. Portlandite volume fraction evolution in the 2D ILW cell in granite.....	172
Figure 6-17. pH evolution in the 2D ILW cell in granite.....	173
Figure 6-18. Porosity evolution in the 2D ILW cell in granite.	174
Figure 6-19. Comparison of the 1D and 2D models in the Y-direction for the ILW disposal cell in granite.	175
Figure 6-20. Comparison of the 1D and 2D models in the X-direction of the ILW cell in granite.....	175

List of Tables

<i>Table 2-1. Base run, sensitivity cases and variants considered for the reactive transport model of the HLW disposal cell in granite. The specific features of each sensitivity case and variant are highlighted with boldface. Non-isothermal conditions are assumed in all cases. Partial desaturation is disregarded.</i>	29
<i>Table 2-2. Chemical reactions and equilibrium constants for aqueous complexes and minerals at 25°C taken from ThermoChimie v10.a (Giffaut et al., 2014).</i>	34
<i>Table 2-3. Chemical composition of the ISG and the French reference glass SON-68 (Debure et al., 2012).</i>	35
<i>Table 2-4. Chemical and elemental compositions of the ISG (Gin et al., 2015).</i>	36
<i>Table 2-5. Initial and residual kinetic constants, k_0 and k_r, saturation threshold, CSi^*, specific surface, σ, effective diffusion coefficient, and porosity, Φ, of the ISG (De Windt et al., 2006).</i>	37
<i>Table 2-6. Thermal and hydrodynamic parameters of the bentonite and granite (Zheng and Samper 2008; Zheng et al., 2011, based on ENRESA 2006, Samper et al., 2016, 2018).</i>	39
<i>Table 2-7. Initial chemical composition of the FEBEX bentonite, EDZ and granite porewater (Samper et al., 2016).</i>	40
<i>Table 2-8. Protolysis constants for surface complexation reactions for a triple-site sorption model (Bradbury and Bayens, 2005) and selectivity constants for cation exchange reactions in the FEBEX bentonite (ENRESA, 2006).</i>	41
<i>Table 2-9. Chemical composition of the granite boundary water used in Sensitivity Case 2 (Samper et al., 2016).</i>	42
<i>Table 2-10. Calculated chemical composition of the MX-80 bentonite porewater at pH = 8 and at initial dry density of 1600 kg/m³ (Bradbury and Baeyens, 2003).</i>	43
<i>Table 2-11. Cation occupancies and selectivity coefficients for cation exchange reactions in the MX-80 bentonite (Bradbury and Baeyens, 2002; 2003).</i>	43
<i>Table 2-12. Chemical composition of the SGW2 and SGW3 Czech crystalline rock porewaters (Červinka et al., 2018).</i>	44
<i>Table 3-1. Base and variant configurations investigated by HYTEC modelling of the chemical evolution of the HLW cell.</i>	86
<i>Table 3-2. Initial mineralogy, specific surface area and cation exchange properties the clay host rock considered in the HYTEC modelling (adapted from Marty et al., 2015).</i>	90
<i>Table 3-3. Initial porewater chemistry of the clay host rock at 25°C considered in the HYTEC modelling (adapted from Marty et al., 2015).</i>	90
<i>Table 3-4. Initial porosity and mineralogical composition of the CEM I-based concrete at 25°C considered in the HYTEC modelling (adapted from Kosakowski, 2020).</i>	92
<i>Table 3-5. Initial porewater chemistry of the CEM I-based concrete at 25°C considered in the HYTEC modelling.</i>	92
<i>Table 3-6. Recipe of the bentonite/cement grout used in the BACUCE experiment (De Windt et al., 2020; Wittebroodt et al., 2023).</i>	93
<i>Table 3-7. Simplified initial mineralogy of the bentonite/cement grout at 25°C considered in the HYTEC modelling.</i>	93

EURAD Deliverable 2.17 – Integrated reactive transport models for assessing the chemical evolution at the disposal cell scale

Table 3-8. Initial chemical composition of the <i>international simple glass</i> (adapted from Debure et al., 2012) considered in the HYTEC modelling.	95
Table 3-9. Kinetic parameters for glass dissolution considered in the HYTEC modelling (Equation [3-5]).	96
Table 3-10. Base Case – 30 cm CEM I buffer. Duration indicators of the durability of the CEM I concrete buffer with respect to high-pH buffering and the completion of decalcification.	107
Table 3-11. Modelling cases for different buffer thicknesses. Duration indicators of the durability of the CEM I concrete buffer with respect to high-pH buffering and the completion of decalcification.	116
Table 4-1. Base and variant configurations investigated by HYTEC modelling of the chemical evolution of the HLW cell.	124
Table 4-2. Assemblage of mineralogical phases of sound COx adapted from Marty et al. (2014). The chemical composition of the minerals and their equilibrium constants are coming from the <i>Thermochimie</i> database. Selectivity coefficients for illite/smectite mix (Gaucher et al., 2009).	125
Table 4-3. Initial pore water composition in the Callovo-Oxfordian clay.	126
Table 4-4. Secondary minerals allowed to precipitate in the COx claystone.	126
Table 4-5. Assemblage of mineralogical phases of the concrete components adapted from the OPC chemical description in BRGM (2013).	128
Table 4-6. Initial concrete porewater composition, including dissolved alkali.	128
Table 4-7. Secondary minerals allowed to precipitate in the concrete domain.	129
Table 4-8. Comparison of the decalcification duration in the concrete materials by considering or not the thermal transient and for both thicknesses of concrete.	133
Table 4-9. Comparison of the decalcification duration in the concrete materials by considering or not the thermal transient and the partial desaturation for both thicknesses of concrete.	135
Table 10. Simulation cases for the ILW disposal cell in clay.	138
Table 11. Simulation cases for the ILW disposal cell in granite.	156
Table 6.12. Chemical composition of the granite boundary water (Samper et al., 2016).	159

Abbreviations

CEC: Cation Exchange Capacity

CEM: Concrete-Equivalent Mortar

COx: Callovo-Oxfordian

EDZ: Excavated Disturbed Zone

HLW: High-Level radioactive Waste

ILW: Intermediate radioactive Waste

ISG: International Simple Glass

OPC Ordinary Portland Cement

PFE: Porosity Feedback Effect

RTM: Reactive Transport Model

SF: Spent Fuel

SRG: Spanish Reference Granite

TSO: Technical Safety Office

URF: Underground Research Facility

WMO: Waste Management Organization

1. Introduction

1.1 Reactive transport modelling of the multiple barrier system

Most strategies of geologic radioactive disposal rely on a multiple barrier system, consisting of both natural and engineered materials, to prevent or delay the contact of groundwater with the waste and radionuclide release to the environment. The waste packages and their immediate surroundings (near field) are a subsystem of particular interest for both intermediate or high-level radioactive waste (ILW/HLW).

The modelling of the chemical evolution of such a subsystem in space and time is a key point for assessing the durability of the different near-field components (used in performance assessment) but as well a chemical background for modelling the speciation and migration of radionuclides (used in safety assessment). Reactive transport models (RTM) have been central to understanding and assessing how thermal, hydrological, and geochemical processes are coupled in these containment barriers, which are expected to experience a range of temperatures and geochemical conditions, yet, must maintain their integrity for more than 100,000 years.

Reactive transport models are an invaluable component in assessing the potential performance of a repository, which requires understanding how the barriers evolve in space and time (De Windt and Spycher, 2019; Idiart *et al.*, 2020). Reactive transport models can simulate the transport and chemical reactions of multiple solutes (and gases) and their chemical interactions within the multi-barrier system over various temporal and spatial scales (Bildstein *et al.*, 2019). Reactive transport modelling is also capable of great generality and flexibility and can be applied to a wide range of natural processes, as well as to engineering issues such as metal corrosion or bentonite alteration. Although the use of RTMs for deterministic predictive simulations is limited, these models can help constrain future repository behaviour with sensitivity analyses and scenario modelling of the various disposal subsystems (e.g., the sealing of a disposal cell).

1.2 Aims and structure of this deliverable

The Task 4 of the ACED Work Package addresses the following key tasks: 1) upscaling the experimental degradation processes of tasks 2 and 3 of ACED to the scale of a disposal cell; 2) discriminating by modelling the chemical interactions between the cell components and quantifying their chemical degradation and durability over space and time; and 3) integrating of all the knowledge gained within the ACED WP into a robust and manageable numerical model, which reflects the current state-of-the-art (SOTA).

The Subtask 4.1 of the ACED WP is devoted to the conceptual and mathematical formulations for a mechanistic based model (reactive transport model) to simulate the chemical evolution at the disposal cell scale. Subtask 4.1 tackled with the full design of the cell, not only at the waste package scale. That is to say, the waste form and its overpack, all the engineered barriers, but also the host-rock (granitic or argillaceous geological formations).

The work performed in the Subtask 4.1 has been distributed among two consecutive and consistent deliverables. The deliverable D2.16 (Samper *et al.*, 2021) has compiled the conceptual and mathematical formulations of mechanistic-based models which took into account the initial state-of-the-art (SOTA) knowledge on models and parameters. Deliverable D2.16 has provided for detailed information on the definition of the generic configurations of the different disposal cells, the evolution scenarios, the selection of the modelling laws and parameters... For the sake of a stand-alone understanding, the present deliverable D2.17 has given the configurations, scenarios and parameters that were eventually used in the HLW simulations. The changes between the reactive transport configurations, scenarios and parameters of two deliverables were, nevertheless, minor.

This deliverable D2.17 is divided into four main chapters following the same reference system as D2.16. The first two chapters focus on the RTM of a HLW disposal cell, Chapter 2 in a granitic host rock, and

EURAD Deliverable 2.17 – Integrated reactive transport models for assessing the chemical evolution at the disposal cell scale

Chapter 3 in a clay host rock. The sequences of these chapters on HLW are very similar: i) configuration and conceptual models, ii) numerical parameters, iii) modelling of the base case, iv) modelling of the variant cases and sensitivity analysis, v) conclusion and perspectives. The next two chapters are devoted to the RTM of a ILW disposal cell, similarly divided in clay (Chapter 4) and granitic (Chapter 5) host rocks

2. Modelling of a full HLW disposal cell in granite

The work has been done by Javier Samper, Luis Montenegro, Alba Mon and Aurora-Core Samper from University Da Coruña (UDC) and Enrique García (ENRESA).

This chapter presents the reactive transport model of a HLW disposal cell in granite. It is divided in 8 sections starting with the description of the HLW disposal cell, and continuing with the description of the conceptual and numerical models, and the computer code. Then, model predictions for the base run are presented for Period II (canister corrosion and interactions of corrosion products and bentonite) and Period III (glass dissolution, canister corrosion and interactions of glass, corrosion products and bentonite). Afterwards, the main results of the sensitivity analysis, the sensitivity cases and the variants are presented. The chapter concludes with the summary and main conclusions.

2.1 Description of the disposal cell concept

The materials and dimensions of the waste form, the overpack, the engineered barrier and the host rock selected for the HLW disposal cell in granite were defined by De Windt et al. (2020). The selected materials are similar to those considered in Task 3 of ACED. The generic configuration of the HLW disposal cell concept in granitic host rock includes (De Windt et al., 2020; Samper et al. 2021):

- 1) The vitrified waste (40 cm in diameter) which is explicitly considered in the reactive transport model and is coupled with the rest of the engineered barrier components.
- 2) The carbon-steel canister (5 cm thick).
- 3) The bentonite buffer (75 cm thick) which is composed of water-saturated FEBEX bentonite with a dry density of 1600 kg/m³.
- 4) The Spanish Reference Granitic (SRG) host rock. A thickness of 25 m is considered in the calculations.

The layout of the representative HLW disposal cell concept in a granitic host rock is shown in Figure 2-1. The HLW disposal cell concept in granite is based on the Spanish spent fuel reference concept in granite, known as ENRESA 2000 (ENRESA, 2001). The main differences are the type of waste (vitrified waste vs. spent fuel) and the dimensions of the carbon-steel canister (45 cm in diameter for vitrified waste and 90 cm for spent fuel). In ENRESA (2001) the carbon steel canisters are placed in long horizontal disposal drifts. Canisters are surrounded by compacted bentonite. Access is accomplished by "main drifts" which run perpendicular to the disposal drifts. The main drifts meet at a central area, which includes the required underground infrastructure. Communications between the surface and the central underground area are accomplished by 3 access shafts and a ramp. Figure 2-2 shows a scheme of the underground infrastructure in the ENRESA 2000 spent-fuel repository concept in granite.

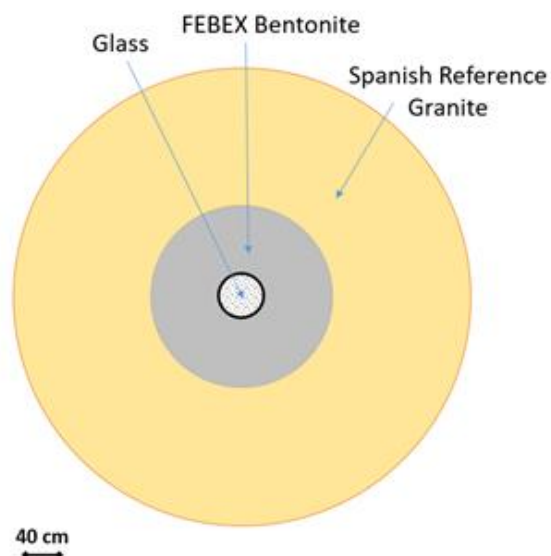


Figure 2-1. Layout of the representative HLW disposal cell concept in a granitic host rock which includes: vitrified waste (40 cm diameter), steel canister (5 cm thick), FEBEX bentonite (75 cm thickness) and Spanish Reference Granite.

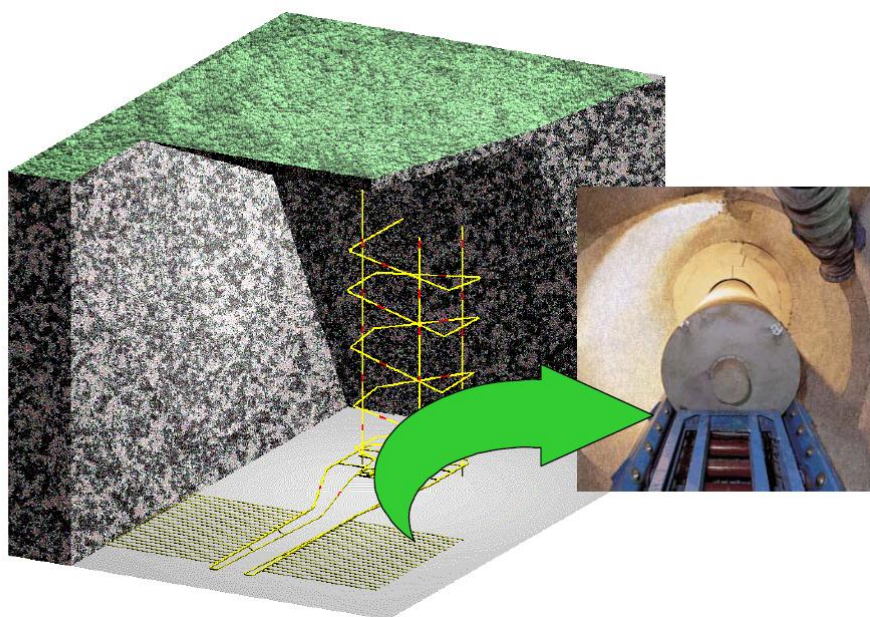


Figure 2-2. Underground installations of a radioactive waste repository in granite according to the spent-fuel Spanish Reference Concept (ENRESA, 2001).

The canister measures 4.54 m in length and 0.90 m in diameter in the Spanish spent fuel reference concept in granite (ENRESA, 2001). The thickness of the wall of the spent-fuel canister in the Spanish concept is 0.10 m at the cylindrical shield and 0.12 m at the ends. After being unloaded from the reactor, the fuel elements are temporarily stored for their thermal power to decay to a level at which they may be disposed. It should be pointed out that the thickness of the overpack in the Spanish concept is larger than that adopted for the ACED disposal cell in granite, which is equal to 5 cm to take it to the thickness of the overpack in the ACED disposal cell concept in clay.

EURAD Deliverable 2.17 – Integrated reactive transport models for assessing the chemical evolution at the disposal cell scale

Canisters are disposed in cylindrical disposal cells, constructed with blocks of precompacted bentonite of 1.700 kg/m³ dry density to achieve a final dry density of 1.600 kg/m³. The blocks are initially unsaturated with a gravimetric water content of 14%. The disposal drifts of 500 m in length and 2.4 m in diameter (Figure 2-3) are located at a depth of 500 m in the granitic host formation. Canisters are separated 2 m apart one another. Galleries are separated 35 m to prevent exceeding a temperature of 100 °C in the bentonite. The detailed dimensions of a disposal cell are shown in Figure 2-4.

DISPOSAL CONCEPT

- Deep disposal
- Crystalline rock
- Spent fuel
- Carbon steel canister
- Horizontal emplacement
- Bentonite buffer

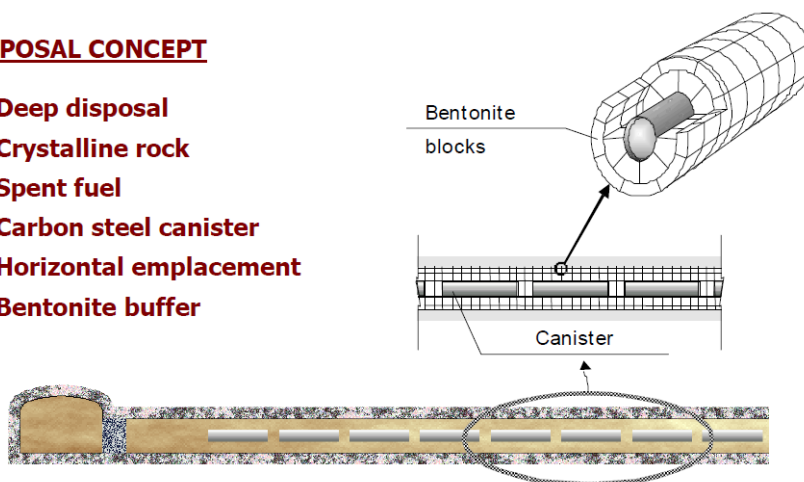


Figure 2-3. Longitudinal section of a disposal drift in the spent fuel Spanish repository concept in granite (ENRESA, 2001).

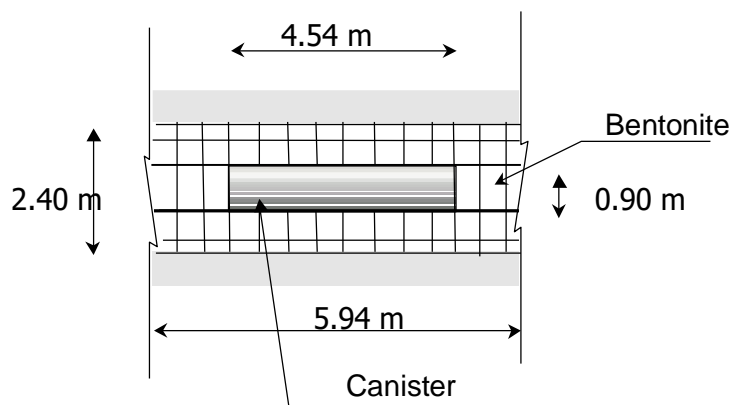


Figure 2-4. Dimensions of a disposal cell in the spent fuel Spanish repository concept in granite (ENRESA, 2001).

It is important to point out that the reference HLW disposal cell concept in granite used in ACED is a generic concept which is not specific for any country, but aims at being representative for several national concepts. In fact, the Spanish HLW disposal cell concept in granite does not include vitrified waste. For simplification purposes, it was decided to select for the disposal cell in granite the same type of glass as that of the HLW disposal cell in clay: the International Simple Glass, ISG (Samper et al., 2021).

2.2 Conceptual model

2.2.1 Narrative evolution

The HLW disposal cell in granite involves the following interfaces: bentonite/granite host rock, carbon-steel/bentonite and vitrified waste/carbon-steel canister. A detailed conceptual description of the geochemical evolution of these three interfaces was presented in EURAD Deliverable 2.16 (Samper et al., 2021) based on EURAD Deliverables D2.4 (Neeft et al., 2020b) and D2.5 (Deissmann et al., 2020).

A reference base case and several sensitivity cases and variants have been performed for the reactive transport model of the geochemical evolution of the HLW disposal cell in granite. The model considers three successive periods. The first one (Period I) covers the oxic transient stage. Period II starts when the bentonite barrier is fully saturated, and the anoxic conditions are prevailing. Canister corrosion, the interactions of corrosion products and the bentonite and the interactions of bentonite and granite are considered in this period. Finally, Period III starts after canister failure and considers glass alteration and the interactions of glass with corrosion products and uncorroded iron. These three periods are consistent with those adopted for the HLW disposal cell in clay in the D2.16 (Samper et al., 2021). It is important to point out that only Periods II and III are considered in the model.

2.2.2 Sensitivity cases and variants

Sensitivity cases and variants were selected based on the following criteria:

- 1) A priori expert evaluation of potentially relevant processes and features for the long-term geochemical evolution of the repository. Examples of these processes and features include: the consideration of a different value of the silica saturation threshold in the glass kinetic dissolution model and the consideration of the excavation damaged zone (EDZ) and a larger hydraulic conductivity of the host rock.
- 2) The variants needed to account for the differences in the components, geometry, and properties of the different materials among national concepts. Examples of these variants include: the type of bentonite (FEBEX and MX80) and the host rock (Spanish granite and reference Czech crystalline rock).

The sensitivity cases and variants for the reactive transport model of the geochemical evolution in a HLW disposal cell in granite are listed in Table 2-1.

Sensitivity Case 1 considers the same vitrified waste ISG in Period III but with a different value of the silica saturation threshold, C_{Si}^* , used in the kinetic rate law of glass dissolution (see Eq. 2.7). Sensitivity Case 2 considers a granitic porewater with a chloride concentration 8 times greater ($3.2 \cdot 10^{-3}$ mol/L) than the value used in the base case ($3.949 \cdot 10^{-4}$ mol/L).

Compacted MX-80 bentonite (instead of FEBEX bentonite) with a thickness of 35 cm is considered in the Variant 1 (Figure 2-5). Variant 2 considers the EDZ and a larger hydraulic conductivity of the host rock (Figure 2-5). Variant 3 considers the conditions of the Reference Czech crystalline rock (Figure 2-5). Additional information and specific references for the sensitivity cases and variants are presented in Section 2.3.4.

The results of Sensitivity Case 1 are not shown here, but are presented in Deliverable D2.19 (Samper et al., 2023).

Table 2-1. Base run, sensitivity cases and variants considered for the reactive transport model of the HLW disposal cell in granite. The specific features of each sensitivity case and variant are highlighted with boldface. Non-isothermal conditions are assumed in all cases. Partial desaturation is disregarded.

Case	Period	Steel canister	Bentonite buffer	Host rock	Nuclear Glass
Base	II	Chemical form: Fe(0) Thickness = 5 cm. Porous.	Water-saturated FEBEX bentonite Thickness =75 cm	Spanish Reference Granite (SRG)	No
	III	Porous, partly filled with corrosion products			ISG
Sensitivity case 1	II	Chemical form: Fe(0) Thickness = 5 cm. Porous.	Water-saturated FEBEX bentonite Thickness =75 cm	SRG	No
	III	Porous, partly filled with corrosion products			ISG with different saturation threshold
Sensitivity case 2	II	Chemical form: Fe(0) Thickness = 5 cm. Porous.	Water-saturated FEBEX bentonite Thickness =75 cm	SRG with a larger Cl⁻ concentration in granitic porewater	No
	III	Porous, partly filled with corrosion products			ISG
Variant 1	II	Chemical form: Fe(0) Thickness = 5 cm. Porous.	MX80 bentonite Thickness = 35 cm	SRG	No
	III	Porous, partly filled with corrosion products			ISG
Variant 2	II	Chemical form: Fe(0) Thickness = 5 cm. Porous.	Water-saturated FEBEX bentonite Thickness =75 cm	SRG with an EDZ (1 m thickness) and a larger hydraulic conductivity of the host rock	No
	III	Porous, partly filled with corrosion products			ISG
Variant 3	II	Chemical form: Fe(0) Thickness = 5 cm. Porous.	Water-saturated FEBEX bentonite Thickness =75 cm	Czech Reference Crystalline Rock	No
	III	Porous, partly filled with corrosion products			ISG

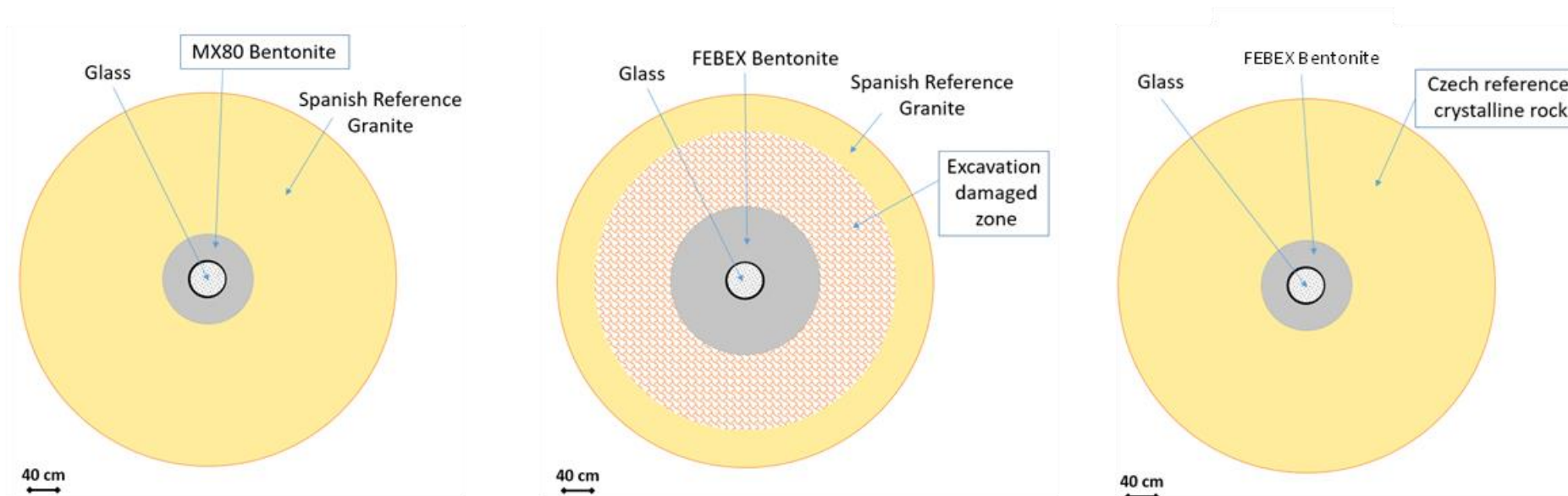


Figure 2-5. Geometric configurations of the variants considered for the HLW disposal cell in granite. Variant 1 considers MX bentonite (35 cm thick). Variant 2 considers an excavation damaged zone (EDZ) of 1 m thickness. Variant 3 considers the Czech reference crystalline rock.

2.2.3 Hydrodynamic processes

Although the bentonite blocks are initially unsaturated, the reactive transport model of the HLW disposal cell in granite assumes that the bentonite is initially water-saturated because the bentonite barrier will become fully saturated in less than 50 years (Zheng and Samper, 2008).

The model accounts for molecular diffusion. The hydraulic conductivity of the bentonite is extremely low ($6 \cdot 10^{-14}$ m/s). Therefore, advection is negligible and solute diffusion is the main solute transport mechanism. All the water is assumed to be accessible to solutes.

Solute transport processes in the granite include molecular diffusion and advection which is assumed to be parallel to the axis of gallery.

As pointed by Ortiz *et al.* (2002), it is assumed in the model that $H_2(g)$ migrates through cyclic opening and closure of discrete preferential pathways in the bentonite buffer. Therefore, partial desaturation of the bentonite barrier due to the formation of gas phase is disregarded in the HLW disposal cell in granite. The model considers the diffusion of dissolved hydrogen, $H_2(aq)$, and disregards $H_2(g)$ gas transport through the gaseous phase.

2.2.4 Thermal processes

The thermal transient stage and the cooling of the vitrified waste is considered in the reactive transport model of the HLW disposal cell in granite. Figure 2-6 shows the time evolution of the temperature at the canister-bentonite and the bentonite-granite interfaces computed by E. Neeft (COVRA) with the thermal parameters of the dry and saturated FEBEX bentonite for a HLW disposal cell in granite (Neeft, 2020a). These calculations are based on the requirement that the temperature in the bentonite buffer does not exceed 100°C and correspond to the following geometric configuration: 1) Vitrified waste (0.42 m of diameter), 2) Stainless steel (5 mm thick), 3) Air gap (13 mm thick), 4) Carbon-steel overpack (7.5 cm), 5) Bentonite buffer (75 cm); and 6) Granitic rock (100 m long).

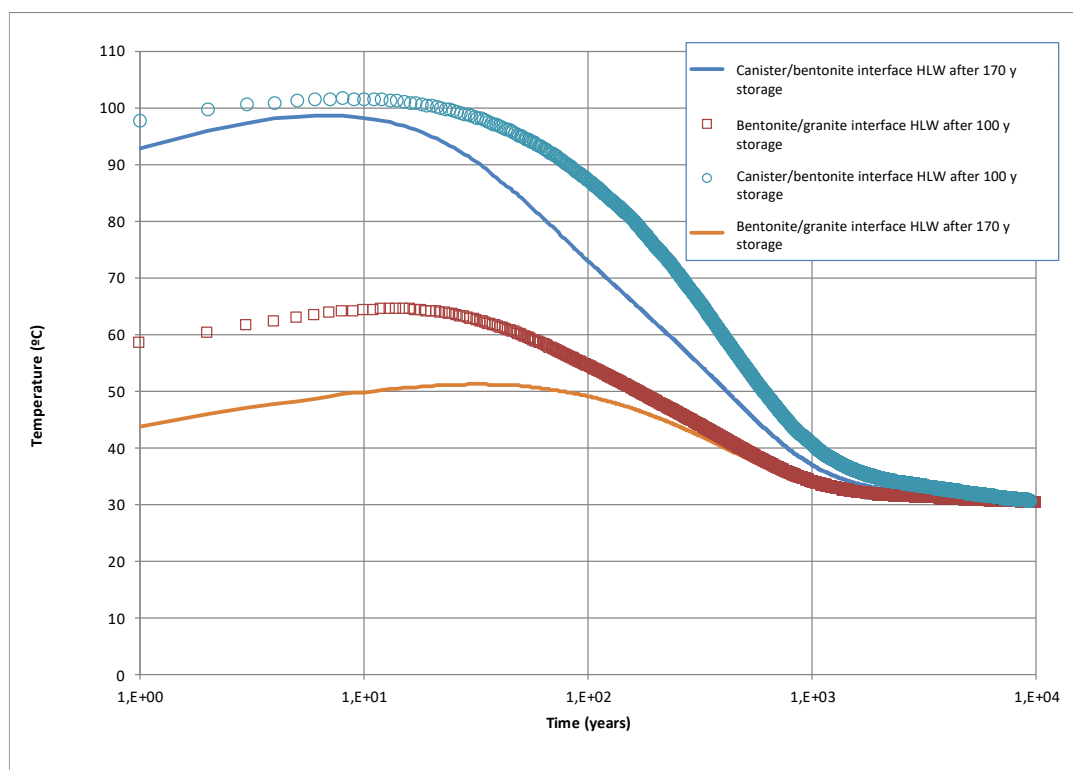


Figure 2-6. Calculated time evolution of the temperature in a HLW disposal cell in granite after 100 years of storage (wet bentonite) and 170 years of storage (dry bentonite) at the canister-bentonite and the bentonite-granite interfaces (Neeft, 2020a; personal communication).

It should be pointed out that the temperature at the buffer/canister interface depends on the decay time, the canister loading and the distance between galleries. The thermal properties for the bentonite buffer and the granitic host rock used in the calculations were taken from the Spanish Reference Granite (Neeft et al., 2020a). The time evolution of the temperatures at the canister-bentonite and the bentonite-granite interfaces was calculated by assuming a storage time during which the fuel elements are kept releasing heat and radioactivity to acceptable levels. The considered storage times range from 100 to 170 years (Neeft, 2020a). These storage times correspond to the Reference Concept of the Netherlands.

All the runs (base, sensitivity cases and variants) in the reactive transport model of the HLW disposal cell in granite are non-isothermal. The heat transport equation was solved together with the reactive transport equations. The temperatures were prescribed at the inner and outer bentonite boundaries (canister/bentonite and bentonite/granite interfaces). The time evolution of the temperatures at the boundaries is shown in Figure 2-7.

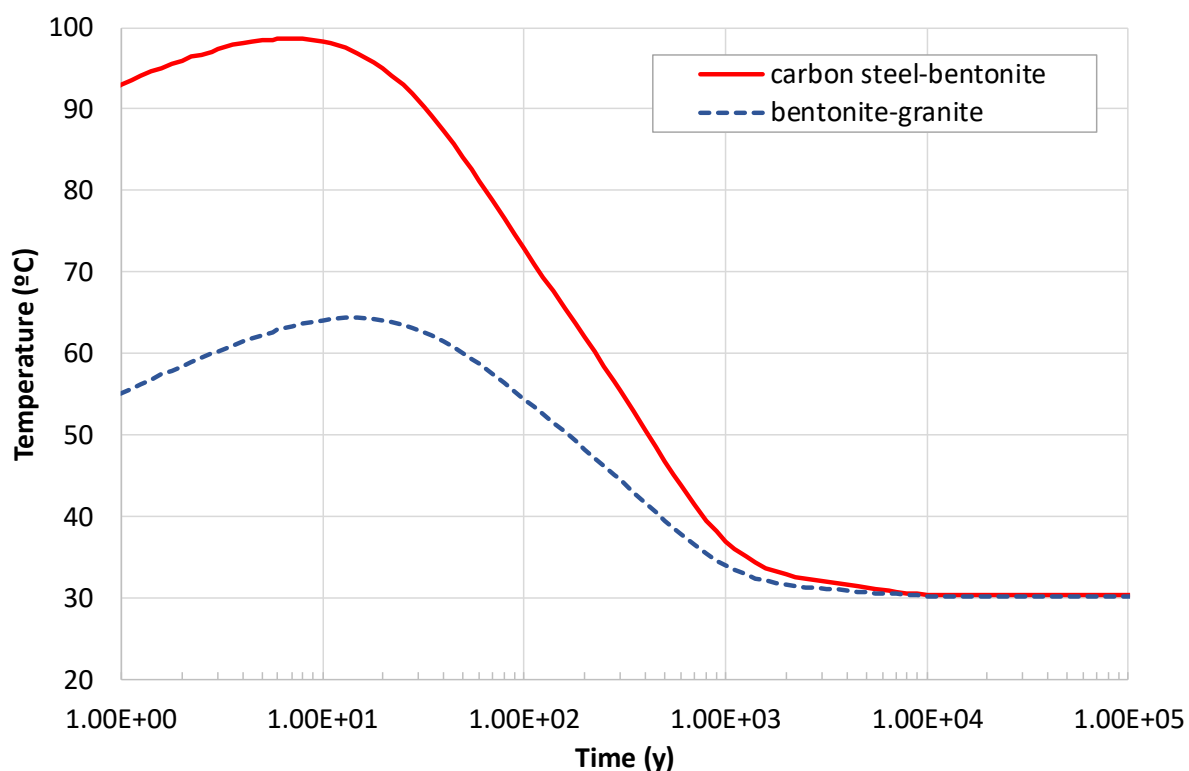


Figure 2-7. Time evolution of the temperatures at the canister/bentonite and bentonite/granite interfaces. These temperatures were prescribed in the reactive transport model of the HLW disposal cell in granite.

2.2.5 Chemical processes

The conceptual geochemical model of the HLW disposal cell in granite includes the following processes: 1) Carbon-steel canister corrosion, 2) Vitrified waste dissolution, 3) Aqueous complexation; 4) Acid/base aqueous reactions; 5) Redox aqueous reactions; 6) Mineral dissolution/precipitation; 7) Cation exchange of Ca^{2+} , Mg^{2+} , Fe^{2+} , Na^+ and K^+ ; and 8) Surface complexation of H^+ on three types of sorption sites (strong sites, $\text{S}^{\circ}\text{OH}$, weak #1 sites, $\text{S}^{\text{w}1}\text{OH}$ and weak #2 sites, $\text{S}^{\text{w}2}\text{OH}$). While aqueous complexation, acid/base, redox and dissolution/precipitation reactions take place in all the materials

considered in the HLW disposal cell, cation exchange and surface complexation reactions occur only in the bentonite barrier.

The chemical processes were selected based on their relevant role in each of the four materials considered in the model of the HLW disposal cell in granite. The set of chemical processes could be improved, especially for mineral dissolution/precipitation in the granitic host rock by considering the geochemical processes of other national programmes in crystalline rocks such as those of Sweden and Finland which have been compiled in Deliverable D2.4 of ACED WP (Neeft et al., 2019). The geochemical system is defined in terms of 14 aqueous primary species (H_2O , H^+ , $O_2(aq)$, Ca^{2+} , Mg^{2+} , Na^+ , K^+ , Fe^{2+} , Al^{3+} , Cl^- , SO_4^{2-} , HCO_3^- , H_4SiO_4 , and $B(OH)_4^-$), 3 surface primary species (S^sOH , $S^{w1}OH$ and $S^{w2}OH$), 39 secondary aqueous species, 11 mineral phases, 5 exchanged cations and 13 surface complexes. The secondary aqueous species were identified from speciation runs performed with EQ3/6 (Wolery, 1992). The Gaines-Thomas convention is used for cation exchange reactions (Appelo and Postma, 1993). The secondary surface complexes include: S^sOH^{2+} , S^sO^- , S^sOFe^+ , S^sFeOH , $S^sFe(OH)^{2-}$, $S^{w1}OH^{2+}$, $S^{w1}O^-$, $S^{w1}OFe^+$, $S^{w2}OH^{2+}$, and $S^{w2}O^-$. Surface complexation reactions in the bentonite were modelled with the non-electrostatic triple-site sorption model of Bradbury and Baeyens (1997) and (2005). Chemical reactions and the equilibrium constants at 25°C for aqueous species and mineral dissolution/precipitation used in the model are listed in Table 2-2.

All the reactions are assumed at chemical equilibrium, except smectite dissolution, carbon-steel corrosion and vitrified waste dissolution are kinetically controlled. The following kinetic rate law is used for the former two:

$$r_m = s_m k_m e^{\frac{-E_a}{RT}} \left(\prod_{i=1}^{N_T} a_i^{p_{mi}} \right) |(\Omega_m^\Theta - 1)^\eta| \quad [2.1]$$

where r_m is the dissolution/precipitation rate ($mol/m^2/s$), k_m is the kinetic rate constant ($mol/m^2/s$) at 25°C, E_a is the activation energy, R is the gas constant ($J/K \cdot mol$), T is the temperature (K), Ω_m is the saturation index which is equal to the ratio of the ion activity product to the equilibrium constant (dimensionless), Θ and η are empirical parameters, $|\cdot|$ is the absolute value operator, and $\prod_{i=1}^{N_T} a_i^{p_{mi}}$ is a catalytic term which accounts for the activities a_i of the aqueous species and p_{mi} is the exponent for the i -th aqueous species in the m -th mineral phase dissolution reaction. Variable s_m is taken equal to -1 for precipitation and 1 for dissolution to ensure that the dissolution/precipitation rate is always positive for dissolution and negative for precipitation for any values of the parameters Θ and η . Details for the kinetic reaction equations for carbon steel, vitrified waste and smectite are given below.

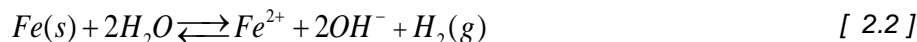
The dissolution/precipitation rate in $mol/m^2/s$, r_m , is multiplied by the mineral specific surface area, σ , to get the dissolution/precipitation rate in $mol/m^3/s$, R_m . The specific surface area, σ , is the surface area of the mineral per unit fluid volume. It is assumed that σ remains constant.

Table 2-2. Chemical reactions and equilibrium constants for aqueous complexes and minerals at 25°C taken from ThermoChimie v10.a (Giffaut et al., 2014).

Aqueous complexes	Log K
$\text{CaCO}_3(\text{aq}) + \text{H}^+ \Leftrightarrow \text{Ca}^{2+} + \text{HCO}_3^-$	7.1100
$\text{CaHCO}_3^+ \Leftrightarrow \text{Ca}^{2+} + \text{HCO}_3^-$	-1.100
$\text{CaSO}_4(\text{aq}) \Leftrightarrow \text{Ca}^{2+} + \text{SO}_4^{2-}$	-2.310
$\text{CaOH}^+ + \text{H}^+ \Leftrightarrow \text{Ca}^{2+} + \text{H}_2\text{O}$	12.78
$\text{CO}_2(\text{aq}) + \text{H}_2\text{O} \Leftrightarrow \text{H}^+ + \text{HCO}_3^-$	-6.350
$\text{CO}_3^{2-} + \text{H}^+ \Leftrightarrow \text{HCO}_3^-$	10.33
$\text{KOH}(\text{aq}) + \text{H}^+ \Leftrightarrow \text{K}^+ + \text{H}_2\text{O}$	14.460
$\text{KSO}_4^- \Leftrightarrow \text{K}^+ + \text{SO}_4^{2-}$	-0.8796
$\text{MgCO}_3(\text{aq}) \Leftrightarrow \text{Mg}^{2+} + \text{CO}_3^{2-}$	-2.980
$\text{MgHCO}_3^+ \Leftrightarrow \text{Mg}^{2+} + \text{HCO}_3^-$	-1.040
$\text{MgSO}_4(\text{aq}) \Leftrightarrow \text{Mg}^{2+} + \text{SO}_4^{2-}$	-2.230
$\text{MgOH}^+ + \text{H}^+ \Leftrightarrow \text{Mg}^{2+} + \text{H}_2\text{O}$	11.680
$\text{NaHCO}_3(\text{aq}) \Leftrightarrow \text{Na}^+ + \text{HCO}_3^-$	0.250
$\text{NaSO}_4^- \Leftrightarrow \text{Na}^+ + \text{SO}_4^{2-}$	-0.940
$\text{NaCO}_3^- \Leftrightarrow \text{Na}^+ + \text{CO}_3^{2-}$	-1.270
$\text{NaOH}(\text{aq}) + \text{H}^+ \Leftrightarrow \text{Na}^+ + \text{H}_2\text{O}$	14.750
$\text{OH}^- + \text{H}^+ \Leftrightarrow \text{H}_2\text{O}$	14.000
$\text{HSO}_4^- \Leftrightarrow \text{H}^+ + \text{SO}_4^{2-}$	1.9791
$\text{HS}^- + 2\text{O}_2(\text{aq}) \Leftrightarrow \text{H}^+ + \text{SO}_4^{2-}$	138.27
$\text{Fe}^{3+} + 0.5\text{H}_2\text{O} \Leftrightarrow \text{H}^+ + 0.25\text{O}_2 + \text{Fe}^{2+}$	-8.485
$\text{FeHCO}_3^+ \Leftrightarrow \text{Fe}^{2+} + \text{HCO}_3^-$	-1.440
$\text{FeCO}_3(\text{aq}) \Leftrightarrow \text{Fe}^{2+} + \text{CO}_3^{2-}$	4.640
$\text{FeCl}^+ \Leftrightarrow \text{Fe}^{2+} + \text{Cl}^-$	-0.140
$\text{FeCl}^{2+} + 0.5\text{H}_2\text{O} \Leftrightarrow \text{Fe}^{2+} + \text{Cl}^- + \text{H}^+ + 0.25\text{O}_2(\text{aq})$	-9.885
$\text{FeOH}^+ + \text{H}^+ \Leftrightarrow \text{Fe}^{2+} + \text{H}_2\text{O}$	9.500
$\text{FeOH}^{2+} \Leftrightarrow \text{Fe}^{2+} + 0.5\text{H}_2\text{O} + 0.25\text{O}_2(\text{aq})$	-6.295
$\text{Fe}(\text{OH})_2(\text{aq}) + 2\text{H}^+ \Leftrightarrow \text{Fe}^{2+} + 2\text{H}_2\text{O}$	20.60
$\text{Fe}(\text{OH})_3(\text{aq}) + 2\text{H}^+ \Leftrightarrow \text{Fe}^{2+} + 2.5\text{H}_2\text{O} + 0.25\text{O}_2(\text{aq})$	4.075
$\text{Fe}(\text{OH})_4^- + 3\text{H}^+ \Leftrightarrow \text{Fe}^{2+} + 3.5\text{H}_2\text{O} + 0.25\text{O}_2(\text{aq})$	13.115
$\text{Fe}(\text{OH})_2^+ + \text{H}^+ \Leftrightarrow \text{Fe}^{2+} + 1.5\text{H}_2\text{O} + 0.25\text{O}_2(\text{aq})$	-2.815
$\text{Fe}(\text{SO}_4)_2^- + 0.5\text{H}_2\text{O} \Leftrightarrow \text{Fe}^{2+} + 2\text{SO}_4^{2-} + \text{H}^+ + 0.25\text{O}_2(\text{aq})$	-13.885
$\text{FeSO}_4(\text{aq}) \Leftrightarrow \text{Fe}^{2+} + \text{SO}_4^{2-}$	-2.200
$\text{FeHSO}_4^{2+} + 0.5\text{H}_2\text{O} \Leftrightarrow \text{Fe}^{2+} + 2\text{H}^+ + \text{SO}_4^{2-} + 0.25\text{O}_2(\text{aq})$	-12.955
$\text{Fe}_2(\text{OH})_2^{4+} + 2\text{H}^+ \Leftrightarrow 2\text{Fe}^{2+} + \text{H}_2\text{O} + 0.5\text{O}_2(\text{aq})$	-14.020
$\text{H}_2(\text{aq}) + 0.5\text{O}_2 \Leftrightarrow \text{H}_2\text{O}$	46.07
$\text{Al}(\text{OH})_2^+ + 2\text{H}^+ \Leftrightarrow \text{Al}^{3+} + 2\text{H}_2\text{O}$	10.580
$\text{Al}(\text{OH})_3(\text{aq}) + 3\text{H}^+ \Leftrightarrow \text{Al}^{3+} + 3\text{H}_2\text{O}$	16.420
$\text{Al}(\text{OH})_4^- + 4\text{H}^+ \Leftrightarrow \text{Al}^{3+} + 4\text{H}_2\text{O}$	22.870
$\text{Al}(\text{OH})_2^+ + \text{H}^+ \Leftrightarrow \text{Al}^{3+} + \text{H}_2\text{O}$	4.9500
$\text{H}_3(\text{SiO}_4)^- + \text{H}^+ \Leftrightarrow \text{H}_4(\text{SiO}_4)(\text{aq})$	9.8400
$\text{H}_2(\text{SiO}_4)^{2-} + 2\text{H}^+ \Leftrightarrow \text{H}_4(\text{SiO}_4)(\text{aq})$	23.140
$\text{Ca}(\text{H}_3\text{SiO}_4)^+ + \text{H}^+ \Leftrightarrow \text{Ca}^{2+} + \text{H}_4(\text{SiO}_4)(\text{aq})$	8.8300
$\text{Mg}(\text{H}_3\text{SiO}_4)^+ + \text{H}^+ \Leftrightarrow \text{Mg}^{2+} + \text{H}_4(\text{SiO}_4)(\text{aq})$	8.5800
Minerals	LogK
$\text{Calcite} + \text{H}^+ \Leftrightarrow \text{Ca}^{2+} + \text{HCO}_3^-$	1.850
$\text{Gypsum} \Leftrightarrow \text{Ca}^{2+} + \text{SO}_4^{2-} + 2\text{H}_2\text{O}$	-4.610
$\text{Fe}(\text{s}) + 2\text{H}^+ \Leftrightarrow \text{Fe}^{2+} + 2\text{H}_2\text{O} + 2\text{OH}^- + \text{H}_2(\text{aq})$	58.85
$\text{Magnetite} + 6\text{H}^+ \Leftrightarrow 3\text{Fe}^{2+} + 0.5\text{O}_2(\text{aq}) + 3\text{H}_2\text{O}$	-6.560
$\text{Siderite} + \text{H}^+ \Leftrightarrow \text{Fe}^{2+} + \text{HCO}_3^-$	-0.470
$\text{Goethite} + 2\text{H}^+ \Leftrightarrow \text{Fe}^{2+} + 1.5\text{H}_2\text{O} + 0.25\text{O}_2(\text{aq})$	-8.090
$\text{ISG} + 0.103\text{H}^+ + 0.5\text{H}_2\text{O} \Leftrightarrow 0.023\text{Al}^{3+} + 0.096\text{B}(\text{OH})_4^- + 0.017\text{Ca}^{2+} + 0.076\text{Na}^+ + 0.18\text{H}_4\text{SiO}_4$	9.722
$\text{Greenalite} + 6\text{H}^+ \Leftrightarrow 3\text{Fe}^{2+} + 2\text{H}_4\text{SiO}_4 + \text{H}_2\text{O}$	21.770
$\text{Smectite} + 10\text{H}_2\text{O} \Leftrightarrow 0.255\text{Na}^+ + 0.095\text{K}^+ + 0.0975\text{Ca}^{2+} + 0.55\text{Mg}^{2+} + 1.605\text{Al}(\text{OH})_4^- + 3.885\text{H}_4\text{SiO}_4(\text{aq}) + 0.04\text{OH}^-$	-22.404
$\text{Mg-saponite} + 7.36\text{H}^+ + 2.64\text{H}_2\text{O} \Leftrightarrow 3.17\text{Mg}^{2+} + 3.66\text{H}_4\text{SiO}_4 + 0.34\text{Al}^{3+}$	28.670
$\text{Mg-nontronite} + 5.69\text{H}^+ + 3.475\text{H}_2\text{O} \Leftrightarrow 0.17\text{Mg}^{2+} + 3.66\text{H}_4\text{SiO}_4 + 0.67\text{Al}^{3+} + 1.67\text{Fe}^{2+} + 0.418\text{O}_2(\text{aq})$	-17.540

2.2.5.1 Carbon steel corrosion

The available oxygen in the HLW disposal cell in granite is consumed soon after its closure, and anaerobic conditions are expected to prevail in the long term. The canister is treated as a porous material made of metallic iron, Fe(s). Under anaerobic conditions, H₂O is the oxidizing agent of Fe(s) (Lu et al., 2011; Samper et al., 2016; and Mon et al., 2017). The reaction of anaerobic Fe(s) corrosion is given by:



By rewriting this reaction in terms of the primary species used in the numerical model, one obtains:



The carbon-steel corrosion is kinetically controlled and assumed to corrode at a constant rate (it should be noticed that $\eta = 0$ for constant canister corrosion). The corrosion rate, r_c , in $\mu\text{m}/\text{year}$ is calculated as:

$$r_c = \frac{r_m b V_m \sigma \phi 10^6}{f_v} \quad [2.4]$$

where r_m is the corrosion rate per unit mineral surface ($\text{mol}/\text{m}^2/\text{year}$), b is the canister thickness (m); V_m is the molar volume of iron (dm^3/mol); σ is iron specific surface area (m^2/L); ϕ is porosity; and f_v is the mineral volume fraction (dimensionless).

A constant corrosion rate of $1.41 \mu\text{m}/\text{year}$ was used in the model of the HLW disposal cell in granite (Samper et al., 2016; Mon et al., 2017), which amounts to $0.281 \text{ mol}/\text{m}^2/\text{year}$. Period II is assumed to last 25,000 years which coincides with the time at which the remaining thickness of the overpack is 1.5 cm. The corrosion rate is such that 3.5 cm of canister corrode after 25,000 years. Canister corrosion proceeds until all the carbon steel is fully corroded at $t = 35,300$ years. The porosity of the canister is 0.3.

2.2.5.2 Vitrified waste dissolution

According to Samper et al. (2021), modelling the dissolution of the vitrified waste is probably the most critical aspect for modelling the chemical evolution in a HLW disposal cell in granite.

Although the SON-68 glass was the reference vitrified waste in the HLW disposal cell in granite, a simpler synthetic glass, the ISG (International Simple Glass), was adopted in the model instead of the SON-68. The chemical compositions of the ISG and the French reference SON-68 glasses are listed in Table 2-3 (Debure et al., 2012). ISG and SON-68 have a similar composition. They differ on minor components such as Ba, Ln or Mo. Based on the elemental composition (in mol%) of the ISG of Gin et al. (2015) presented in Table 2-4, the ISG chemical reaction can be obtained (De Windt, 2021, personal communication). This reaction was included in the ThermoChimie v10a thermodynamic database (Giffaut et al., 2014). The calculated ISG molecular weight is $19.25 \text{ g}/\text{mol}$ and the molar volume is $7.70 \text{ cm}^3/\text{mol}$.

Table 2-3. Chemical composition of the ISG and the French reference glass SON-68 (Debure et al., 2012).

[wt.%]	SiO ₂	Na ₂ O	B ₂ O ₃	Al ₂ O ₃	CaO	ZrO ₂	Others
ISG	56.2	12.2	17.3	6.0	5.0	3.3	
SON68	45.5	9.9	14.0	4.9	4.0	2.7	19.0

Table 2-4. Chemical and elemental compositions of the ISG (Gin *et al.*, 2015).

	SiO ₂	Na ₂ O	B ₂ O ₃	Al ₂ O ₃	CaO	ZrO ₂	
[wt.%]	56.2	12.2	17.3	6.1	5.0	3.3	
[mol%]	60.1	12.7	16.0	3.8	5.7	1.7	
	Si	Na	B	Al	Ca	Zr	O
[wt.%]	26.3	9.0	5.4	3.2	3.6	2.4	50.1
[mol%]	18.0	7.6	9.6	2.3	1.7	0.5	60.3

The stoichiometry of the ISG dissolution is given by:



The dissolution of the ISG was modelled with the simplified R7T7 glass dissolution model of De Windt *et al.* (2006). More complex models such as the GRAAL model (Frugier *et al.*, 2008; 2018) are being used for modelling glass dissolution at the waste package scale in ACED Task 3.2.

The dissolution of the simplified R7T7 glass is controlled by two temperature-dependant kinetic terms according to the conceptual model of Gin *et al.* (2013). The kinetic dissolution rate includes an initial dissolution rate, r_0 , and a long-term residual rate r_r . The rate law is given by:

$$\frac{d[glass]}{dt} = r_0(T, pH, Si \dots) + r_r(T) \quad [2.6]$$

Assuming a congruent dissolution of the vitrified waste, these two kinetic terms can be assumed as (De Windt *et al.*, 2006): (1) A first-order initial dissolution rate which is chemistry-dependant (pH and dissolved silica concentration); and (2) A long-term residual dissolution rate which is chemistry-independent. The kinetic rate law is given by:

$$\frac{d[glass]}{dt} = -k_{0,pH} (H^+)^{-0.4} A_v \left(1 - \frac{C_{Si}}{C_{Si}^*} \right) - k_r A_v \quad [2.7]$$

where $k_{0,pH}$ is the initial kinetic constant (in mol/m²·s), $(H^+)^{-0.4}$ is the activity term of the proton which includes the effect of pH, A_v is the reactive surface, C_{Si} is the concentration of dissolved silica, C_{Si}^* is a threshold silica concentration which ensures that glass dissolution stops when $C_{Si} > C_{Si}^*$, and k_r is the residual kinetic rate constant (in mol/m²·s).

This first-order rate law was used by De Windt *et al.* (2006) for modelling the dissolution of the R7T7 glass in a HLW disposal cell in clay host rock. Originally, it only gives a rough estimation of the rate in a narrow range of pH (7-9.5) and a temperature of 90 °C, but it has been extended to 50 °C (Samper *et al.*, 2021). Figure 2-8 shows the dissolution rate versus pH for several silica concentrations. The dissolution rate increases with pH and decreases when the silica concentration increases.

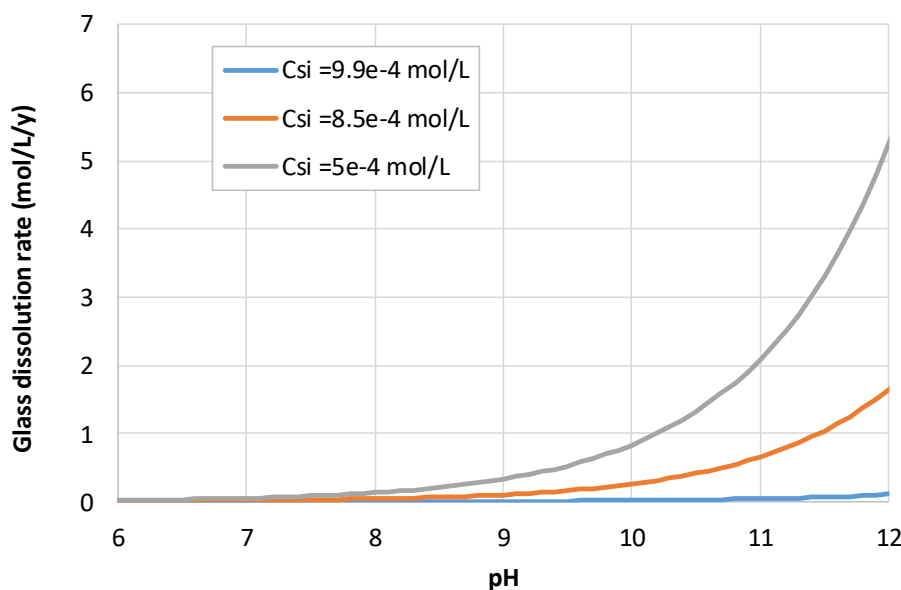


Figure 2-8. Glass dissolution rate for different values of pH .

The initial and residual kinetic constant values and a first estimation of the saturation threshold were taken from Table 3.13 of D2.16 (Samper et al., 2021). That table gives a set of parameters for Eq. (2-7) that are assumed to be operational for a temperature of 50 °C and a pH range of 7-9.5. However, these parameters at 50 °C can be used even if the temperature is lower in Period III. This assumption could overestimate the degradation of the glass because the rate of glass dissolution decreases with temperature. According to De Windt et al. (2006), the most critical parameter in the R7T7 dissolution rate is the silica threshold at saturation C_{Si}^* . The sensitivity analysis of model predictions due to uncertainties in the silica threshold at saturation, C_{Si}^* , will be addressed in Sensitivity Case 1. Table 2-5 summarizes the key kinetic and transport parameters of the ISG, including the initial and residual kinetic constants, the silica threshold C_{Si}^* , the effective diffusion coefficient (D_e) of dissolved species in the glass, the specific surface and the porosity of the glass. It is important to point out that in the glass the numerical model only considers glass dissolution. No other mineral phases are allowed to dissolve or precipitate in the glass.

Table 2-5. Initial and residual kinetic constants, k_0 and k_r , saturation threshold, C_{Si}^* , specific surface, σ , effective diffusion coefficient, and porosity, Φ , of the ISG (De Windt et al., 2006).

$k_{0,pH}$ [g/m ² /d]	3×10^{-5}	$k_{0,pH}$ [mol/m ² /s]	1.8×10^{-11}
k_r [g/m ² /d]	10^{-4}	k_r [mol/m ² /s]	6×10^{-11}
C_{Si}^* [mol/L]	1×10^{-3}	Φ	0.3
σ [m ² /g]	5×10^{-5}	σ [dm ² /L]	29.2
D_e [m ² /s] ($0 < t < 25,000$ years)	1×10^{-13}	D_e [m ² /s] ($t > 25,000$ years)	1×10^{-10}

2.2.5.3 Smectite dissolution

Smectite dissolution is simulated by assuming the chemical formulation of the FEBEX bentonite proposed by Fernández et al. (2009) and by using the kinetic rate law of Eq. (2.1). The kinetic rate constant, k_m , at 25 °C is equal to $1.58 \cdot 10^{-13}$ mol/m²·s (Cama et al., 2000; Bildstein et al., 2006; Chaparro et al., 2021). The activation energy, E_a , is equal to 60 KJ/mol (Chaparro et al., 2021). The kinetic parameters Θ and η are both equal to 1.

To improve the convergence of the sequential iterative approach used to solve the highly nonlinear reactive transport equations and reduce the computation time, the smectite specific surface area, σ , was taken 10 times smaller than the value proposed by Fernández et al. (2009) (250 dm²/L). This reduced surface area leads to smectite dissolution rates similar to those reported by Chaparro et al. (2021).

2.3 Numerical model

This section presents the grid, the simulated time and the values of the key hydrodynamic, thermal, and chemical parameters considered in the water flow and non-isothermal multicomponent reactive transport model of the HLW disposal cell in granite. The transport, heat and chemical equations, and the initial and boundary conditions can be found in Samper et al. (2021).

2.3.1 Grid and simulated time

The numerical water flow and multicomponent reactive transport model of the HLW disposal cell in granite was performed with a 1-D axisymmetric finite element mesh with 152 nodes: 12 nodes in the vitrified waste, 8 nodes in the Fe powder, 90 nodes in the bentonite, 10 nodes in the EDZ and 32 in the granite rock. The spatial mesh discretization is non uniform. The grid size, Δx , of the elements is equal to 0.25 dm in the glass interval $0.5 < r < 1.2$ dm, Δx is equal to 0.125 dm in the glass interval $1.2 \text{ dm} < r < 1.99$ dm; Δx is equal to 0.05 dm at the glass/canister interface ($1.99 < r < 2.1$ dm), $\Delta x = 0.1$ dm in the canister interval $2.1 < r < 2.4$ dm; $\Delta x = 0.05$ dm at the canister/bentonite interface ($2.4 < r < 3$ dm) and $\Delta x = 0.088$ dm in the bentonite interval $3 < r < 10$ dm. The grid size in the EDZ is equal to 0.2 dm ($10 < r < 12$ dm). The mesh extends to 25 m in the granite. The grid size in the granite increases geometrically from $\Delta x = 1.2$ dm at $r = 12$ dm to $\Delta x = 160$ dm at $r = 250$ dm. Figure 2-9 shows the finite element mesh used in the numerical model.

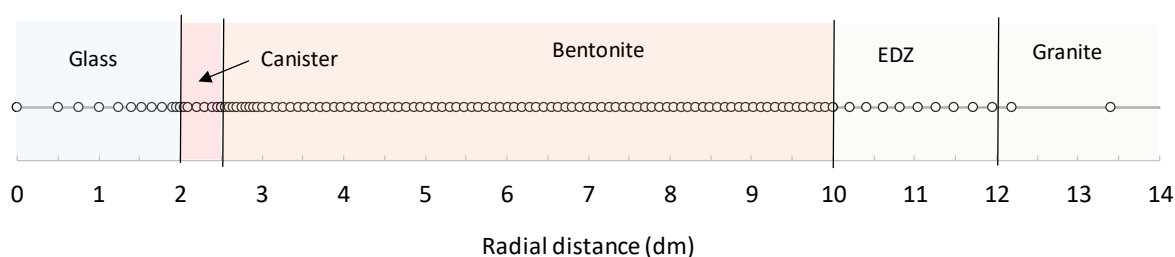


Figure 2-9. Scheme of the finite element mesh used in the model of the HLW disposal cell in granite.

The model of the base case, the sensitivity cases and the variants of the HLW disposal cell in granite considers three successive periods. The first one (Period I) covers the oxic transient stage. Period II starts when the bentonite barrier is fully saturated, and the anoxic conditions are prevailing. Canister corrosion, the interactions of corrosion products and the bentonite and the interactions of bentonite and granite are considered in this period. Finally, Period III starts after canister failure and considers glass alteration and the interactions of glass with corrosion products and uncorroded iron.

Only Periods II and III are considered in the model of the HLW disposal cell in granite. Period II is assumed to last 25,000 years, after which the canister fails. Period III starts at 25,000 years and considers glass dissolution. The final time of simulation is 50,000 years.

2.3.2 Flow and transport parameters

The FEBEX bentonite is considered saturated with a thickness of 75 cm. The hydraulic conductivity of the bentonite is extremely low, with a value of $6 \cdot 10^{-14}$ m/s (Samper et al., 2016). Therefore, solute advection is negligible, and diffusion is the main solute transport mechanism. All the water is assumed to be accessible to solutes. Water flow through the granite was simulated with a constant water flux of 0.1 L/y parallel to the axis of the gallery.

The bentonite porosity, ϕ , is equal to 0.407. The effective diffusion coefficient, D_e , of the bentonite is equal to $4.07 \cdot 10^{-11}$ m²/s (Samper et al., 2016). The solid density of the bentonite is 2700 kg/m³. The specific heat capacity and the saturated thermal conductivity of the bentonite are equal to 847 J/kg°C and 1.15 W/m°C, respectively (Samper et al., 2016). The thermal conductivity of 1.5 W/m°C was used for the granitic rock. This value is in the lower range of the reported values thermal conductivities of granites. However, the value of the thermal conductivity of the granite does not have a major effect on the long-term geochemical simulations because the most reactive zones are located at the glass/canister and canister/bentonite interfaces.

The hydraulic conductivity of the glass and the canister are assumed equal to that of the bentonite. Glass porosity is assumed equal to 0.3 (De Windt et al., 2006). The effective diffusion coefficient, D_e , of the glass is equal to 10^{-10} m²/s (De Windt et al., 2006).

The porosity of the SRG granite and the EDZ is equal to 0.005 (Samper et al., 2008). Their hydraulic conductivities are equal to $8.72 \cdot 10^{-12}$ m/s and $8.72 \cdot 10^{-11}$ m/s, respectively (Samper et al., 2008). The effective diffusion coefficient, D_e , of the granite and EDZ is equal to $5.02 \cdot 10^{-14}$ m²/s (Samper et al., 2008). The thermal and hydrodynamic parameters of the bentonite and granite are listed in Table 2-6 (Samper et al., 2016, 2018).

Table 2-6. Thermal and hydrodynamic parameters of the bentonite and granite (Zheng and Samper 2008; Zheng et al., 2011, based on ENRESA 2006, Samper et al., 2016, 2018).

Parameter	Glass	Canister	Bentonite	EDZ	Granite
Hydraulic conductivity (m/s)	$6 \cdot 10^{-14}$	$6 \cdot 10^{-14}$	$6 \cdot 10^{-14}$	$8.72 \cdot 10^{-11}$	$8.72 \cdot 10^{-12}$
Porosity	0.3	0.3	0.407	0.005	0.005
Effective diffusion coefficient (m ² /s)	10^{-10}	$2.72 \cdot 10^{-11}$	$4.07 \cdot 10^{-11}$	$5.02 \cdot 10^{-14}$	$5.02 \cdot 10^{-14}$
Solid density (kg/m ³)	2513	2513	2700	2700	2700
Specific heat of the solid (J/kg °C)	482	482	847	1029	1029
Thermal conductivity of the solid (W/m °C)	50	50	1.15	1.5	1.5

2.3.3 Chemical parameters

The initial chemical composition of the bentonite, EDZ and granite porewater (Samper et al., 2016) is listed in Table 2-7. The initial porewater composition of the glass and canister is assumed to be the same as the bentonite porewater. The initial accessory mineral volume fractions considered in the

EURAD Deliverable 2.17 – Integrated reactive transport models for assessing the chemical evolution at the disposal cell scale

bentonite include: calcite (1%) and smectite (57%). The initial mineral volume fraction of calcite in the granite is 5%. The initial volume fraction of canister (Fe(s)) and ISG are 0.99 and 0.7 respectively.

The cation exchange capacity (CEC) of the bentonite is 102 meq/100 g (Fernández et al., 2004). Cation selectivity coefficients for exchanged Ca^{2+} , Mg^{2+} , K^{+} and Fe^{+} were taken from Samper et al. (2008) and Tournassat (2003). Surface complexation reactions in the bentonite are modelled with the triple sorption site model of Bradbury and Baeyens (1997, 2005). The total concentration of sorption sites is 0.322 mol/L. The first type of sorption sites corresponds to the strong sites which have a large binding affinity but a small concentration (0.0079 mol/L). The other two types are the weak #1 and #2 sorption sites which have binding constants weaker than those of the strong sites although their concentrations (0.16 mol/L) are larger than those of the strong sorption sites. Table 2-8 shows the protolysis constants for surface complexation reactions for a triple-site sorption model and the selectivity constants for cation exchange reactions in the FEBEX bentonite.

Table 2-7. Initial chemical composition of the FEBEX bentonite, EDZ and granite porewater (Samper et al., 2016).

Species (mol/L)	FEBEX bentonite porewater	EDZ and granite porewater
pH	6.46	7.825
Eh (V)	-0.078	-0.188
Ca^{2+}	$3.32 \cdot 10^{-2}$	$1.522 \cdot 10^{-4}$
Mg^{2+}	$3.67 \cdot 10^{-2}$	$1.604 \cdot 10^{-4}$
Na^{+}	$1.88 \cdot 10^{-1}$	$4.350 \cdot 10^{-3}$
K^{+}	$1.55 \cdot 10^{-3}$	$5.371 \cdot 10^{-5}$
Fe^{2+}	$1.43 \cdot 10^{-4}$	$1.791 \cdot 10^{-8}$
Al^{3+}	$1.0 \cdot 10^{-8}$	$1.85 \cdot 10^{-8}$
Cl^{-}	$2.75 \cdot 10^{-1}$	$3.949 \cdot 10^{-4}$
HCO_3^{-}	$7.59 \cdot 10^{-3}$	$5.049 \cdot 10^{-3}$
SO_4^{2-}	$2.05 \cdot 10^{-2}$	$1.561 \cdot 10^{-5}$
SiO_2 (aq)	$9.67 \cdot 10^{-5}$	$3.761 \cdot 10^{-4}$

Table 2-8. Protolysis constants for surface complexation reactions for a triple-site sorption model (Bradbury and Bayens, 2005) and selectivity constants for cation exchange reactions in the FEBEX bentonite (ENRESA, 2006).

Cation exchange		$K_{\text{Na-cation}}$
$\text{Na}^+ + \text{X-K} \leftrightarrow \text{K}^+ + \text{X-Na}$		0.138
$\text{Na}^+ + 0.5 \text{X}_2\text{-Ca} \leftrightarrow 0.5 \text{Ca}^{2+} + \text{X-Na}$		0.2924
$\text{Na}^+ + 0.5 \text{X}_2\text{-Mg} \leftrightarrow 0.5 \text{Mg}^{2+} + \text{X-Na}$		0.2881
$\text{Na}^+ + 0.5 \text{X}_2\text{-Fe} \leftrightarrow 0.5 \text{Fe}^{2+} + \text{X-Na}$		0.5
Surface complexation		$\text{Log } K_{25}$
$\text{S}^{\text{SOH}_2^+}$	$\text{=S}^{\text{SOH}_2^+} \leftrightarrow \text{=S}^{\text{SOH}} + \text{H}^+$	-4.5
S^{SO^-}	$\text{=S}^{\text{SO}^-} + \text{H}^+ \leftrightarrow \text{=S}^{\text{SOH}}$	7.9
S^{SOFe^+}	$\text{=S}^{\text{SOFe}^+} \leftrightarrow \text{=S}^{\text{SOH}} + \text{Fe}^{2+} - \text{H}^+$	0.6
S^{SOFeOH}	$\text{=S}^{\text{SOFeOH}} \leftrightarrow \text{=S}^{\text{SOH}} + \text{Fe}^{2+} - 2\text{H}^+ + \text{H}_2\text{O}$	10.0
$\text{S}^{\text{SOFe(OH)}_2^-}$	$\text{=S}^{\text{SOFe(OH)}_2^-} \leftrightarrow \text{=S}^{\text{SOH}} + \text{Fe}^{2+} - 3\text{H}^+ + 2\text{H}_2\text{O}$	20.0
$\text{S}^{\text{W1OH}_2^+}$	$\text{=S}^{\text{W1OH}_2^+} \leftrightarrow \text{=S}^{\text{W1OH}} + \text{H}^+$	-4.5
S^{W1O^-}	$\text{=S}^{\text{W1O}^-} + \text{H}^+ \leftrightarrow \text{=S}^{\text{W1OH}}$	7.9
$\text{S}^{\text{W1OFe}^+}$	$\text{=S}^{\text{W1OFe}^+} \leftrightarrow \text{=S}^{\text{W1OH}} + \text{Fe}^{2+} - \text{H}^+$	3.3
$\text{S}^{\text{W2OH}_2^+}$	$\text{=S}^{\text{W2OH}_2^+} \leftrightarrow \text{=S}^{\text{W2OH}} + \text{H}^+$	-6.0
S^{W2O^-}	$\text{=S}^{\text{W2O}^-} + \text{H}^+ \leftrightarrow \text{=S}^{\text{W2OH}}$	10.5

2.3.4 Parameters for the sensitivity cases and variants

This section presents the parameters used in the sensitivity cases and variants of the reactive transport model of the geochemical evolution in a HLW disposal cell in granite. Sensitivity cases and variants are listed in Table 2-1.

Sensitivity Case 1 considers the same vitrified waste ISG in Period III but with a different value of the silica saturation threshold used in the kinetic rate law of glass dissolution. According to De Windt et al. (2006), it is the most critical parameter in the R7T7 dissolution rate. The new value of this parameter used in this sensitivity case was $5 \cdot 10^{-4}$ mol/L.

Sensitivity Case 2 considers a granitic porewater with a chloride concentration greater than the value used in the base case. A plausible range of chloride concentrations was selected based on data from Gómez et al. (2006). These authors include a synthesis of the results on the site investigations carried out in Spain on hydrogeochemical characterization of different rock types (granite and schist) up to 500 m depth. The sites investigated are ancient uranium mines located in the Central-Iberian Zone of the Hesperian Massif: (1) El Berrocal (Toledo) is a granite pluton with a high fracture density and strong hydraulic gradients conditioned by the topography, which acts as a recharge zone; (2) Los Ratones (Cáceres) is a granite pluton that acts as a discharge zone of the surrounding mountain range; and (3) Sageras-Mina Fe (Salamanca) is a highly fractured schistose rock in which the recharge comes from the infiltration in the surrounding mountains, and the discharge occurs in the Águeda and Yeltes rivers, bordering to the S-NW and the NE to the mine, respectively. The hydrogeochemical interpretations of the three sites show that Los Ratones is the most representative of prolonged water-rock interaction processes and old groundwaters. The deep waters (500 m depth) flowing through the fracture system at Los Ratones are diluted ($< 500 \mu\text{S/cm}$) and Na-HCO₃ type. The pH value is about 7.8 ± 0.2 and the redox potential is reduced (-242 ± 62 mV). The range of Cl⁻ concentrations is: 5.4-26 mg/L ($1.52 \cdot 10^{-4}$ - $7.32 \cdot 10^{-4}$ mol/L). A chloride concentration value in the granitic water 8 times greater ($3.2 \cdot 10^{-3}$ mol/L) than the value used in the base case ($3.949 \cdot 10^{-4}$ mol/L) was adopted for the Sensitivity Case 2 (see

Table 2-9). Akaganeite and Cl-green rust are added to the list of secondary minerals in this sensitivity case.

Table 2-9. Chemical composition of the granite boundary water used in Sensitivity Case 2 (Samper et al., 2016).

Species (mol/L)	Granite boundary water
pH	7.825
Eh (V)	-0.188
Ca ²⁺	1.522·10 ⁻⁴
Mg ²⁺	1.604·10 ⁻⁴
Na ⁺	4.350·10 ⁻³
K ⁺	5.371·10 ⁻⁵
Fe ²⁺	1.791·10 ⁻⁸
Al ³⁺	1.85·10 ⁻⁸
Cl ⁻	3.2·10 ⁻³
HCO ₃ ⁻	5.049·10 ⁻³
SO ₄ ²⁻	1.561·10 ⁻⁵
SiO ₂ (aq)	3.761·10 ⁻⁴

Variant 1 considers compacted MX-80 bentonite instead of FEBEX bentonite with a thickness of 35 cm (Figure 2-5). The compacted MX-80 bentonite consists mainly of a low charge montmorillonite with Na⁺ and Ca²⁺ as interlayer cations. The porosity of the MX-80 bentonite is equal to 0.39 for an initial dry density of 1.6 g/cm³. The porewater composition of compacted MX-80 bentonite was taken from Bradbury and Baeyens (2003) who provided a geochemical model for the chemical composition as a function of dry density and by taking into account montmorillonite swelling, the semi-permeable membrane effects, different types of water (interlayer, double layer and free water), the highly effective buffering characteristics of exchangeable cations and the amphoteric edge sites which buffers the pH in the porewater of the resaturated bentonite at a value of 8. Bradbury and Baeyens (2003) assumed that free water is the accessible porosity for chloride. This assumption is considered in Variant 1. The chemical composition of the MX-80 bentonite porewater at pH = 8 and for a dry density of 1600 kg/m³ is listed in Table 2-10. The calculated porewater is a NaCl/Na₂SO₄ type water with a relatively high ionic strength (I = 0.327 M). Montmorillonite is the main mineral component of the MX-80 bentonite. Its content ranges from 65 to 75%. The initial accessory mineral volume fractions of the MX-80 bentonite include (Pusch, 2001): Quartz (10-14%), feldspars (5-9%), mica and chlorite (2-4%), carbonates and chlorite (3-5%). The cation exchange capacity (CEC) of the MX-80 bentonite is 78.7 meq/100 g (Bradbury and Baeyens, 2002). Cation selectivity coefficients for exchanged Ca²⁺, Mg²⁺ and K⁺ have been taken from Bradbury and Baeyens (2002). Cation occupancies and selectivity coefficients for cation exchange reactions in the MX-80 bentonite are listed in Table 2-11. Surface complexation reactions in the MX-80 bentonite are modelled with the triple sorption site model of Bradbury and Baeyens (1997, 2005). The total concentrations of sorption sites and the protolysis constants for the surface complexation reactions are the same than those adopted for the base run in the FEBEX bentonite (Table 2-8).

Variant 2 considers the EDZ and a larger hydraulic conductivity of the host rock (Figure 2-5). The hydraulic conductivity and porosity of the host rock were taken from data published by Martínez-Landa et al. (2016) from the Mina Ratones site in Southwestern Spain. The thickness of the EDZ varies from 1 to 1.5 m based on the results of Kwon et al. (2009). The porosity is assumed equal to twice the porosity of the intact rock. The hydraulic conductivity and the effective diffusion of the EDZ were calculated from those of the intact rock by using the Kozeny-Karman equation for permeability and Archie's law for the

EURAD Deliverable 2.17 – Integrated reactive transport models for assessing the chemical evolution at the disposal cell scale

effective diffusion. The overall effect of the presence of EDZ and a larger hydraulic conductivity of the host rock has been taken into account by increasing the granite hydraulic conductivity of the base model by a factor which ranges from 10 to 47”.

Table 2-10. Calculated chemical composition of the MX-80 bentonite porewater at pH = 8 and at initial dry density of 1600 kg/m³ (Bradbury and Baeyens, 2003).

Species (mol/L)	MX-80 bentonite porewater
pH	6.46
Eh (V)	-0.078
Ca ²⁺	1.01·10 ⁻²
Mg ²⁺	7.69·10 ⁻³
Na ⁺	2.61·10 ⁻¹
K ⁺	1.32·10 ⁻³
Cl ⁻	1.08·10 ⁻¹
HCO ₃ ⁻	7.80·10 ⁻⁴
SO ₄ ²⁻	9.45·10 ⁻²

Table 2-11. Cation occupancies and selectivity coefficients for cation exchange reactions in the MX-80 bentonite (Bradbury and Baeyens, 2002; 2003).

Exchangeable cations	Cation occupancies (meq/kg)
Na ⁺	668 ± 40
K ⁺	13 ± 2
Ca ²⁺	66 ± 3
Mg ²⁺	40 ± 3
Cation exchange reactions	Selectivity coefficients K _{NA/K}
Na-montmorillonite + K ⁺ ⇌ K-montmorillonite + Na ⁺	4.0 ± 1.6
2 Na-montmorillonite + Mg ²⁺ ⇌ Mg-montmorillonite + 2 Na ⁺	2.2 ± 1.1
2 Na-montmorillonite + Ca ²⁺ ⇌ Ca-montmorillonite + 2 Na ⁺	2.6 ± 1.2

Variant 3 considers the conditions of the Reference Czech crystalline rock (Figure 2-5). The required parameters (rock porewater chemical composition, mineral composition, hydraulic conductivity and porosity) were derived from those reported by Červinka et al. (2018) for the Bukov underground Research Facility (URF). The Czech Reference crystalline rock has a porosity of 0.05 and a hydraulic conductivity of 5.0·10⁻⁹ m/s. (Červinka et al., 2018). The chemical composition of two types of synthetic rock porewaters, SGW2 and SGW3, is listed in Table 2-12 (Červinka et al., 2018). The SGW2 chemical composition was derived from the average physico-chemical parameters and average chemical composition of real groundwater at the URF Bukov about 600 m below the surface. Its composition corresponds to the groundwater in deeper circulation in the fracture environment of the crystalline rocks of the Bohemian Massif, type Ca-HCO₃. The SGW3 chemical composition was derived from the physico-chemical parameters and chemical analysis of groundwater at the Rožná mine from the 22-24 level about 1000 m below the surface. The groundwater composition represents a very slow circulation of deep groundwater in the fracture environment of the crystalline rocks of the Bohemian Massif, type Na-HCO₃.

Červinka *et al.* (2018) estimated the mineral composition in the following three rock types: 1) Compact fine-grained amphibolite with biotite; 2) Migratised amphibolic gneiss with biotite; and 3) Biotite migmatite with amphibole. Amphibole, plagioclase, quartz and biotite are the main minerals. The accessory minerals include pyrite, pyrrhotine, chalcopyrite, zircon, monazite, apatite and titanite and secondary minerals include apatite, titanite, sericite, chlorite, K-feldspar and calcite. Other parameters of the Czech Reference Crystalline rock were derived from the EURAD Deliverable 2.4 (Neeft *et al.*, 2020b). The chemical composition of the SGW2 was used as representative of the Czech granite in Variant 3.

Table 2-12. Chemical composition of the SGW2 and SGW3 Czech crystalline rock porewaters (Červinka *et al.*, 2018).

Species (mol/L)	SGW2	SGW3
pH	8.2	9.4
Eh (V)	0.237	0.237
T (°C)	25	25
Ca ²⁺	8.64·10 ⁻⁴	3.24·10 ⁻⁵
Mg ²⁺	3.42·10 ⁻⁴	4.12·10 ⁻⁶
Na ⁺	8.65·10 ⁻⁴	3.81·10 ⁻³
K ⁺	5.37·10 ⁻⁵	1.79·10 ⁻⁵
Fe ²⁺	1.79·10 ⁻⁶	1.79·10 ⁻⁶
Al ³⁺	3.71·10 ⁻⁶	3.71·10 ⁻⁶
Cl ⁻	9.31·10 ⁻⁵	5.28·10 ⁻⁴
HCO ₃ ⁻	2.77·10 ⁻³	2.68·10 ⁻³
SO ₄ ²⁻	2.19·10 ⁻⁴	1.09·10 ⁻⁴
SiO ₂ (aq)	5.20·10 ⁻⁴	4.18·10 ⁻⁴

2.4 Computer code

This section presents a short description of CORE^{2D} V5, the reactive transport code used for modelling the HLW disposal cell in granite. CORE^{2D} V5 is a code for transient saturated and unsaturated water flow, heat transport and multicomponent reactive solute transport under both local chemical equilibrium and kinetic conditions in heterogeneous and anisotropic media (Samper *et al.*, 2009; Fernández, 2017; Águila *et al.*, 2020). The flow and transport equations are solved with Galerkin finite elements and an Euler scheme for time discretization. The solute transport equation accounts for advection, molecular diffusion and mechanical dispersion. The chemical formulation is based on the ion association theory and uses an extended version of the Debye-Hückel equation (B-dot) for the activity coefficients of aqueous species. The following chemical reactions are considered: aqueous complexation, acid-base, redox, mineral dissolution/precipitation, cation exchange, surface complexation and gas dissolution/exsolution. CORE^{2D} V5 relies on several thermodynamic databases. ThermoChimie v10.a (Giffaut *et al.*, 2014) was used for the model presented here. The Gaines-Thomas convention is used for cation exchange. Surface complexation is modelled by using three types of protonation/deprotonation sites, S^S-OH, S^{W1}-OH and S^{W2}-OH, as proposed by Bradbury and Baeyens (1997). CORE^{2D} V5 is based on the sequential iteration approach to solve the coupled solute transport and chemical equations. Iterations between transport and chemistry are repeated until some prescribed convergence criteria are attained (Samper *et al.*, 2009). CORE^{2D} V5 takes into account the changes in porosity due to mineral dissolution/precipitation reactions and their feedback effect on the flow and transport parameters under isothermal and non-isothermal conditions (Águila *et al.*, 2020).

2.5 Differences between D2.16 and D2.17

This section presents a short description of the main differences between the features of the reactive transport model proposed in Deliverable D2.16 and those finally adopted for the calculations presented here in Deliverable D2.17 in the features of the conceptual and numerical models, the computed codes and the sensitivity cases.

2.5.1 Conceptual model

Thermodynamic and chemical data for dissolved species and mineral phases were not provided in D2.16. The chemical reactions and the equilibrium constants at 25°C for the 39 aqueous species and 11 mineral phases used in the model are now listed in Table 2-2 of the D2.17.

SON-68 glass was the reference vitrified waste selected in the D2.16 for the HLW disposal cell in granite. It was agreed that the complexities of the glass dissolution model could be better addressed in ACED Task 3. A simpler synthetic glass, the ISG (International Simple Glass), has been used in the model presented here instead of the SON-68. The ISG has a composition similar to that of SON-68, except for some minor components such as Ba, Ln or Mo. The dissolution of the ISG has been modelled with the simplified R7T7 glass dissolution model of De Windt et al. (2006).

Smectite dissolution was not considered in D2.16. However, it has been included in the model reported here.

2.5.2 Numerical model

The main thermal and hydrodynamic parameters of the glass, the canister, the bentonite, the EDZ and the granite were presented in D2.16. The list of the parameter values has been revised, corrected and expanded in D2.17 (see Table 2-6).

Similarly, the initial volume fractions of the canister and mineral phases have been updated in D2.17. The revised initial mineral volume fractions adopted in D2.17 include: 1) Carbon-steel canister (99% for Fe(0)); 2) Bentonite (1% for calcite, 57% for smectite and 0% for quartz and gypsum); and 3) Granite (5% for calcite and 0% for chalcedony).

2.5.3 Computer codes

Two codes were proposed in D2.16. CORE^{2D} V5 was proposed for nonisothermal single-phase water-saturated conditions while INVERSE-FADES-CORE V2 was proposed for nonisothermal multiphase flow. All the calculations reported here were performed with CORE^{2D} V5 for water-saturated conditions.

2.5.4 Sensitivity cases

A base case and six sensitivity cases were proposed in D2.16 for the reactive transport model of the geochemical evolution in a HLW disposal cell in granite. The sensitivity cases proposed in Deliverable D2.16 have been split into Variants 1, 2 and 3 and Sensitivity Cases 1 and 2. The ISG and the R7T7 glass dissolution model have been adopted for the vitrified waste in the base run and all the variants and sensitivity cases. Instead of considering different types of glasses (SON88 and Belgian SM539), we report the sensitivity of model predictions to changes in the silica saturation threshold (see Deliverable D2.19), which is the most critical parameter in the R7T7 dissolution model (Sensitivity Case 1). The sensitivity cases and variants adopted for D2.17 are listed in Table 2-1.

The base run is based on the assumption that the canister fails when 70% of the canister is corroded after 25,000 years. Then, the dissolution of the ISG starts. A sensitivity run was performed by assuming an earlier canister failure with a shorter duration of Period II. In this sensitivity run ISG dissolution is assumed to start after 10,000 years when 30% of the canister is corroded. The results of this sensitivity run are presented in Deliverable D2.19 (Samper et al., 2023).

2.6 Calculated results of the base case

Model results for Periods II (canister corrosion) and III (glass dissolution) are reported in this section. The base case model starts at period II when the bentonite barrier is fully saturated and the anoxic conditions are prevailing and continues from the canister failure until 50,000 years (Period III) in a single run. *Figure 2-10* shows the mineral volume fraction at several times of Period I and period II.

Period II. Mineral precipitation is prevented in the glass in Period II. Canister corrosion causes an increase in pH (pH ~ 9) and an early increasing of dissolved Fe²⁺. Magnetite precipitation takes place mostly in the canister and proceeds as long as the canister is corroding (*Figure 2-10b*). Siderite precipitates at both sides of the canister/bentonite interface and greenalite volume fraction increases especially in the bentonite becoming the main corrosion product in the bentonite (*Figure 2-10c*). The small amount of smectite dissolution is largest near the canister/bentonite interface and triggers the precipitation of Mg-saponite in the bentonite at 25,000 years (*Figure 2-10c*). Calcite precipitates in the canister near the bentonite/canister interface and in the bentonite. Pore clogging is predicted to occur at 10,000 years in the canister and also porosity is reduced in the bentonite 2 cm from the canister/bentonite interface due to the precipitation of calcite, siderite and greenalite.

Period III. The canister failure at 25,000 years triggers the glass dissolution. Computed glass dissolution front (ISG) increases with time from 25,000 to 50,000 years (*Figure 2-10 c, d, e*). Glass dissolution leads to an increase of pH with time in the glass (pH ~ 8). The diffusive flux of silica from glass dissolution causes the precipitation of greenalite at the glass-canister and canister-bentonite interfaces. Once the canister is fully corroded, magnetite redissolves near the glass/canister interface and greenalite precipitates instead (*Figure 2-10 d*). Greenalite precipitates in the canister and the bentonite, especially at the glass/canister interface. Siderite precipitates at the canister/bentonite interface. Smectite dissolution keeps increasing slowly with time from 25,000 to 50,000 years and it continues triggering Mg-saponite precipitation in the bentonite (*Figure 2-10 e*). Calcite re-dissolves in the canister and in the bentonite/canister interface at 50,000 years (*Figure 2-10e*). The porosity in the glass increases due to glass dissolution and it decreases in the bentonite in 2 cm from the canister interface due to the precipitation of calcite, siderite and greenalite (*Figure 2-10d*).

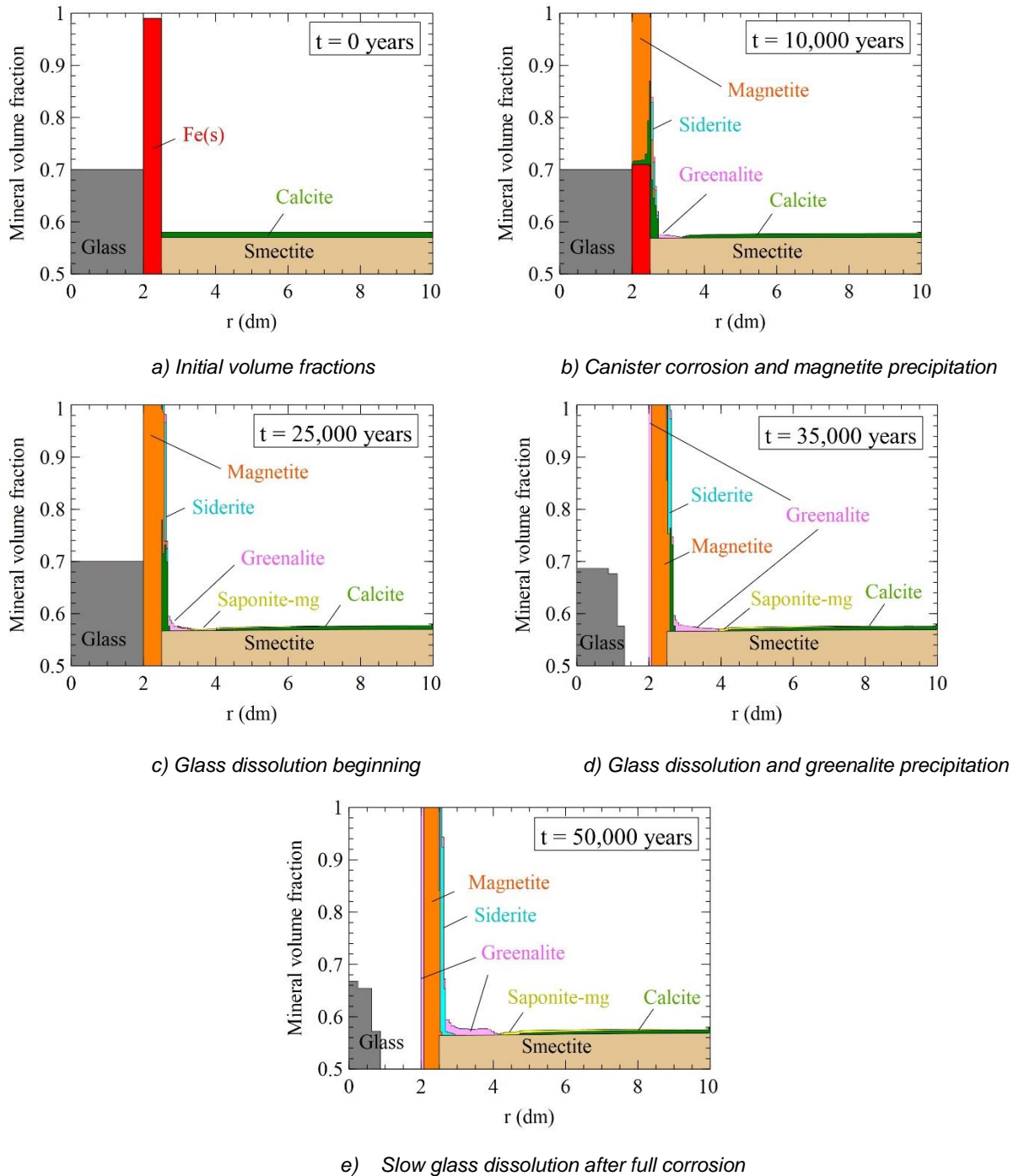


Figure 2-10. Spatial distribution of the computed mineral volume fractions at selected times of Period II and Period III. The left axis is a ampliation from 0.5 to 1.

2.6.1 Model results for Period II: canister corrosion

Period II starts when the bentonite barrier is fully saturated and the anoxic conditions are prevailing. Canister corrosion, the interactions of corrosion products and the bentonite, and the interactions of bentonite and granite are considered in this period. Period II is assumed to last 25,000 years which coincides with the time at which the remaining thickness of the overpack is 1.5 cm. The corrosion rate is such that 3.5 cm of canister corrode after 25,000 years. Canister corrosion proceeds until all the carbon steel is fully corroded at $t = 35,300$ years.

EURAD Deliverable 2.17 – Integrated reactive transport models for assessing the chemical evolution at the disposal cell scale

Canister corrosion causes an increase in pH (Figure 2-11) in the canister and the bentonite near the canister/bentonite interface. The computed pH at the end of Period II (25,000 years) is equal to 9.25 in the canister and ranges from 9.25 to 7.82 in the bentonite. The concentration of dissolved Fe^{2+} increases in the first 1,000 years and later decreases (Figure 2-12). The time evolution of the computed pH and the concentration of dissolved Fe^{2+} is controlled by: 1) The dissolution/precipitation of Fe minerals in the canister and in the bentonite near the bentonite/canister interface, 2) Fe exchange and 3) Fe and proton surface complexation reactions.

Figure 2-13 show the spatial distribution of the computed magnetite precipitation at 1,000, 10,000 and 25,000 years. Magnetite precipitation takes place mostly in the canister and proceeds as long as the canister is corroding. The thickness of magnetite precipitation band in the bentonite is about 1 cm at $t = 25,000$ years.

Siderite precipitates at both sides of the canister/bentonite interface (Figure 2-14). The precipitation front penetrates in the bentonite about 1 cm. Goethite does not precipitate. Figure 2-15 shows the spatial distribution of the computed greenalite precipitation at selected times. The greenalite volume fraction increases with time in the canister, especially near the canister/bentonite interface and in the bentonite. The thickness of the greenalite precipitation band in the bentonite is larger than those of magnetite and siderite. Clearly, greenalite is the main corrosion product in the bentonite.

Figure 2-16 shows the spatial distribution of the computed smectite dissolution in the bentonite at 1,000, 10,000 and 25,000 years. Smectite dissolution increases with time. The dissolution of smectite is largest near the canister/bentonite interface. Model results show that smectite dissolution triggers the precipitation of a small amount of Mg-saponite in the bentonite at 25,000 years (not shown here). Mg-nontronite does not precipitate. Calcite precipitates in the canister near the bentonite/canister interface, in the bentonite and also in the granite (Figure 2-17). Gypsum does not precipitate.

Figure 2-18 shows the time evolution of the calculated porosity changes due to mineral dissolution/precipitation at three selected points in the glass ($r = 0.125$ dm), the canister ($r = 2.2$ dm) and the bentonite ($r = 2.605$ dm). Porosity in the glass does not change because glass dissolution is prevented in Period II ($t \leq 25,000$ years). Moreover, mineral precipitation is also prevented in the glass in Period II. The canister is treated as a porous medium. The volume of voids in the canister decreases due to magnetite precipitation. The voids of the canister are fully filled with corrosion products at $t = 10,000$ years. The porosity in the bentonite at 1 cm from the canister/bentonite interface decreases with time due to the precipitation of calcite, siderite and greenalite.

Figure 2-19 shows the spatial distribution of the dissolved concentration of a conservative species such as Cl^- at 1,000, 10,000 and 25,000 years. The concentration of Cl^- decreases with time in the bentonite by solute diffusion into the granite because the initial Cl^- concentration in the granite porewater ($3.95 \cdot 10^{-4}$ M) is much smaller than the initial concentration in the bentonite ($2.75 \cdot 10^{-1}$ M). It should be pointed out that the profiles of the concentration of Cl^- show very small gradients because the solute transfer from the bentonite into the granite is not controlled by solute diffusion through the bentonite, but by solute advection and diffusion in the granite. The computed concentrations of dissolved calcium, magnesium, sodium and potassium decrease with time due to solute diffusion into the granite (not shown here). On the other hand, the computed concentration of dissolved aluminum in the bentonite increases with time due to smectite dissolution (Figure 2-20). The concentrations of dissolved species in the glass do not change because the diffusion in the glass is disabled until the glass starts to dissolve.

Figure 2-21 shows the spatial distribution of the computed concentrations of exchanged cations in the bentonite at 25,000 years. The concentrations of exchanged calcium and magnesium are the largest with values around 43 and 37 meq/100g in most of the bentonite, respectively. The concentration of exchanged sodium is 22 meq/100g while that of potassium is equal to 1.6 meq/100g. The concentration of exchanged Fe is largest near the canister interface and decreases with distance from the canister/bentonite interface. The spatial distribution of the concentration of exchanged Fe is similar to that of the concentration of dissolved Fe.

EURAD Deliverable 2.17 – Integrated reactive transport models for assessing the chemical evolution at the disposal cell scale

Figure 2-22 shows the spatial distribution of the concentrations of surface complexes at strong, weak #1 and weak #2 sites in the bentonite at $t = 25,000$ years. The concentration of $XOFe^+$ is the largest in the strong sorption sites. There is also a clear peak in the concentration of $XOFeOH$ in the strong sorption sites near the canister/bentonite interface. The concentration of XXO^- in the weak #1 sorption sites is largest near the canister interface and decreases with distance from the canister/bentonite interface while the $XXOH$ concentration is increasing. The concentration of $XXOFe^+$ in weak #1 sorption sites shows also a maximum near the canister/bentonite interface. The concentrations of the surface complexes in weak #2 sites show small changes because Fe is not sorbed on these sites.

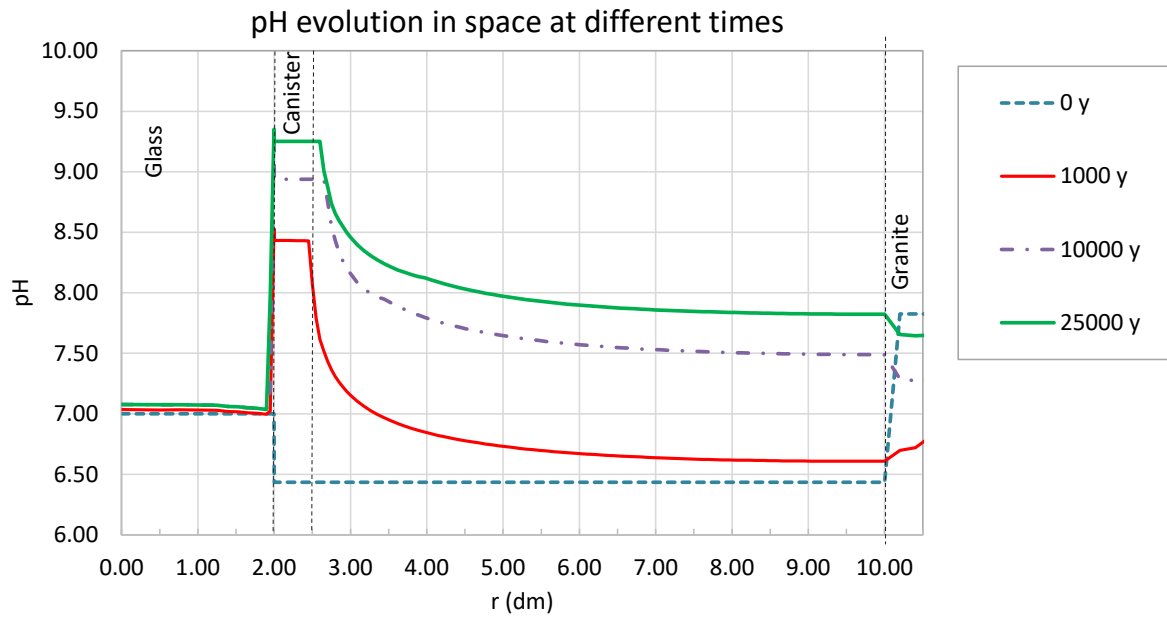


Figure 2-11. Spatial distribution of the computed pH at selected times of Period II.

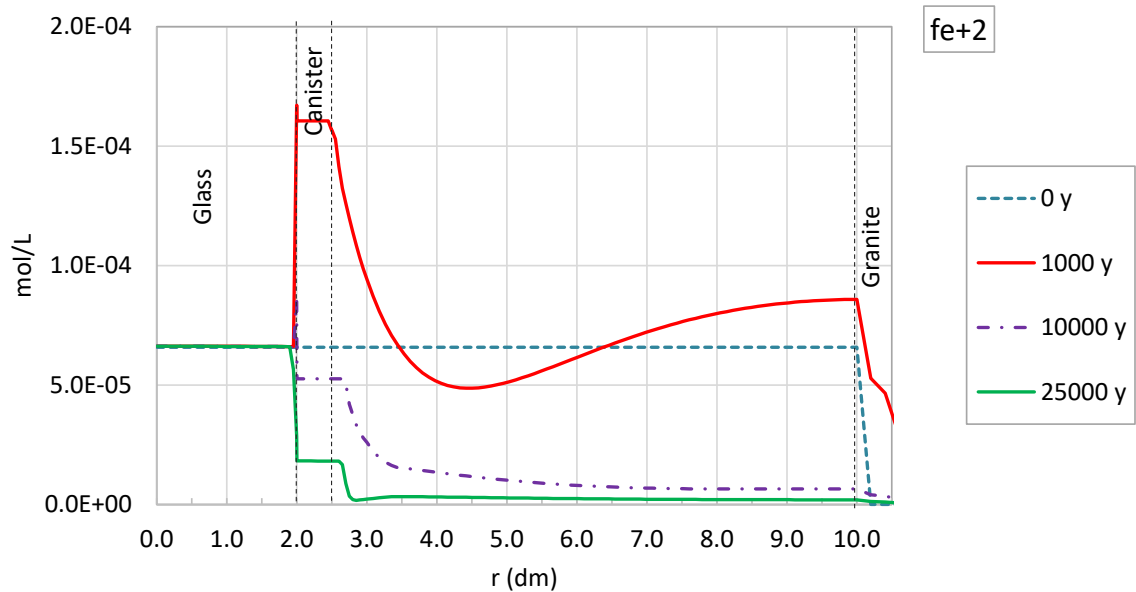


Figure 2-12. Spatial distribution of the computed concentration of dissolved Fe at selected times of Period II.

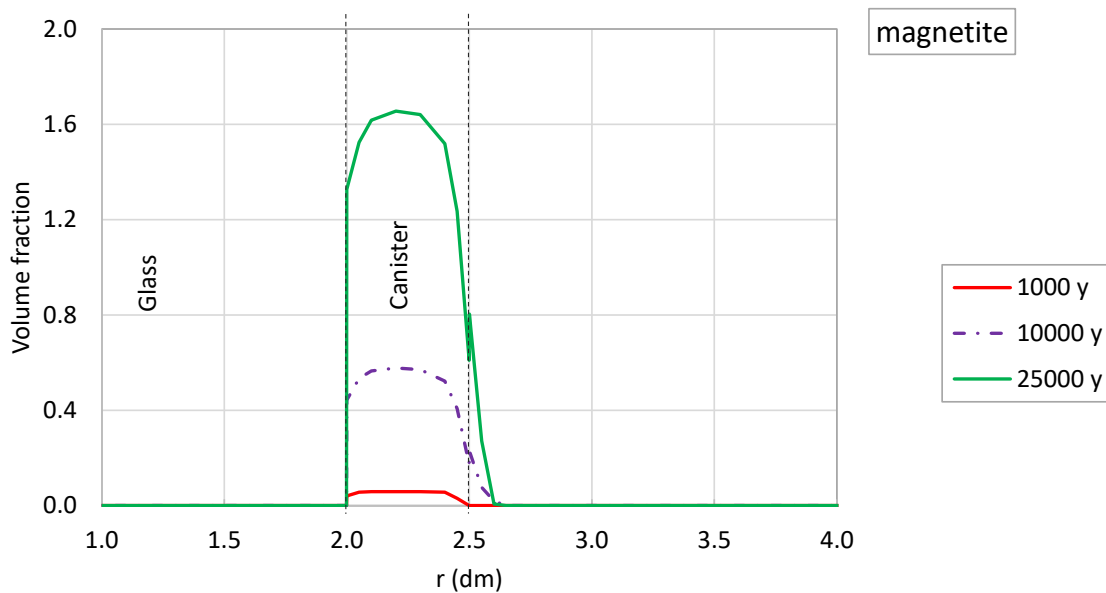


Figure 2-13. Spatial distribution of the computed volume fraction of magnetite at selected times of Period II. The bottom plot shows an enlargement around the canister ($1 < r < 4$ dm).

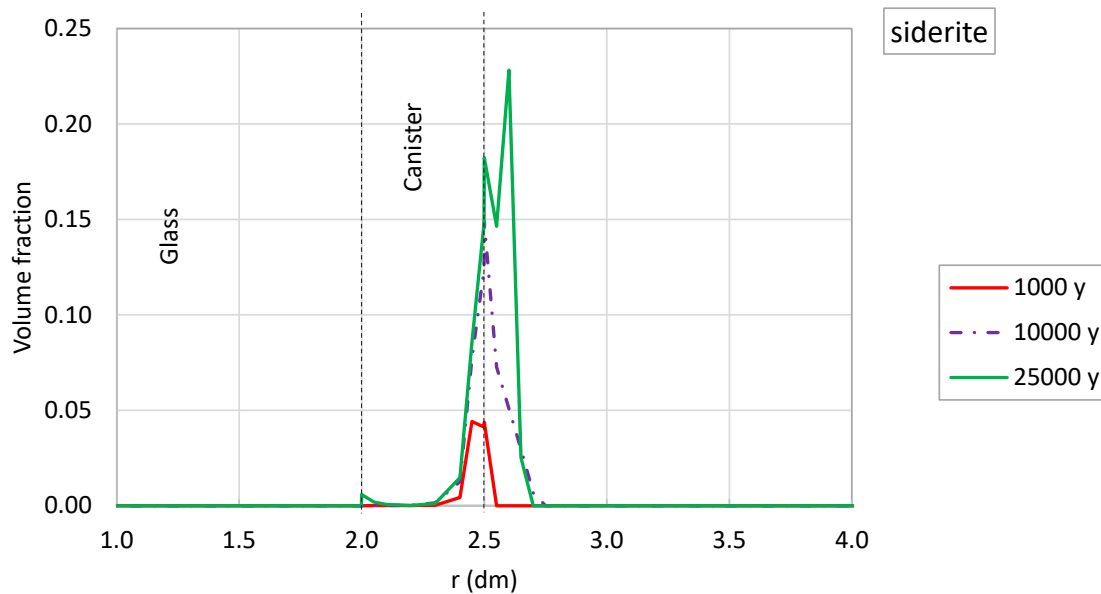


Figure 2-14. Spatial distribution of the computed volume fraction of siderite at selected times of Period II. The bottom plot shows an enlargement around the canister ($1 < r < 4$ dm).

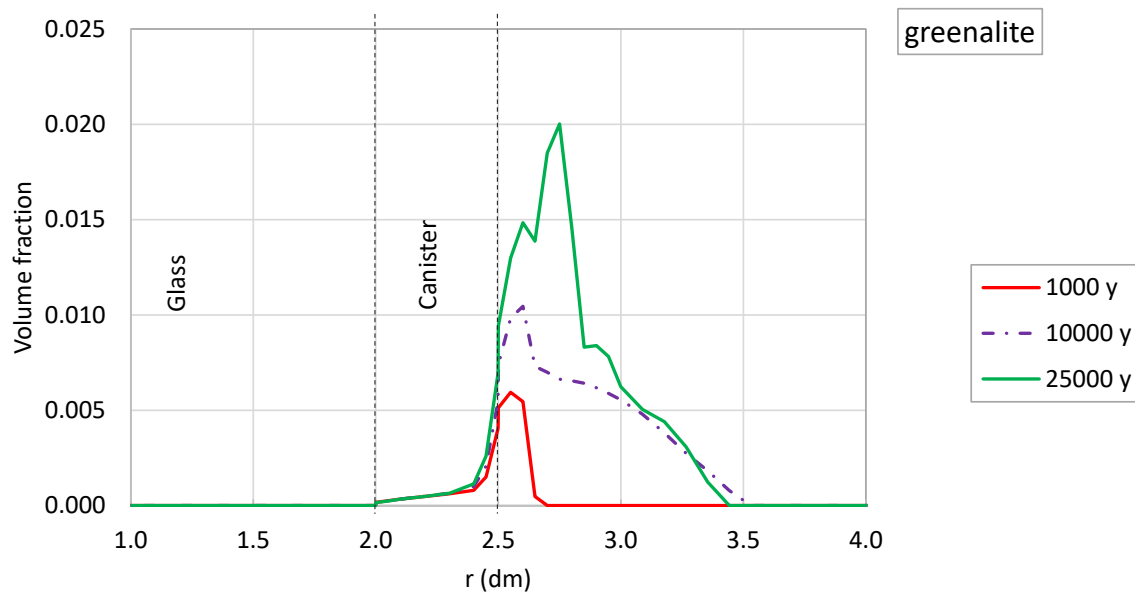


Figure 2-15. Spatial distribution of the computed volume fraction of greenalite at selected times of Period II. The bottom plot shows an enlargement around the canister ($1 < r < 4$ dm).

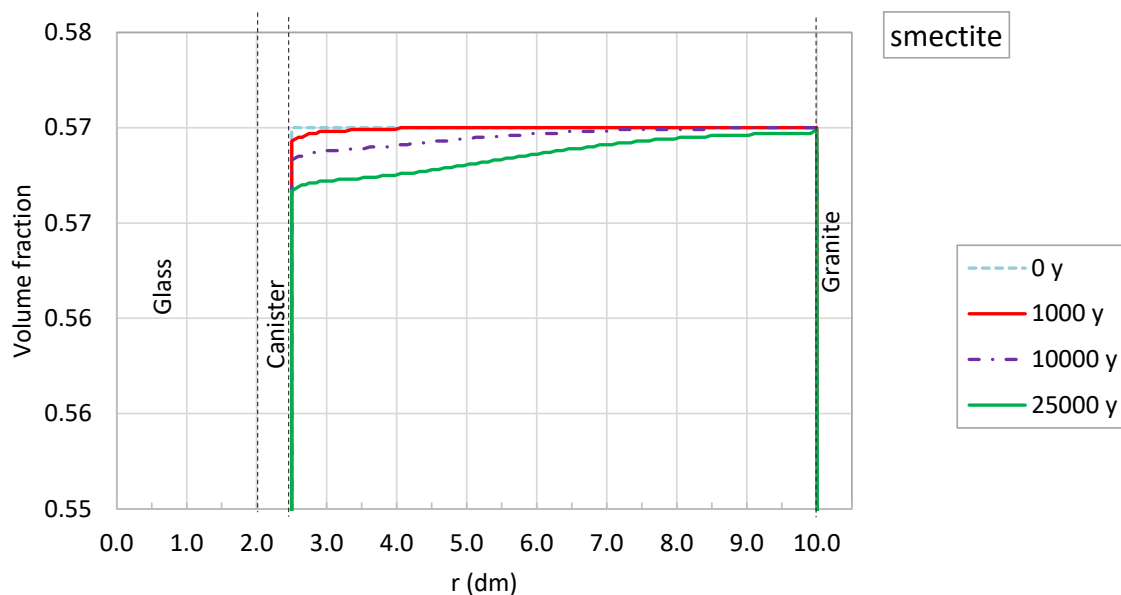


Figure 2-16. Spatial distribution of the computed volume fraction of smectite at selected times of Period II.

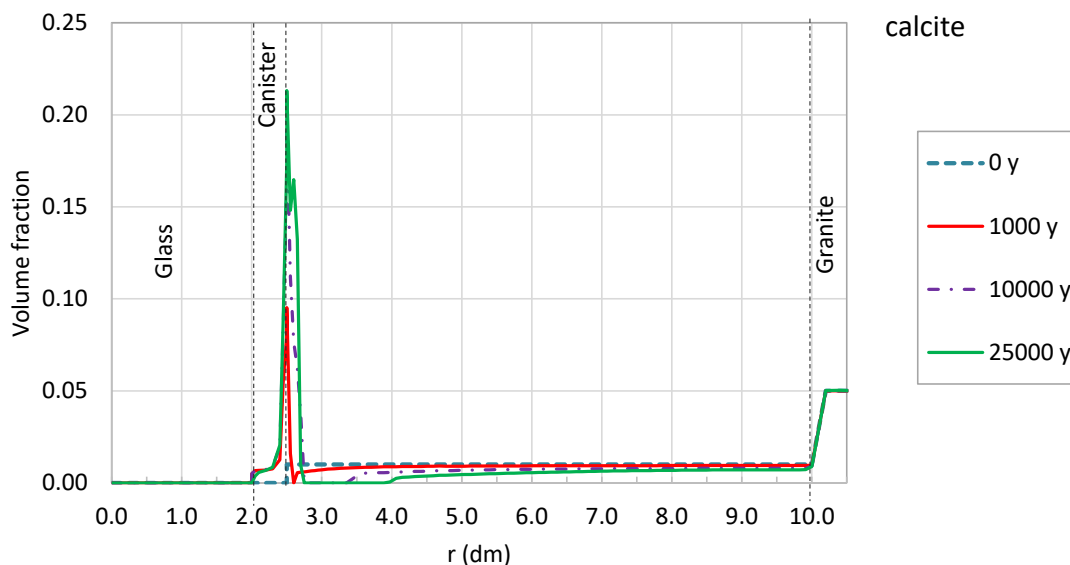


Figure 2-17. Spatial distribution of the computed volume fraction of calcite at selected times of Period II.

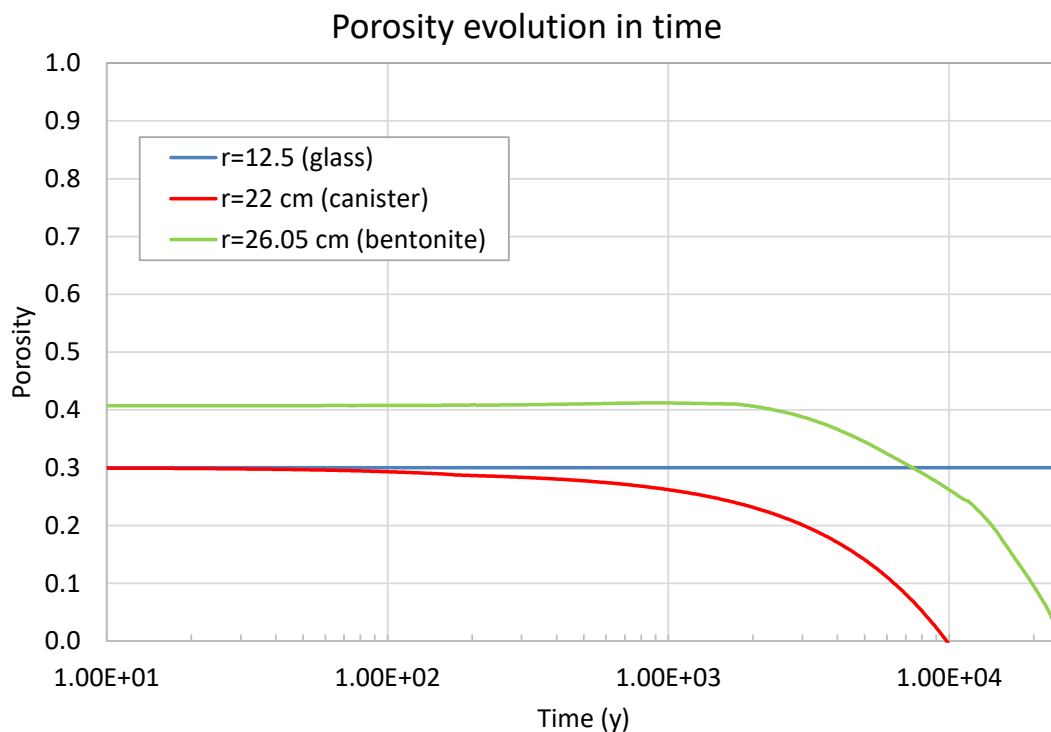


Figure 2-18. Time evolution of the porosity during Period II due to changes in mineral dissolution/precipitation in the glass ($r = 12.5$ cm), the canister ($r = 22$ cm) and the bentonite ($r = 26.5$ cm).

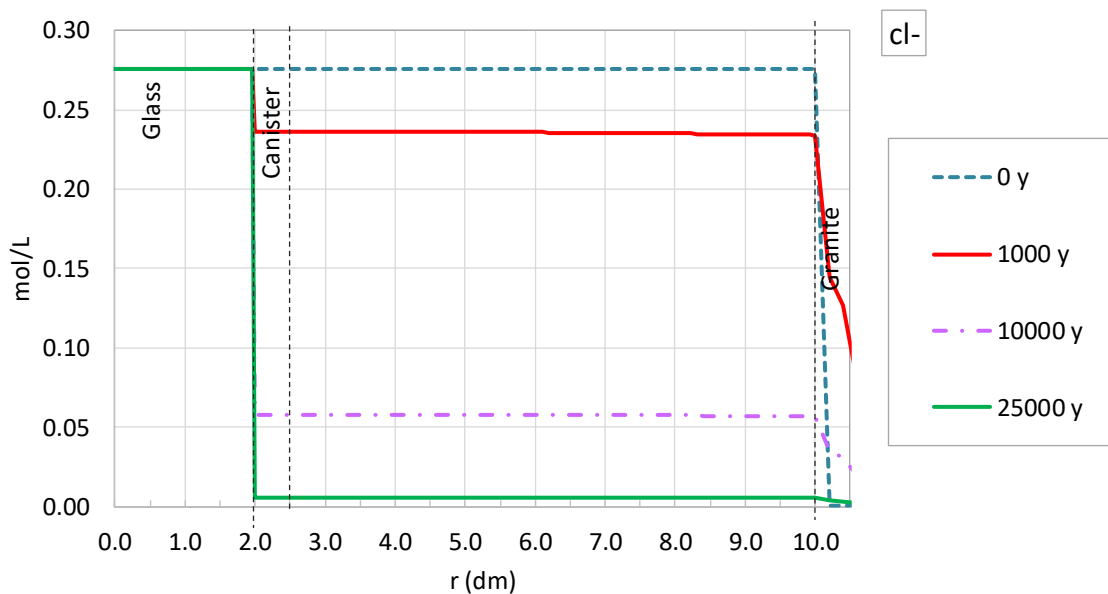


Figure 2-19. Spatial distribution of the computed concentration of dissolved Cl^- at selected times of Period II.

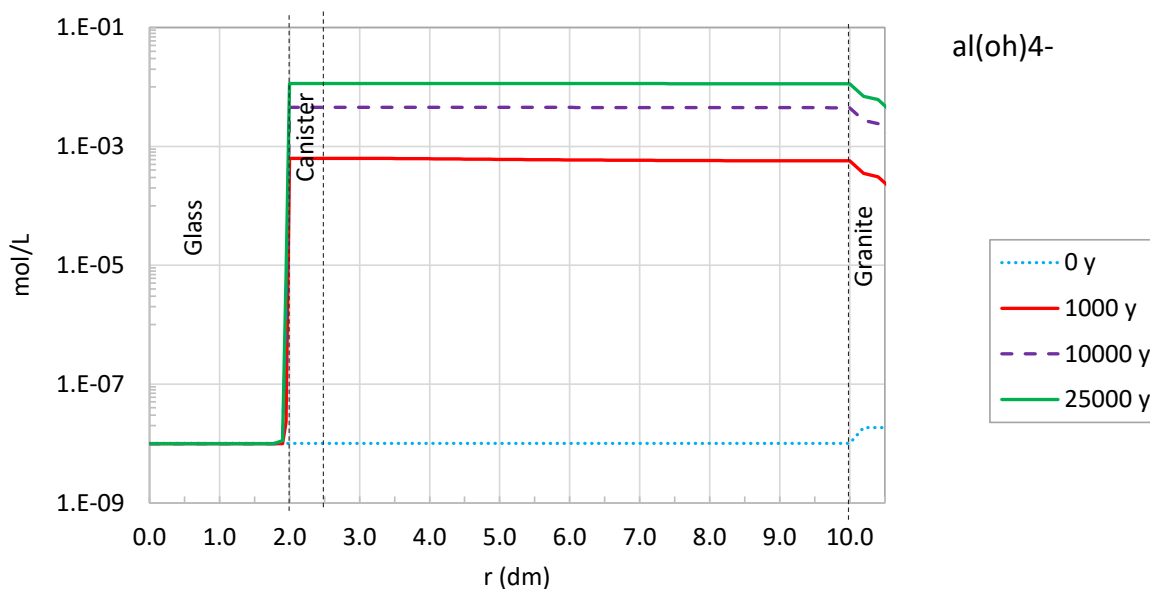


Figure 2-20. Spatial distribution of the computed concentration of dissolved aluminum at selected times of Period II.

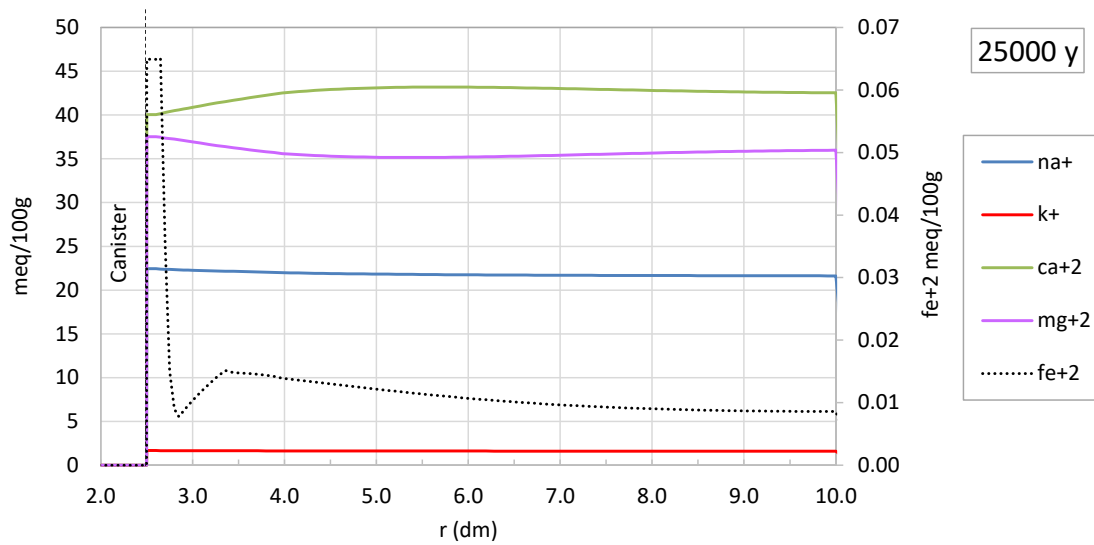


Figure 2-21. Spatial distribution of the computed concentration of exchanged cations at the end of Period II ($t = 25,000$ years).

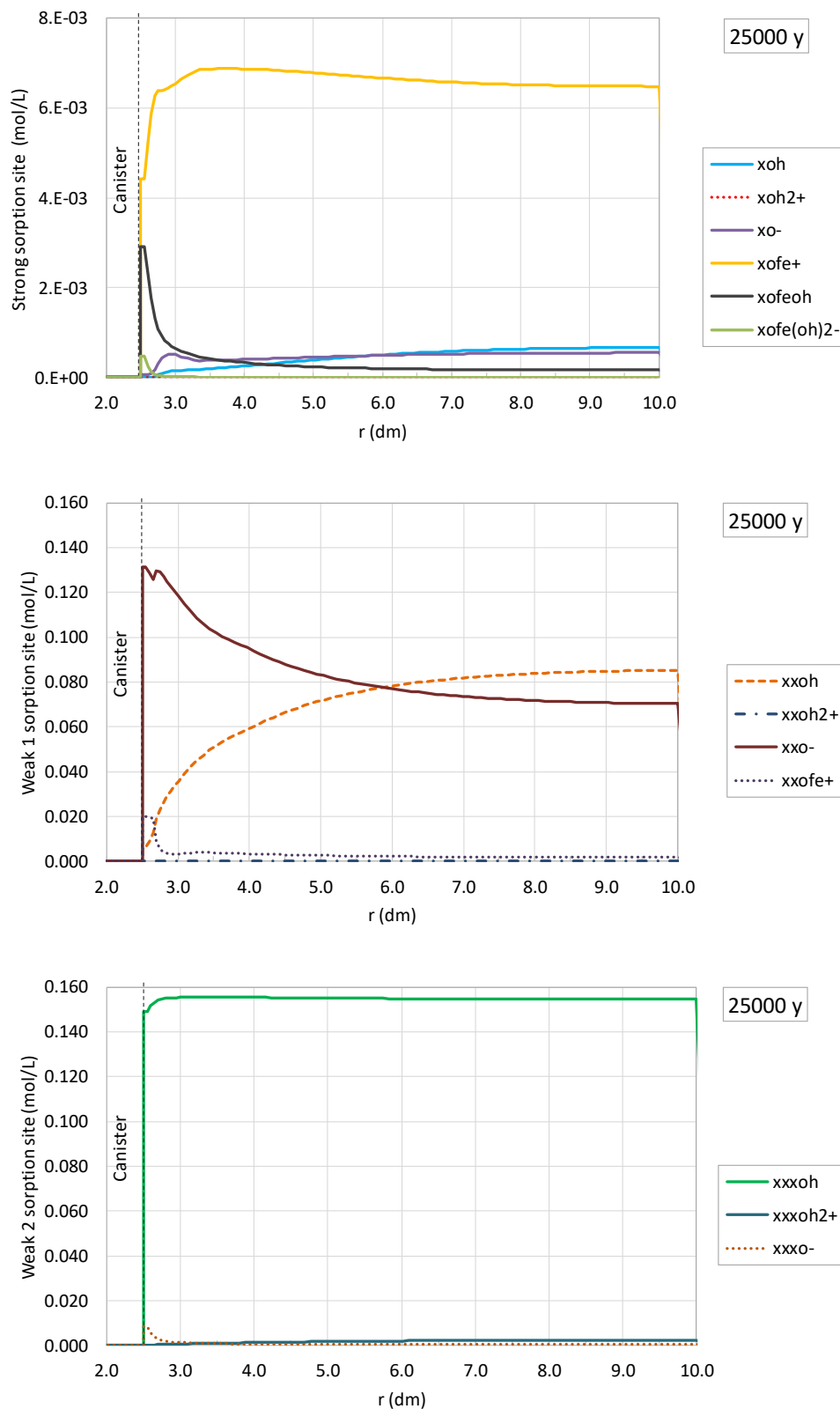


Figure 2-22. Spatial distribution of the computed concentration of surface complexes at strong (upper plot), weak #1 (intermediate plot) and weak #2 (bottom plot) sites at the end of Period II ($t = 25,000$ years).

2.6.2 Calculated results at Period III: glass dissolution

Period III starts after canister failure at 25,000 years and considers glass dissolution and the interactions of glass with corrosion products and uncorroded carbon steel. The final time of simulation of this period is 50,000 years.

Computed glass dissolution (ISG) increases with time from 25,000 to 50,000 years. Model results show a dissolution front which moves into the glass (Figure 2-23). Glass dissolution leads to an increase of pH with time in the glass (Figure 2-24). The concentration of dissolved silica increases in the inner part of the glass until $t = 30,000$ years (Figure 2-25). The concentration of dissolved silica in the outer part of the glass decreases with time due to the diffusion of dissolved silica into the canister and the bentonite. This diffusive flux causes the precipitation of greenalite at the glass-canister and canister-bentonite interfaces. The pH at 50,000 years ranges from 7.93 to 7.89 in the glass, from 7.89 to 8.66 in the canister and from 7.87 to 8.6 in the bentonite.

Figure 2-26 show the spatial distribution of the computed magnetite precipitation. After 25,000 years magnetite precipitates in the canister as long as the remaining carbon steel corrodes. Once the canister is fully corroded, magnetite redissolves near the glass/canister interface and greenalite precipitates (Figure 2-27). Greenalite precipitates in the canister and the bentonite, especially at the glass/canister interface. Siderite precipitates at the canister/bentonite interface (Figure 2-28). Goethite does not precipitate.

Figure 2-29 shows the computed smectite dissolution in the bentonite. Smectite dissolution keeps increasing with time from 25,000 to 50,000 years and is largest near the canister/bentonite interface. Smectite dissolution triggers Mg-saponite precipitation in the bentonite (in a small amount) and especially in the canister near the glass/canister interface (Figure 2-30). Mg-nontronite does not precipitate. Calcite re-dissolves in the canister and in the bentonite/canister interface at 50,000 years (Figure 2-31).

Figure 2-32 shows the time evolution of the changes in porosity caused by mineral dissolution/precipitation at selected locations in the glass, the canister and the bentonite. The porosity in the glass increases due to glass dissolution. The porosity in the bentonite at 1 cm from the canister interface decreases with time due to the precipitation of calcite, siderite and greenalite, keeps decreasing until $t = 28,000$ years, when reaches clogging due to the precipitation of siderite and calcite and later increases slightly up to 0.05.

The concentration of dissolved Cl^- at the canister, the bentonite and the granite keeps decreasing from 25,000 to 50,000 years, reaching a uniform concentration equal to $6.9 \cdot 10^{-4}$ M in the three materials at 50,000 years (Figure 2-33). In Period III the diffusion in the glass is allowed. The computed concentrations of dissolved aluminum, calcium, magnesium, sodium and potassium show similar trends with an increase in the concentrations from 25,000 to 30,000 years. Later, the concentrations decrease until $t = 50,000$ years (not shown here).

The computed concentration of dissolved Fe^{2+} in the glass decreases with time from 25,000 to 50,000 years. The concentration of dissolved Fe^{2+} in the canister, however, increases due to the re-dissolution of magnetite. The concentration is largest near the glass/canister interface. The peak of Fe^{2+} concentration moves slightly towards the canister/bentonite.

Figure 2-35 shows the spatial distribution of the computed concentrations of exchanged cations in the bentonite at 50,000 years. The concentrations of exchanged calcium, magnesium, sodium and potassium in the bentonite are uniform. The concentration of exchanged sodium in Period III increases from 22 to 26 meq/100g while that of exchanged calcium increases from 43 to 55 meq/100g. The concentration of exchanged magnesium, however, decreases from 37 to 18 meq/100g. The concentration of exchanged potassium shows no major changes. The concentration of exchanged Fe at 50,000 years decreases with distance from the canister/bentonite interface in a manner similar to Period II. Figure 2-36 shows the spatial distribution of the surface complexes at strong, weak #1 and #2 sites at 50,000 years. The peaks of the concentrations of XOFe^+ and XOFeOH in strong sites and

XXOFe⁺ in weak #1 sites near the canister/bentonite interface are similar to those computed at 25,000 years.

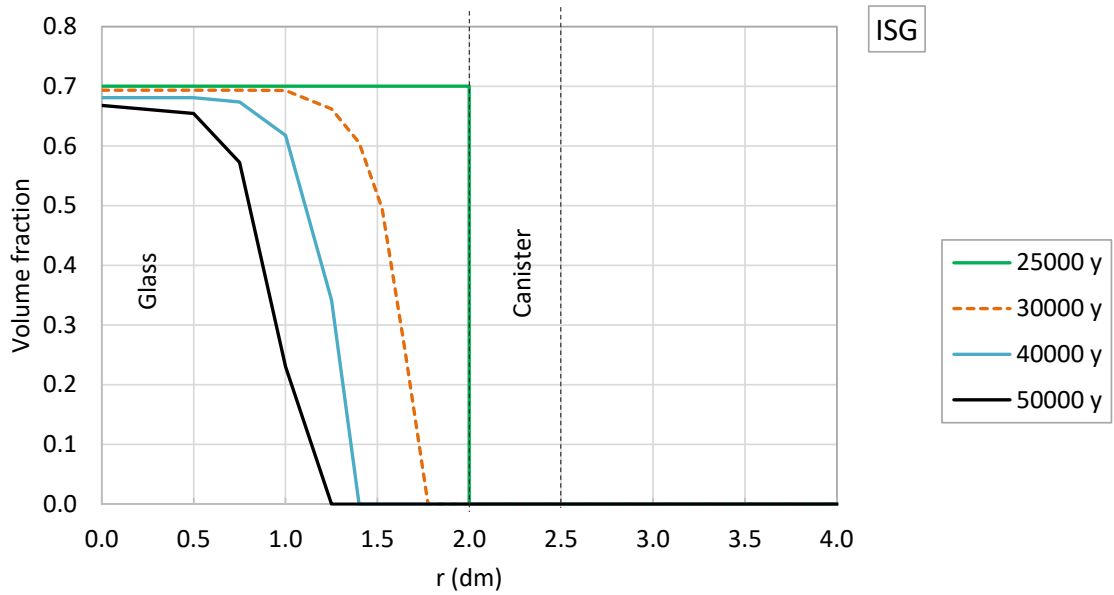


Figure 2-23. Spatial distribution of the computed volume fraction of ISG at selected times of Period III.

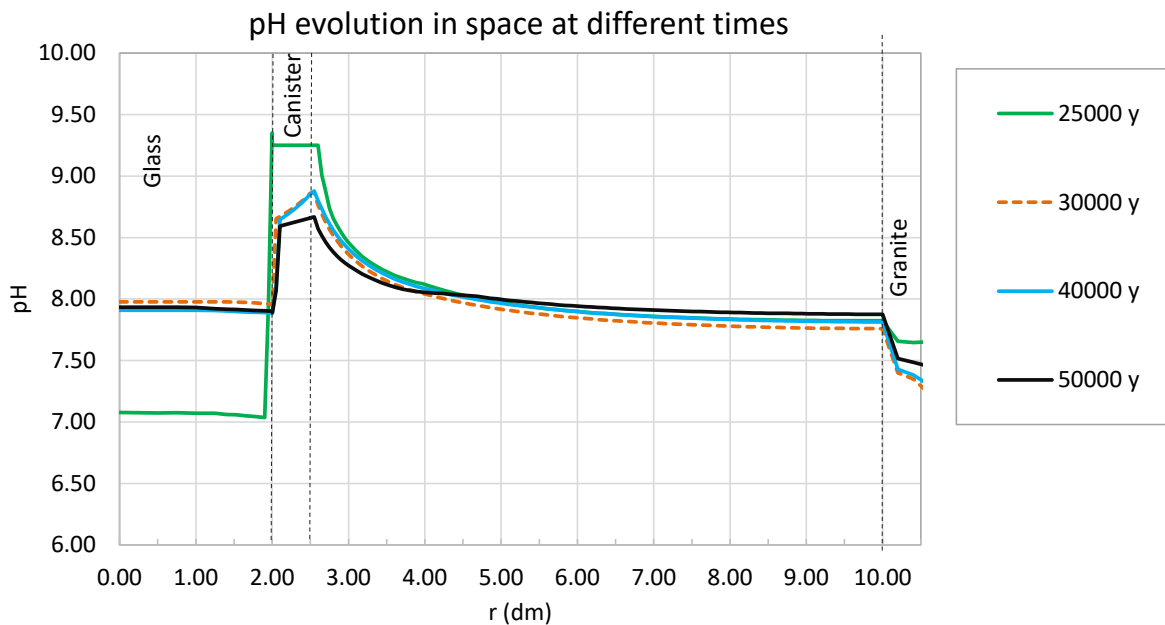


Figure 2-24. Spatial distribution of the computed pH at selected times of Period III.

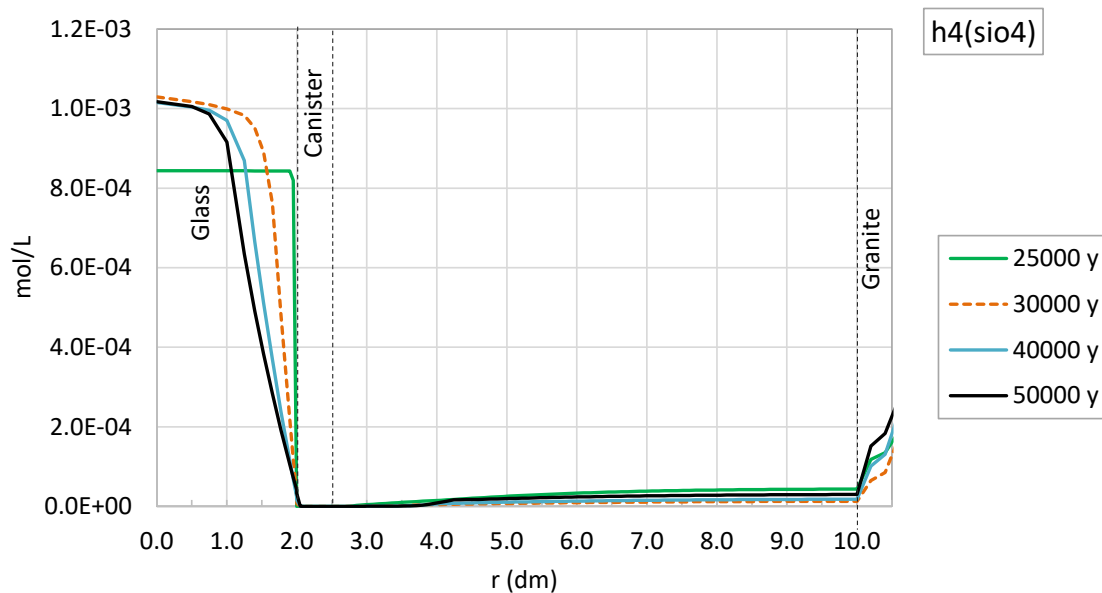


Figure 2-25. Spatial distribution of the computed concentration of dissolved silica at selected times of Period III.

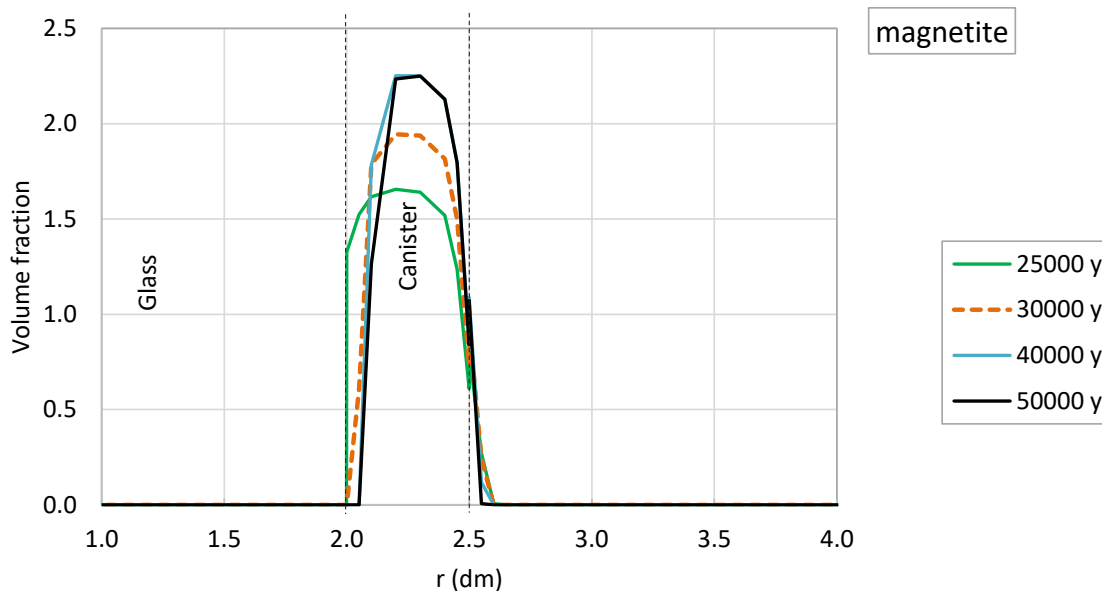


Figure 2-26. Spatial distribution of the computed volume fraction of magnetite at selected times of Period III. The bottom plot shows an enlargement around the canister ($1 < r < 4$ dm).

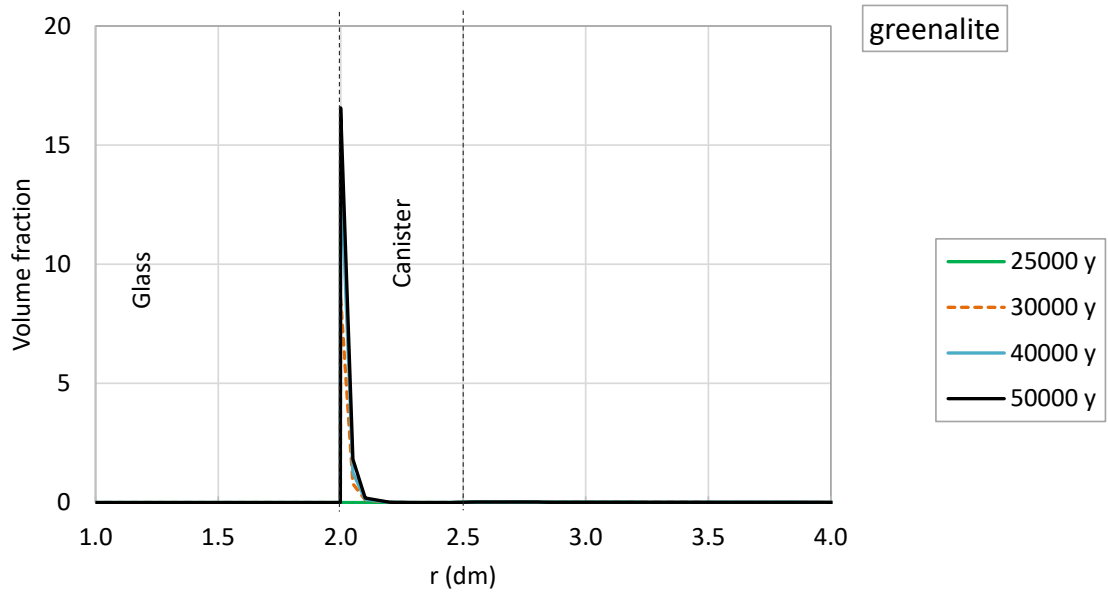


Figure 2-27. Spatial distribution of the computed volume fraction of greenalite at selected times of Period III.

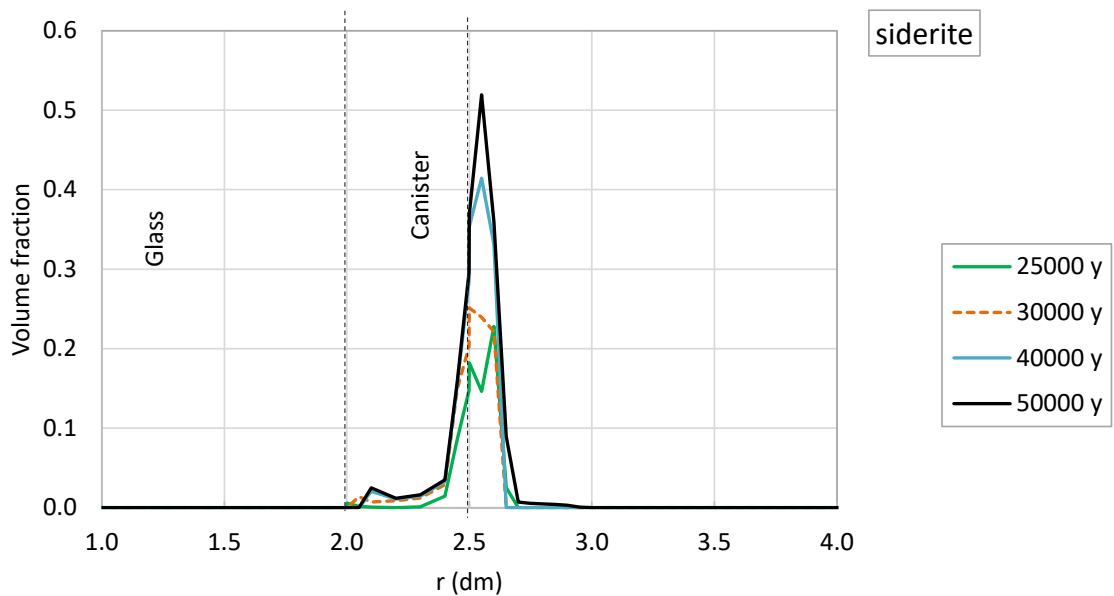


Figure 2-28. Spatial distribution of the computed volume fraction of siderite at selected times of Period III.

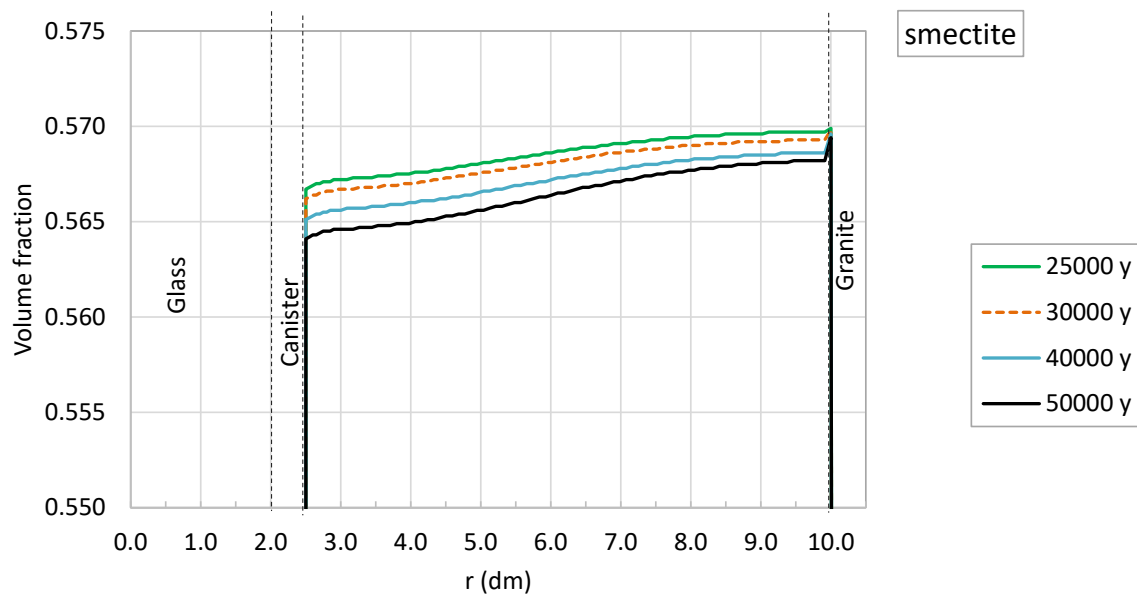


Figure 2-29. Spatial distribution of the computed volume fraction of smectite at selected times of Period III.

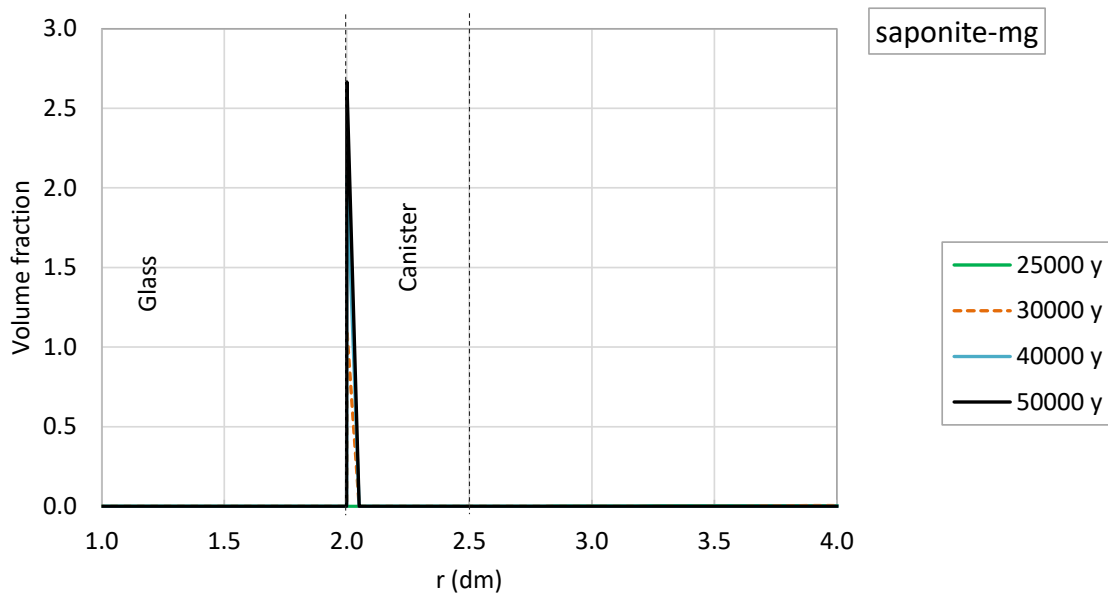


Figure 2-30. Spatial distribution of the computed volume fraction of Mg-saponite at selected times of Period III.

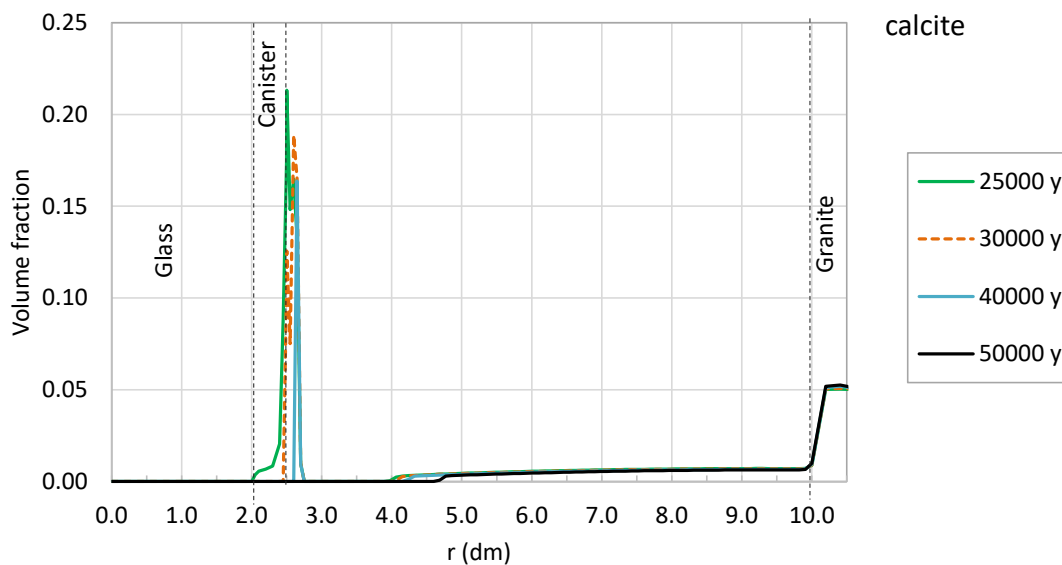


Figure 2-31. Spatial distribution of the computed volume fraction of calcite at selected times of Period III.

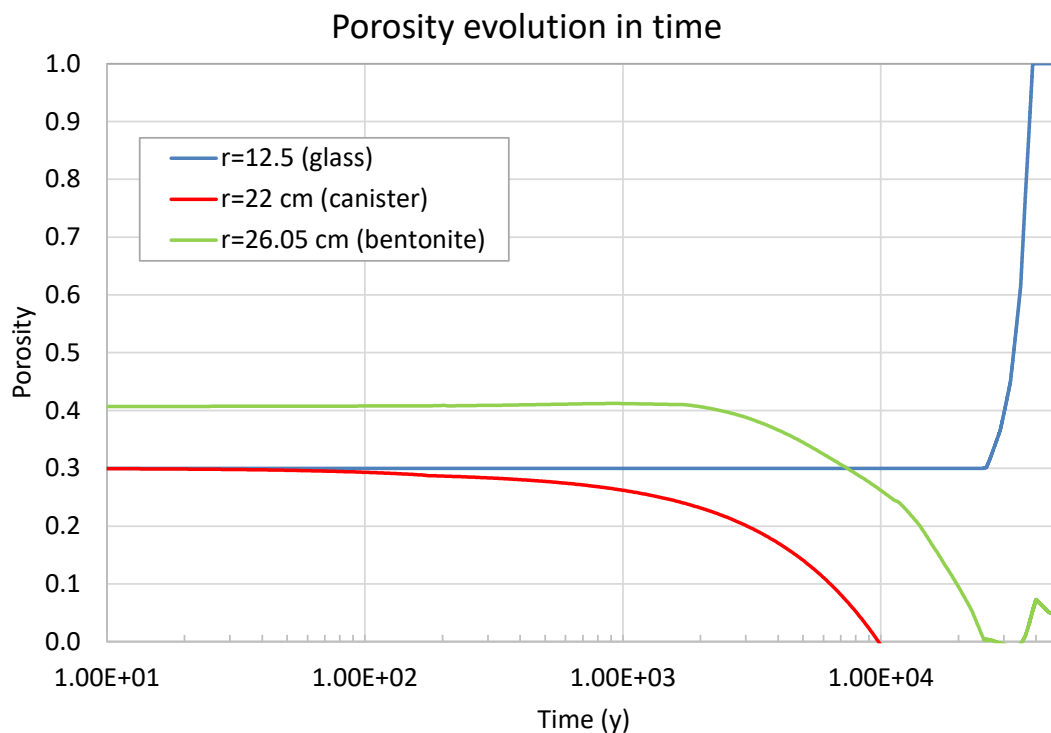


Figure 2-32. Time evolution of the porosity changes caused by mineral dissolution/precipitation during Periods II and III in the glass ($r = 12.5$ cm), the canister ($r = 22$ cm) and the bentonite ($r = 26.5$ cm).

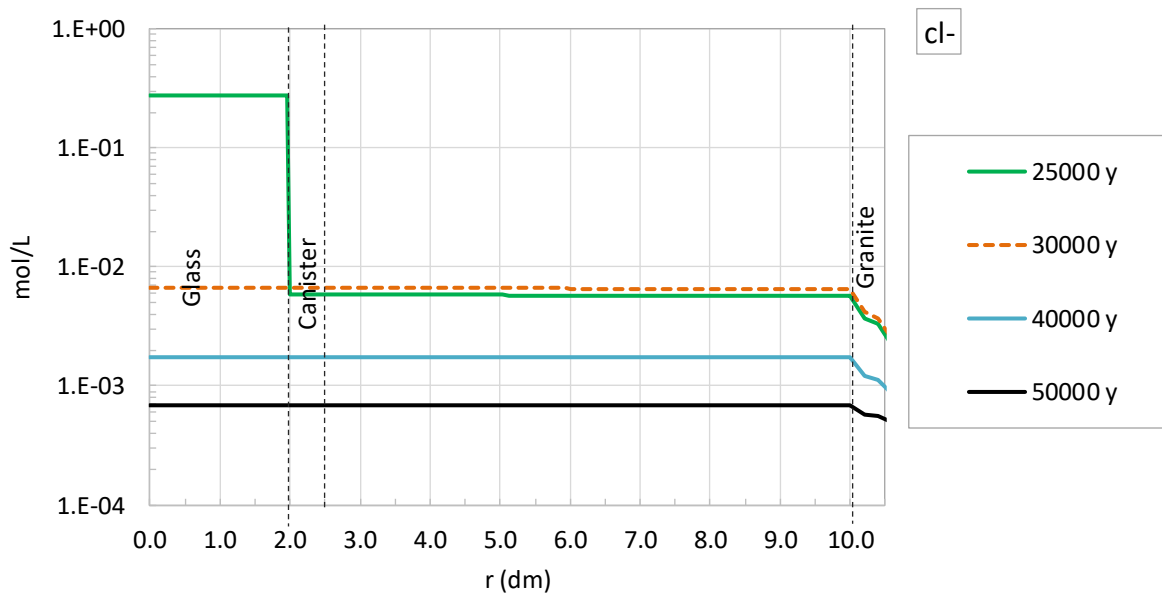


Figure 2-33. Spatial distribution of the computed concentration of dissolved Cl^- at selected times of Period III.

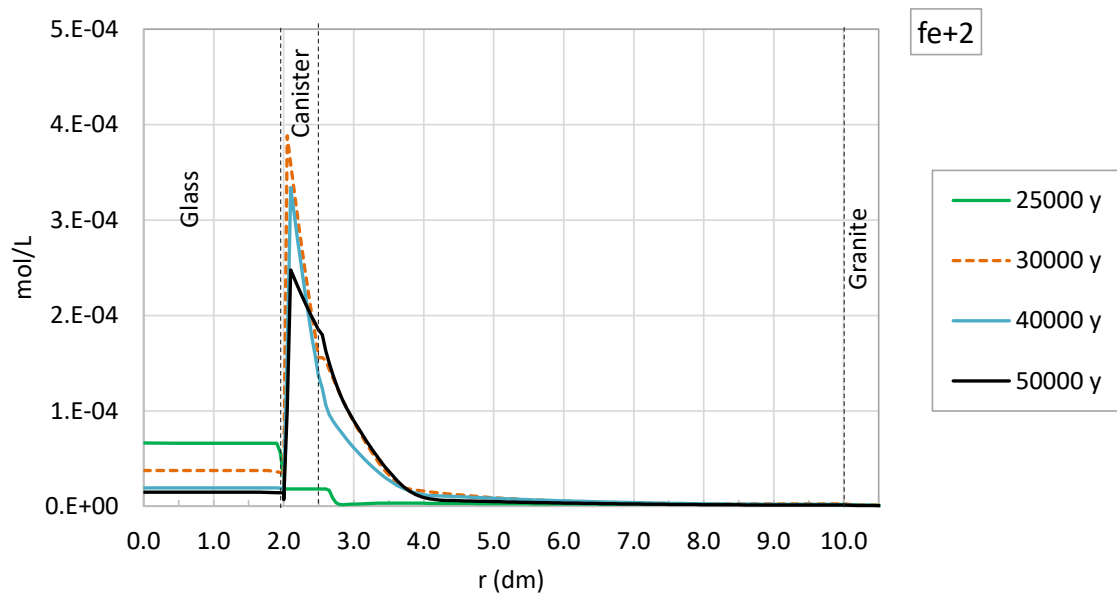


Figure 2-34. Spatial distribution of the computed concentration of dissolved Fe^{2+} at selected times of Period III.

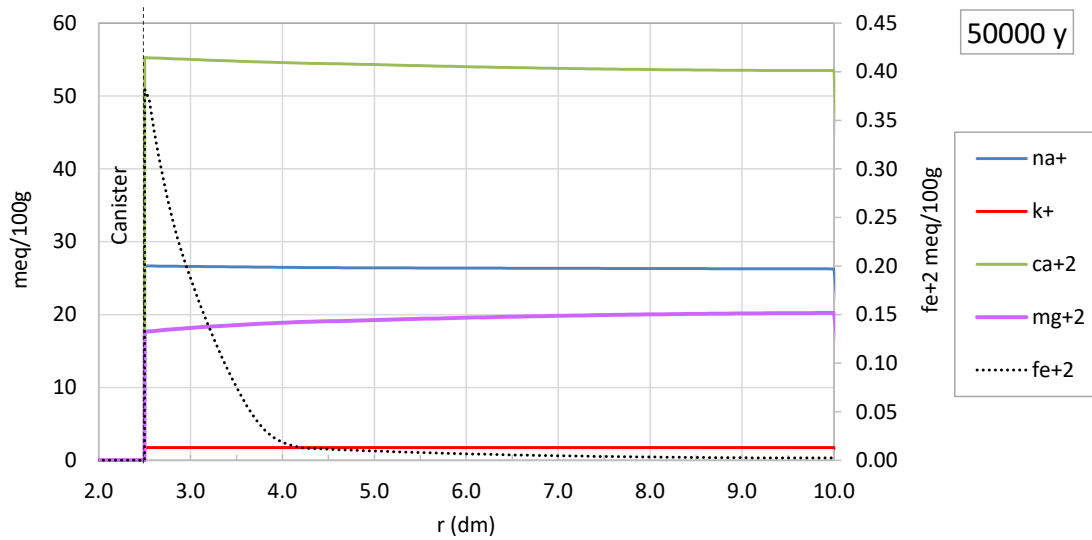


Figure 2-35. Spatial distribution of the computed concentration of exchanged cations at the end of Period III ($t = 50,000$ years).

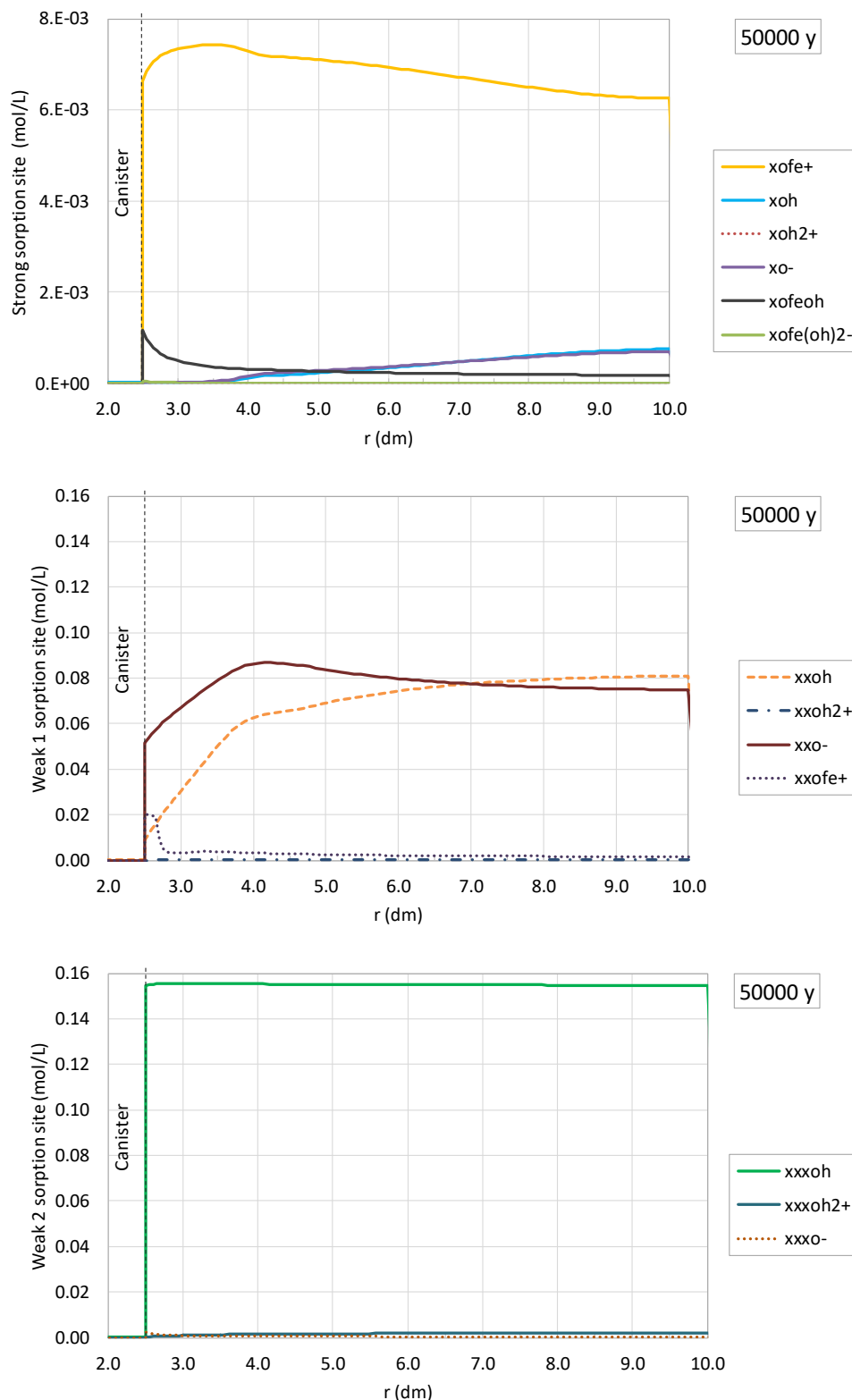


Figure 2-36. Spatial distribution of the computed concentration of surface complexes at the strong (upper plot), weak #1 (intermediate plot) and weak #2 (bottom plot) sites at the end of Period III ($t = 50,000$ years).

2.7 Model results for variants and sensitivity cases

This section presents the calculated results of the sensitivity cases and variants for the reactive transport model of the geochemical evolution in a HLW disposal cell in granite listed in Table 2-1.

To reduce the computation time, the model runs for the sensitivity cases and variants were performed with a less refined mesh by neglecting smectite dissolution and simplifying the bentonite/granite boundary condition. The role of the EDZ and the granite was simulated by considering a flux boundary condition at the bentonite/granite boundary.

2.7.1 Sensitivity Case 1

Sensitivity Case 1 aims at evaluating the sensitivity of the predictions to the silica saturation threshold used in the kinetic glass dissolution rate (Equation 2.7). The value used in the base case is 10^{-3} mol/L while in the sensitivity case it was $5 \cdot 10^{-4}$ mol/L. A decrease in C_{Si}^* leads to a decrease in glass dissolution rate. The results of Sensitivity Case 1 are presented in Deliverable D2.19 (Samper et al., 2023).

2.7.2 Sensitivity Case 2

Sensitivity Case 2 considers a granitic porewater with a dissolved concentration of Cl^- 8 times larger than the value used in the base case. The concentration of dissolved Cl^- shows a slight increase near the bentonite/granite interface times at the end of Period III (Figure 2-37). Numerical results of the rest of the chemical system are not sensitive to the increase of Cl^- concentration in the granite boundary water. Green-rust and akaganeite do not precipitate.

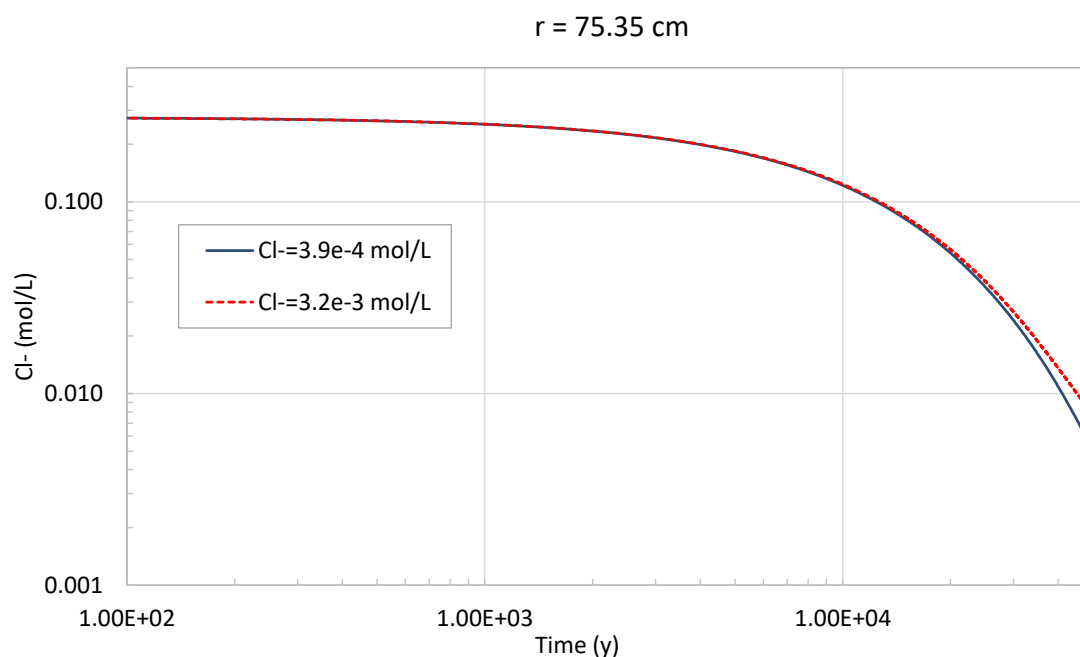


Figure 2-37. Time evolution of the computed concentration of dissolved Cl^- in the bentonite ($r = 7.535$ dm) for the base case and the Sensitivity Case 2.

2.7.3 Variant 1

Compacted MX-80 bentonite instead of FEBEX bentonite is considered in Variant 1 (Figure 2-5). The thickness of the compacted MX-80 bentonite is equal to 3.5 dm, Figure 2-38 shows the 1D mesh adopted for the Variant 1, which is similar to that for the base run with 7.5 dm of bentonite.

EURAD Deliverable 2.17 – Integrated reactive transport models for assessing the chemical evolution at the disposal cell scale

MX80 bentonite dissolution is simulated by assuming the chemical formulation of the MX-80 bentonite proposed by Chaparro et al. (2021) and by using the kinetic rate law of Eq. (2.1) and the same parameters as those considered for the FEBEX bentonite. The same initial and secondary mineral phases as those for the base run was considered for the Variant 1.

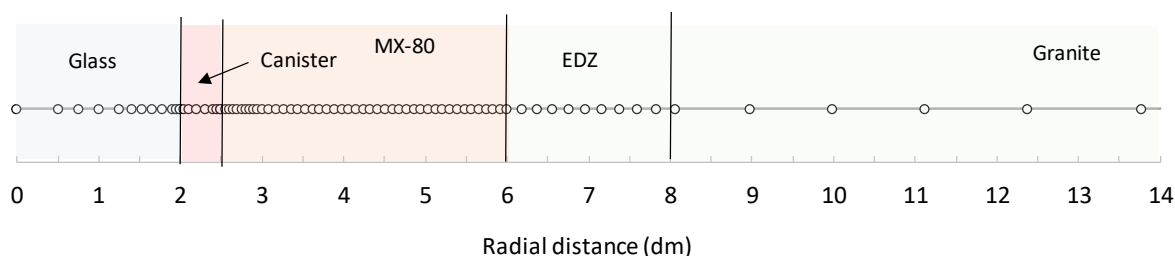


Figure 2-38. Finite element mesh used in Variant 1 which considers MX-80 bentonite with a thickness of 35 cm instead of FEBEX bentonite.

Figure 2-39 shows the computed pH at 25,000 and 50,000 years for the base run and Variant 1. The computed pH in Variant 1 is larger than that in the base run. The trend of the computed dissolved Fe^{+2} is similar in the base run and in the Variant 1 however; the computed dissolved iron is larger in the base run than that in Variant 1 (Figure 2-40). Computed dissolved concentrations are slightly different in the base run and in Variant 1 due to the differences in the initial bentonite pore water (not shown here). Computed exchanged cations and sorbed concentrations are similar in the base run and in Variant 1 (not shown here).

Computed magnetite precipitation is similar in the base run and in the Variant 1 (Figure 2-41). Computed siderite and greenalite precipitation trend are similar in the base run and in Variant 1, but the precipitation at the bentonite/canister interface for the siderite (Figure 2-42) and at the glass/canister interface for the greenalite (Figure 2-43) are slightly larger in the base run than those in Variant 1.

Computed ISG and smectite dissolution in the base run is slightly larger than that in the Variant 1 (Figure 2-44 and Figure 2-45).

Figure 2-46 shows the porosity changes due to mineral dissolution/precipitation. The porosity changes are similar in the base run and in Variant 1 at the glass ($r = 12.5$ cm) and at the canister ($r = 22$ cm). The porosity changes in the base run is larger than that in Variant 1 due to the mineral precipitation is larger in the base run.

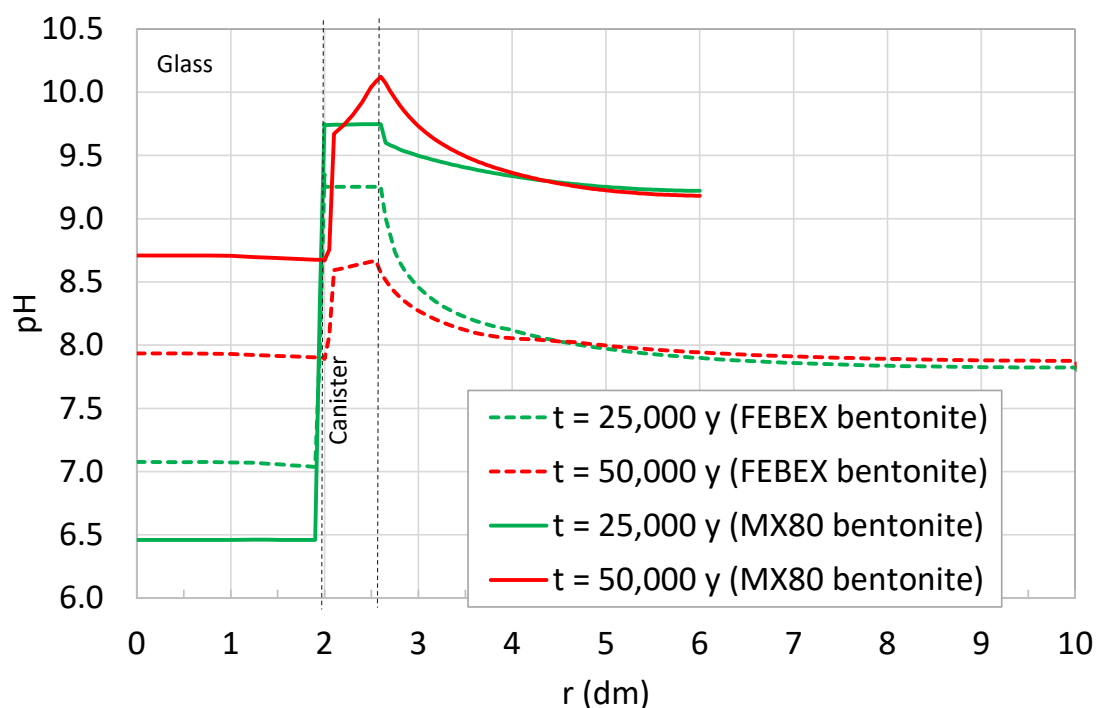


Figure 2-39. Spatial distribution of the computed pH at 25,000 years and at 50,000 years for the base case (FEBEX bentonite) and Variant 1 (MX80 bentonite). Results are presented for the glass, canister and bentonite FEBEX (7.5 dm) and MX80 (3.5 dm).

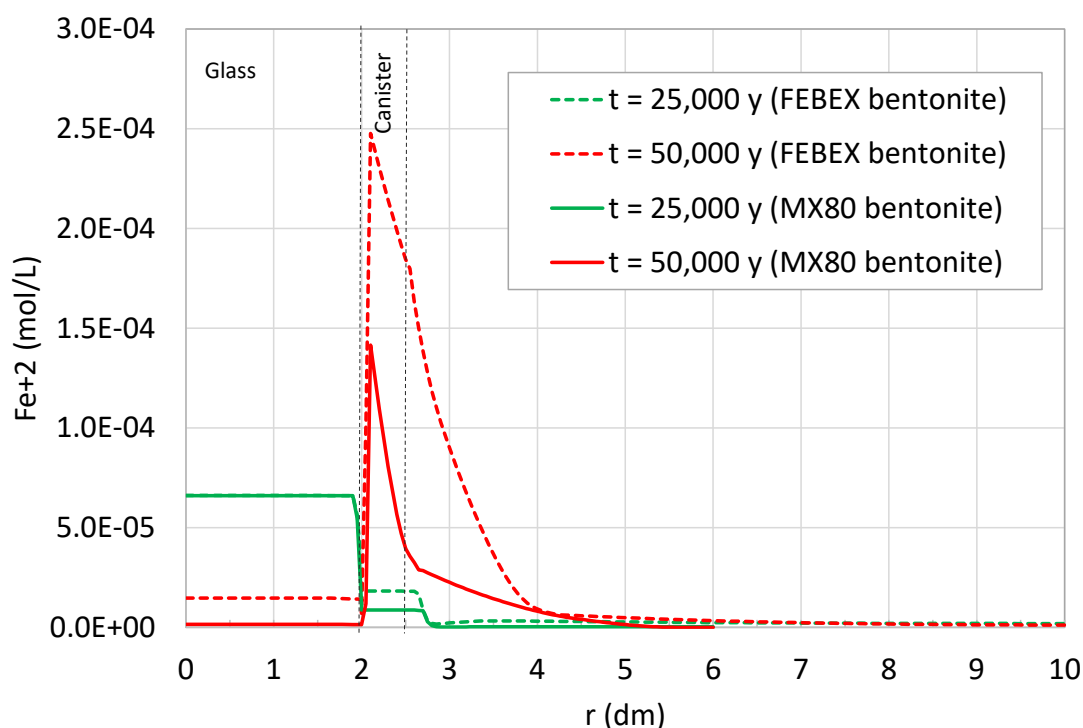


Figure 2-40. Spatial distribution of the computed dissolved Fe⁺² at 25,000 years and at 50,000 years for the base case (FEBEX bentonite) and Variant 1 (MX80 bentonite). Results are presented for the glass, canister and bentonite FEBEX (7.5 dm) and MX80 (3.5 dm).

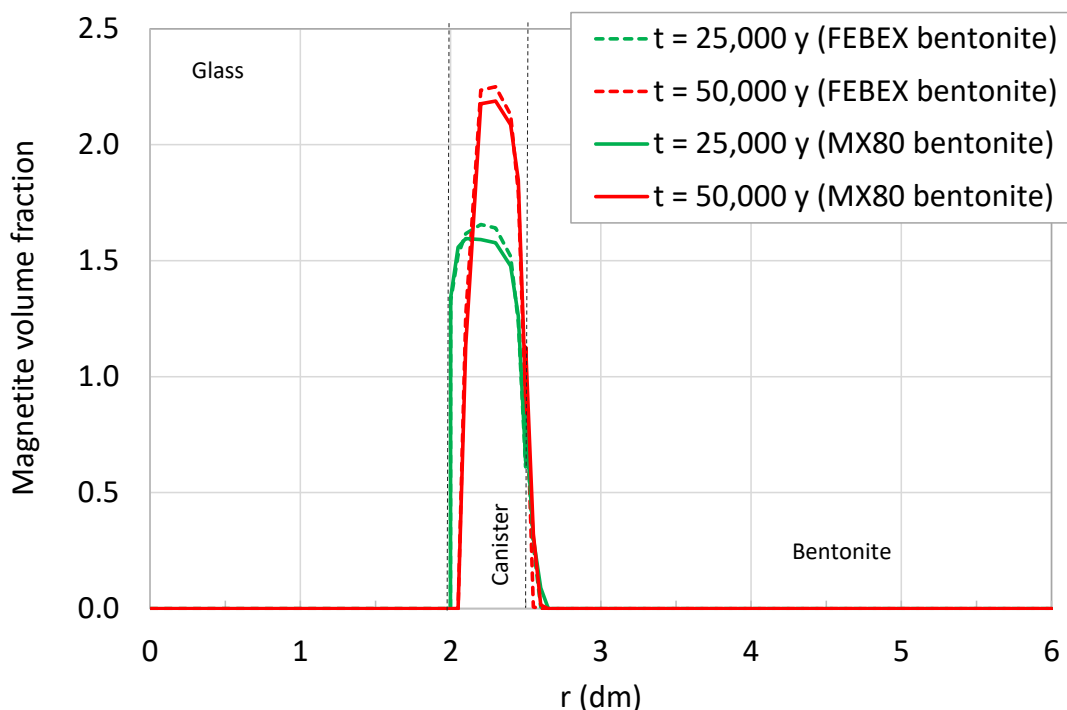


Figure 2-41. Spatial distribution of the computed magnetite volume fraction at 25,000 years and at 50,000 years for the base case (FEBEX bentonite) and Variant 1 (MX80 bentonite). Results are presented for the glass, canister and bentonite FEBEX (7.5 dm) and MX80 (3.5 dm).

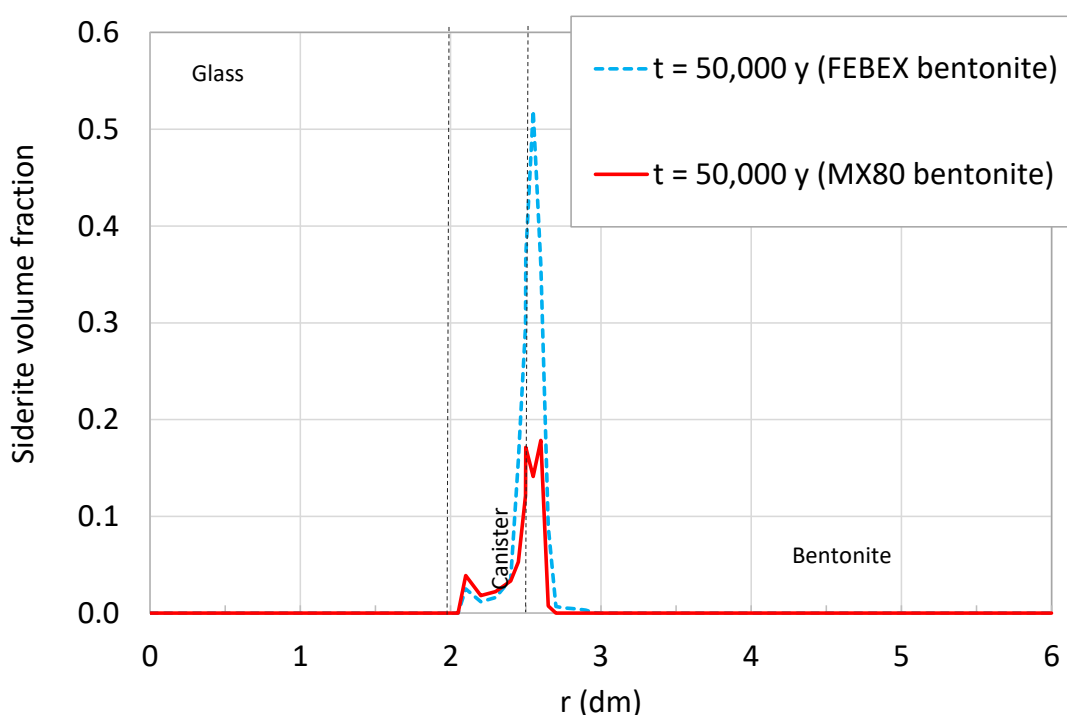


Figure 2-42. Spatial distribution of the computed siderite volume fraction at 50,000 years for the base case (FEBEX bentonite) and Variant 1 (MX80 bentonite). Results are presented for the glass, canister and bentonite FEBEX (7.5 dm) and MX80 (3.5 dm).

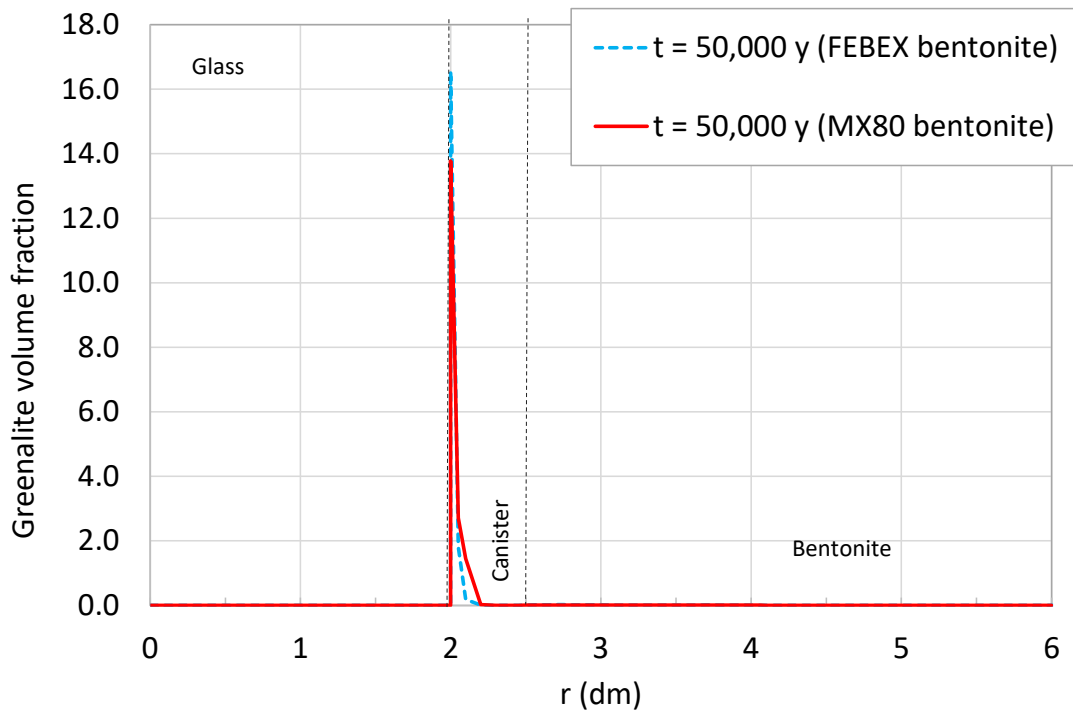


Figure 2-43. Spatial distribution of the computed greenalite volume fraction at 50,000 years for the base case (FEBEX bentonite) and Variant 1 (MX80 bentonite). Results are presented for the glass, canister and bentonite FEBEX (7.5 dm) and MX80 (3.5 dm).

mjkm

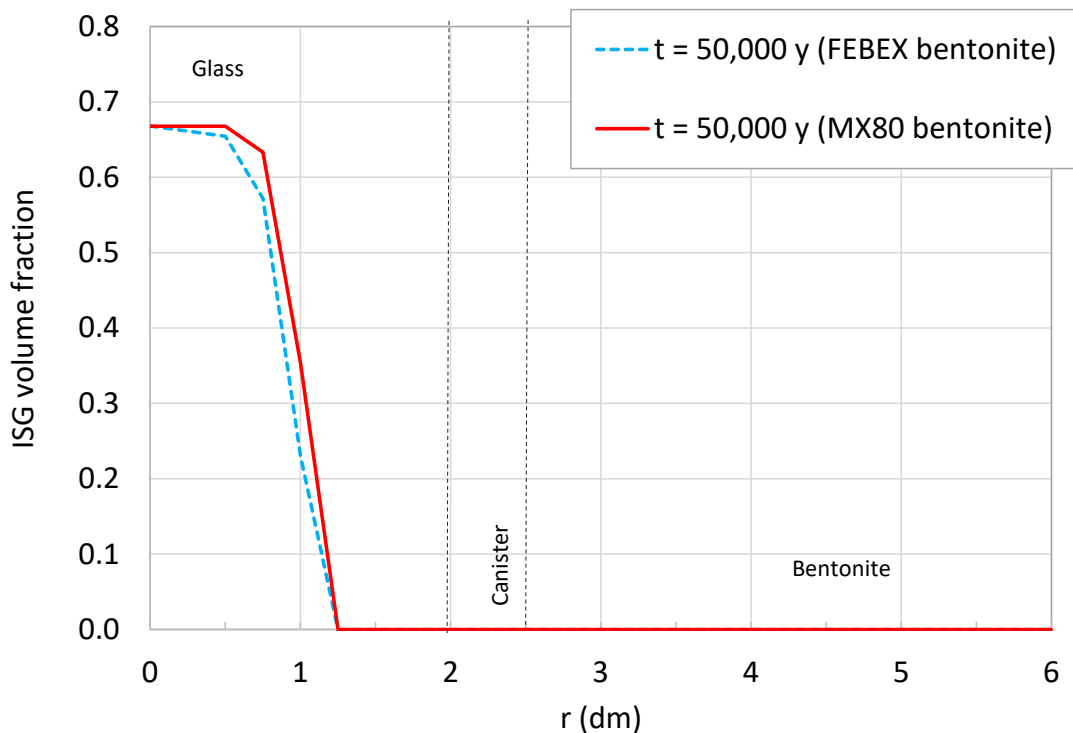


Figure 2-44. Spatial distribution of the computed ISG volume fraction at 50,000 years for the base case (FEBEX bentonite) and Variant 1 (MX80 bentonite). Results are presented for the glass, canister and bentonite FEBEX (7.5 dm) and MX80 (3.5 dm).

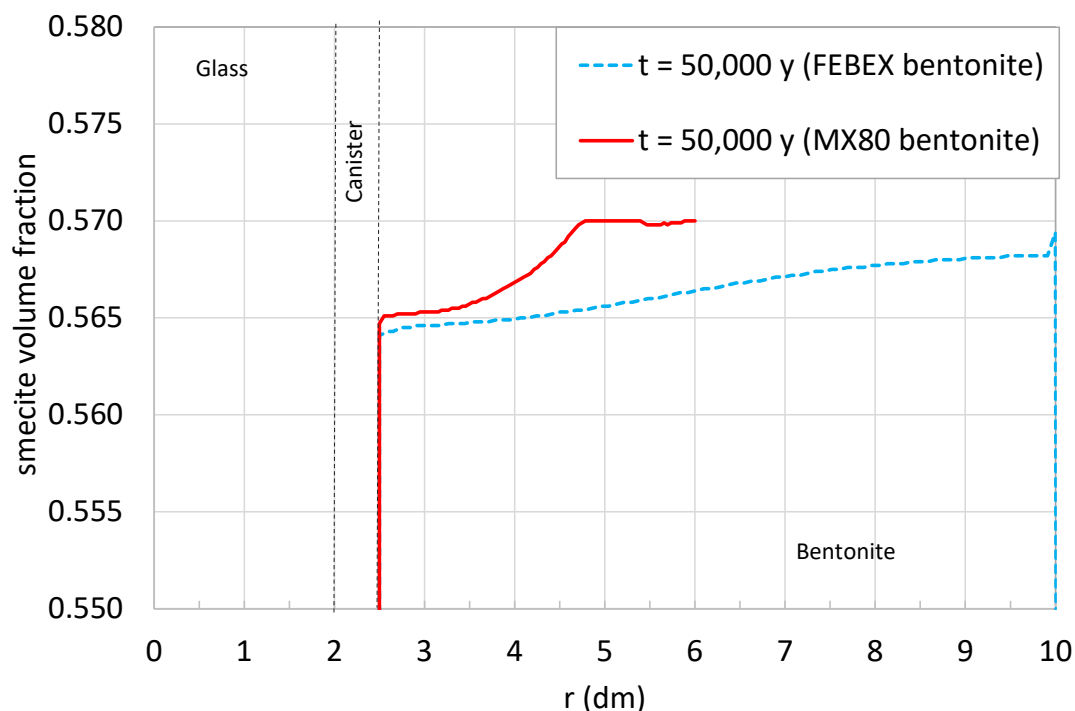


Figure 2-45. Spatial distribution of the computed smectite volume fraction at 50,000 years for the base case (FEBEX bentonite) and Variant 1 (MX80 bentonite). Results are presented for the glass, canister and bentonite FEBEX (7.5 dm) and MX80 (3.5 dm).

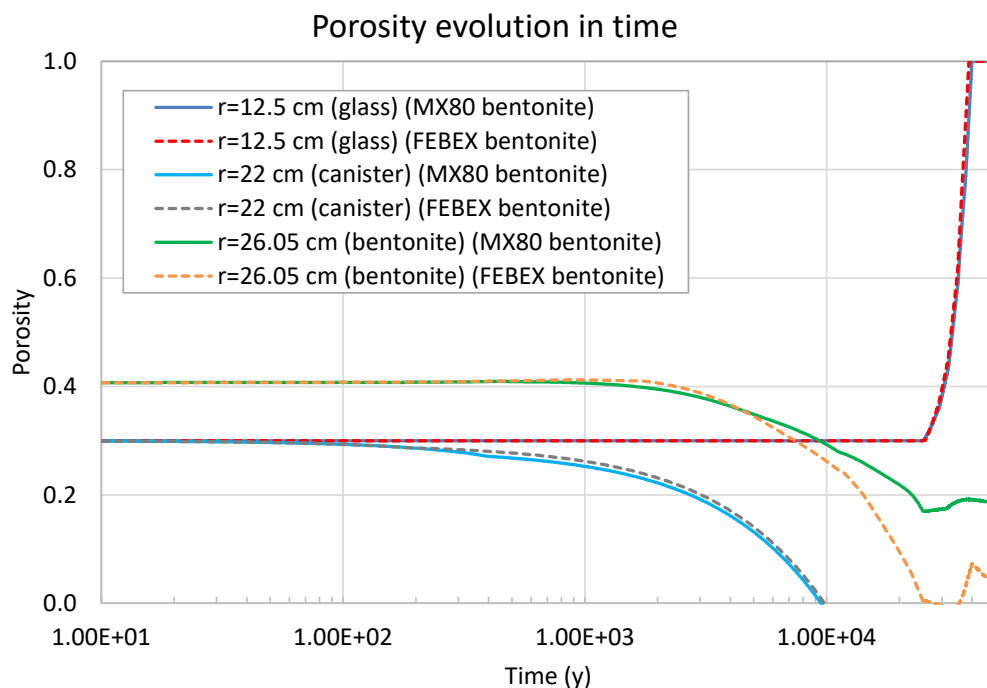


Figure 2-46. Time evolution of the porosity changes caused by mineral dissolution/precipitation during Periods II and III in the glass ($r = 12.5$ cm), the canister ($r = 22$ cm) and the bentonite ($r = 26.5$ cm) for the base case (FEBEX bentonite) and the Variant 1 (MX80 bentonite).

2.7.4 Variant 2

Variant 2 considers the EDZ and a larger hydraulic conductivity of the host rock (Figure 2-5). The combined effect of the EDZ and the increase in the hydraulic conductivity of the rock leads to an increase of groundwater flux through the granite, which increases from 0.1 L/y in the base run, to 1 and 4.7 L/y in Variant 2.

Figure 2-47 shows the computed pH in the canister at the end of Periods II (25,000 years) and III (50,000 years) for granite fluxes equal to 0.1, 1 and 4.7 L/y. The computed pH in the canister and the bentonite at 25,000 years increases with increasing granite flux. The computed values of pH at 50,000 years are smaller than those computed at the end of Period II. The profiles of pH at the end of Period III show mild gradients, especially for a granite flux equal to 4.7 L/y.

The concentrations of the aqueous species in Variant 2 show a strong decrease after 100 years due the combined effect of solute out diffusion from the bentonite into the granite and the flushing of the solutes by groundwater flow (Figure 2-48 and Figure 2-49). The larger the granite flux, the larger the decrease of solute concentrations in the bentonite.

The precipitation of corrosion products is sensitive to the increase in granite flux. Figure 2-50 and Figure 2-51 show the time evolution of the computed magnetite, greenalite and siderite precipitation in the canister and the bentonite near the canister interface. Magnetite precipitation in the canister in Variant 2 is slightly smaller than that of the base run. Greenalite precipitation in the bentonite increases with increasing granite flux. On the other hand, siderite precipitation in the canister in Variant 2 is larger than that of the base. Siderite precipitation in the bentonite shows an opposite pattern. The concentrations of other mineral phases, such as calcite, quartz, gypsum, and concentrations of exchanged cations and surface complexes are not sensitive to the increase in granite flux (not shown here).

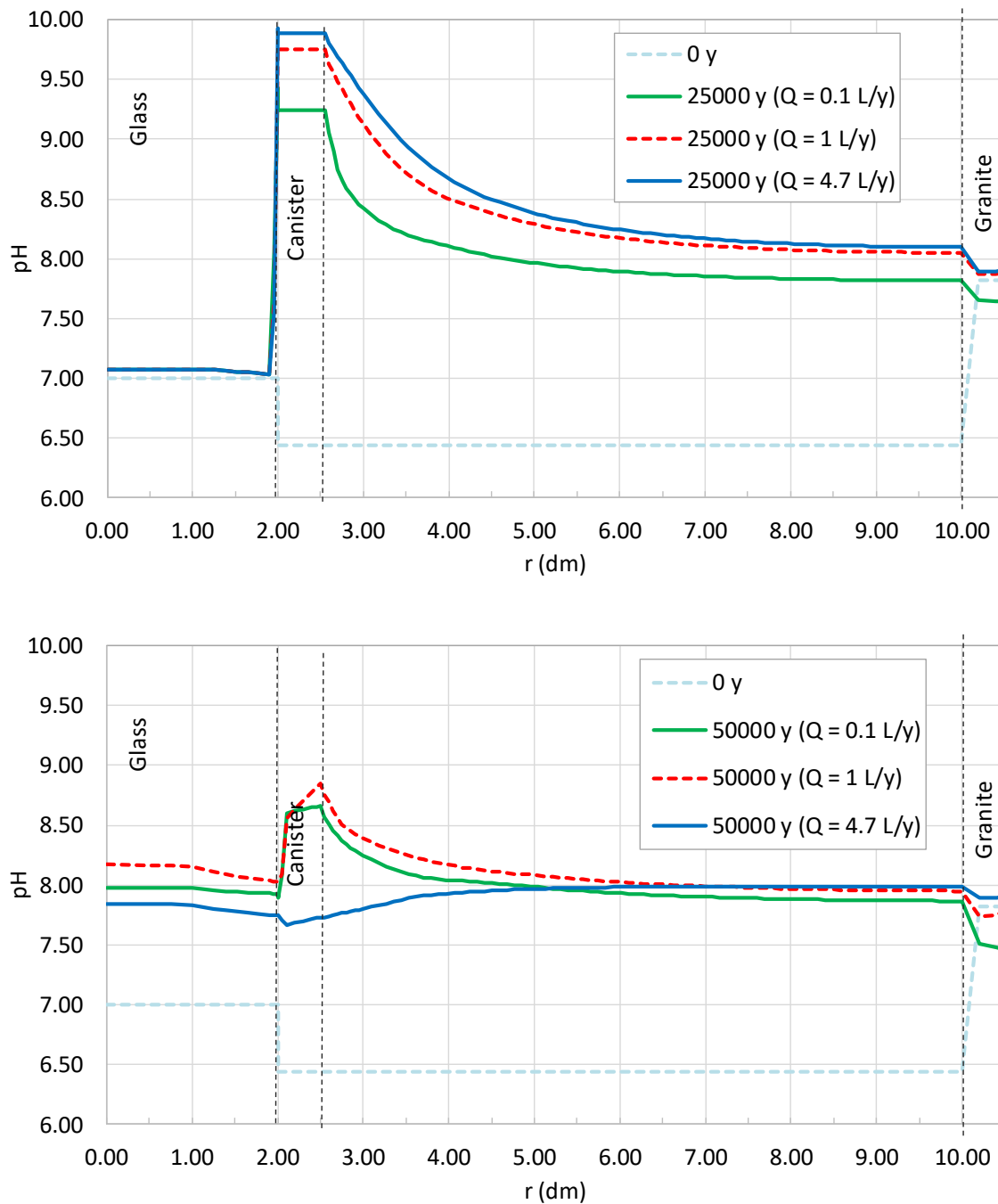


Figure 2-47. Spatial distribution of the computed pH at 25,000 years (top) and at 50,000 years (bottom) for the base case ($Q = 0.1$ L/y) and Variant 2 ($Q = 1$ L/y and $Q = 4.7$ L/y).

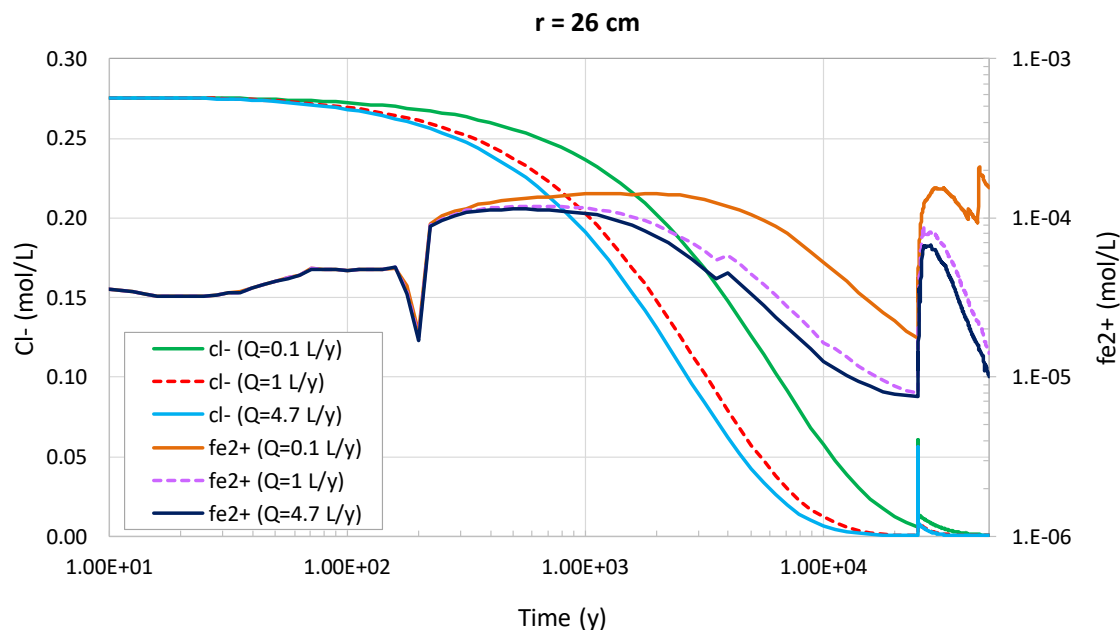


Figure 2-48. Time evolution of the computed concentrations of dissolved Cl⁻ and Fe in the bentonite near the canister interface ($r = 26$ cm) for the base case ($Q = 0.1$ L/y) and Variant 2 ($Q = 1$ L/y and $Q = 4.7$ L/y).

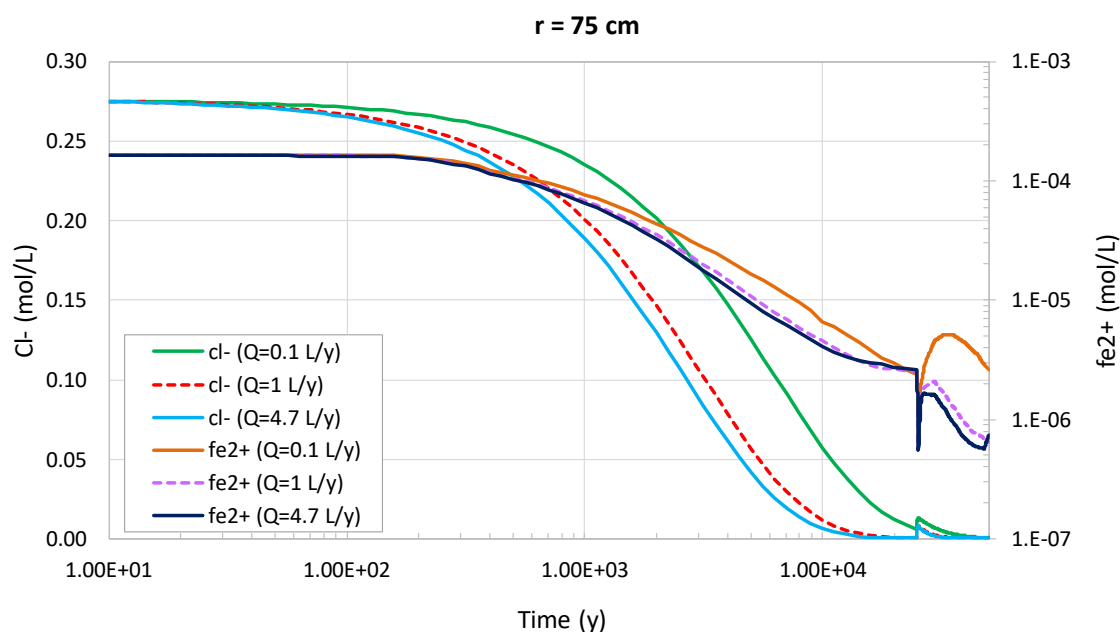


Figure 2-49. Time evolution of the computed concentration of dissolved Cl⁻ and Fe in the bentonite near the granite interface ($r = 75$ cm) for the base case ($Q = 0.1$ L/y) and Variant 2 ($Q = 1$ L/y and $Q = 4.7$ L/y).

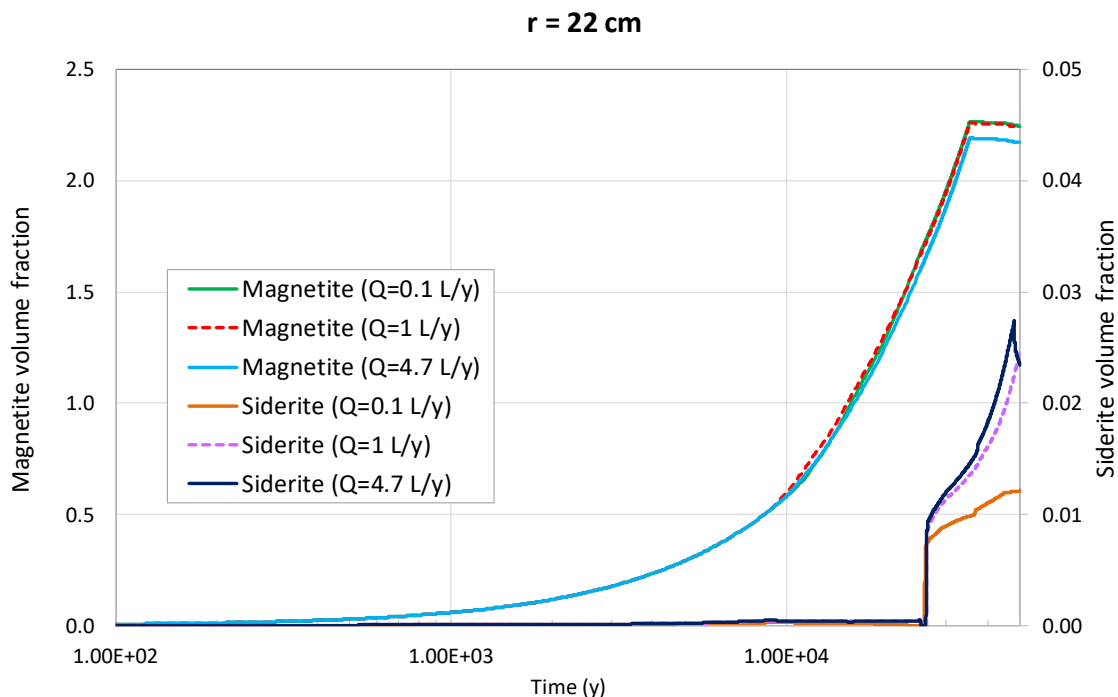


Figure 2-50. Time evolution of the computed volume fraction of magnetite and siderite in the canister ($r = 22$ cm) for the base case ($Q = 0.1$ L/y) and Variant 2 ($Q = 1$ L/y and $Q = 4.7$ L/y).

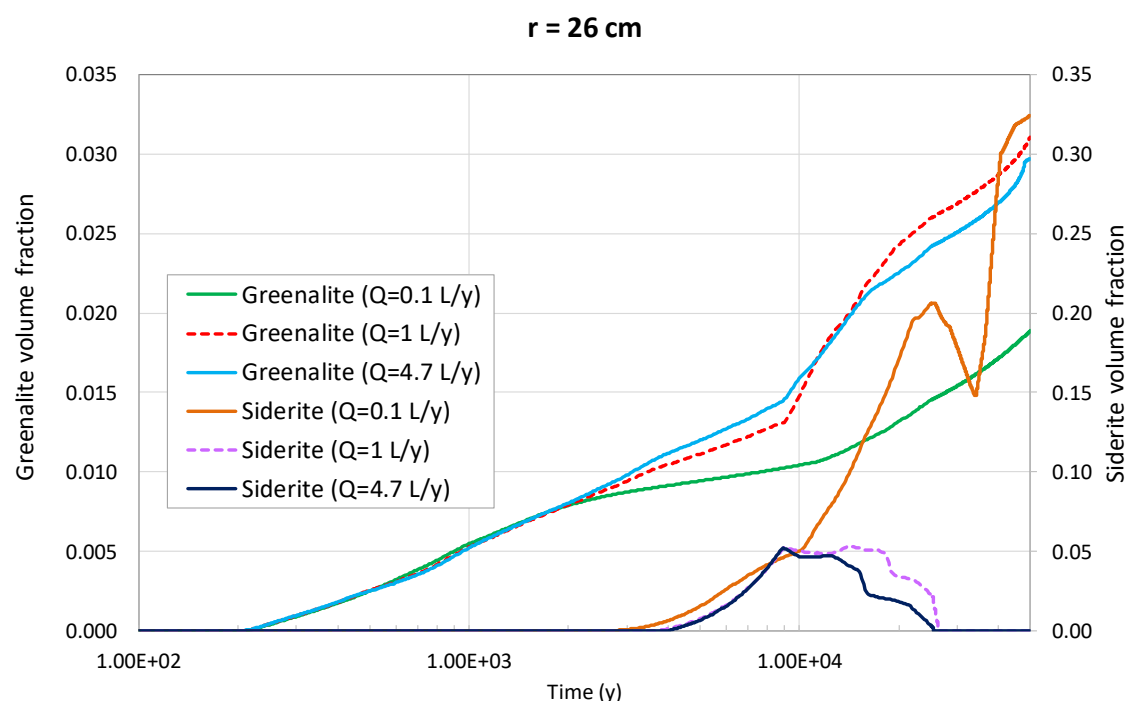


Figure 2-51. Time evolution of the computed volume fraction of greenalite and siderite in the bentonite near the canister interface ($r = 26$ cm) for the base case ($Q = 0.1$ L/y) and Variant 2 ($Q = 1$ L/y and $Q = 4.7$ L/y).

2.7.5 Variant 3

Variant 3 considers the conditions of the Reference Czech crystalline rock (Figure 2-5). The chemical composition of the SGW2 was used for the Czech granite porewater (Table 2-12).

Predictions are not sensitive to the chemical composition of the granite porewater. Figure 2-52 shows the spatial distribution of the computed pH at 25,000 and 50,000 years for Variant 3 and the base run. Figure 2-53 shows the time evolution of the computed concentrations of Cl^- and Fe^{2+} . Clearly, there are no significant differences between the computed results for both runs. Computed mineral phases dissolution/precipitation, surface complexation and cation exchange are not sensitive to the change in the chemical composition of the rock porewater (not shown here).

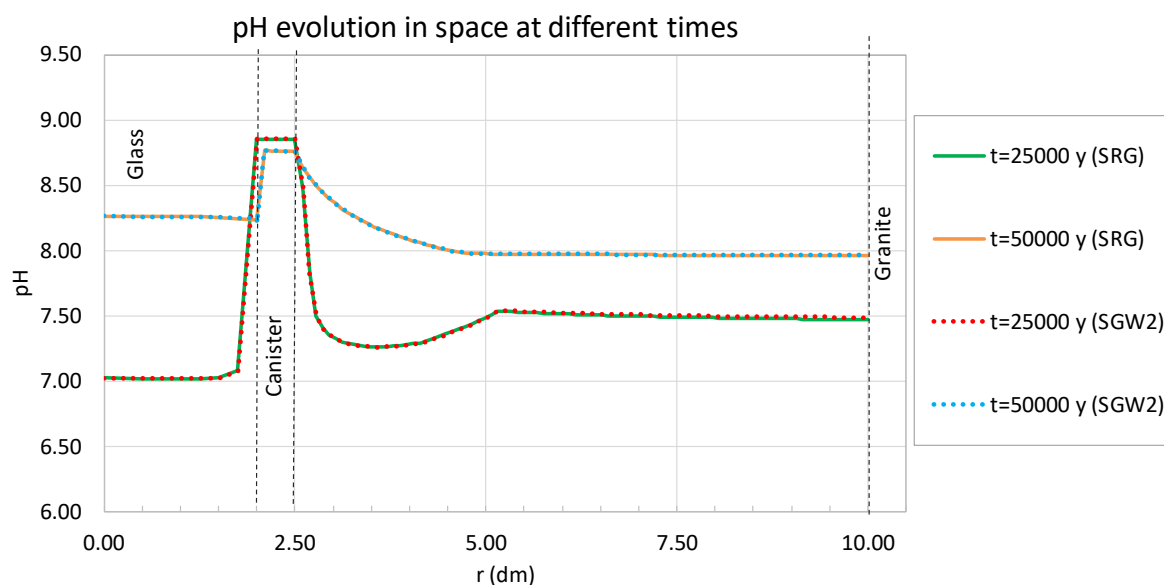


Figure 2-52. Spatial distribution of the computed pH for the base run and Variant 3.

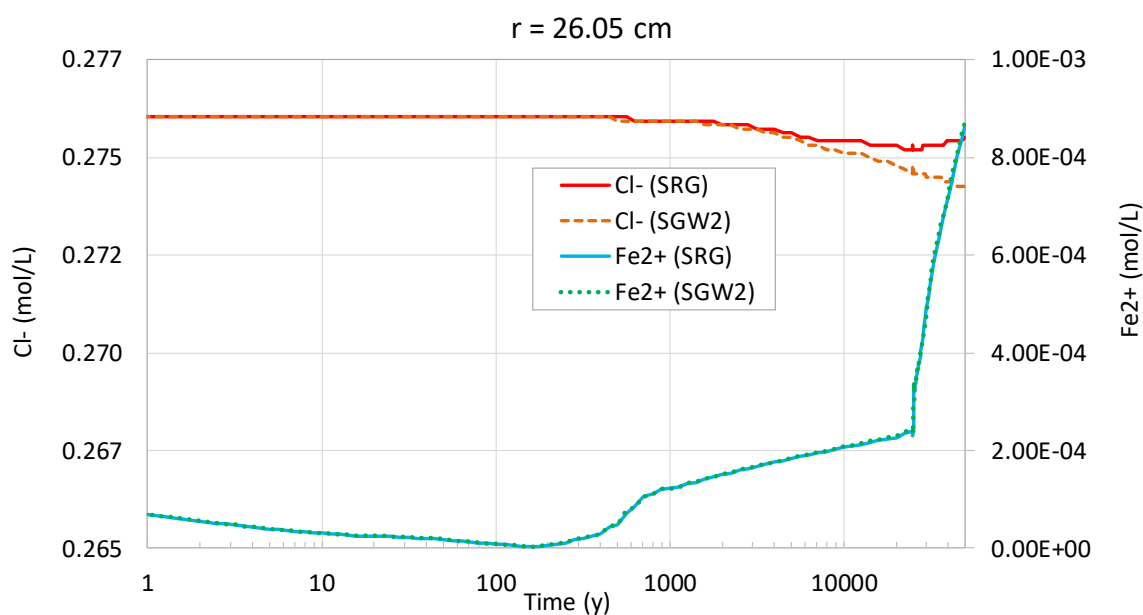


Figure 2-53. Time evolution of the computed concentrations of dissolved Cl^- and Fe^{2+} siderite in the bentonite near the canister interface ($r = 2.605 \text{ dm}$) for the base case and Variant 3.

2.8 Summary and Conclusions

A reactive transport model of the geochemical evolution of a HLW disposal cell in granite has been presented. Model predictions have been performed for a base run and several sensitivity cases and variants. The base run considers a 75 cm thick saturated FEBEX bentonite buffer and the Spanish Reference granitic rock. The model is non-isothermal, accounts for the thermal transient stage and assumes generalized carbon steel corrosion under anaerobic conditions. Corrosion consumes water and releases ferric iron and $H_2(aq)$. The relevance of the excavation damaged zone (EDZ) is evaluated in a sensitivity case. A simple glass dissolution model is used for the numerical model at the scale of the disposal cell and considers the ISG for vitrified waste.

The base run and the sensitivity runs consider Periods II and III. Period II starts when the bentonite barrier is fully saturated and anoxic conditions are prevailing. Canister corrosion, the interactions of corrosion products and the bentonite and the interactions of bentonite and granite take place in Period II. Period II is assumed to last 25,000 years which coincides with the time at which the remaining thickness of the overpack is 1.5 cm. The corrosion rate is equal to $1.41 \mu\text{m/y}$ and is such that 3.5 cm of canister corrodes after 25,000 years. Canister corrosion proceeds until all the carbon steel is fully corroded at $t = 35,300$ years. Period III starts after canister failure and considers glass alteration and the interactions of glass with corrosion products and uncorroded iron. The model accounts for Periods II and III. This approach is consistent with that used for the HLW disposal cell in clay.

The concentration of dissolved Cl^- in the bentonite in Period II decreases with time due to Cl^- diffusion from the bentonite into the granite because the initial Cl^- concentration in the granite porewater is much smaller than the initial concentration in the bentonite. The profiles of the concentration of Cl^- show very small gradients because the solute flux from the bentonite into the granite is not controlled by solute diffusion through the bentonite, but by solute advection and diffusion in the granite. Canister corrosion causes an increase in pH. The computed pH at the end of Period II (25,000 years) is equal to 9.25 in the canister and ranges from 9.25 to 7.82 in the bentonite. The concentration of dissolved Fe^{2+} increases in the first 1,000 years and later decreases. The time evolution of the computed pH and the concentration of dissolved Fe^{2+} is controlled by: 1) The dissolution/precipitation of Fe minerals in the canister and in the bentonite near the bentonite/canister interface, 2) Fe exchange and 3) Fe and proton surface complexation reactions.

Magnetite precipitates mostly in the canister in Period II. Magnetite precipitation proceeds as long as the canister is corroding. The thickness of magnetite precipitation band in the bentonite at $t = 25,000$ years is about 1 cm. Siderite precipitates at both sides of the canister/bentonite interface. The precipitation front penetrates more than 1 cm into the bentonite. Goethite does not precipitate. The greenalite volume fraction in the canister increases with time, especially near the canister/bentonite interface and in the bentonite. The thickness of the greenalite precipitation band in the bentonite is larger than those of magnetite and siderite. Greenalite is the main corrosion product in the bentonite in Period II. Smectite dissolution increases with time and is largest near the canister/bentonite interface. Model results show that smectite dissolution triggers the precipitation of a small amount of Mg-saponite in the bentonite at 25,000 years. Mg-nontronite does not precipitate. Calcite precipitates in the canister near the bentonite/canister interface, the bentonite and the granite. Gypsum does not precipitate. The concentrations of exchanged calcium and magnesium in the bentonite at 25,000 years are the largest with values around 43 and 37 meq/100g respectively. The concentration of exchanged sodium is 22 meq/100g while that of potassium is equal to 1.6 meq/100g. The concentration of exchanged Fe is largest near the canister interface and decreases with distance from the canister/bentonite interface. Model results show also the sorption of Fe in the strong and weak #1 sorption sites of the bentonite near the canister interface at 25,000 years.

The base run does not consider the porosity feedback effect (PFE) on chemical and transport parameters. The time evolution of the porosity calculated from the computed mineral volume fractions

EURAD Deliverable 2.17 – Integrated reactive transport models for assessing the chemical evolution at the disposal cell scale

shows that the porosity in the canister decreases mostly due to magnetite precipitation. Clogging is predicted to occur after 10,000 years. The calculated porosity in the bentonite at a point 1 cm away from the canister interface decreases with time due to the precipitation of calcite, siderite and greenalite.

Period III starts after canister failure at 25,000 years and considers glass dissolution and the interactions of glass with corrosion products and uncorroded carbon steel. The final time of simulation of this period is 50,000 years. The computed glass dissolution increases with time from 25,000 to 50,000 years. Model results show a dissolution front which moves into the glass. Glass dissolution leads to an increase of pH with time in the glass. The concentration of dissolved silica increases in the inner part of the glass until $t = 30,000$ years while it decreases in the outer part of the glass due to the out diffusion of dissolved silica into the canister and the bentonite. This diffusive flux causes the precipitation of greenalite at the glass-canister and canister-bentonite interfaces. The pH at 50,000 years ranges from 7.93 to 7.89 in the glass, from 7.89 to 8.66 in the canister and from 7.87 to 8.6 in the bentonite. The concentration of dissolved Cl^- in the canister, bentonite and granite keeps decreasing from 25,000 to 50,000 years, reaching a uniform concentration equal to $6.9 \cdot 10^{-4}$ M at 50,000 years in the three materials. Magnetite precipitates in the canister as long as there is carbon steel to corrode. Once the canister is fully corroded, magnetite redissolves near the glass/canister interface and greenalite precipitates. Greenalite precipitates in the canister and the bentonite, especially at the glass/canister interface. Siderite precipitates at the canister/bentonite interface and goethite does not precipitate. Smectite dissolution triggers Mg-saponite precipitation in the bentonite (in a small amount) and especially in the canister near the glass interface. Mg-nontronite does not precipitate. Calcite re-dissolves in the canister and the bentonite/canister interface at 50,000 years. The computed concentration of dissolved Fe^{2+} in the glass decreases with time from 25,000 to 50,000 years. The concentration of dissolved Fe^{2+} in the canister, however, increases due to the re-dissolution of magnetite. The concentration of dissolved Fe^{2+} is largest near the glass/canister interface. The peak of Fe^{2+} concentration moves slightly towards the canister/bentonite.

The concentrations of exchanged calcium, magnesium, sodium and potassium in the bentonite in Period III are uniform. The concentration of exchanged sodium increases during Period III from 22 to 26 meq/100g while that of exchanged calcium increases from 43 to 55 meq/100g. The concentration of exchanged magnesium, however, decreases from 37 to 18 meq/100g. The concentration of exchanged potassium shows no major changes. The concentration of exchanged Fe at 50,000 years decreases with distance from the canister/bentonite interface in a manner similar to Period II. Model results show also the sorption of Fe in the bentonite strong and weak #1 sorption sites near the canister interface at 50,000 years. The porosity in the glass increases due to glass dissolution. The porosity in the canister decreases and pore clogging is predicted at 10,000 years due to calcite, magnetite, siderite and greenalite precipitation. The porosity in the bentonite at 1 cm from the canister interface decreased with time due to the precipitation of calcite, siderite and greenalite, kept decreasing until $t = 28,000$ years, when reached clogging due to the precipitation of siderite and calcite and later increases slightly up to 0.05.

The following sensitivity cases and variants have been performed: 1) Sensitivity Case 1 corresponding to the sensitivity to the silica saturation threshold, C_{Si}^* , used in the kinetic glass dissolution rate; 2) Sensitivity Case 2 in which the granitic porewater has a dissolved concentration of Cl^- 8 times larger than that of the base run; 3) Variant 1 in which a 3.5 dm thick buffer of compacted MX-80 bentonite is considered instead of the 7.5 dm FEBEX bentonite buffer of the base run; 4) Variant 2 which considers a highly-conductive fracture zone normal to the gallery and an excavation damaged zone (EDZ); and 5) Variant 3 which considers the conditions of the Reference Czech crystalline rock. The results of the sensitivity runs and variants lead to the following main conclusions:

- 1) Sensitivity Case 1: Predictions are sensitive to a decrease of C_{Si}^* from 10^{-3} to $5 \cdot 10^{-4}$ mol/L. Computed results are presented in deliverable D2.19 (Samper et al., 2023).
- 2) Sensitivity Case 2: Predictions are not sensitive to the increase of Cl^- concentration in the granite boundary water. Neither green rust nor akaganeite precipitate.

EURAD Deliverable 2.17 – Integrated reactive transport models for assessing the chemical evolution at the disposal cell scale

- 3) Variant 1: Model results are sensitive to considered MX80 bentonite. Computed pH in Variant 1 is larger than that in the base run. Magnetite precipitation in Variant 1 is similar to that of the base run. Siderite and greenalite precipitation and ISG and smectite dissolution in Variant 1 are smaller than those in the base run.
- 4) Variant 2: The computed pH in the canister and the bentonite at 25,000 years increases with increasing granite flux. At 50,000 years, the pH is nearly uniform and equal to 8 for the largest granite flux. The concentrations of the aqueous species show a strong decrease after 100 years due the combined effect of solute out diffusion from the bentonite into the granite and the flushing of the solutes by groundwater flow. The larger the granite flux, the larger the decrease of solute concentrations in the bentonite. The precipitation of corrosion products is slightly sensitive to the increase in granite flux. Magnetite precipitation in the canister in Variant 2 is slightly smaller than that of the base run. Greenalite precipitation in the bentonite increases with increasing granite flux. On the other hand, siderite precipitation in the canister in Variant 2 is larger than that of the base. Siderite precipitation in the bentonite shows an opposite pattern. The concentrations of other mineral phases, such as calcite, quartz, gypsum, and concentrations of exchanged cations and surface complexes are not sensitive to the increase in granite flux (not shown here).
- 5) Variant 3: Model results are not sensitive to the chemical composition of the granite porewater SGW2.

The reactive transport model of the geochemical evolution of a HLW disposal cell in granite presented here could be expanded and improved by: 1) Considering a 2D axisymmetric model; 2) Replacing the assumption of porous canister by a model of progressive canister corrosion with a dynamic update of material properties; 3) Considering additional Fe mineral phases; 4) Adopting a more realistic complex glass dissolution model such as the GRAAL model used in ACED Task 3.2; 5) Adopting a multiple porosity model with adsorbed, interlayer and free water; and 6) Using different effective diffusion coefficients for each dissolved chemical species.

3. Modelling of a full HLW disposal cell in clay

The work has been done by Laurent De Windt (Mines Paris), Louis Raimbault (Mines Paris) and Edouard Veilly (IRSN).

This chapter presents the reactive transport model on the chemical evolution of the full HLW disposal cell system in clay, i.e., including the multi-barrier components “vitrified waste – steel overpack – concrete buffer – clay host rock”. It is divided in 8 sections starting with the presentation of the disposal cell configuration, the description of the conceptual and numerical models, and the computer code. The global evolution of the system obtained by modelling with HYTEC is first discussed for the base case. Then, a more detailed analysis of the evolution at the different interfaces follows, and eventually the modelling predictions for the variant cases versus the thickness and nature of the buffer. The chapter ends with a summary and main conclusions.

3.1 Disposal cell configuration

3.1.1 European HLW disposal concepts in clay

The present contribution focused on two major European concepts of disposal cells embedded in an argillaceous sedimentary formation. A common point between the two types of concepts is that the steel overpack encapsulates the waste canisters that contain the vitrified waste but the role and features of the cement buffer is quite different among the scenarios (Andra, 2016a; Deissmann et al., 2016).

The Belgian and Dutch programs rely upon the so-called supercontainer concept as well as rather poorly indurated clay formations (Weetjens et al., 2012; Neeft et al., 2019). The supercontainer diameter is about 2 m, and consists of a carbon steel overpack containing the HLW, which is itself inserted in prefabricated cylindrical concrete buffer material. The concrete is made from ordinary Portland Cement (OPC or CEM I type) and limestone aggregates. The pH has to be kept at high values during the thermal phase, and much longer beyond, in order to keep the carbon steel overpack passivated, limit corrosion and ultimately radionuclide release.

The French concept (Andra, 2016a, Neeft et al., 2019) significantly differs from the supercontainer concept by considering a 25 mm thick liner (sleeve) made of low-carbon steel in an indurated clay formation. The annular gap between the liner and the host rock is filled with a bentonite/cement grout that imposes corrosion-limiting environmental condition during the thermal phase only. The oxidation by atmospheric oxygen of pyrite from the surrounding host-rock may lead to acidification of the porewater (pH ~ 4.5), which may sustain irreversible high corrosion rates of the steel. The injection of the cement-bentonite grout is thus considered to counter this acidic pH transient stage. The grout also passivates metallic surfaces and prevents any possible diffusion of oxygen from the gallery to the steel during the operation phase. The alkalinity of the grout should have been neutralized readily after the very first thousand of years to prevent the dissolution of the vitrified waste (also simply named nuclear glass) under high pH values in the scenario of early breakage of the waste canister.

3.1.2 The generic configuration of the HLW cell

The rather large discrepancies in the supercontainer and sleeve/liner concepts did not facilitate the development of a common definition of a representative HLW disposal cell in a clay host rock. Therefore, a generic configuration of the HLW disposal cell in a clay host rock was set as a base case and variants were then applied to fulfil more explicitly one feature of the Belgian/Dutch concept or one feature of the French concept.

Figure 3-1 shows the initial state of the generic configuration of the HLW disposal cell in a clay host rock:

- The vitrified waste (40 cm in diameter) was explicitly considered in reactive transport modelling (not as boundary conditions) for coupling with the barriers and host-rock evolutions.

EURAD Deliverable 2.17 – Integrated reactive transport models for assessing the chemical evolution at the disposal cell scale

- The overpack (5 cm thick) consisted of low alloy carbon-steel. A mechanical breaching was assumed when the non-corroded thickness reached 1.5 cm, allowing for the nuclear glass degradation to start. A technical gap of 1 cm thick was considered in contact with the overpack.
- The cement-based buffer (30 cm thick in the base case, 5 or 100 cm in variants) was composed of Portland cement (CEM I) and calcareous aggregate without any reinforcement by steel structures.
- The clay host rock (several meter thick in the calculations) was the French Callovo-Oxfordian (COx) claystone.

Several elements of the usual concepts for HLW were not taken into account:

- The stainless-steel envelope (0.5 cm thick) was not included due to the strong uncertainty on the (pitting) corrosion mechanism and its small thickness.
- The carbon steel liner in which the waste packages are inserted was not simulated, the focus was put on the steel overpack protecting the nuclear glass from dissolution.
- The technological gap was not simulated explicitly but assumed to be filled by corrosion products.
- The configuration did not consider any explicit EDZ within the argillaceous host rock, i.e. a full self-healing of the fissures in the EDZ was assumed in the base case scenario.

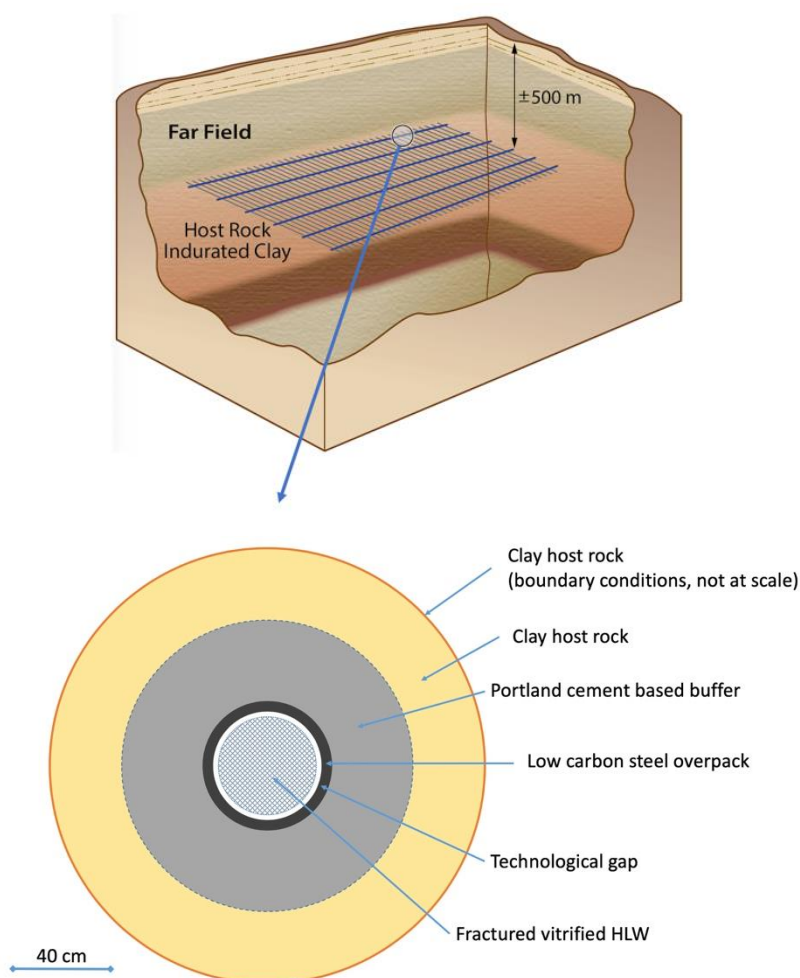


Figure 3-1. Initial geometry of the generic configuration of the HLW disposal cell in a clay host rock.

3.1.3 Variants of the HLW cell configuration

As shown in Figure 3-2, a variant extended the cement buffer thickness up to 100 cm (maximum of the sensitivity analysis for Belgian/Dutch concept based on the supercontainer design). Inversely, reducing the buffer thickness to 5 cm led to a configuration similar to the French concept with steel protected against corrosion by the cementitious buffer.

Two chemical compositions of the cement-base buffer were considered for the smallest thickness (Figure 3-2): either a bentonite/cement grout buffer (low-pH cement) more relevant for the French concept, or an ordinary Portland cement (OPC/CEM I) for the sake of comparison.

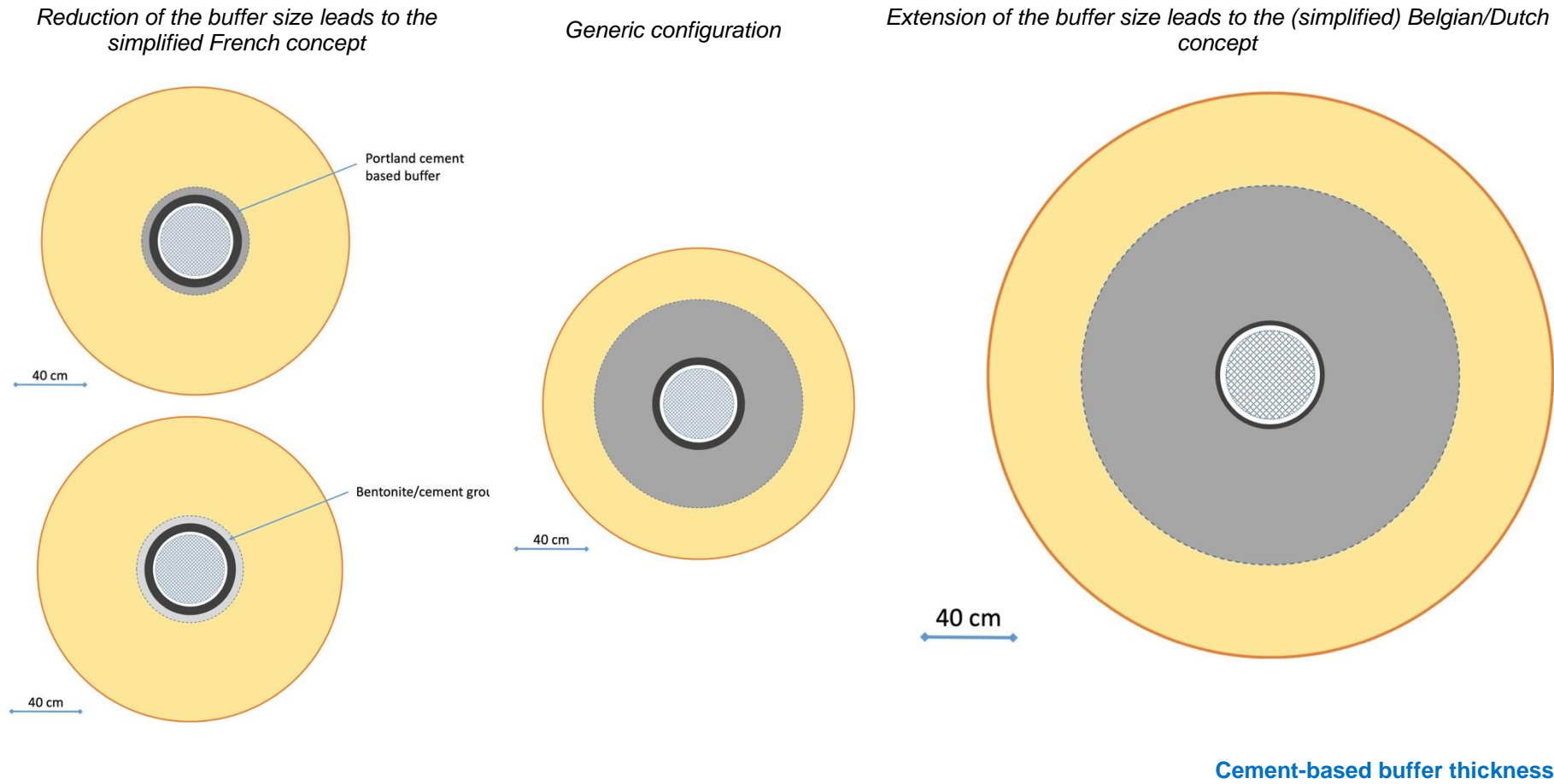


Figure 3-2. Variants in terms of buffer thickness of generic HLW disposal cell towards the French liner concept or the Belgian/Dutch super container concept; another variant of the liner concept considers a low-pH cement/bentonite grout instead of the CEM I based buffer.

3.2 Conceptual model and evolution scenarios

3.2.1 Successive periods considered in the evolution of the HLW cell

Figure 3-3 schematically represents the three successive periods over a very long duration of 100,000 years that occur during the lifetime of HLW repository in clay (e.g. Weetjens *et al.*, 2012; Andra, 2016b). Period I is a short-term transient period of partial water desaturation, possible oxygen presence leading to oxic conditions. Period II starts when the near field components are fully water saturated and anoxic conditions are prevailing. The interaction between the clay host rock and the cement buffer are the main processes. Steel corrosion also progresses but at a very low rate. However, the cement buffer is in an advanced state of chemical degradation at the end of period II and the corrosion of steel speeds up. Eventually, Period III begins when the non-corroded thickness of the overpack/canister reaches 1.5 cm and a mechanical failure is assumed. Period III include, therefore, the modelling of glass dissolution and interaction with corrosion products and uncorroded iron.

Only periods II and III were investigated in the present modelling. The initial state of Period II did not consider any effect of the transient period I and any alteration of the initial properties of the materials for the sake of simplicity. That is to say the starting point considered pristine materials only. The modelling of period I is the specific issue of the Chap 4 of this report.

In this chapter devoted to the long term HYTEC modelling, stationary temperature of 25°C was only considered in periods II and III. Indeed, the decrease in temperature in the cell from 80°C to 25°C will be relatively fast. The temperature at the steel overpack will decrease to 40°C in less than 200 years for most nuclear glasses and in 1,000 years for the warmest wastes (Neeft *et al.*, 2019). Afterwards, the temperature will continue to decrease to the natural background temperature (about 25°C, depending on depth) but more slowly. Chapter 4 deals with the effect of the thermal transient on the concrete buffer.

The computed hydrogen generation by corrosion was not modelled by HYTEC. It is likely that hydrogen will not be fully evacuated to the host rock in the French concept. The “drying” effect of hydrogen neither its effect on the water saturation degree were not assessed by HYTEC. Fully water saturated conditions were, therefore, set in periods II and III in this chapter devoted to the long term HYTEC modelling. Chapter 4 deals with the effect of partially water saturated state on the concrete buffer.

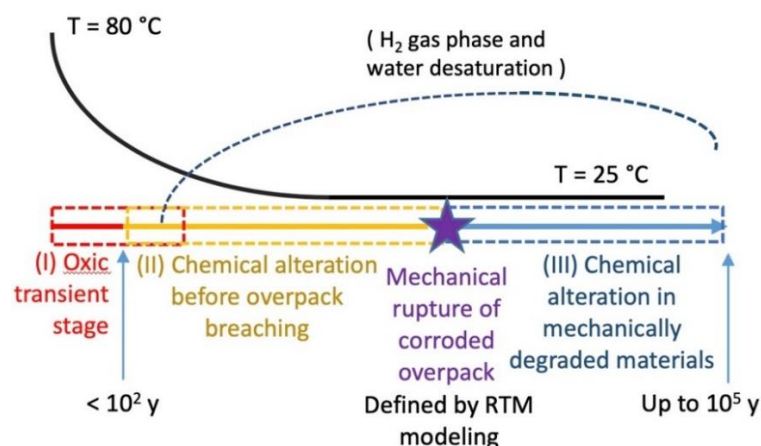


Figure 3-3. Successive periods considered in reactive transport modelling (RTM) and evolution of temperature in the disposal cell; the effect of hydrogen production on water saturation was not taken into account (although indirectly in Chap 4). Only, periods II and III were considered in the present reactive transport modelling. It is worth noting that the safety function of the cement buffer with respect

to the steel overpack breaching significantly differs between the Belgian/Dutch and the French disposal concepts.

3.2.2 Base case and variants of the HLW cell modelling

The main objective of the base case of Table 3-1 was to study into detail the strongly coupled chemical evolution of the full HLW cell from the waste form until the host rock over periods II and III altogether. A second objective of the base case was to define the near-field evolution at the time of the overpack perforation, i.e. the mineralogy, geochemistry, porosity... of the different components. Information that could be useful as boundary conditions when modelling in more detail processes at interfaces.

The objective of the first and second variants was to assess the sensitivity of the chemical evolution of the full system with respect to the buffer size or composition. The CEM-I buffer was replaced by a bentonite/cement grout buffer (of lower pH). This configuration was the closest to the French concept in terms of thickness and material composition.

The objective of the modelling of the last variant of Table 3-1 was to mainly estimate the lifetimes of the CEM I based buffer as a function of the buffer thickness during period II. The corresponding lifetimes could then be used to calculate by hand the duration before steel overpack breaching, since steel corrosion is very low as long as the pH of the cement porewater is above 11.

It is worth noting that an early breaching of the overpack due to design defect or mechanical stress (i.e. not chemical corrosion) was not investigated in the present evolution scenario.

In another manner than Table 3-1, Figure 3-4 summarizes the key parameters that were used for the sensitivity analysis of the chemical evolution of the HLW cell, in particular to assess the durability of the steel overpack, which is tightly linked to the lifetime of the cement buffer, and the dissolution rate of the nuclear glass. These parameters were the thickness of the cement-based buffer and the chemical nature of the buffer (CEM I concrete vs low-pH cement grout) in the present section. Clogging effect on diffusion due to chemical feedback of mineral precipitation was also studied in one case. The effect of the degree of water saturation is discussed in Chapter 4, whereas the breaching/fracturing of the cement buffer will be modelled in the subtask 4.2 (see D2.19, Samper et al., 2023).

Table 3-1. Base and variant configurations investigated by HYTEC modelling of the chemical evolution of the HLW cell.

Period (see Figure 3-3)	Buffer thickness	Temp.	Water saturation	Concrete type	Steel canister	Nuclear glass
Base case						
Periods II + III altogether	30 cm	25°C	100 %	CEM I + calcareous aggregates	Porous, partly filled with corrosion products	Yes
Variants						
Periods II + III altogether	100 cm	25°C	100 %	CEM I + calcareous aggregates	Porous, partly filled with corrosion products	Yes
Periods II + III altogether	5 cm	25°C	100 %	CEM I + calcareous aggregates	Porous, partly filled with corrosion products	Yes
Periods II + III altogether	5 cm	25°C	100 %	Low-pH cement - bentonite grout	Porous, partly filled with	Yes

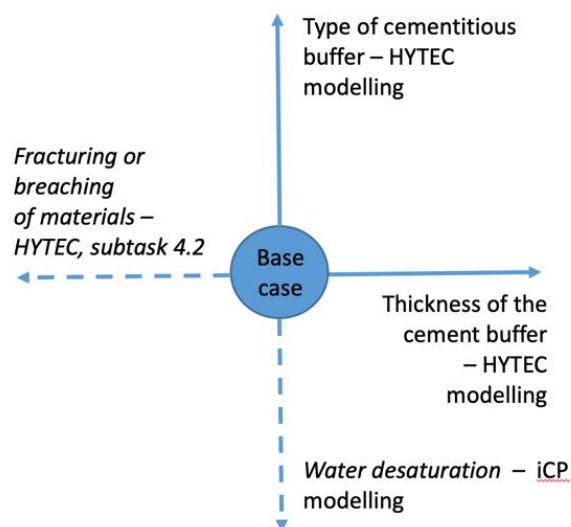


Figure 3-4. Key parameters used for the sensitivity analysis of the reactive transport modelling of the HLW cell, in particular for the durability of steel overpack and dissolution of the nuclear glass.

3.3 Computer code and thermodynamic database

3.3.1 The reactive transport code HYTEC

The modelling of the full HLW disposal cell in clay host rock without transient stage was performed with the reactive transport modelling code HYTEC (van der Lee *et al.*, 2003).

The code forms part of a module-oriented structure which facilitates maintenance and improves coding flexibility in object-oriented C++ and parallel computing with MPI. The full set of non-linear equations of thermodynamic equilibrium is numerically solved according to the basis component approach and its matrix-algebra, using an improved Newton-Raphson scheme. The transport module is based on the representative elementary volume (REV) approach with finite volume calculation. All boundary conditions normally used by hydrogeologists are available, such as constant head or pressure, constant flow, constant concentration. They can be modified during the course of the modelling, allowing for the temporal application of different scenarios for instance.

HYTEC searches for an accurate solution to the multicomponent transport problem using an iterative, sequential, so-called strong coupling scheme. Strong coupling permits variable hydrodynamic parameters as a function of the local chemistry. For example, the porosity of a porous medium decreases after massive precipitation of newly formed mineral phases, which modifies the water flow paths and transport parameters, e.g., diffusion coefficients. HYTEC handles 1D – 3D grids in Cartesian coordinates as well as 1D in radial and 2D in cylindrical (axis symmetric) coordinates.

3.3.2 Thermodynamic database

3.3.2.1 Thermochemie database

All chemical reactions (aqueous, sorption and solid phases) were modelled at thermodynamic equilibrium, except for the clay phase dissolution, steel corrosion and nuclear glass dissolution that were

EURAD Deliverable 2.17 – Integrated reactive transport models for assessing the chemical evolution at the disposal cell scale

modelled under kinetic constraints. The aqueous chemistry included acid/base reactions, oxidation and reduction (redox) processes and aqueous complexation by inorganic ligands.

Activity corrections were calculated with the truncated Davies model applicable from low to moderate ionic strength ($I \leq 0.5$ mol/kg). Sensitivity tests made with the B-dot model did not show any significant modifications of the modelling results.

The thermodynamic database of reference was ThermoChimie v10.a. This is the thermodynamic database developed by ANDRA, ONDRAF and RWM for the performance assessment of the geologic disposal of radioactive waste (Giffaut *et al.*, 2014, <https://www.thermochimie-tdb.com>). ThermoChimie provides formation constants (at temperatures ≤ 80 °C) for a wide range of radionuclides and the mineral component of multi-barrier systems, including host-rock solid phases, bentonites, cements, steel, and their evolving secondary phases. The C-A-S-H and C-S-H phases are introduced as discrete elements. The database is formatted for several reactive transport models including HYTEC and iCP. The M-S-H phases of Bernard *et al.* (2018) and the International Simple glass (ISG) were added to the database.

Sulphates was decoupled from the redox couples. That is to say that SO_4^{2-} could not be reduced by the aqueous species resulting from iron corrosion (H_2 and Fe^{2+}), which seemed relevant at 25°C and the assumed lack of microbial activity. Indeed, under alkaline and reducing conditions hydrogen sulphide (HS^-) is the stable sulphur species, but the reduction of sulphate to sulphide is extremely slow at <150 °C and will not proceed unless it is mediated by microbial activity (Truche *et al.*, 2009).

The subset of minerals from ThermoChimie considered in the present HYTEC modelling were in most cases the following:

- Primary minerals of the host rock and the cementitious buffers.
- Steel, modelled as Fe(0).
- Secondary phases, all primary minerals could precipitate, plus brucite, gibbsite, stratlingite, gypsum, monosulfoaluminate, C-S-H of decreasing Ca/Si ratio, $\text{SiO}_2(\text{am})$, M-S-H (bentonite grout only), Ca-saponite, Ca-clinoptilolite, greenalite, magnetite.

3.3.2.2 Sorption

Table 4-2 gives the selectivity constants of cation exchange considered in the HYTEC modelling of the clay host rock are detailed in D2.16 (Sampers *et al.*, 2021). Sorption was not considered for C-S-H (concrete buffer) and magnetite (corrosion product of steel).

3.4 Numerical model parameters

3.4.1 Grid, boundary/initial conditions and simulated times

The HYTEC modelling was performed in 1D-radial (axis-symmetry) geometry. The grid mesh size was 5 mm. The steel overpack (5 cm) zone and the technical gap/void (1 cm) was merged as a single homogenized zone of 6 cm in which steel could be corroded and corrosion product could precipitate. The only boundary condition was constant chemical aqueous conditions (Dirichlet type) imposed at the outer boundary of the host rock section. This boundary condition was set about 2.5 m away from the concrete/clay interface in order to minimize any boundary artefacts.

The simulated time varied according to the concrete buffer thickness, with a maximal duration of 10^5 years for 100 cm. Fully water saturated conditions (i.e. 100 %) and isothermal conditions at 25°C were fixed in the HYTEC modelling.

The reactive transport model required the following geochemical parameters as initial conditions:

- The initial mineralogy of the cementitious buffers and clay rock, the chemical composition for the steel and IS glass.
- The initial pore water chemistry of the cementitious buffers and clay rock.
- The initial contents of exchangeable cations of the clay minerals.

Almost all HYTEC simulations of this chapter 3 were done under constant porosities and diffusion coefficients since clogging occurred rather quickly at the concrete/clay interface and stopped any further evolutions of the entire system. In a sensitivity case, porosity could locally change according to the evolution of the mineral concentrations. The diffusion coefficient also changed according to an empirical Archie-type law:

$$D_e = D_e(\omega_0) \left(\frac{\omega - \omega_c}{\omega_0 - \omega_c} \right)^m \quad [3-1]$$

where ω_0 is the initial porosity, ω_c is a critical porosity threshold under which diffusion stops (set to 0) and m is an empirical Archie's coefficient (set to 3).

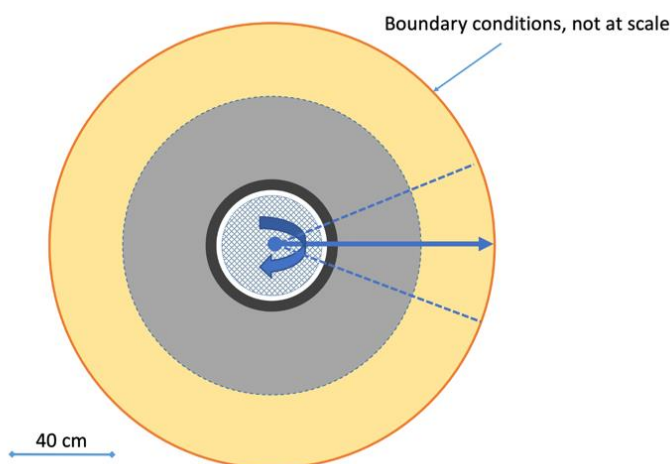


Figure 3-5. The HYTEC modelling was set in 1D-radial (axis-symmetric) geometry with boundary conditions located in the far-field of the clay host rock.

3.4.2 Clay rock parameters

3.4.2.1 Initial porosity and diffusion coefficient

The porosity ω of the clay host rock was fixed to 18 %. A single effective diffusion coefficient D_e of 3×10^{-11} m²/s was considered for the initial state of the host rock ($D_e = \omega D_p$ where D_p is the pore diffusion coefficient).

3.4.2.2 Initial mineralogy and porewater chemistry

The clay host rock considered in the modelling was the French Callovo-Oxfordian (COx) claystone.

The COx claystone mineralogy is summarized in Table 3-2. Calcite was the predominant carbonate mineral and quartz the predominant silicate. The clayey part was abundant. It was composed of illite and interstratified illite/smectite, but also chlorite. The carbonate phases were represented by their main component, i.e. calcite (23 wt.%). Dolomite (4 wt.%) was not included in the HYTEC modelling. Siderite was nevertheless kept since it was considered as a possible corrosion product of steel. Pyrite was not taken into account in the HYTEC modelling since Fe(II)-sulphides were not assumed as corrosion products of steel in this study.

EURAD Deliverable 2.17 – Integrated reactive transport models for assessing the chemical evolution at the disposal cell scale

The divalent Ca^{2+} and Mg^{2+} were the main cations of the exchangeable cation population of the host rock.

The hydrochemistry of the pristine COx claystone is detailed in Table 3-3. The porewater was moderately mineralized. Sodium was the dominant cation, chloride and sulphate were the dominant anions. The partial pressure of CO_2 was set to 1.6×10^{-2} atm. By comparison, the Belgian Boom Clay pore water (De Craen *et al.*, 2004; Wang *et al.*, 2010) is less concentrated and the partial pressure of CO_2 is also lower. The redox potential was about -0.165 V at pH 7.

Table 3-2. Initial mineralogy, specific surface area and cation exchange properties the clay host rock considered in the HYTEC modelling (adapted from Marty *et al.*, 2015).

	Volume fraction [%]	SSA [m ² /g of mineral]	Exchangeable cation	
Carbonate			% equivalent	
Calcite	23	-	Na	18
Siderite	1	-	K	2
Clay-like phase			Mg	32
Chlorite(Cca-2)	2	30	Ca	48
Illite-Mg	33	30	CEC	
Montmorillonite(HcCa)	8	8.5	in meq/100g	17.4
Others			of rock	
Quartz	25	0.05		

Table 3-3. Initial porewater chemistry of the clay host rock at 25°C considered in the HYTEC modelling (adapted from Marty *et al.*, 2015).

Aqueous species	Total concentration (mol/L)
-----------------	-----------------------------

pH	7.0
K ⁺	3×10 ⁻⁴
Na ⁺	4×10 ⁻²
Mg ²⁺	6×10 ⁻³
Ca ²⁺	9×10 ⁻³
Fe ²⁺	5×10 ⁻⁵
H ₄ SiO ₄	5×10 ⁻⁴ (1×10 ⁻³ (*))
HCO ₃ ⁻	4×10 ⁻³
Cl ⁻	4×10 ⁻²
SO ₄ ²⁻	1×10 ⁻²

(*) Boundary conditions.

3.4.2.3 Geochemical kinetic constraints

The dissolution and precipitation were modelled under kinetics controlled according to rate laws and parameters adapted from Marty *et al.* (2015) for the following solid phases:

- chlorite, illite, montmorillonite, quartz (primary phases);
- Ca-clinoptilolite, Ca-saponite (secondary phases).

with this generic kinetic law:

$$\frac{d[M_i]}{dt} = (k_{alk,i} (OH^-)^{p_i} + k_{neutr,i}) A_{v,i} \left(\left(\frac{Q_i}{K_{s,i}} \right) - 1 \right) \quad [3-2]$$

where the intrinsic kinetic constants of the reaction k were set for the alkaline and neutral pH domain, A_v is the mineral surface area per unit volume and the last term is dependent on the deviation from thermodynamic equilibrium.

For the sake of simplicity, the kinetics of carbonates (calcite, dolomite, siderite) were assumed to be sufficiently fast as to be calculated at thermodynamic equilibrium.

3.4.3 CEM I concrete (buffer) parameters

3.4.3.1 Initial porosity and diffusion coefficient

The total porosity of the concrete was set to 11.5 %. The D_e value for the initial state of concrete was set to 1×10⁻¹¹ m²/s as in agreement with the modelling of Govaerts and Weetjens (2010).

3.4.3.2 Initial mineralogy and porewater chemistry

The supercontainer concept served as a reference for the reactive transport modelling of the cementitious buffer. The concrete consisted of a fully hydrated CEM I/42.5N HSR LA and limestone aggregates (70 % in volume). The cement content was 350 g per dm³ with a water on cement weight ratio (w/c) of 0.47 (Liu *et al.*, 2014). The thermodynamic modelling of the composition of the CEM I based concrete (Table 3-4) was calculated by Kosakowski (2020) with GEMS and slightly modified to fit with the HYTEC database (discrete set of C-S-H from Thermochimie). The initial pore water of the concrete was a K-Na-OH fluid with a pH of 13.5 (Table 3-5).

Table 3-4. Initial porosity and mineralogical composition of the CEM I-based concrete at 25°C considered in the HYTEC modelling (adapted from Kosakowski, 2020).

	Volume fraction [%]
<i>Aggregates</i>	
Calcite	70
<i>Hydrated cement</i>	
Calcite	0.3
CSH 1.6	9.5
Ettringite	3.2
Monocarboaluminate	2.0
Portlandite	4.6

Table 3-5. Initial porewater chemistry of the CEM I-based concrete at 25°C considered in the HYTEC modelling.

Aqueous species	Total concentration (mol/L)
pH	13.5
Na ⁺	8×10 ⁻³
K ⁺	4×10 ⁻¹
Ca ²⁺	7×10 ⁻⁴
Al ³⁺	9×10 ⁻⁵
H ₄ SiO ₄	1×10 ⁻⁴
CO ₃ ²⁻	2×10 ⁻⁴
SO ₄ ²⁻	6×10 ⁻³

3.4.3.3 No kinetic constraints

The dissolution/precipitation of the concrete phases were modelled at thermodynamic equilibrium, as commonly assumed due to the high reactive surface of the cement phases (e.g. Marty et al., 2015).

3.4.4 Low-pH cement/bentonite grout (buffer) parameters

3.4.4.1 Initial porosity and diffusion coefficient

A porosity of 70 % and an effective diffusion coefficient D_e of 7×10^{-11} m²/s for the present HYTEC modelling.

3.4.4.2 Initial mineralogy and porewater chemistry

Table 3-6 summarizes the recipe of the low-pH cement/bentonite grout before hydration, which was used in the BACUCE experiment (De Windt et al., 2020; Wittebroodt et al., 2023). The water on cement

EURAD Deliverable 2.17 – Integrated reactive transport models for assessing the chemical evolution at the disposal cell scale

ratio was much higher than for classical cements: $w/c = 2$ instead of w/c around 0.5. This bulk composition included an OPC clinker, blast-furnace slag and gypsum additive (i.e. CEM III cement) on the one hand and addition of silica fume and bentonite on the other hand.

The literature indicates that the hydration of slag and silica fume is relatively slow at room temperature (Lothenbach et al., 2012 & 2014). However, a simple thermodynamic equilibrium modelling with HYTEC was performed assuming a complete hydration in a very first approximation (Table 3-7). At 25°C, the porewater has a pH about 11 and a moderate ionic strength (4×10^{-2} mol/kg_{aq}).

Table 3-6. Recipe of the bentonite/cement grout used in the BACUCE experiment (De Windt et al., 2020; Wittebroodt et al., 2023).

Mineral	Composition [kg]
CEM III Rombas (35% clinker + 65% blast-furnace slag)	0.60
Silica fume	0.60
Bentonite	0.16
Hydrotalcite	0.04
Water	2.40

Table 3-7. Simplified initial mineralogy of the bentonite/cement grout at 25°C considered in the HYTEC modelling.

Mineral	Content ⁽¹⁾ [wt.%]
C-S-H 0.8	60
Ettringite	5
Hydrotalcite	3
Quartz	20

(1) The montmorillonite and C-A-H components were not taken into account.

3.4.4.3 No kinetic constraints

The dissolution/precipitation of the concrete phases were modelled at thermodynamic equilibrium.

3.4.5 Low carbon steel parameters

3.4.5.1 Diffusion properties in a porous approach

The initial metallic iron and the subsequent corrosion products were modelled as a discretized equivalent porous medium (opposite to a layer per layer corrosion front). The porosity and effective diffusion coefficient of the porous zone were set to 17 % and 2×10^{-11} m²/s, respectively.

3.4.5.2 Initial chemical composition

The low-carbon steel of the overpack was composed of pure metallic iron Fe(0), whose corrosion was controlled by kinetics.

3.4.5.3 Steel corrosion kinetics

Only generalized uniform corrosion under anaerobic condition was assumed, i.e. any localized corrosion processes (e.g. pitting) were ruled out in this HYTEC modelling study. However, the increase of corrosion rate when the pH decreased from 12.5 to 7 was implemented in the corrosion kinetics, as depicted in Figure 3-6. The selected anaerobic corrosion rates at neutral pH (5 μm/y) and high pH (0.1 μm/y) corresponded to the upper limits of the data range found in the literature (Deissmann *et al.*, 2021). Since the anaerobic corrosion rates under moderately alkaline pH (10.5 – 11.5) were still unknown, a sigmoidal relationship between the anoxic corrosion rate and the pH was implemented in HYTEC with an inflection point at the threshold pH of 10.5 (or pH 11 optionally):

$$r_{total,pH} = r_{neutral} \left(\frac{(10^{-3.5})^p}{(10^{-3.5})^p + (OH^-)^p} \right) + r_{alkaline} \quad [3-3]$$

In the porous media approach followed in the present modelling, the dissolution rates were uniformly applied over the full grid zone of the steel overpack (i.e. 5 cm thick). To fix ideas, the steel had to be fully corroded over the whole zone in 5×10^5 years at pH 12 or higher, and 1×10^4 years at pH 9 or lower (with any intermediate durations within the pH range 9 – 12).

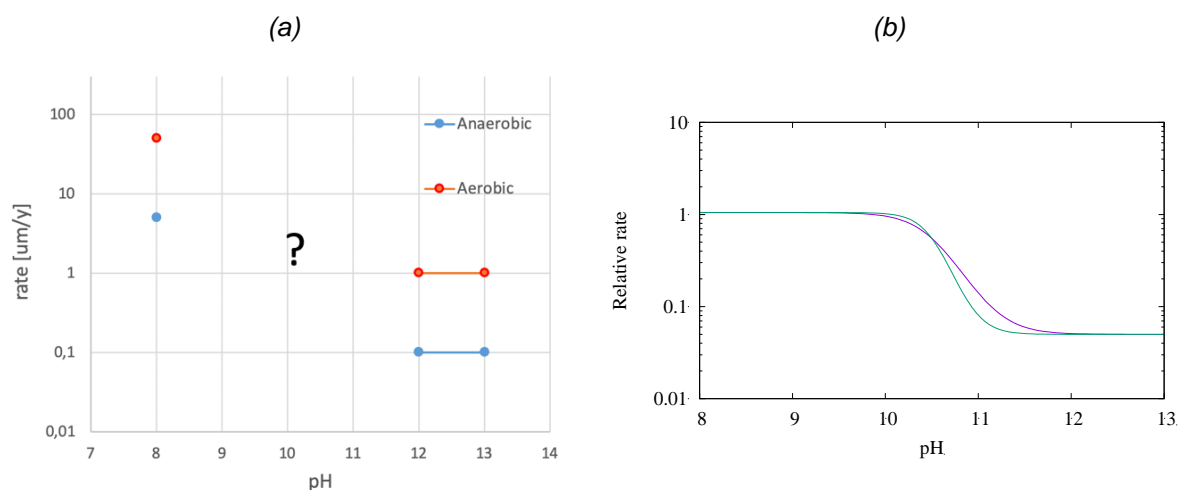


Figure 3-6. (a) Long-term generalized corrosion rates of carbon steel under anaerobic conditions selected for the reactive transport modelling at 25°C at neutral and high pH values where aerobic rates are also given for comparison). (b) Relationships that could be used to simulate the evolution from hyperalkaline pH values to more neutral values during the alteration of the cement-based buffer (relative rate = 1 corresponds to the anaerobic corrosion rate at neutral pH).

3.4.5.4 Steel corrosion products

The precipitation of the corrosion products was modelled under thermodynamic equilibrium in a first approach due to the significant uncertainties in the parameters such as surface area and kinetic rate constants (Bildstein *et al.*, 2019).

Under the anoxic/anaerobic conditions assumed in the present modelling, the most stable corrosion product of metallic iron is magnetite (Fe₃O₄) at high alkaline pH, but iron carbonates such as siderite (FeCO₃) or chukanovite (Fe₂(OH)₂CO₃) are also likely at slightly alkaline pH values (Odorowski *et al.*, 2017). Chukanovite is usually metastable versus siderite in the long term. Fe(II)-silicates (e.g. greenalite Fe₃(Si₂O₅)(OH)₄ or cronstedtite) are also likely, in particular in the presence of a silica source such as

dissolution of nuclear glass. Iron sulphides (e.g. mackinawite) form when corrosion is driven by bacteria activity, but this microbial process was not considered in the present study.

The present HYTEC modelling took into account magnetite, siderite and greenalite as possible corrosion products.

3.4.6 Vitrified waste parameters

3.4.6.1 Diffusion properties in a porous approach

Water intrusion and glass dissolution were allowed within the whole glass zone, which was assumed as a porous medium due to the initial cracking of the glass block before disposal (Repina et al., 2019), and not at the glass/canister boundaries only. The porosity and effective diffusion coefficient of the porous zone were set to 15 % and 1.5×10^{-10} m²/s, respectively. Diffusion in the glass zone only occurred after overpack breaching in the modelling.

3.4.6.2 Initial chemical composition

The vitrified waste was modelled by the international simple glass (ISG) for the sake of simplicity like in Debure *et al.* (2012). To ease numerical convergence, the ZrO₂ component was neglected in the present modelling due to the very low solubility of zirconium. The stoichiometry of the IS glass considered in the HYTEC modelling is given in Table 3-8.

Table 3-8. Initial chemical composition of the *international simple glass* (adapted from Debure et al., 2012) considered in the HYTEC modelling.

Oxide	SiO ₂	Na ₂ O	B ₂ O ₃	Al ₂ O ₃	CaO
[wt.%]	58	13	18	6	5

3.4.6.3 Dissolution kinetics

Modelling the dissolution of the nuclear glass constituting the vitrified waste was probably the most critical aspect for modelling the chemical evolution in a HLW disposal cell in a clay host rock. For the sake of simplicity, the present modelling relied on a previous operational HYTEC modelling calibrated for the dissolution of the R7T7 glass (De Windt *et al.*, 2006). The modelling is performance assessment oriented and considered realistic but pessimistic hypothesis on the fractures and reactive surfaces of the glass blocks.

The dissolution of this simplified glass was controlled by two kinetic processes according to the conceptual model of Gin *et al.* (2013). The global rate was the combination of an initial forward dissolution rate r_0 and long-term residual dissolution rate r_r

$$\frac{d[\text{glass}]}{dt} = r_0(T, pH, Si \dots) + r_r(T) \quad [3-4]$$

Assuming congruent dissolution of the glass matrix, the kinetic process was described in the HYTEC modelling by the combination of a first-order initial dissolution rate $k_{0,pH}$, combined to a dependency with the bulk solution chemistry (pH, dissolved silica activity), and long-term residual dissolution rate k_r which is chemistry independent:

$$\frac{d[\text{glass}]}{dt} = -k_0 (H^+)^{-0.4} A_v \left(1 - \frac{C_{Si}}{C_{Si}^*} \right) - k_r A_v \quad [3-5]$$

This first-order rate law has already been used by De Windt *et al.* (2006) for modelling the dissolution of the R7T7 glass in a HLW disposal cell in clay host rock. The activity term $(H^+)^{-0.4}$ in Eq. [3-5] stands for the effect of pH, and C_{Si}^* is a saturation threshold for which the first-order dissolution stops. The reactive surface area A_v depends on the degree of cracking of the vitrified waste. The rate drops when the silica concentrations approach saturation. The most critical parameter is the silica threshold at saturation C_{Si}^* .

The forward rate constant and residual dissolution rate are both temperature-dependent. Table 3-9 gives the set of parameters for Eq. [3-5] at 50 °C and a pH range of 7 – 10 used in the present HYTEC modelling. These parameters were assumed to be operational in a crude approximation, even if the temperature was fixed at 25°C. These parameters were selected from the studies on the dissolution kinetics of the SON68 glass from Jollivet *et al.* (2012), Fleury *et al.*, (2014), De Echave *et al.* (2018) and Debure *et al.* (2019). From a mechanistic point of view, the parameters are only applicable up to pH 10. However, Ferrand *et al.* (2015) measured a long-term dissolution rate of the ISG glass in old cement water (pH ~11.5) that was not too far from the selected value of Table 3-9. More details on the selection of the glass dissolution model can be found in Deliverable 2.16 (Samper *et al.*, 2021).

Table 3-9. Kinetic parameters for glass dissolution considered in the HYTEC modelling (Equation [3-5]).

k_0 [g m ⁻² d ⁻¹]	3×10^{-5}	e.g. $k_0 (H^+)^{-0.4} = 2 \times 10^{-2}$ g m ⁻² d ⁻¹ at pH = 7
k_r [g m ⁻² d ⁻¹]	10^{-4}	
C_{Si}^* [mol L ⁻¹]	10^{-3}	
Total surface S (glass block of 400 kg)		S = 20 m ² for a cracking ratio ⁽¹⁾ of 10 ==> $A_s = 5 \times 10^{-5}$ m ² g ⁻¹

(1) Ratio of the total surface on the surface of the unfractured glass block.

3.5 Differences between D2.16 and D2.17

Deliverable D2.16 (Samper *et al.*, 2021) provides more information on the definition of the generic configurations of the HLW cell in clay, the evolution scenarios, the selection of the modelling laws and parameters. The present chapter 3 of deliverable D2.17 has given the configurations, scenarios and parameters that were eventually used in HYTEC simulations. The changes between the reactive transport models of two deliverables were, nevertheless, minor.

3.5.1 Conceptual model

The sorption of dissolved silica on magnetite (as corrosion product of steel) was not modelled. It has been shown by modelling that silica sorption on magnetite had almost no effect on glass durability for duration relevant of HLW disposals (De Windt *et al.*, 2006). Fe(II)-silicate precipitation was much more important in terms of quantity of silica released from the glass and trapped by the corrosion products.

The ageing of cement may generate a few transversal cracks or a transversal network of interconnected cracks within the cement buffer (Seetharam and Jacques, 2015). In that case, diffusive mass transfer is enhanced and may accelerate the degradation of the buffer. The effect of fracture network in the degraded concrete on the buffer durability are further described in deliverable D2.19 (Samper *et al.*, 2023).

3.5.2 Numerical model

The initial parameters of the materials were very close to the reference states selected in D2.16.

As mentioned earlier, pyrite was not included in the primary mineral of the COx clay since sulphide corrosion products were not selected (both in D2.16 and D2.17), or Zr was not included in the nuclear glass composition. All this had no significant effect on the modelled chemical evolution. Computer codes

The reactive transport codes iCP and HYTEC were used as scheduled.

3.5.3 Sensitivity cases

The base case and sensitivity cases were mostly similar to the choices made in D2.16.

The transient stages in thermal and water content during the first 2,000 years were investigated with iCP only to avoid duplication. HYTEC dealt with coupling of the full system components, especially the effect on the durability of the nuclear glass, over very long durations (up to 10^5 years).

The buffer thickness of 75 cm was not modelled, the set 5 – 30 – 100 cm was sufficiently informative and relevant for the European concepts under consideration.

3.6 Modelling results of the Base Case – 30 cm CEM I buffer

The HYTEC modelling treated the chemical evolution of the full HLW cell from the vitrified waste form until the clay host rock in a single simulation. With this respect, this section starts with the base case with the 30 cm CEM I buffer and a first global analysis of the processes. In a second step, a detailed discussion of the calculated chemical evolution at each interface between the cell components is given.

Figure 3-7 summarizes the key “disruptive” processes of the chemical evolution of the HLW cell with time. Again, it is worth mentioning that all the components could react from the beginning of the calculation, excepted the IS glass that was isolated from the environment as long as the steel overpack was not breached.

Stage 1. The comparison of the initial mineral profiles (Figure 3-7a) with those calculated after 7,000 years (Figure 3-7 b) demonstrates that the main driving force responsible for the full HLW cell chemical evolution was the chemical destabilization of the cement buffer by the host-rock. Both materials have low porosity and diffusion coefficients. These physical features were clearly favourable for the stability of the HLW cell components. But, on the contrary, the initial pH of the Cox claystone was much lower than the initial pH of the cementitious buffer, leading to a strong chemical gradient between the two components of the multi-barrier system. The chemical alteration was more important in the concrete than in the clay host-rock in terms of spatial extension. The hydrated cement phases were indeed in rather low amount compared to the reactive minerals in the host-rock. Therefore, the durability of the cement buffer would strongly affect the duration of the containment properties of the complete multi-barrier system as a whole.

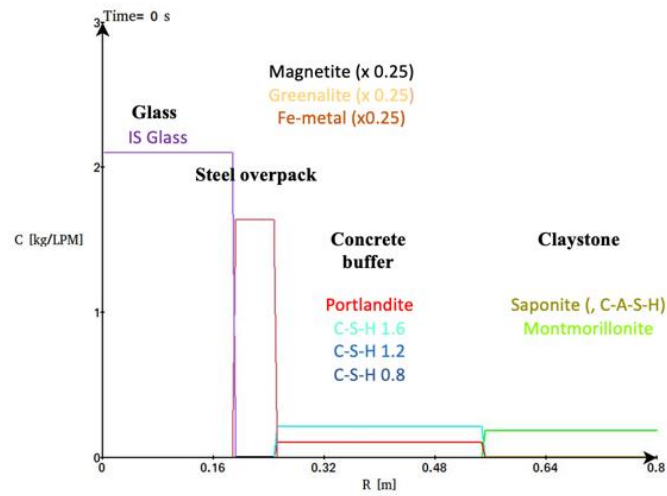
Stage 2. As long as the high-pH buffering capacity by portlandite and the C-S-H of high C/S ratio lasted, steel corrosion was minimized and magnetite was the main corrosion product. The pH decrease due to cement buffer alteration plays a role on the kinetics of the key processes responsible for the HLW chemical evolution. The lower the pH, the slower the chemical degradation of the host rock (and IS glass) but, on the opposite, the faster the corrosion rate of steel. Accordingly, the loss of such high-pH conditions after about 20,000 years led to the speed-up of the corrosion of the C-steel waste overpack. Fe(II)-silicate became also a corrosion product when the pH dropped along with magnetite. The condition for the overpack breaching in the Base Case were reached at approximately 25,000 years (Figure 3-7 c).

Stage 3. The overpack breaching led to the income of aqueous solution in contact with the IS glass (Figure 3-7 d), which released boron, silica and other constitutive elements of the glass. The important

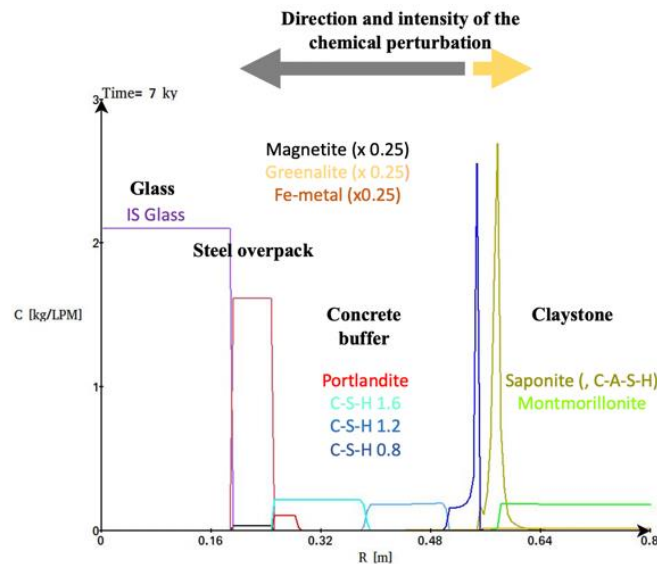
EURAD Deliverable 2.17 – Integrated reactive transport models for assessing the chemical evolution at the disposal cell scale

formation of Fe-silicates corrosion products at the glass/overpack-steel interface sustained glass dissolution as long as uncorroded metallic iron Fe(0) remained. In the present modelling (Figure 3-7 d), the full depletion of Fe(0) corresponded to a strong decrease in the glass dissolution that shifted to the low residual rate mode of Equation 3-4.

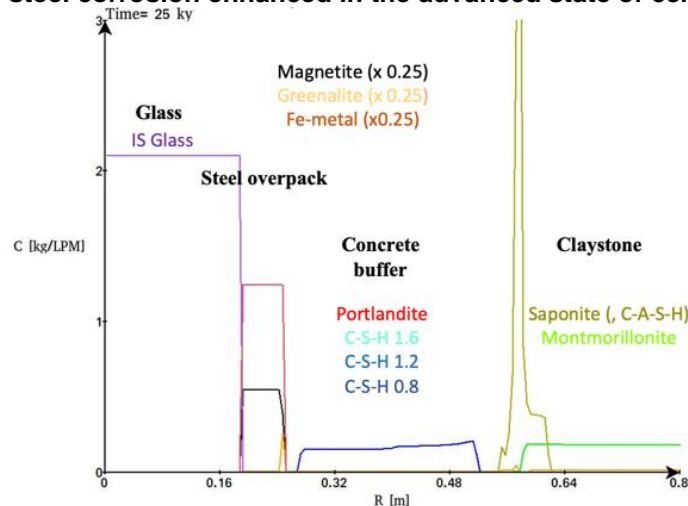
(a) Initial state of the cell component



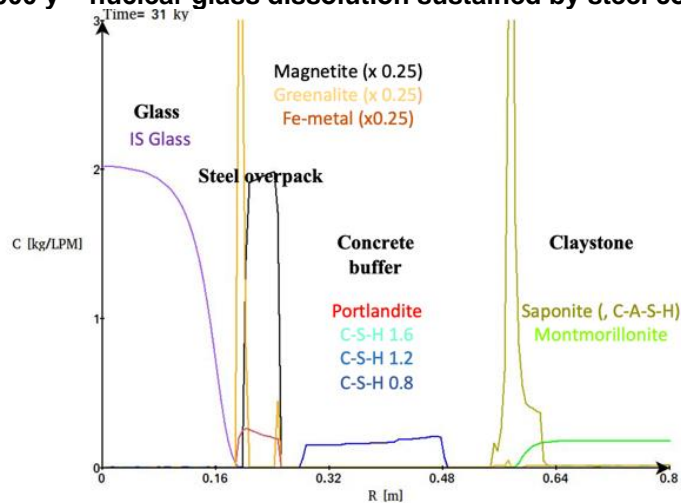
(b) 7,000 y – cement alteration driven by the clay host rock



(c) 25,000 y – steel corrosion enhanced in the advanced state of cement alteration



(d) 31,000 y – nuclear glass dissolution sustained by steel corrosion



(e) 37,000 y – slow glass dissolution after full corrosion of steel

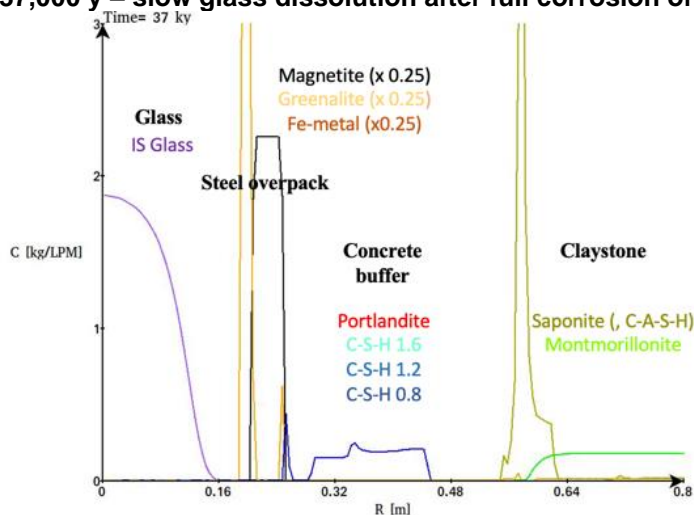


Figure 3-7. Base Case – 30 cm CEM I buffer. HYTEC modelling of the chemical evolution of the HLW cell with time with a selection of the key “disruptive” processes. Base Case – 30 cm CEM I buffer.

3.6.1 Near field perturbation of the clay

The chemical interactions between the concrete and the clay rock, mainly induced by the strong pH gradient between these two porous media, led to the dissolution of the primary phases of the COx

claystone, i.e., the partial dissolution of calcite, chlorite, montmorillonite and quartz (

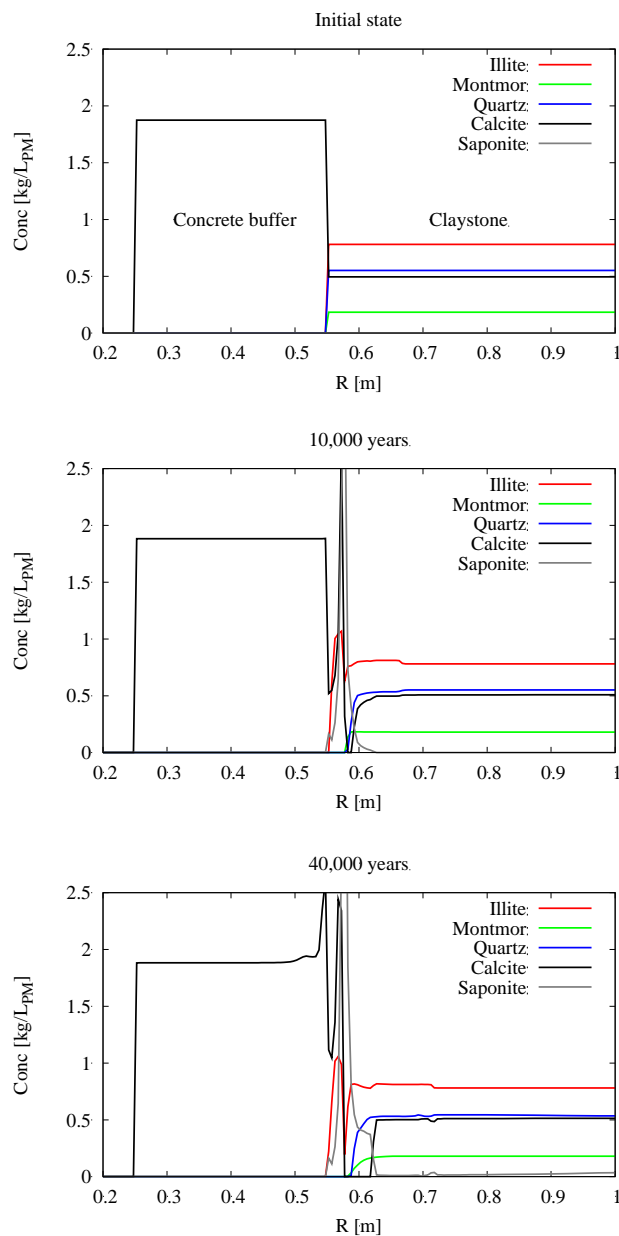


Figure 3-8). The degradation of the concrete was already significant during the first 1,000 years, but the progression of the dissolution fronts inside the host rock decreased with time in relation of the decrease of pH that controlled the kinetics of primary phase dissolution. The overall extend of the mineralogical perturbation front was restricted to about a dozen of centimetres after 40,000 years.

The dissolution induced precipitation of new solid phases around the concrete/clay interface, mostly C-S-H 0.8 (decalcification of primary C-S-H, see next section) and saponite and, to a lesser extent, calcite and stratlingite (proxy for C-A-S-H, not shown). Illite also formed at the interface, that could be seen as corresponding to a partial illitization of montmorillonite.

The pore water chemistry (see Section 3.6.5) and the cation exchange occupancy (

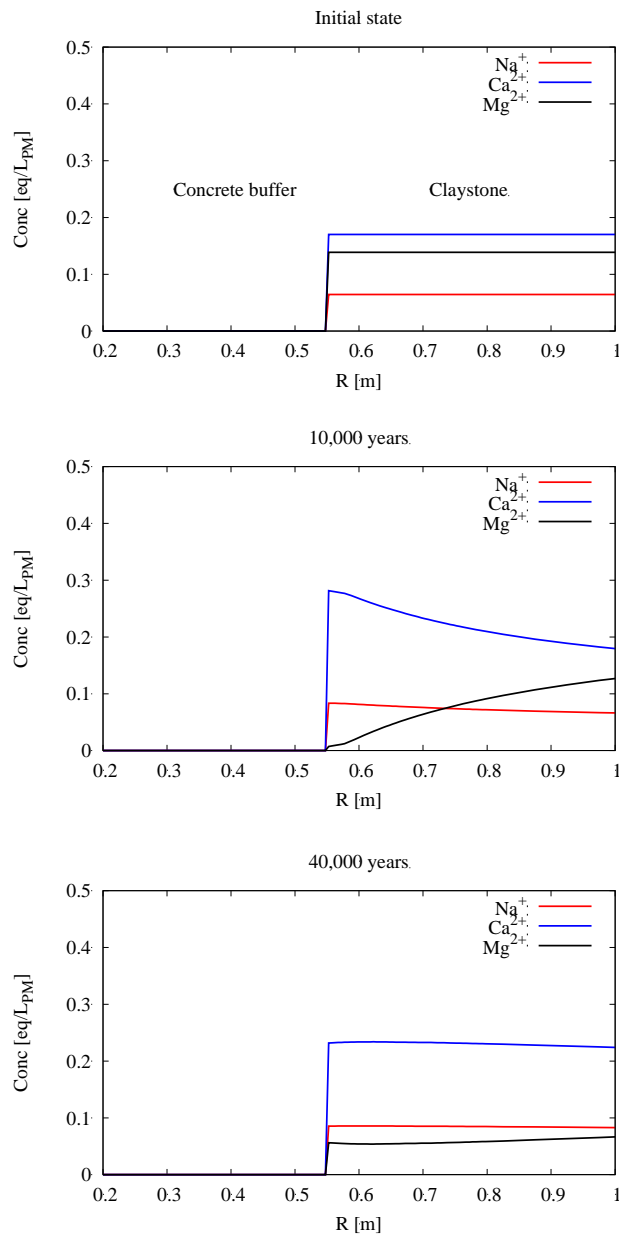


Figure 3-9) of the clay host-rock were impacted by the attenuated alkaline plume much further away than the mineralogical front. There was the relative enrichment in exchangeable Ca²⁺ as long as decalcification of the cement phases of the concrete buffer was active.

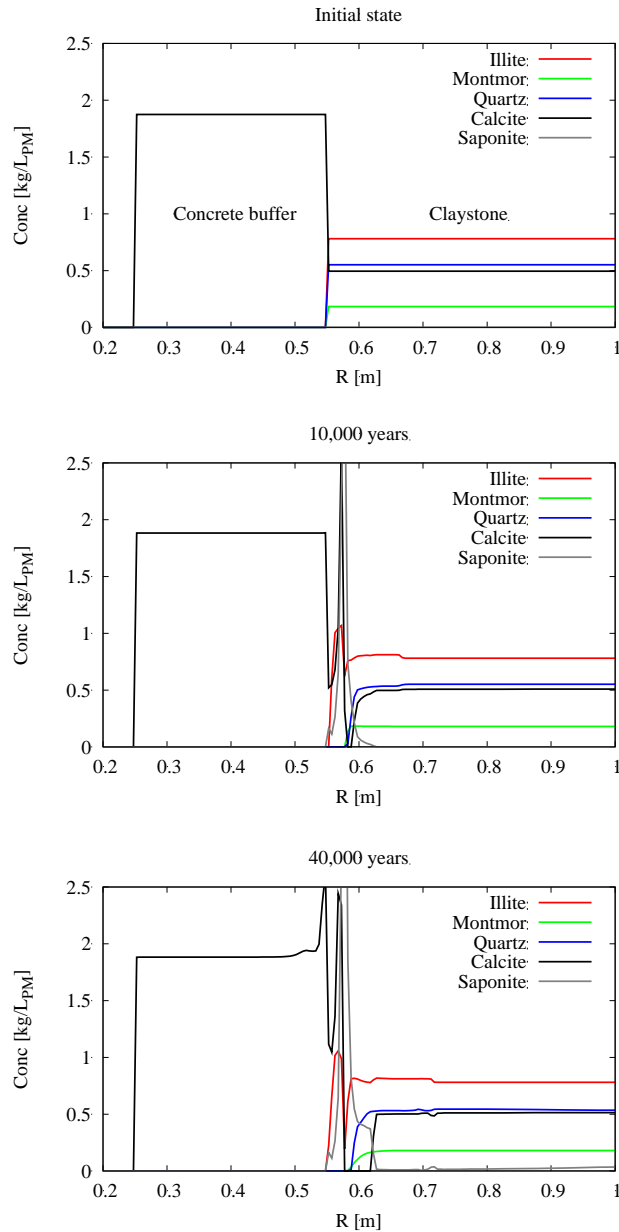
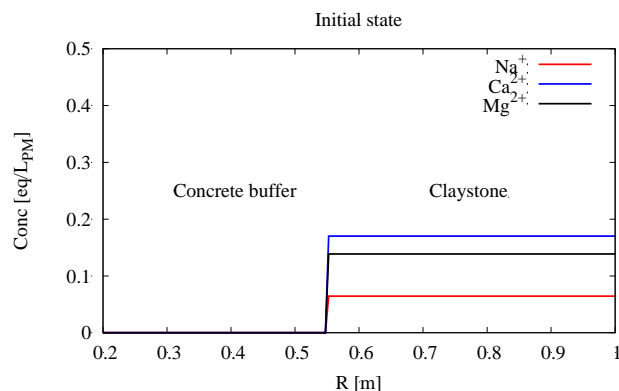


Figure 3-8. Base Case – 30 cm CEM I buffer. HYTEC modelling of the progressive and moderate alteration of the solid phases of the host-rock.



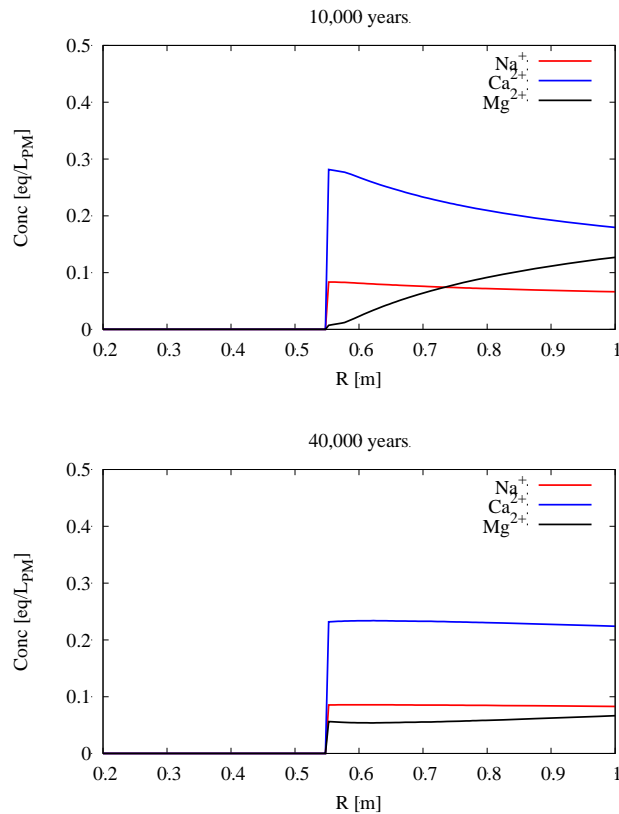
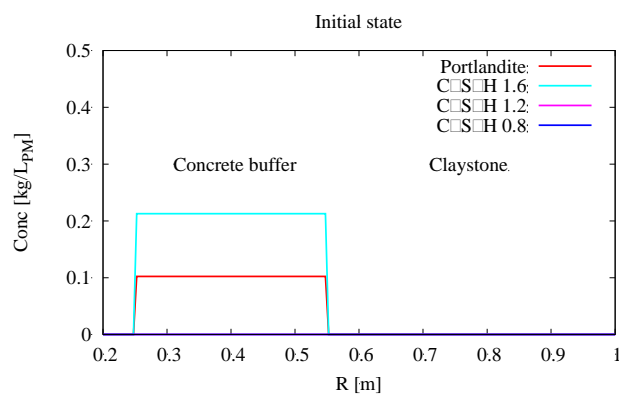


Figure 3-9. Base Case – 30 cm CEM I buffer. HYTEC modelling of evolution with time of the cationic exchangeable occupancy of the host-rock.

3.6.2 Degradation of the cementitious buffer

The decalcification of the hydrated cement as the main alteration process of the CEM I concrete buffer. The decalcification followed a thermodynamic equilibrium sequence: first the dissolution of portlandite, then a progressive decalcification of the C-S-H phases. These decalcification pattern progressed in time and space by diffusion inside the concrete buffer (



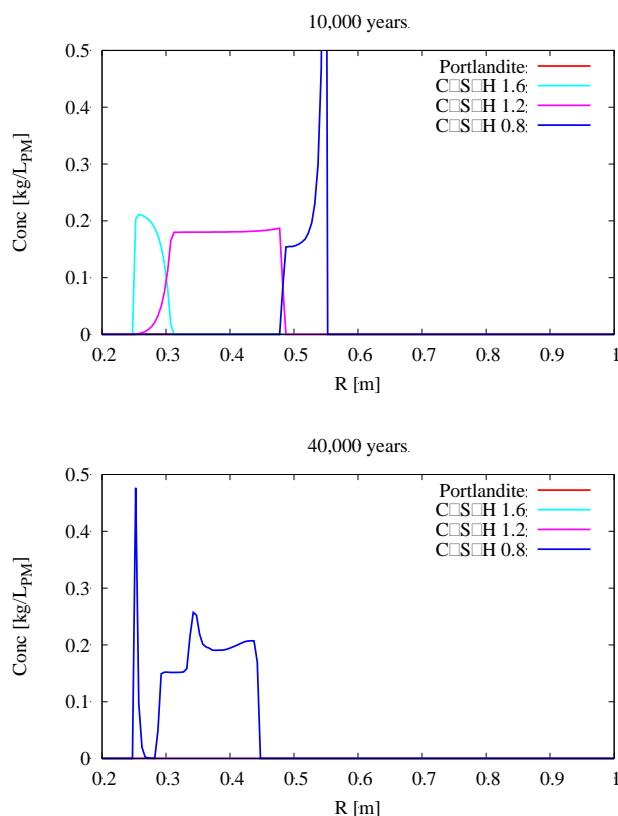


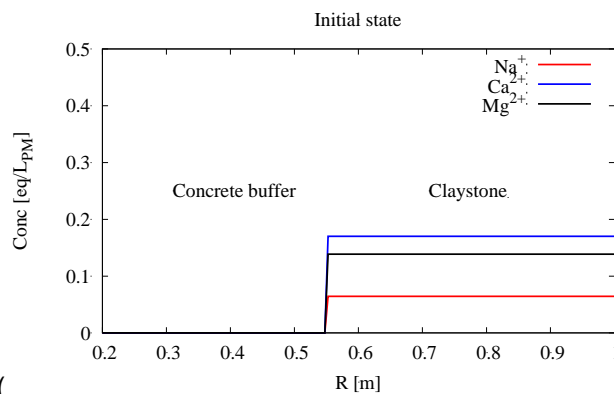
Figure 3-10). With this respect, two indicators of the concrete durability were estimated in this report:

- the full portlandite dissolution corresponding to the loss of high-pH buffering capacity;
- the complete transformation of the C-S-H phases into C-S-H 0.8 corresponding to a complete decalcification with mechanical loss and pH buffered by calcite.

The two durations were 8,000 y and about 22,000 y for the Base Case 30 cm buffer, respectively (Table 3-10).

External sulphate attack was a second but less important source of mineralogical perturbation of the buffer. Additional amounts of ettringite precipitated at the expense of monocarboaluminate due to the diffusion of sulphates from the clay host rock (Figure 3-11). Such a precipitation of ettringite usually favoured a mechanical stress. However, all the ettringite was fully dissolved to form gibbsite after about 25,000 years (Figure 3-11).).

Eventually, calcite precipitation (carbonation) was permanently but moderately active, especially at the



interface with the COx claystone (

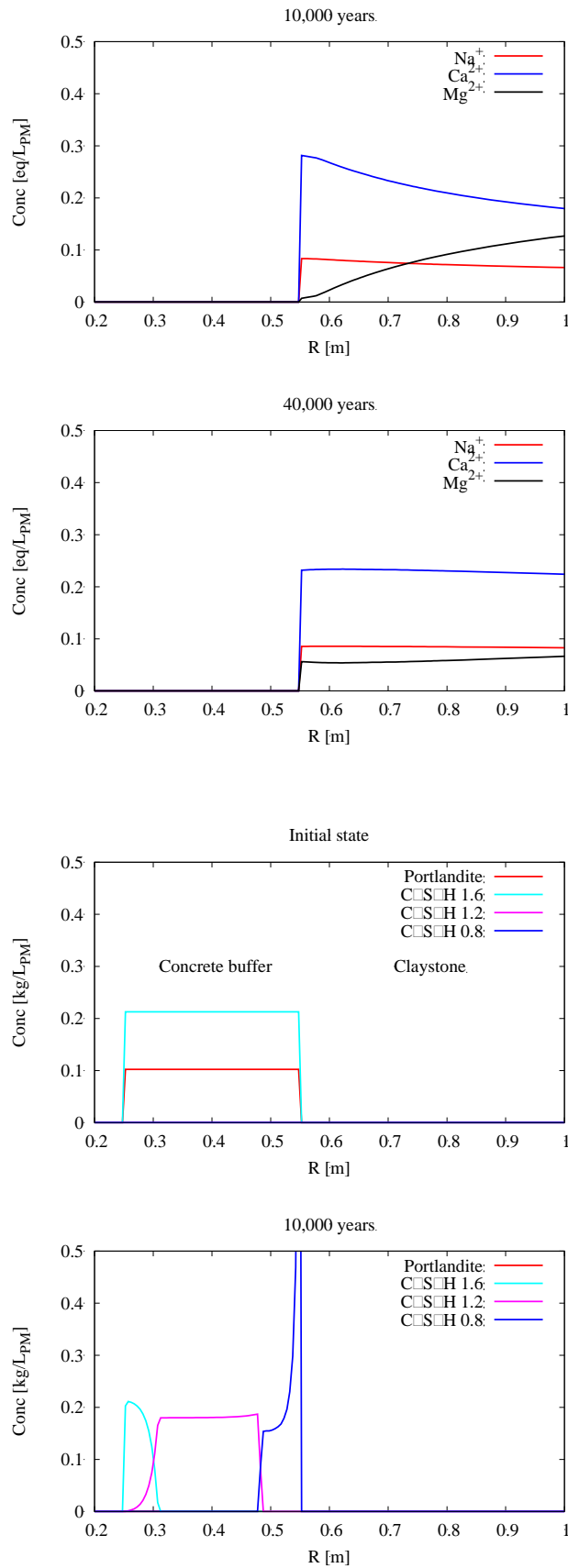


Figure 3-9).

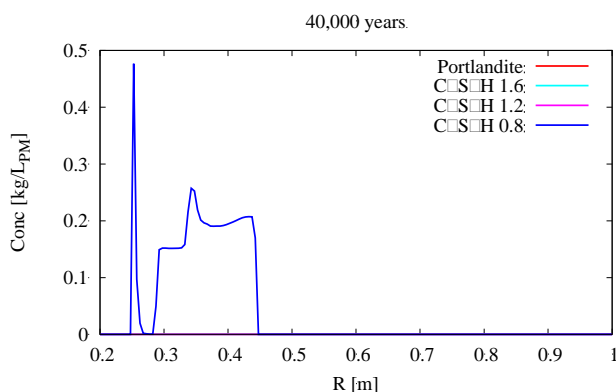


Figure 3-10. Base Case – 30 cm CEM I buffer. HYTEC modelling of the progressive and significant decalcification of the cement phase in the concrete buffer.

Table 3-10. Base Case – 30 cm CEM I buffer. Duration indicators of the durability of the CEM I concrete buffer with respect to high-pH buffering and the completion of decalcification.

Cementitious buffer thickness	Full portlandite dissolution (pH ≤ 12)	Advanced decalcification CSH 0.8 (pH ~ 10)
30 cm (constant porosity)	8,500 y	22,000 y

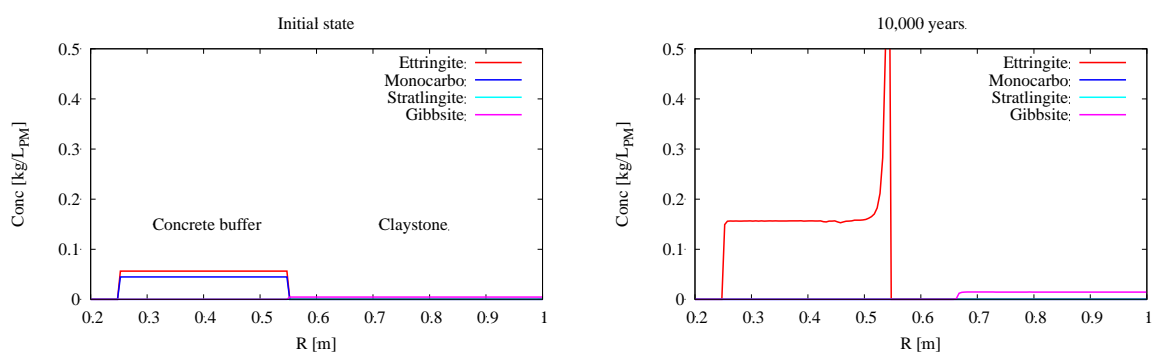
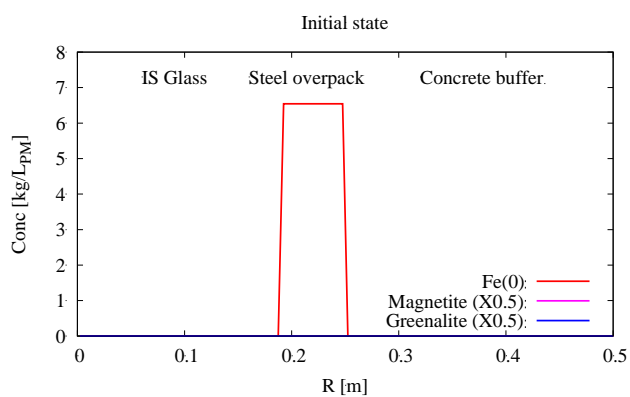


Figure 3-11. Base Case – 30 cm CEM I buffer. HYTEC modelling of the progression of a moderate sulphate attack of the cement phase in the concrete buffer.

3.6.3 Corrosion of the steel waste overpack

As shown by the modelling results of Figure 3-12 corresponding to the steel/concrete interface, as long as the pH remained alkaline, one had very small rates of generalized corrosion of the overpack metallic iron and precipitation of magnetite as the main corrosion product. The corrosion rate of the low carbon steel was then strongly enhanced when C-S-H 0.8 became predominant and pH dropped

below 11. Greenalite became a stable corrosion product under such anoxic and lower pH conditions



as indicated by the Pourbaix diagram of

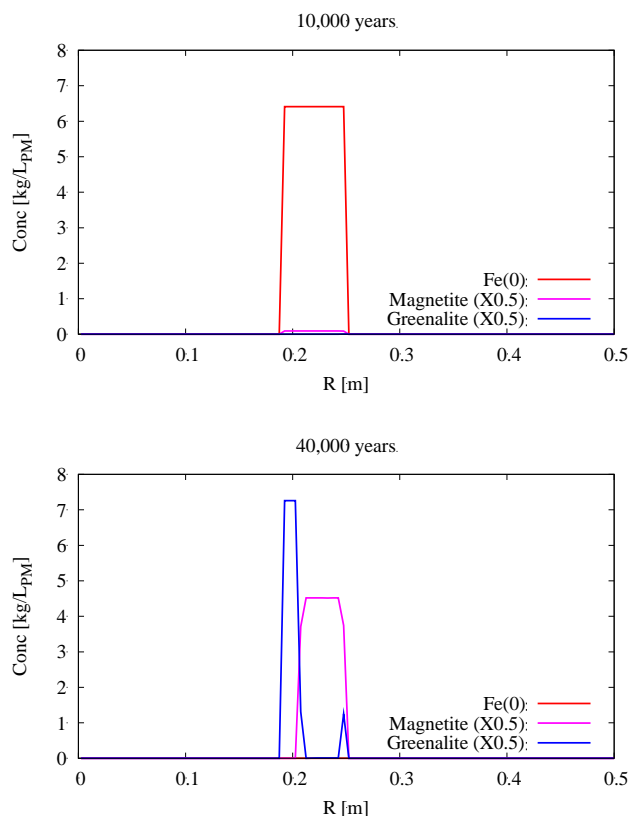
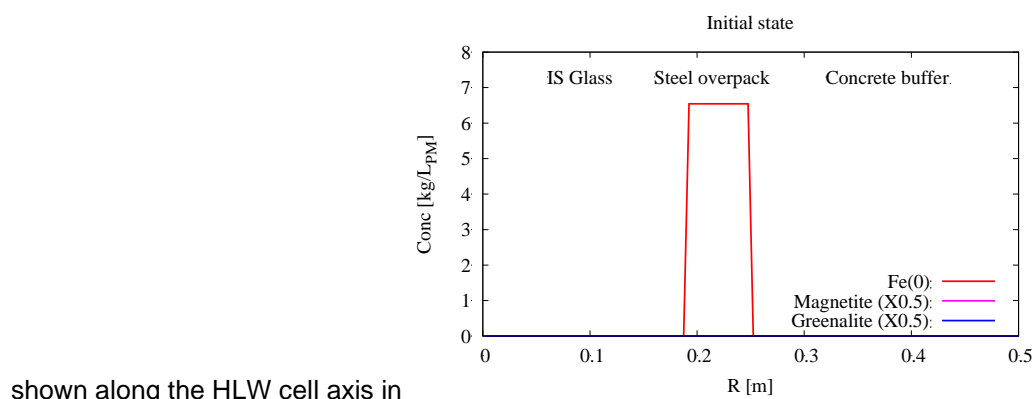


Figure 3-14.

The breaching of the overpack (after 70% of steel corrosion) took place around 29,000 years. The full corrosion of the metallic iron occurred around 34,000 years.

The progressive changes in the corrosion rate and nature of corrosion products with time is also



shown along the HLW cell axis in

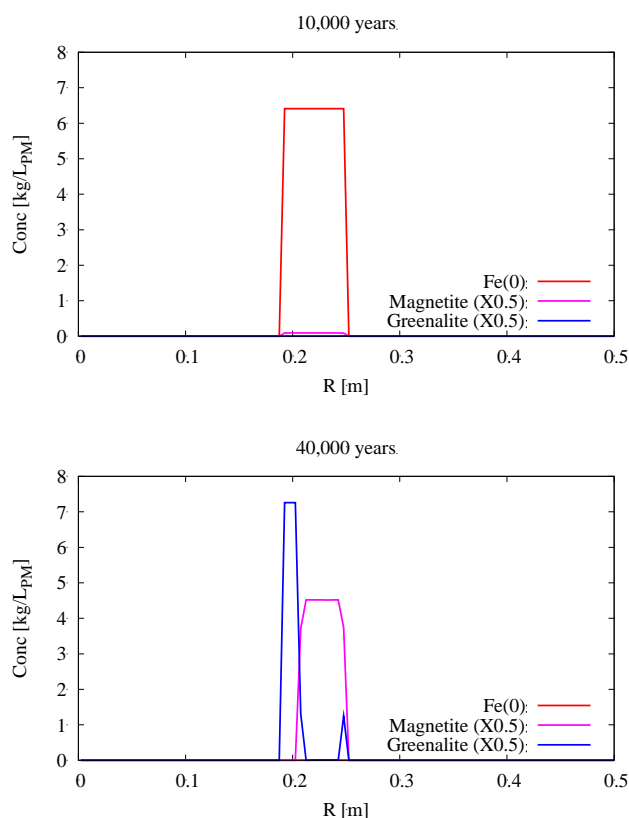


Figure 3-14. Greenalite precipitated in the vicinity of the source of dissolved silica from the multi barrier components, i) first, silica from the degraded cement buffer where C-S-H 0.8 dissolved further, ii) latter, silica from the dissolution of the IS glass. Glass dissolution led to a higher amount of greenalite than the buffer degradation.

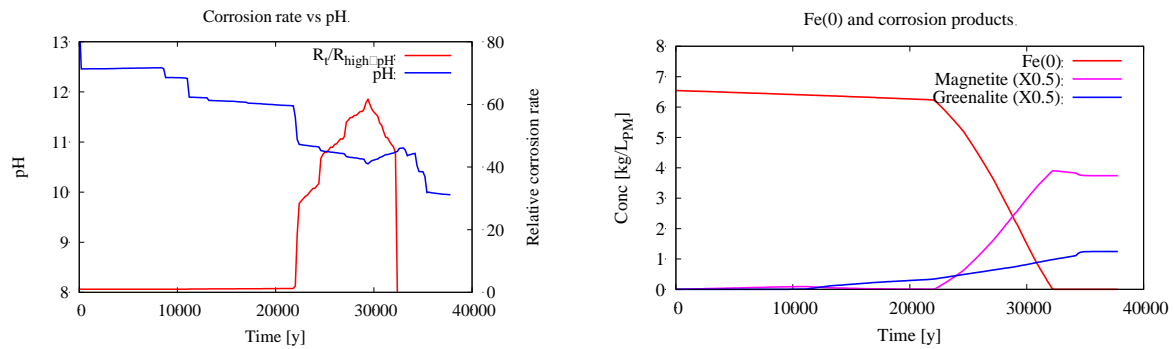


Figure 3-12. Base Case – 30 cm CEM I buffer. HYTEC modelling of the evolution of the generalized corrosion rate of Fe(0) with time, i.e. with the degree of chemical alteration of the CEM I buffer, close to the steel/concrete interface.

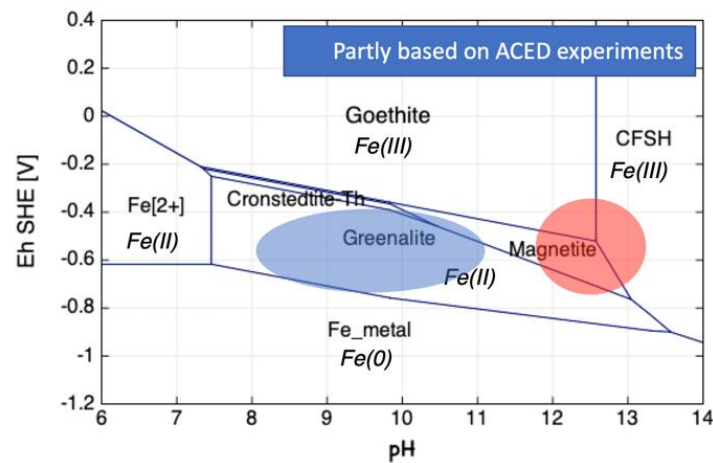


Figure 3-13. Pourbaix diagrams of the oxyhydroxide-silicate iron system iron calculated with CHES/HYTEC at 25°C; activity $Fe^{2+} = 1 \times 10^{-5}$, activity $Ca^{2+} = 4 \times 10^{-3}$, total $H_4SiO_4 = 2 \times 10^{-4}$; in red highly alkaline conditions, in blue weakly alkaline conditions.

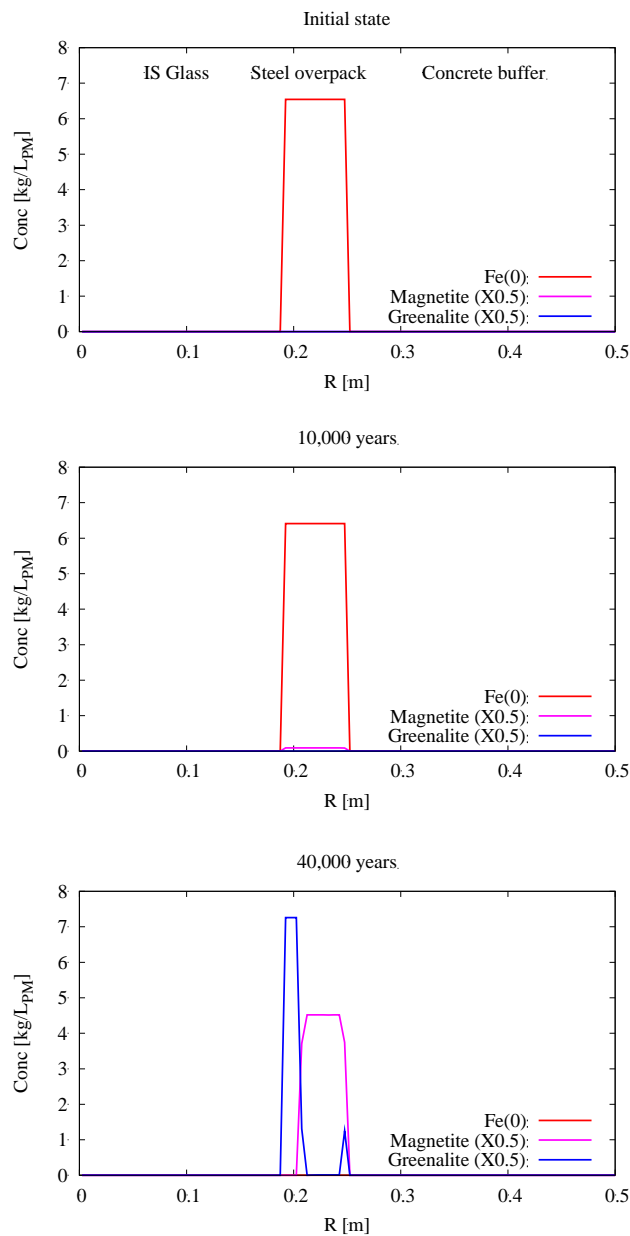


Figure 3-14. Base Case – 30 cm CEM I buffer. HYTEC modelling of steel generalized corrosion and formation of the two main corrosion products magnetite and greenalite.

3.6.4 Dissolution of the international standard glass (ISG)

The dissolution of the international standard glass (ISG) started once the steel overpack was breached

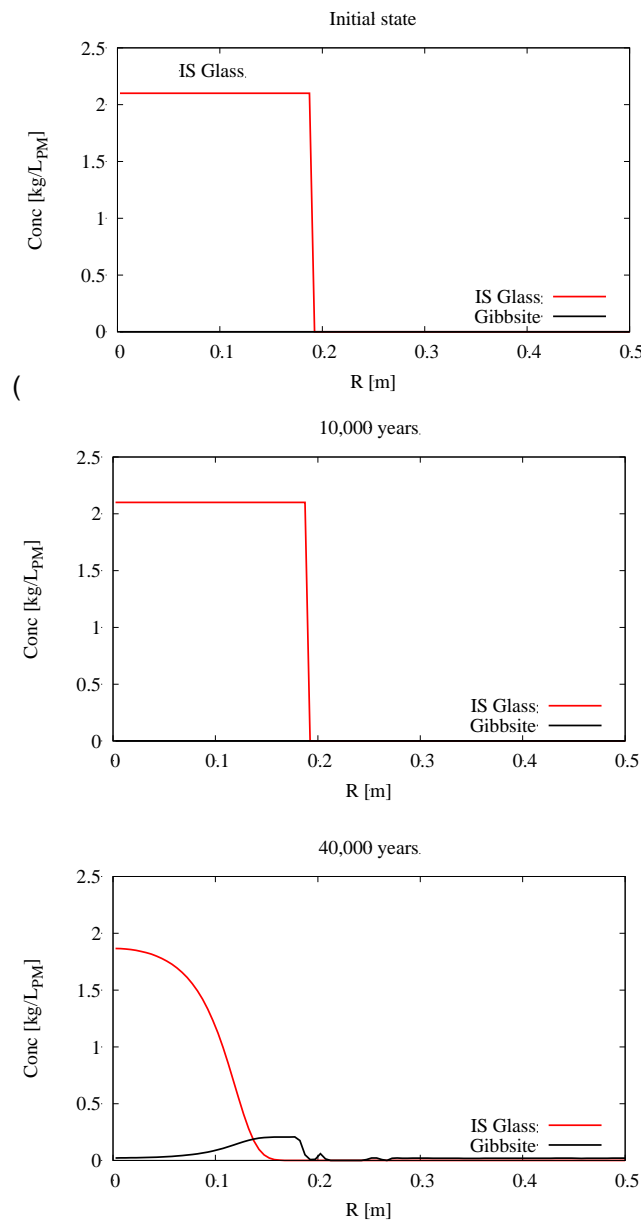
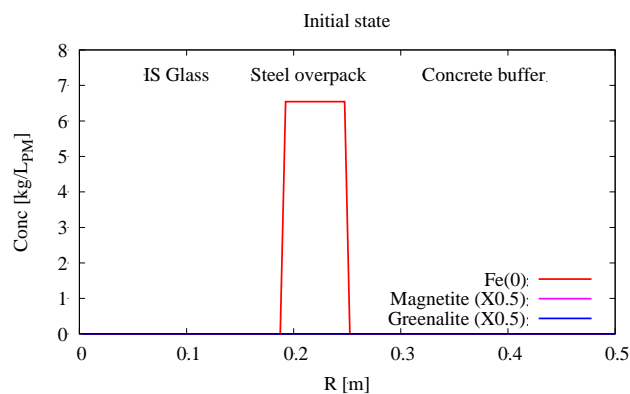


Figure 3-15). The dissolution was mostly coupled with steel corrosion through the control of the dissolved silica by the precipitation of secondary greenalite (



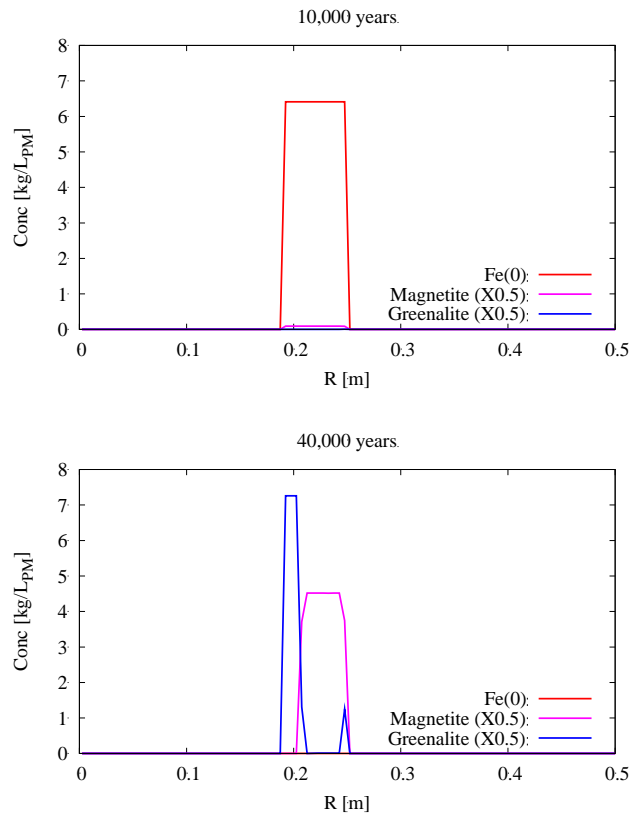
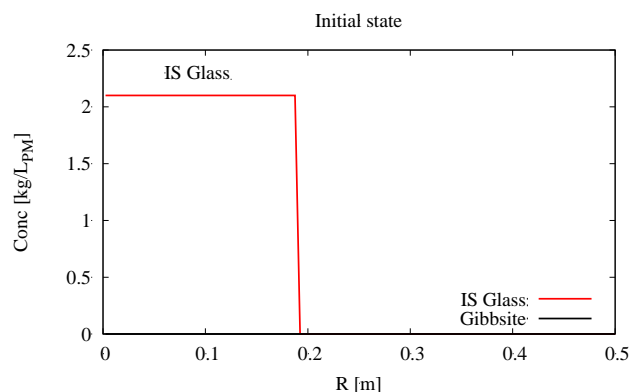


Figure 3-14), a silicate phases containing Fe^{2+} from Fe(0) corrosion. Greenalite precipitation clearly sustained glass dissolution by acting as a silica sink as long as Fe(0) is present and corroding. Once all Fe(0) was completely dissolved, the ISG glass dissolution was under residual kinetic only and slowed down considerably.

The diffusion of dissolved species (e.g. HCO_3^- , SO_4^{2-}) from the altered cement and from host-rock zones into the waste zone had a lower impact on glass dissolution than steel corrosion. These multi-barrier components played nevertheless some role by providing silica by diffusion and rising the dissolved silica concentration that controlled glass dissolution on the very long term, once Fe(0) was depleted. C-S-H precipitation was prohibited in the grid zone corresponding to the glass.

The HYTEC modelling of Figure 3-16 showed a protective effect of the glass internal zones by the most external ones. Silica from the external zones diffused in the internal zone, the silica concentration threshold was reached and inhibited the first term and rapid term of the kinetic Equation 3-5.



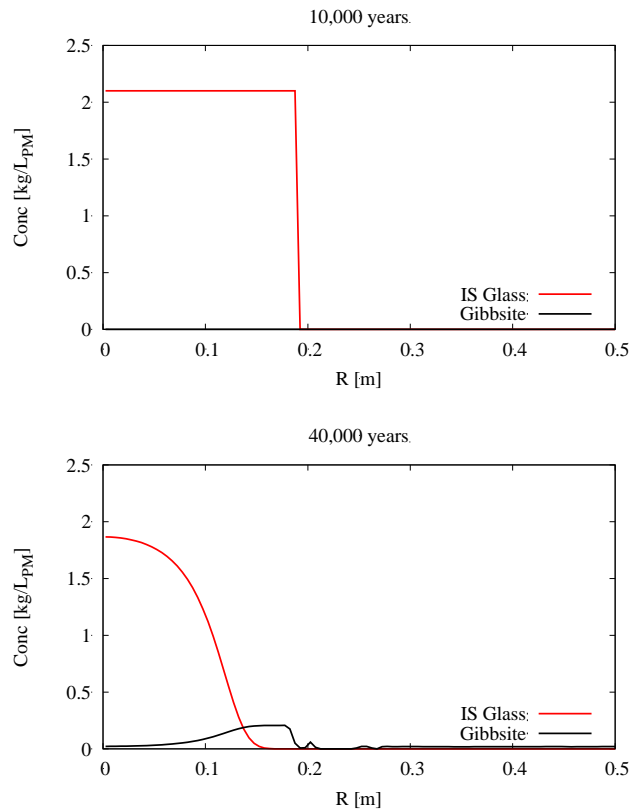


Figure 3-15. Base Case – 30 cm CEM I buffer. HYTEC modelling of the partial dissolution of the international simple glass.

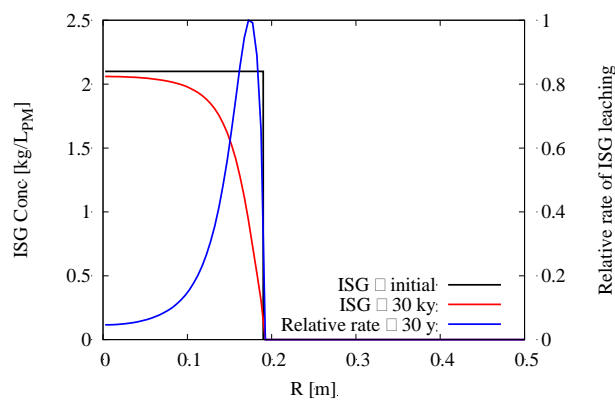


Figure 3-16. Base Case – 30 cm CEM I buffer. HYTEC modelling of the distribution of the IS glass mass initially and after 30,000 y, as well as of the relative kinetic rate of IS glass dissolution.

3.6.5 Evolution of the aqueous chemistry

Evolution of the pH (Figure 3-17). Due to the short-term diffusion of the Na-K-OH plume and the long-term chemical interactions between the COx claystone and the concrete, the porewater in the concrete buffer progressively evolved from a hyperalkaline fresh state (pH > 13), to a depletion in portlandite (pH ~ 12), and the subsequent decalcification of the C-S-H (10.5 < pH < 12), up to eventually to C-S-H 0.8. It is a classical sequence of pH dependency with the decalcification of hydrated cement phases (e.g. De Windt et al., 2004). On the contrary, the pH in the claystone porewater was efficiently buffered around 8 by the dissolution/precipitation reactions. The pH during glass dissolution remained slightly below 10, which ensured the domain of validity of Equation 3-5.

Evolution of the redox potential (Figure 3-17). The redox potential Eh was constantly reducing in the full domain of the cell. The lowest values calculated in the cementitious buffer were lower because the pH was higher compared to the host-rock. The corrosion of Fe(0) drove the redox potential to a very low value by releasing reducing dissolved species such as Fe²⁺ and H₂. The Eh values rose again when Fe(0) was completely corroded.

Evolution of the silica concentration (Figure 3-17). The total dissolved silica concentration was kept relatively low, first by the alkaline-pH conditions inside the buffer, then by the precipitation of greenalite. The silica concentration eventually rose when Fe(0) was completely corroded and greenalite formation stopped.

Evolution of boron concentration (not shown). Boron release in the aqueous solution was a good indicator of the degree of IS glass alteration. The boron concentration diffused in the near field of the clay host rock during the first thousand of years. But the concentration decreased with time due to the decrease of the IS glass dissolution kinetic to reach a low concentration despite that a large part of ISG was still present.

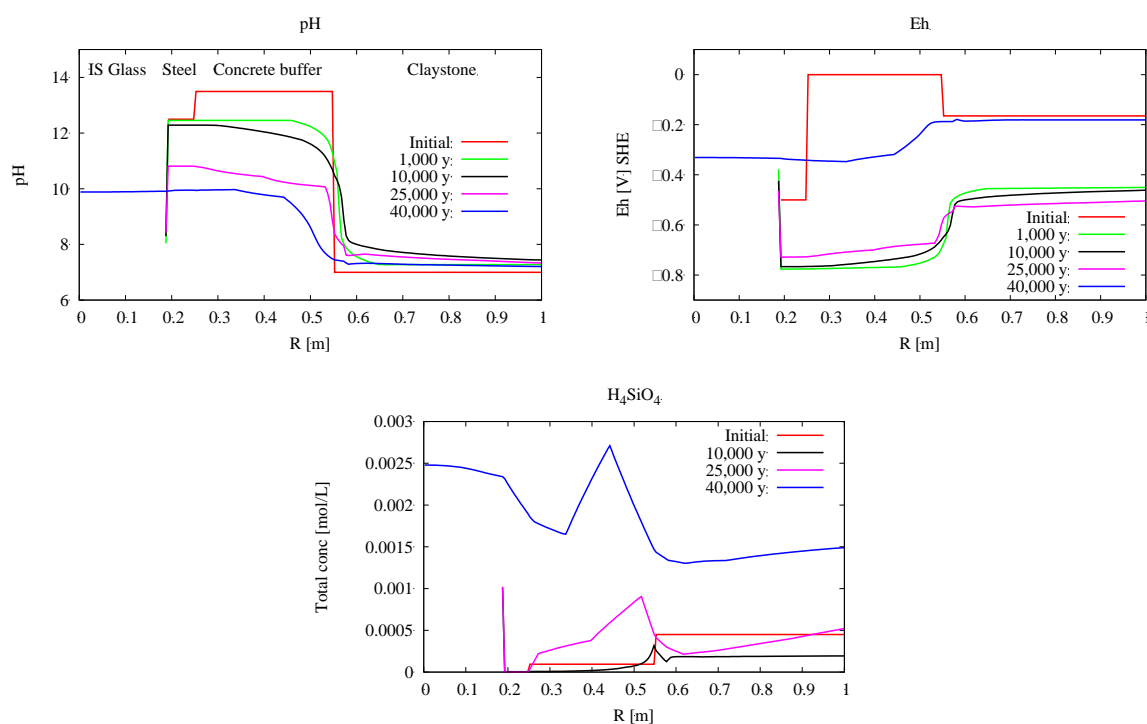


Figure 3-17. Base Case – 30 cm CEM I buffer. HYTEC modelling of evolution of some key aqueous parameters in the full HLW cell.

3.7 Modelling results of the Variant Cases

3.7.1 CEM I buffer thickness of 5 cm and 100 cm

HYTEC led to a similar sequence of chemical alteration of the cementitious buffer for the different buffer thicknesses (5 – 30 – 100 cm) but the fronts of the mineralogical perturbation were spatially larger and

shifted in time while the thickness increased. All cases presented successive moving fronts of decalcification of the cement phases and another front of secondary ettringite formation at the expense of monocarboaluminate (*Figure 3-18* for 5 cm, *Figure 3-11* for 30 cm, *Figure 3-19* for 100 cm). The host rock also showed similar alteration patterns, such as dissolution of montmorillonite, partial illitization and neoformation of saponite and calcite. Notably, the higher the buffer thickness, the larger the lateral extension of the host-rock alteration.

Table 3-11 reports the two indicators of durability already used in the Base Case, i.e. the duration for high-pH buffering and the duration to fully decalcify the C-S-H up to C-S-H 0.8. The pH buffer lost its capacity after about 300, 8,500 and 82,000 years for the 5, 30 and 100 cm cases, respectively. The durations were roughly linked to the thicknesses by a diffusion law relationship in 1D radial since the HYTEC modelling was performed under constant porosity (without chemical feedback effect of mineralogical evolution on the porosity and diffusion coefficient). This was an approximation of the reality. From the one hand, clogging at the cement/clay interface might rapidly stop any chemical and mineralogical perturbations. From the other hand, decalcification might increase the porosity and D_e parameters, enhance the progression of the diffusion fronts and reduce the durability of the cement buffer.

Table 3-11. Modelling cases for different buffer thicknesses. Duration indicators of the durability of the CEM I concrete buffer with respect to high-pH buffering and the completion of decalcification.

Cementitious buffer thickness	Full portlandite dissolution (pH ≤ 12)	Advanced decalcification CSH 0.8 (pH ~ 10)
5 cm (constant porosity)	300 years	~ 1,000 years
30 cm (constant porosity) – base case	8,500 y	~ 25,000 y
100 cm (constant porosity)	82,000 y	> 100,000 y
30 cm (variable porosity)	Never, clogging before 2,000 y	Never

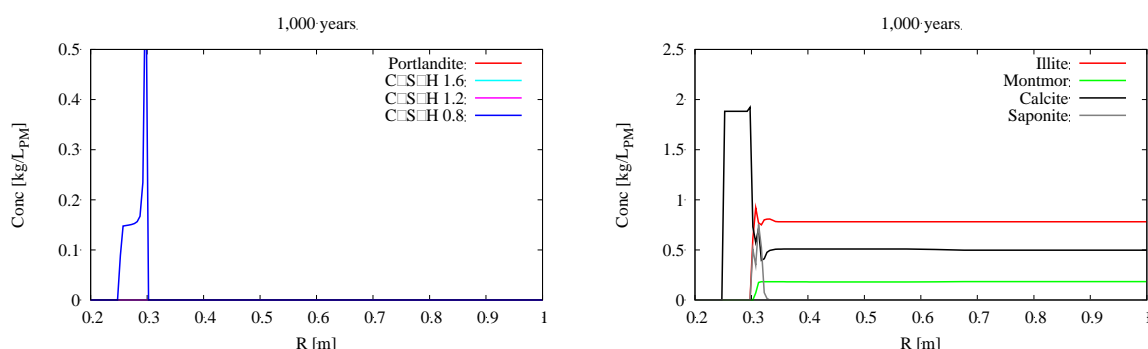


Figure 3-18. Variant Case – 5 cm CEM I buffer. HYTEC modelling of the chemical alteration of the concrete buffer and host-rock.

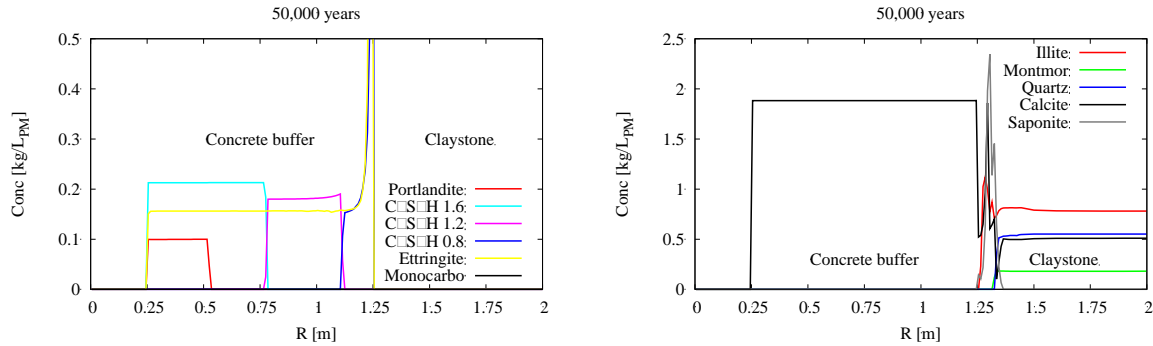
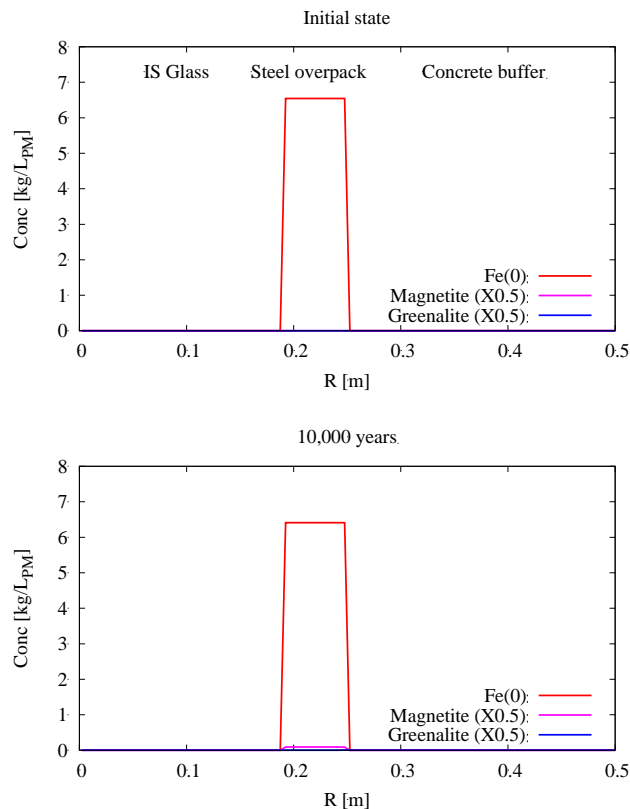


Figure 3-19. Variant Case – 100 cm CEM I buffer. HYTEC modelling of the chemical alteration of the concrete buffer and host-rock at 50,000 years.

The corrosion processes and IG glass dissolution were both approximately the same for the three thicknesses. That is to say slow generalized corrosion, with mostly magnetite as corrosion product, as long as the buffer kept its alkaline-pH conditions, then speeding up of the corrosion with formation of greenalite, and eventually breaching of the overpack (Figure 3-20Figure 3-18 for 5 cm,



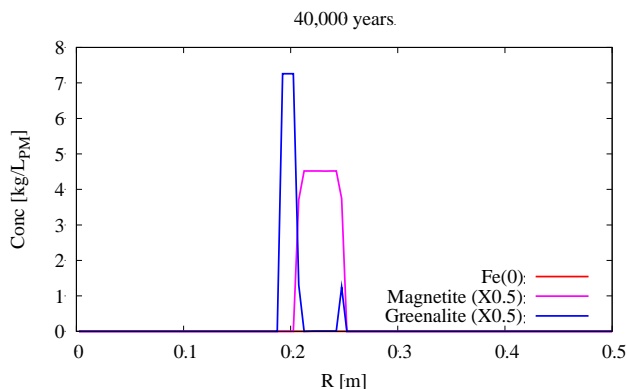


Figure 3-14 for 30 cm, Figure 3-21 for 100 cm). The increase of steel corrosion did not occur in the case of the 100 cm thickness during 100,000 years. Accordingly, the steel overpack remained watertight and the IS glass did not alter over 100,000 years.

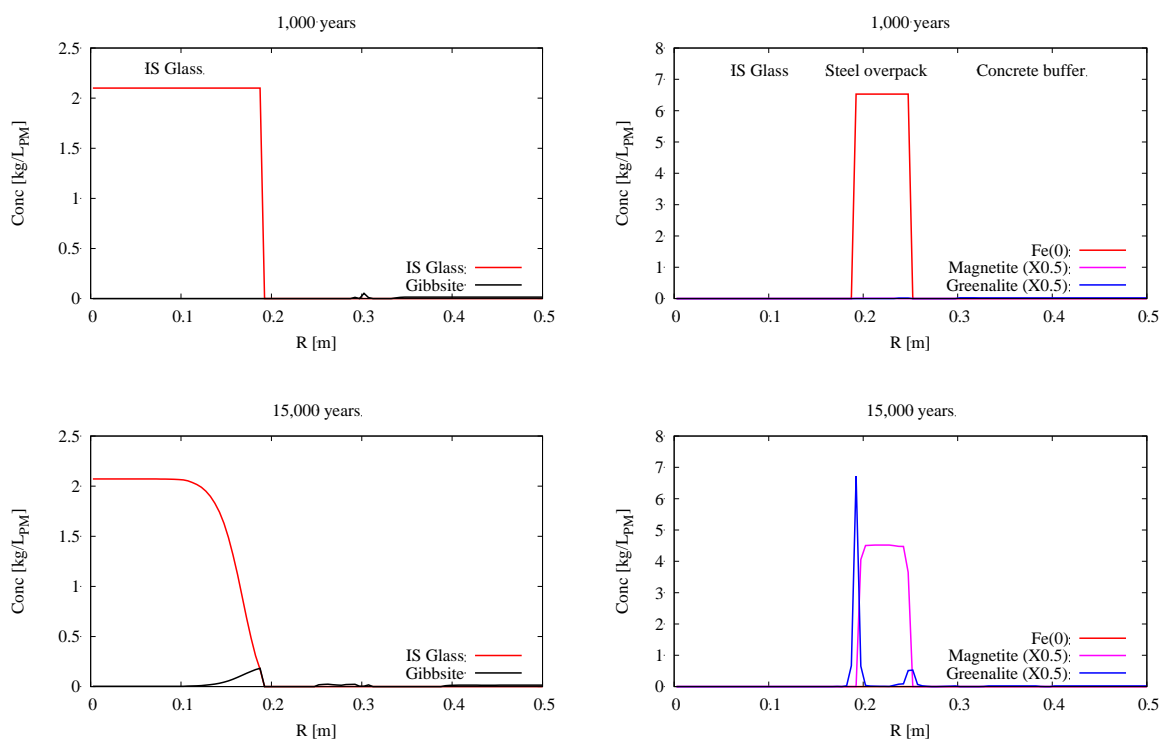


Figure 3-20. Variant Case – 5 cm CEM I buffer. HYTEC modelling of the steel generalized corrosion and IS glass dissolution.

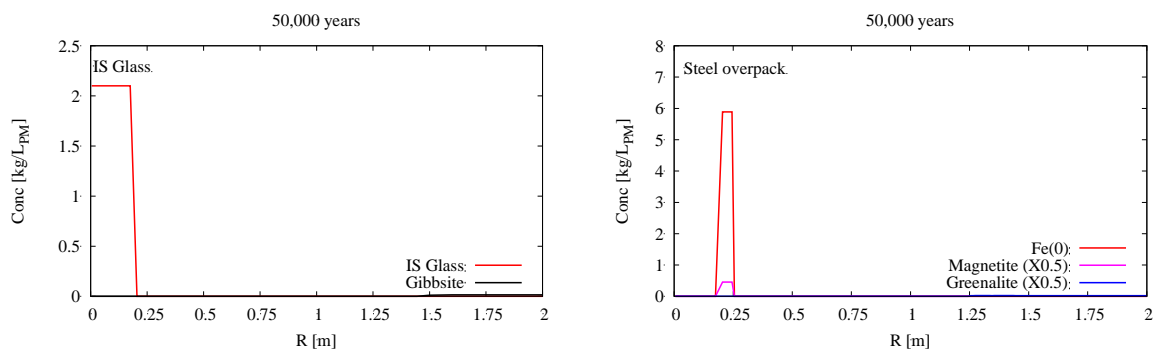


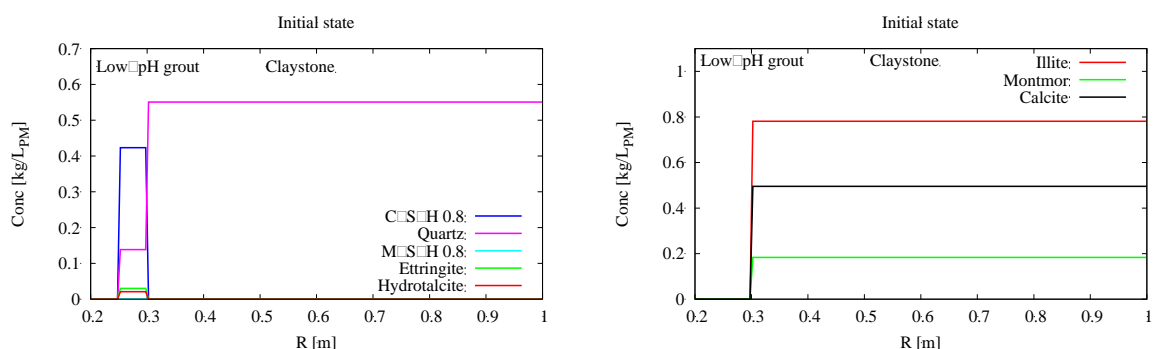
Figure 3-21. Variant Case – 100 cm CEM I buffer. HYTEC modelling of the chemical evolution of all HLW components at 50,000 years.

3.7.2 Low-pH cement/bentonite grout

Inside the low-pH/bentonite grout, there was a combination of hydrolysis and magnesium attack, resulting to the formation of magnesium silicate hydrates M-S-H at the expense of the initial C-S-H 0.8 phase (Figure 3-22). The primary ettringite readily dissolved and there was no significant formation of secondary ettringite as calculated in the CEM I case. Calcite precipitated at the interface with the COx claystone (partial carbonation).

Inside the claystone, the alteration of the primary minerals was much weaker and thinner than in the CEM I case. The source of Mg^{2+} to form M-S-H mostly came from the cation exchangeable occupancy of the COx claystone. Dolomite, which was not included as a primary phase, would have most probably enhanced the transformation of C-S-H into M-S-H by providing more Mg^{2+} in the solution.

Due to the small thickness of the grout material (5 cm), there was no significant difference on the long term with respect to the effect of the buffer nature on the corrosion of steel and the dissolution of the IS glass. There was no high-pH conditions that prevented the steel generalized corrosion in the grout case as in the CEM I, but the high pH-buffering capacities of CEM I were lost in less than 1,000 years with the 5 cm thickness. On the long term, 1 000 years did not make a strong difference for steel corrosion. Due to lower pH conditions, greenalite precipitated earlier and larger amount in the low-pH grout than in the CEM I case.



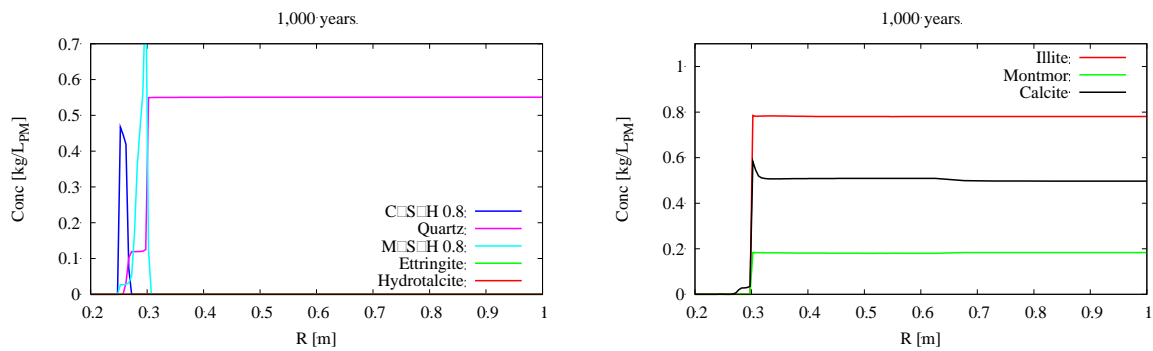


Figure 3-22. Variant Case – 5 cm low-pH grout. HYTEC modelling of the chemical alteration of the low-pH grout and host-rock.

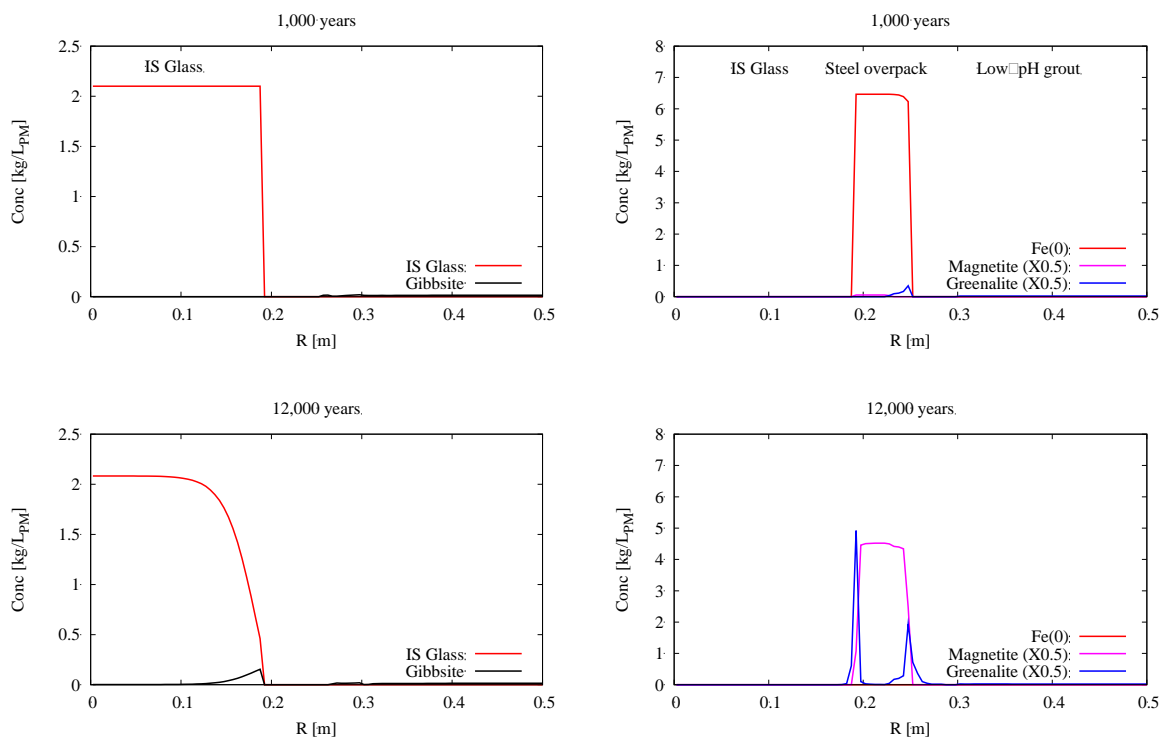


Figure 3-23. Variant Case – 5 cm low-pH grout. HYTEC modelling of the steel corrosion and IS glass dissolution.

3.7.3 Complementary sensitivity simulations

The sensitivity of the reactive transport modelling to the chemical feedback on diffusion, the cracking state of the concrete buffer and the number of discretized C-S-H phases is presented in the deliverable D2.19 (Samper et al., 2023).

Briefly, the effect of the cement thickness cannot be separated from the evolution of the porosity and transport properties of the materials around the cement/clay interface. When the feedback effect of the mineral dissolution/precipitation was taken into account in the HYTEC modelling, clogging occurred at the cement/clay interface due to saponite, CASH and calcite precipitation in less than 1,000 years.

3.8 Conclusions and perspectives

Reactive transport modelling with HYTEC was developed to assess of the chemical evolution of the full cell system in clay, i.e. including in a common model the multi-barrier components “vitrified waste – steel overpack – concrete buffer – clay host rock”. It went a step further than the previous modelling of subsystems such as cement/clay interface within the CEBAMA project (Duro *et al.*, 2020).

The modelling of the full system showed that the driving force was the chemical destabilization of the cement phases of the concrete buffer by the clay rock. This perturbation (decalcification, sulphate attack, carbonation) slowly propagated by diffusion towards the steel overpack with a pH decrease. The durability of the cement buffer would strongly affect the duration of the containment properties of the complete multi-barrier system as a whole.

As long as the high-pH buffering capacity lasted, steel generalized corrosion was minimized and magnetite was the main corrosion products. The loss of such high-pH conditions led to the speed-up of the corrosion of the C-steel waste overpack. Fe(II)-silicate became also a main corrosion product. The overpack breaching led to the income of aqueous solution in contact with the IS glass. The important formation of Fe-silicates corrosion products at the glass/overpack-steel interface sustained glass dissolution as long as uncorroded metallic iron Fe(0) remained. The corrosion products seemed to be less aggressive than the remaining uncorroded steel. Diffusion-driven transfer led to a protective effect of the inner zone of the fractured glass by the external ones.

The lifetimes of the cement-based buffer and steel overpack were estimated as a function of the thickness and nature of the cementitious buffer. HYTEC led to a similar sequence of chemical alteration of the buffer. The lifetime of the buffer varied from 1,250 years to more than 100,000 years. The low-pH/bentonite grout was subjected to hydrolysis and magnesium attacks. Due to the small buffer thickness (5 cm), there was no significant difference on the long term with respect to the effect of the buffer nature on the corrosion of steel and the dissolution of the IS glass.

Some caution has to be emphasized on key processes modelled in this Chapter. With respect to the more physical processes, clogging seems to possibly have a strong effect by stopping the diffusive mass transfer and progression of the degradation both at the cement/clay and in the steel corroded layer (that would prevent any glass dissolution). But the present modelling only considered one type of porosity in the present REV approach. The pore distribution is more complex in reality. Mechanical stress can also weaken the thin clogging layer. Therefore, clogging was ruled out for performance assessment purpose in this report. Eventually, the next Chapter 4 demonstrated that neglecting the thermal and hydric transient stages in the HYTEC modelling was a reasonable approximation for the 30 – 100 cm buffer thickness but should be considered for the 5 cm cases.

With respect to the more chemical processes, the assumption that corrosion significantly increased once the pH dropped below 10.5 – 11 is not yet well validated by the experiments. The modelling assumption on the fractures and reactive surfaces of the glass block were derived from a previous performance assessment based on realistic but pessimistic hypothesis. Furthermore, the issue of the effect of corrosion of metallic iron vs. the re-dissolution of iron corrosion products (magnetite) on the sustainment of glass dissolution by Fe(II)-silicates precipitation is not fully clear yet. Glass dissolution was only sustained by Fe(0) in this Chapter 3, whereas it was sustained both by Fe(0) and magnetite in Chapter 2. The glass dissolution model followed an empirical law. The present results should be compared to a more mechanistic model such as GRAAL (Frugier *et al.*, 2008).

More generally speaking, modelling of the full system with realistic engineering configurations had a demonstrative force, among other with respect to the feasibility of HLW geologic disposal for stakeholders. Reactive transport models alone cannot fully assess the long-term performance of a nuclear waste disposal repository because of the wide range of length scales and intricately coupled physico-chemical processes that need to be addressed. However, reactive transport models have proven to be highly valuable. They can also be enriched, e.g. by including radionuclide release and

EURAD Deliverable 2.17 – Integrated reactive transport models for assessing the chemical evolution at the disposal cell scale

migration from the glass in the degraded barriers. Reactive transport modelling will remain a unique tool by which to assess and constrain the long-term evolution of nuclear waste geologic repositories.

4. Modelling of the transient stage effects on the cement buffer in a HLW cell in clay

The work has been done by Benoit Cochevin (ANDRA).

In complement to the preceding chapter, this chapter presents the reactive transport model for assessing the effects of the thermal and hydric transient stages in a HLW disposal cell in clay, focusing on the subsystem consisting of the cementitious buffer and the claystone rock. The chapter is divided in 6 sections starting with the description of the conceptual and numerical models, and the computer code. Then, the model predictions successively follow without transient, with the thermal transient stage, and with the combined thermal and hydric transient stages. The chapter concludes with the summary and main conclusions.

4.1 Cell configuration, conceptual model and narrative evolution

As a complementary study to the main simulations performed with HYTEC in chapter 3, the numerical models are implemented in iCP (interface Comsol-Phreeqc) to explore some specific assumptions in the general trend. These numerical simulations aim at covering the post closure phase, but before the overpack fails (i.e. only Period II in *Figure 3-3*). Specific hypotheses about two parameters are actually tested in this part of the project. The first one is the temperature, which will be either considered as constant (Tcte) or varying with time (Tvar). The second one is the liquid saturation, which will also be considered either as constant (Scte) or varying with time (Svar). These different cases will be considered in both configurations for the cementitious material, i.e. the first one with a thickness of 30 cm to be consistent with the generic concept and the second one with a thickness of 5 cm closer to the French concept as illustrated in *Figure 3-2*.

The objective of the iCP modelling in the base case (called “Tcte_Scte”, see *Table 4-1*) is to reproduce/compare with the base case simulated with HYTEC (see *Table 3-1*), in which neither the temperature nor the liquid saturation varies with time. The first sensitivity case (called “Tvar_Scte”, see *Table 3-1*) aims at introducing the variable temperature in the different domains and assessing the influence of neglecting the thermal transient stage on the base case. In the second sensitivity case (called “Tcte_Svar”, see *Table 4-1*), a local desaturation is considered to assess the consequences of the decrease of diffusive transport properties of aqueous species (see Eq. 4-1). The last sensitivity case (called “Tvar_Svar”, see *Table 4-1*) mixes both cases. The results of this modelling program are interpreted from the point of view the kinetic and extent of the chemical alterations, which develop at the interface between the cementitious material and the COx claystone.

Table 4-1. Base and variant configurations investigated by HYTEC modelling of the chemical evolution of the HLW cell.

Period	Buffer thickness	Temperature	Water saturation	Concrete type	Steel canister	Nuclear glass
Base case						
Tcte_Scte	5, 30 cm	25°C constant	100 %	CEM I + calcareous aggregates, non damaged	Corroded	No
Sensitivity						
Tvar_Scte	5, 30 cm	Transient stage previously simulated	100 %	CEM I + calcareous aggregates, non damaged	Corroded	No
Tcte_Svar	5, 30 cm	25°C constant	Partial desaturation	CEM I + calcareous aggregates, non damaged	Corroded	No
Tvar_Svar	5, 30 cm	Transient stage previously simulated	Partial desaturation	CEM I + calcareous aggregates, non damaged	Corroded	No

4.2 Mathematical model

4.3 Parameter values in iCP

This part presents a detailed description of the conceptual geochemical model of each of the materials included in the models. Geochemically speaking, the reactive transport models include two different materials: OPC concrete and Callovo-Oxfordian (COx) clay. The chemical setup is based on the use of the thermodynamic database ThermoChimie version 10a (Giffaut et al., 2014). All chemical reactions have been calculated assuming thermodynamic equilibrium. The aqueous reaction S(-II)/S(+VI) is omitted in the database as in in the modelling cases of Chap. 3.

4.3.1 Clay host rock

The host rock formation surrounding the sealing components is the Callovo-Oxfordian claystone (COx). The chemical composition of COx claystone is extracted from Marty et al. (2014). This clay is mainly composed of illite, calcite and quartz, while smectite content is only 8 wt.% (6.5 vol.%). Its complete mineral assemblage is presented in Table 4.2 together with the cation exchanger composition and selectivity coefficients (Gaucher et al., 2009). The cation exchange capacity (CEC) of the COx claystone is considered to be constant in time.

Table 4-2. Assemblage of mineralogical phases of sound CO_x adapted from Marty et al. (2014). The chemical composition of the minerals and their equilibrium constants are coming from the Thermochemie database. Selectivity coefficients for illite/smectite mix (Gaucher et al., 2009).

Primary minerals	Concentration (mol/L _{medium})	Volume fraction (%)	Reaction type
Calcite	5.04	19	Equilibrium
Celestite	0.12	<1	Equilibrium
Dolomite	0.50	3	Equilibrium
Pyrite	0.19	<1	Equilibrium, Dissolution only
Siderite	0.20	<1	Equilibrium
Illite(IMt-2)	1.96	27	Equilibrium
Montmorillonite(HcCa)	0.41	7	Equilibrium, Dissolution only
Microcline	0.25	2	Equilibrium, Dissolution only
Quartz	9.2	21	Equilibrium.
Chlorite(Cca-2)	0.07	2	Equilibrium, Dissolution only
Mineral volume		0.82	
Porosity		0.18	
Exchanger composition		Equivalent fractions (%)	Log K (versus Na ⁺)
CaX ₂	0.089	45.5	0.7
MgX ₂	0.061	30.9	0.7
NaX	0.072	18.3	0
KX	0.014	3.7	1.2
SrX ₂	0.002	1.1	0.6
FeX ₂	0.0008	0.4	0.8

Porewater in equilibrium with the initial mineralogy is presented in Table 4-3. The set of secondary minerals considered in the clay takes into account the phases expected to form due to the interaction with concrete and CO_x (Table 4-4).

Table 4-3. Initial pore water composition in the Callovo-Oxfordian clay.

Solutes (totals)	Concentration (molality)
pH	7.07
Ionic strength (M)	0.08
Al	$1.27 \cdot 10^{-07}$
C	$3.68 \cdot 10^{-03}$
Ca	$7.75 \cdot 10^{-03}$
Cl	$4.10 \cdot 10^{-02}$
Fe	$4.41 \cdot 10^{-05}$
K	$5.13 \cdot 10^{-04}$
Mg	$5.16 \cdot 10^{-03}$
Na	$4.00 \cdot 10^{-02}$
S	$1.13 \cdot 10^{-02}$
Si	$1.82 \cdot 10^{-04}$
Sr	$2.39 \cdot 10^{-04}$

Table 4-4. Secondary minerals allowed to precipitate in the COx claystone.

Secondary minerals		
Concrete minerals	Argillaceous phases	Zeolites
Portlandite	Saponite Ca	Clinoptilolite Ca
CSH 1.6		
CSH 1.2	<u>Others</u>	
CSH 0.8	SiO ₂ (am)	
C ₃ FH ₆	Gypsum	
Ettringite	Anhydrite	
Ettringite Fe	Goethite	
Hydrotalcite	Magnetite	
Fe(OH) ₂ (cr)		
Monocarboaluminate		
Monosulfate Fe		
Monosulfoaluminate		
Brucite		
Strätlingite		

The porosity of the clay host rock is 18 %. A single effective diffusion coefficient D_e of 3×10^{-11} m²/s will be considered in fully water saturated conditions and for a temperature of 25°C. No impact of the gas build-up is expected in the sound COx claystone (no desaturation).

For a limited extent in the COx claystone around the liner (up to 0.2-0.4 diameter depending on the orientation), a damaged zone is considered in which the porosity is equivalent to the one in the sound host rock but in which the temporary gas pressure increase can induce a partial desaturation of this

area. In that case, the effective diffusion coefficient is calculated with a Millington and Quirk type model (Millington and Quirk, 1960):

$$D_e = D_e(S_l = 1) \cdot S_l^b \quad [4-1]$$

where $D_e(S_l = 1)$ is the effective diffusion at full liquid saturation and b [-] the Millington and Quirk parameter related to the saturation dependence. From Andra's preliminary calculations (not presented here), the variation in time of the liquid saturation in the damaged zone of the COx domain could be simplified in this modelling exercise and considered as constant (with a mean value of 0.98). By considering this partial liquid saturation and $b=8$ as a representative value for the COx, the equation 4.1 shows that the effective diffusion is decreased by 20 % when considering partial liquid saturation in comparison with fully-saturated conditions.

In the cases for which the temperature evolution has an influence on the hydrological and chemical processes, the temperature time series, computed from previous models (Neeft, 2021), have been imported and applied onto the numerical mesh used in the reactive transport simulations with iCP. Each material is then affected by one of the temperature series illustrated in *Figure 4-1*. The consequences of the temperature increase on the effective diffusion of aqueous species in the COx has been previously quantified thanks to dedicated through-diffusion experiments. The following second-degree law allows then to reproduce this dependency.

$$D_e(T[^\circ\text{C}]) = D_e(25^\circ\text{C}) \times (0.0002 \times T[^\circ\text{C}]^2 + 0.02 \times T[^\circ\text{C}] + 0.52) \quad [4-2]$$

In a first approximation, this equation [4-2] has been applied to all materials.

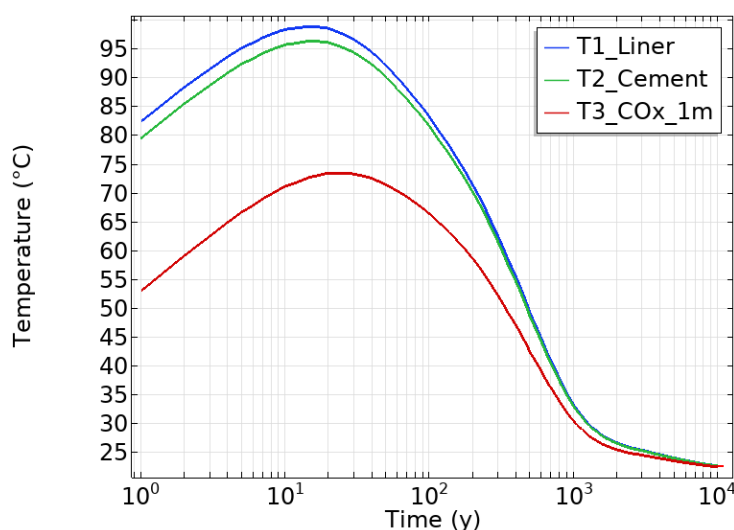


Figure 4-1. Temperature time series simulated a generic HLW cell in clay surrounded by a cement grout buffer of 5 cm thick and after 120 years of storage (communication with E. NEEFT, COVRA).

4.3.2 CEM I-based concrete (buffer)

The chemical composition of concrete is adapted from the mineralogical assemblage presented by Kosakowski (2020). This composition is re-equilibrated using ThermoChimie v10a (Giffaut et al., 2014). As a result, monosulfoaluminate dissolves and ettringite precipitates. This phase change results in an excess in aluminium that precipitates as C3AH6. The final assemblage of mineralogical phases of the concrete domains is presented in Table 4-5. The porewater composition has been calculated based on the mineral assemblage and assuming that all the Na and K alkalis are dissolved in porewater. Aqueous species concentrations in concrete pore water are shown in Table 4-6.

Table 4-5. Assemblage of mineralogical phases of the concrete components adapted from the OPC chemical description in BRGM (2013).

Mineral	Concentration (mol/L _{medium})	Volume fraction (%)	Reaction type
C ₃ FH ₆	0.04	0.8	Equilibrium
Calcite	16.85	68.4	Equilibrium
C-S-H 1.6	0.99	9.2	Equilibrium
Ettringite	0.04	3.1	Equilibrium
Hydrotalcite	0.03	0.7	Equilibrium
Monocarboaluminate	0.07	2.0	Equilibrium
Portlandite	1.22	4.4	Equilibrium
Mineral volume		0.885	
Porosity		0.115	

The alteration of concrete as a result of its interaction with bentonite or CO_x is characterized by the dissolution of cement hydrates due to the near-neutral pH of the clay-based materials and by the precipitation of calcium silicate hydrates (C-S-H) with low Ca/Si ratio, calcite, Mg-bearing phases, saponites and zeolites (Gaucher et al., 2005; Marty et al., 2014). Table 4-7 presents the secondary minerals that are allowed to form if supersaturation of the solution is attained.

Table 4-6. Initial concrete porewater composition, including dissolved alkali.

pH	13.43
Ionic strength (M)	0.4
Solutes (totals)	Concentration (molality)
Al	8.3·10 ⁻⁰⁵
C	1.7·10 ⁻⁰⁴
Ca	9.5·10 ⁻⁰⁴
Cl	5.1·10 ⁻⁰⁷
Fe	9.2·10 ⁻⁰⁷
K	4.2·10 ⁻⁰¹
Mg	8.3·10 ⁻¹⁰
Na	7.7·10 ⁻⁰³
S	4.8·10 ⁻⁰³
Si	9.0·10 ⁻⁰⁵

Table 4-7. Secondary minerals allowed to precipitate in the concrete domain.

Secondary minerals			
Concrete minerals	Argillaceous phases	Zeolites	Others
CSH 1.2	Illite	Clinoptilolite Ca	Gypsum
CSH 0.8	Saponite Ca		Quartz
Monosulfoaluminate			Pyrite
Brucite			Dolomite
Strätlingite			Anhydrite
			Siderite
			Magnetite
			Gibbsite
			Ettringite-Fe
			Monosulfate-Fe
			Fe(OH) ₂ (cr)

A porosity of 11.5 % is considered in the CEM I concrete. A single effective diffusion coefficient D_e of 1×10^{-11} m²/s is considered for all aqueous species in fully water saturated conditions and at a temperature of 25°C. The variation of the effective diffusion coefficient with liquid saturation is described following the formalism proposed by Millington and Quirk (Millington and Quirk, 1960), and in which $b = 4.2$ has been considered in agreement with Thiery et al. (Thiery et al., 2007). As a first approximation, the liquid saturation in the concrete domain is supposed to be constant and equal to 0.9 (a high value classically measured in a High Performance Concrete under few MPa of gas pressure, personal communication) after closure of the cell and for a duration of at least several tens of thousands of years, corresponding to the typical duration of gas pressure increase in the French concept.

The consequences of the temperature increase on the effective diffusion of aqueous species is described in *Figure 4-1*.

4.3.3 Low carbon steel

In the reactive transport models with iCP, the surface of the carbon-steel liner at the interface with the cementitious material is considered as corroded; there is no consideration of the inner oxidation that transforms Fe(0) into iron corrosion products. Even if the nature and the corrosion rate depend on the chemical environment, the reactive transport models implemented in iCP supposed that the metallic domain is composed of iron oxide (magnetite). The dissolution of this mineral is allowed under thermodynamic conditions if the cementitious environment is favourable.

This oxide layer is assimilated as a porous medium with an initial arbitrary porosity of 20 % and an effective diffusion coefficient equivalent to 2×10^{-11} m²/s at 25°C and for saturated conditions. The consequences of unsaturated conditions and temperature variation are supposed to be equivalent to those of the cementitious material in contact.

4.4 Numerical model

The reactive transport model of the HLW disposal cell in Clay with iCP was performed with a 1D-radial finite element mesh with 103 nodes: 5 nodes in the corroded liner, 10 nodes in the cementitious material, 30 nodes in the EDZ and 100 nodes in the COx. The spatial mesh discretization is uniform in the first three domains ($\Delta x = 0.5$ cm, with $0.3 < x < 0.33$ delimiting the liner, $0.33 < x < 0.38$ for the concrete, $0.38 < x < 0.53$ for the EDZ) and progressively increasing in the COx from 0.5 cm to 20 cm (with $0.53 < x < 4.53$ delimiting the COx domain).

The model of the reference and sensitivity cases of the HLW disposal cell in clay considers three successive periods. The first one (period I) covers the oxic transient stage. Period II starts when the waste packages are present in the cell and the chemical alteration begins for the different materials outside the overpack. Finally, period III starts after the overpack failure and considers glass alteration and the interactions of glass with corrosion products and uncorroded iron.

Only period II is considered in the model of the HLW disposal cell in clay simulated with iCP. Considering the different uncertainties in corrosion rates of the overpack and more generally the effect of all other processes that are not neglected in this program (mechanical, hydraulic gas, microbiology...), the typical duration of this period could be reasonably considered between 5,000 y and 50,000 y. So the final time of simulation is at most 50,000 years with iCP.

4.5 Results of iCP simulations: assessing the influence of thermal and saturation transients on the chemical degradation of concrete materials

The results are described by focusing on the duration of the grout alteration and the mineral sequence, especially on sulphate-containing minerals regarding the effect of the temporary temperature increase. To help recognize the materials in the following illustrations, the results for the liner are identifiable by a light green background, for the concrete a light orange background and for the claystone a light blue background.

4.5.1 Results of the base case with iCP: constant temperature and constant saturation

The results of the base case are first described by identifying the mineralogical degradation sequence induced by the interaction between the COx claystone and the concrete material when considering a concrete thickness of 5 cm (*Figure 4-2*) and 30 cm (*Figure 4-3*).

The illustration on the left of *Figure 4-2* presents the temporal sequence of the alkaline mineral perturbation in the first numerical cell of the CEM I concrete material next to the liner with a uniform and constant temperature of 25°C and full water saturation. From portlandite and CSH 1.6 initially present in the sound material, the diffusion of aqueous elements from the COx claystone progressively makes these minerals dissolving. As a consequence, the CSH phases are progressively decalcified until reaching the CSH 0.8 (the lowest Ca/Si ratio available natively in ThermoChimie v10) after almost 3,000 y. The spatial distribution of this mineral sequence shows that we can also expect a moderate increase of pH in the COx and with a limited extent (blue area, illustration on the right) as also found with HYTEC in Chapter 3. In the concrete zone, the pH progressively decreases from 13.4 to 12.5 when the alkali progressively diffuses in the COx, reaching thus the equilibrated state with portlandite. Once portlandite is dissolved, the pH value results from the equilibrium with the decalcification sequence of CSH and thus varying from 12.1 to 10.7. Finally, the pH reaches values below 9 when no more CSH is present. These mineralogical and pH sequences in the concrete material are very similar to the one simulated with HYTEC in Chapter 3.

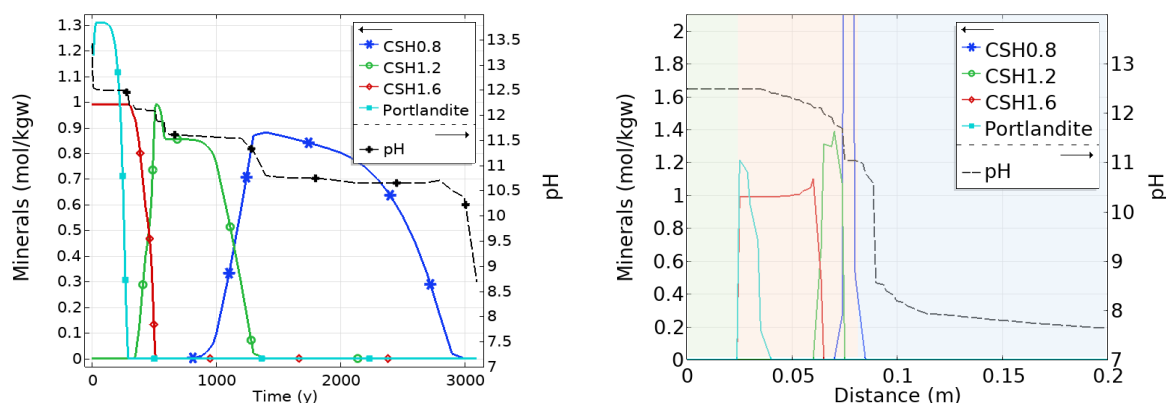


Figure 4-2. Decalcification and pH evolution in the concrete material for the base case simulated with iCP ($T = 25^{\circ}\text{C}$ and full water saturation). Temporal evolution in the first cell next to the liner (left) and spatial profile at $t = 200$ y (right). Concrete thickness = 5 cm.

For a concrete thickness of 30 cm (Figure 4-3), the simulated results show very similar mineral and pH sequences (from Portlandite to CSH 0.8) compared with the results for 5 cm, but the space and time evolution are delayed because of the increased thickness. Thus, CSH 0.8 is not completely dissolved after 50,000 y in the concrete domain with a thickness of 30 cm and the pH is still above 10.5 at that time.

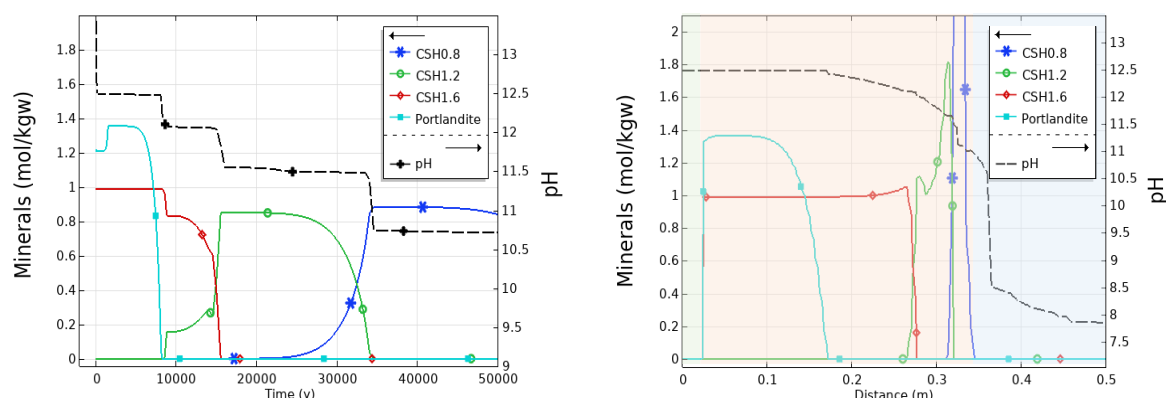


Figure 4-3. Decalcification and pH evolution in the concrete material for the base case simulated with iCP ($T=25^{\circ}\text{C}$ and full water saturation). Temporal evolution in the first cell next to the liner (left) and spatial profile at $t = 3,000$ y (right). Concrete thickness = 30 cm.

Based on this decalcification sequence, two indicators to illustrate the concrete degradation are defined and used for further comparisons:

- The moment at which the portlandite is totally dissolved (degraded state). At that time, the cementitious material becomes significantly altered and it can no longer impose a high pH in the surrounding materials;
- The moment at which the CSH0.8 is the only remaining CSH. At that time, the cementitious material is in an advanced decalcification state.

By considering these two indicators, the concrete material with a thickness of 5 cm (resp. 30 cm) becomes degraded after 300 y (resp. 8,000 y), while the advanced decalcification occurs after 1,300 y (resp. 35,000 y) in this base case. Regarding the first indicator (portlandite), the duration simulated with EURAD (Deliverable n° 2.17) - Integrated reactive transport models for assessing the chemical evolution at the disposal cell scale

iCP is equivalent to the one simulated with Hytec in the same conditions (see Chapter 3), while it is longer with iCP when considering the second indicator (CSH).

The temporal sequence of the other minerals in the concrete material is presented for both thicknesses in Figure 4-4. In both cases, the main Fe-bearing mineral (C3FH6) is soon replaced by magnetite which remains stable for the rest of the simulation. Concerning the Al-bearing minerals, monocarboaluminate is progressively replaced by ettringite which remains present until the final CSH is dissolved. For the Ca-bearing minerals, calcite and saponite-Ca precipitate all along the carbonation of portlandite and CSH (illustrated on Figure 4-2 and Figure 4-3). Advanced degradation is only illustrated with the thickness of 5 cm, in which clinoptilolite-Ca, a zeolite, is transiently stable as well as gypsum. The final stable state is composed of saponite-calcite-gibbsite-hydrotalcite-magnetite.

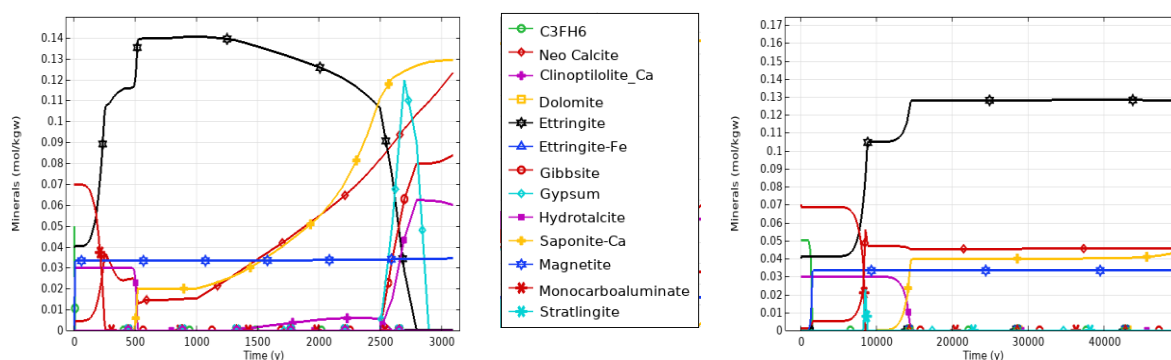


Figure 4-4. Temporal sequence of the other minerals in the first cell of the concrete material next to the liner. Concrete thickness of 5 cm (left) and 30 cm (right) for the base case with iCP.

4.5.2 Consequences of the thermal transient stage on the concrete degradation

This first series of sensitivity analyses intends to assess the consequences of considering a thermal transient state (induced by the heat released by the HL waste) on the mineralogical evolution and the duration of degradation of the cementitious materials. It is shown in Figure 4-5 and Figure 4-6 that the mineral sequence (from Portlandite to CSH 0.8) is equivalent in cases with and without the thermal transient stage and for both thicknesses of concrete. But the transitions happen sooner when considering the thermal transient stage than in the case with a temperature arbitrarily fixed to 25°C.

When the temperature increases up to 90°C the effective diffusion increases but the chemical model also considers the decrease in pH induced by the variation of the ionic water product. In these conditions, the pH reaches values around 10.5 much sooner for a thickness of 5 cm (after only 100 years when considering the thermal transient in comparison with 1,300 y when the temperature increase is disregarded, see Figure 4-5). In the meantime, the CSH 1.6 is also degraded and when the temperature comes back to lower values, no more mineral can impose back higher values of pH.

The overall duration of the decalcification process has also decreased for a thickness of 30 cm but in a minor extent compared to 5 cm (Figure 4-6). In the thicker concrete material, the pH has transiently decreased, but the unaltered fraction of minerals remains higher in this case. Thus, after the thermal transient stage, the pH comes back to values above 12 for several thousands of years.

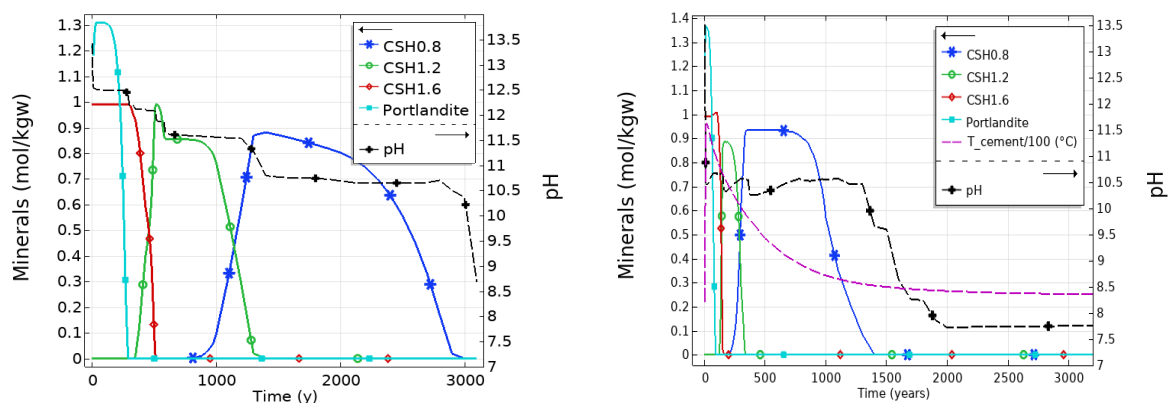


Figure 4-5. Decalcification sequence and pH evolution in the concrete material for the base case (left) and the case considering the thermal transient (right). Concrete thickness = 5 cm.

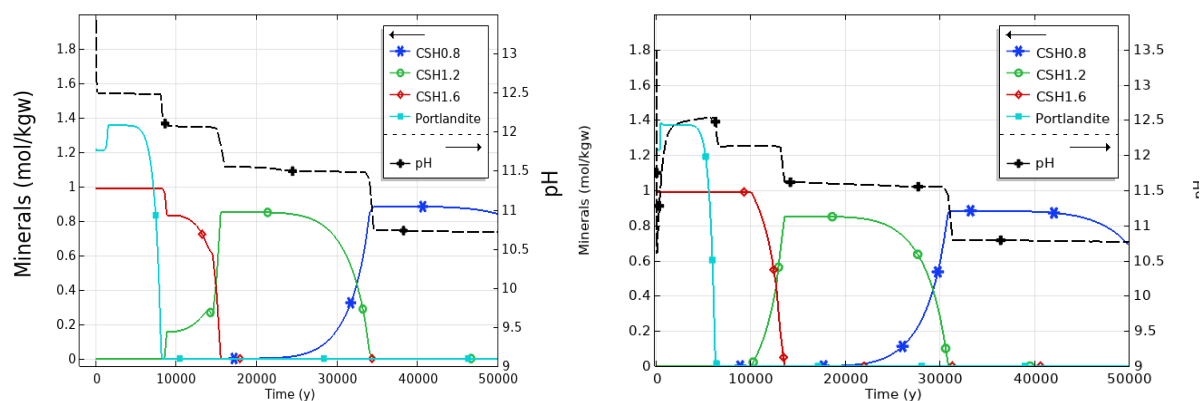


Figure 4-6. Decalcification sequence and pH evolution in the concrete material for the base case (left) and the case considering the thermal transient (right). Concrete thickness = 30 cm.

Table 4-8 compares the quantitative indicators of the concrete degradation with and without the thermal transient. The thermal transient globally speeds up the alteration of the concrete, but the thicker the concrete, the less sensitive it is to this thermal transient stage.

Table 4-8. Comparison of the decalcification duration in the concrete materials by considering or not the thermal transient and for both thicknesses of concrete.

Thickness of concrete	Temperature	Alteration duration, indicator: "total dissolution of Portlandite" (in years)	Alteration duration, indicator: "advanced decalcification (CSH 0.8 remaining)" (in years)
5 cm	Constant (25°C)	300	1,300
	Variable	100 (-67%)	350 (-73%)
30 cm	Constant (25°C)	8,000	35,000
	Variable	6,500 (-19%)	31,000 (-11%)

The thermal transient has also an influence on the stability of (S,Al)-bearing minerals as illustrated by Figure 4-7. Contrary to the case without variation of temperature, ettringite and monocarboaluminate are progressively dissolved when increasing the temperature. Consequently, monosulfoaluminate precipitates as it has already been described by Cloet et al. (2018). Once the temperature has decreased back, secondary ettringite precipitates and remains stable until the last CSH remains also stable. Finally, gibbsite is the final Al-bearing mineral which remains stable in the degraded concrete and the total dissolved sulphate concentration increases since no more mineral appears to control its solubility with these simulation results. Similar results and analyses concerning the Al and S bearing minerals with a 30 cm thick concrete (not illustrated).

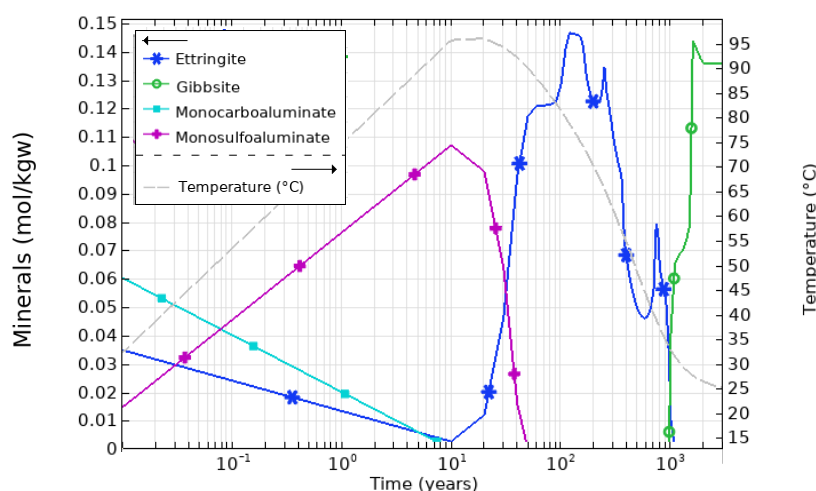


Figure 4-7. Temporal evolution of (S,Al)-bearing minerals during the thermal transient in the concrete material. Concrete thickness = 5 cm.

4.5.3 Consequences of the thermal and partial desaturation transients

In this sensitivity study, the thermal transient (induced by the heat released by the HL waste) and the partial desaturation of the porous materials (induced by gas pressure increase) are considered together and compared with the base case.

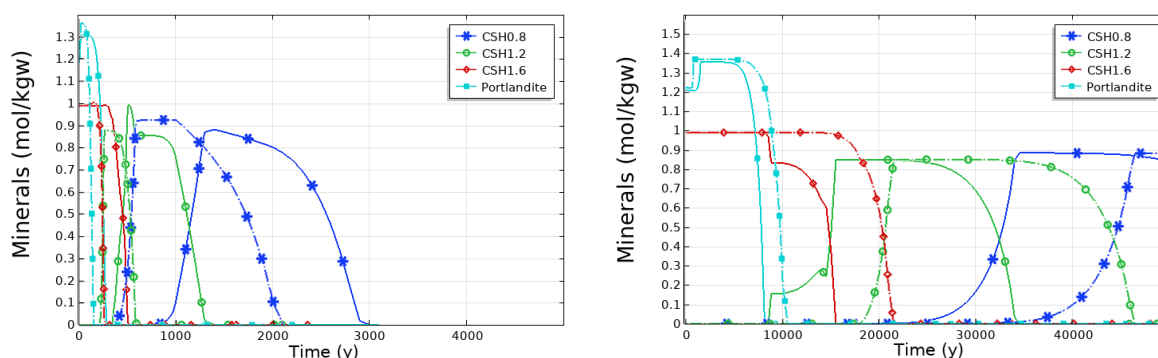


Figure 4-8. Comparison of the decalcification sequences between the base case (full line) and the case considering both the thermal transient and the partial desaturation (dotted line). Temporal evolution in the first cell next to the liner for concrete thicknesses of 5 cm (left) and 30 cm (right).

For a thickness of 5 cm, the fact to consider both transient phenomena contributes to a global speed up of the decalcification process, even if the desaturation tends to decrease the effective diffusion in this simulation (left scheme of *Figure 4-8*). Whereas for a thickness of 30 cm of concrete (right scheme of the *Figure 4-8*), the thermal transient stage is too short in comparison to the mineral sequence and the influence of the desaturation tends globally to slow down the decalcification sequence.

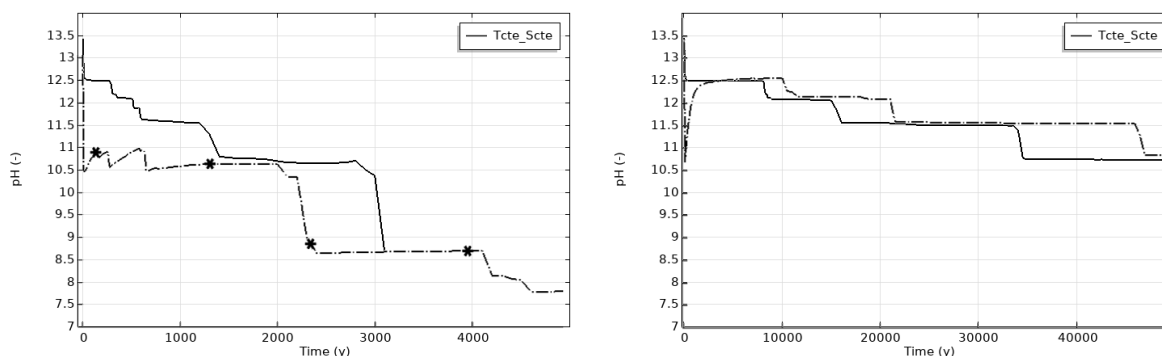


Figure 4-9. Comparison of the pH evolution between the base case (full line) and the case considering both the thermal transient and the partial desaturation (dotted line). Temporal evolution in the first cell next to the liner for concrete thicknesses of 5 cm (left) and 30 cm (right).

This contradictory behaviour between both thicknesses is also highlighted by the pH evolution (*Figure 4-9*). While for low thicknesses of concrete, when considering both transient processes (thermal and water desaturation), it tends to reach lower pH from early stage and keep it low thanks to quite early degradation of the concrete. By considering thicker concrete, there is only a short and early decrease of the pH but the thickness tends to diminish the effects of the thermal transient on the pH on the long term.

Table 4-9. Comparison of the decalcification duration in the concrete materials by considering or not the thermal transient and the partial desaturation for both thicknesses of concrete.

Thickness of concrete	Temperature and Water Saturation	Alteration duration, indicator: "total dissolution of Portlandite" (in years)	Alteration duration, indicator: "advanced decalcification (CSH 0.8 remaining)" (in years)
5 cm	25°C and fully water saturated	300	1,300
	Variable temperature and partial saturation	150 (-50%)	580 (-55%)
30 cm	25°C and fully water saturated	8,000	35,000
	Variable temperature and partial saturation	10,250 (+28%)	46,000 (+31%)

Table 4-9 compares the quantitative indicators of the concrete degradation with and without both transients. Considering both thermal transient stage and partial desaturation globally speeds up the degradation with a factor around 50 % for a 5 cm thick concrete. But the conclusion is the opposite for a 30 cm thick concrete, since it tends to slow down its decalcification process with a factor around 30%.

4.6 Conclusions and implications for the modelling of the full HLW cell in clay

The transient thermal and hydric stages have been investigated with the reactive transport code iCP on a subsystem consisting of magnetite (corroded steel) – CEM I concrete buffer – CO_x rock. The focus has been put on the durability of the cementitious buffer. The properties of the multi-barrier components were very close to those considered in Chapter 3. A main difference was that thermodynamic equilibrium was considered for all the chemical reactions using the ThermoChimie database without any kinetic constraints.

In a preliminary step, the modelling results of the base case (30 cm thick buffer) at a constant temperature and constant saturation were close to those calculated with HYTEC in Chapter 3, especially the duration required for the full depletion of portlandite and for the pH evolution with the degree of the cement hydrate decalcification.

The evolution of temperature in space and time modified the effective diffusion coefficient and the solubility of the minerals for about 1,000 years. In that case (and under water-saturated conditions), temperature increase significantly reduced the lifetime for the lowest thickness and did have a moderate effect in the other case. For the 5 cm thickness, the complete portlandite dissolution occurred faster compared to the case with a constant temperature at 25°C (100 y compared to 300 y). The thermal transient stage has also an influence on the stability of (S,Al)-bearing minerals. Ettringite and monocarboaluminate are progressively dissolved when increasing the temperature to form monosulfoaluminates. Once the temperature decreases back, secondary ettringite precipitates.

The partial water saturation modified the effective diffusion coefficients according to a Millington and Quirk type model. The influence of the desaturation tends globally to slow down the decalcification sequence which is opposite to the effect of temperature change. Considering both transient phenomena contributes to a global speed up of the decalcification process for the case with concrete thickness of 5 cm.

All in all, these iCP calculations demonstrated that neglecting the thermal and hydric transient stages in the HYTEC modelling of Chapter 3 was a reasonable approximation for the 30 – 100 cm buffer thickness but should be considered for the 5 cm case.

5. Modelling of a full ILW disposal cell in clay

The work has been done by Vanessa Montoya (SCK CEN) and Jaime Garibay-Rodriguez (UFZ).

In this section, the results of the ILW disposal cell in clay are presented. The conceptual, mathematical and numerical model were described in detail in Samper et al. (2022). Very briefly, the disposal concept studied here is based on a generic multi-barrier system including the waste matrix, the disposal container, the mortar backfill in the emplacement tunnel (where the disposal containers are located) and the clay host rock. It is assumed that the disposal cell (~ 200 m long) is part of a repository at a depth between 200 and 800 m below the surface in clay (see Figure 5-1 for the cross section of the schematic representation of the generic disposal cell).

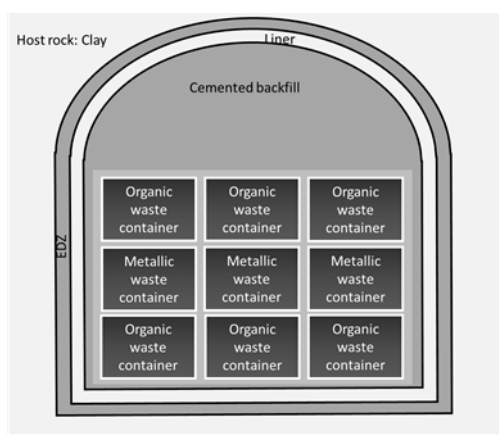


Figure 5-1. – Schematic representations of the generic disposal cell considered for intermediate radioactive waste in clay.

Several simulation cases were carried out under different assumptions, specially related to the saturation of the domain, the final goal was to have a 2D model of the system representing a more realistic geometry, but in order to arrive to this reference case, several 1D cases were run in order to test the capabilities of the code with less computational time. The 1D domain is vertically oriented started from a container wall at the middle of the top waste package up to several meters in the host rock at the right (Figure 5-2). All these cases are listed in Table 10. Please note that in Samper et al. (2022) several sensitivity cases were proposed with increasing chemical complexity: 1) Aqueous complexation + mineral dissolution/precipitation 2) Aqueous complexation + cation exchange + mineral dissolution/precipitation 3) Aqueous complexation + cation exchange + mineral dissolution/precipitation + redox processes 4) Aqueous complexation + cation exchange + mineral dissolution/precipitation + redox processes + porosity diffusion feedback. In this deliverable, we only present results with the most complex chemistry (i.e., aqueous complexation + cation exchange + mineral dissolution/precipitation + redox processes).

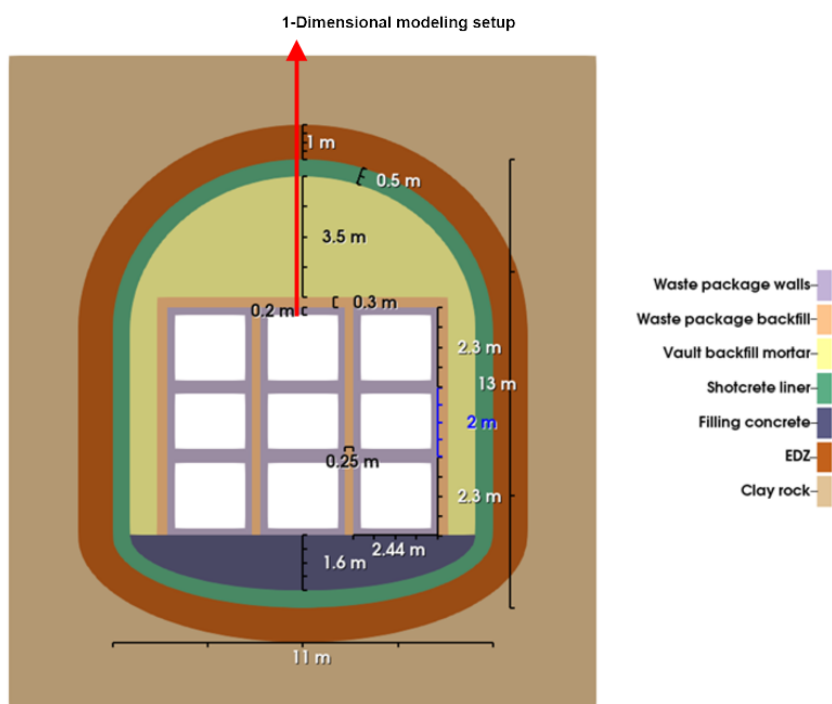


Figure 5-2. Location of the 1D model

The first case (1a) assumes full saturation in the whole domain. In our approach, this means that this case models the most pronounced interaction in the system because the effective diffusion coefficients are the largest. Case 1b, and 1c, are addressed to consider a degree of unsaturation in the system, which is known to happen in this type of system, mainly due to gas generation (Leupin et al. (2016)). However, a simplified approach has been chosen to incorporate the effect of unsaturation. The undersaturated conditions have been modelled by estimating the initial effective diffusion coefficients with the following relationship:

$$D_{eff} = S\phi D_p \quad [5.1]$$

where D_{eff} is the effective diffusion coefficient [m^2/s], S is the saturation degree [-], ϕ is the porosity, and D_p is the pore diffusion coefficient [m^2/s] accounting for tortuosity and connectivity effects which is kept constant. Therefore, in cases 1b and 1c, $S = 0.5$ and 0.1 , respectively.

In case 1d, the system (under fully water-saturated conditions) is simulated without considering the effect of the feedback between the porosity and the mineral dissolution/precipitation reactions. Finally, case 2 shows an up-scaled version of case 1a to a complex 2-D setup. Some simplifications in the spatio-temporal resolution have been made in this case to attain feasible computational costs.

Table 10. Simulation cases for the ILW disposal cell in clay.

Case	Dimension	Description
1a	1	Fully water-saturated porous media.

1b	1	50% uniform saturation (modelled with effective diffusion coefficients).
1c	1	10% uniform saturation.
1d	1	No porosity/clogging feedback.
2	2	Fully water-saturated porous media.

5.1 Simulation in one dimension

5.1.1 Model discretization

The discretization of the 1D models (case 1a, 1b, 1c, 1d) presented in the following sections corresponds to a 1D mesh of 217 linear elements with varying lengths according to the material in the engineered barrier system (EBS) and the interfaces. The mesh discretization is chosen as a compromise between accuracy and computational cost. The configuration of the EBS materials is shown in Figure 5-3. The container wall and the zone with the waste package backfill are discretized with uniform length elements of 0.02 m. The vault backfill uses a non-uniform discretization with the following sequence: $25 \times 0.02 \text{ m} + 15 \times 0.04 + 13 \times 0.1 + 15 \times 0.04 + 25 \times 0.02 = 3.5 \text{ m}$. The liner is discretized again with uniform elements of 0.02 cm. The EDZ uses the following sequence: $6 \times 0.02 \text{ m} + 22 \times 0.04 \text{ m} = 1 \text{ m}$. Finally, the COx domain (host rock) uses the following sequence: $15 \times 0.04 \text{ m} + 10 \times 0.1 \text{ m} + 10 \times 0.5 \text{ m} + 1 \times 0.9 \text{ m} + 10 \times 1 \text{ m} + 1 \times 2.5 \text{ m} = 20 \text{ m}$. Please note that in Samper et al. (2022), we initially selected a domain of 40 m for the host rock in order not to have any artefact in the results due to the boundary condition selected, after some preliminary runs, we realised that due to the slow transport processes (i.e. only diffusion), it is not needed to consider a big domain for the host rock and 20 m is enough not to see any artefact due to the boundary condition selected.

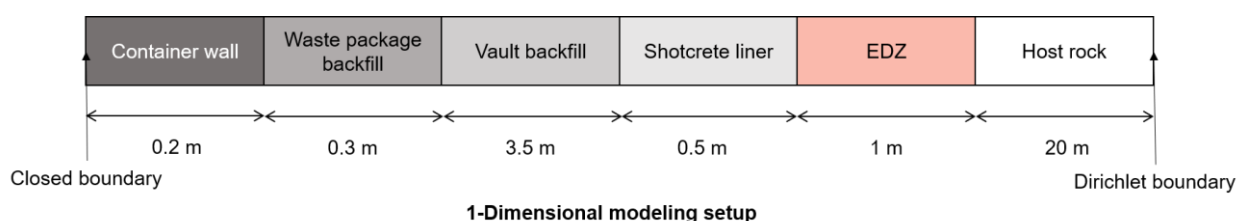


Figure 5-3. 1D configuration of the EBS materials and the host rock for the ILW cell in clay.

Time discretization is also chosen as a compromise between computational cost and accuracy. A non-uniform time-stepping scheme was adopted with the following sequence: $3000 \times 1 \text{ year} + 1000 \times 2 \text{ years} + 1000 \times 3 \text{ years} + 1000 \times 4 \text{ years} + 1000 \times 8 \text{ years} + 8000 \times 10 \text{ years} = 1\text{e}5 \text{ years}$. This is because following extremely small time steps under the von Neumann criterion would ($< 0.1 \text{ y}$) would be computationally costly, considering the long-time horizons required for the assessment ($1\text{e}5 \text{ years}$). Therefore, the results may not capture processes that can only be observed when using an extremely fine time-discretization (e.g., porosity clogging).

The 1D models have been solved using OpenGeoSys-6, with a single Intel(R) Xeon(R) Gold 6148 CPU with only one core @ 2.40GHz. The total simulation time for the 1D cases is 8 hrs. on average.

5.1.2 Case 1a: fully-water saturated media

In Figure 5-4, the mineral changes after 100 000 years are shown. The volume fractions are plotted against the length of the 1-D domain, emphasizing the locations of the interfaces of the different materials in the multi-barrier system. Furthermore, the pH profile of the disposal cell in contact with the clay is shown. The corresponding volume fractions are affected by the mineral dissolution/precipitation reactions in the system. Note that additional volume fractions of inert materials are also present in the system in the form of cement aggregates (sand) in the cement-based materials and clay minerals in the clay domain.

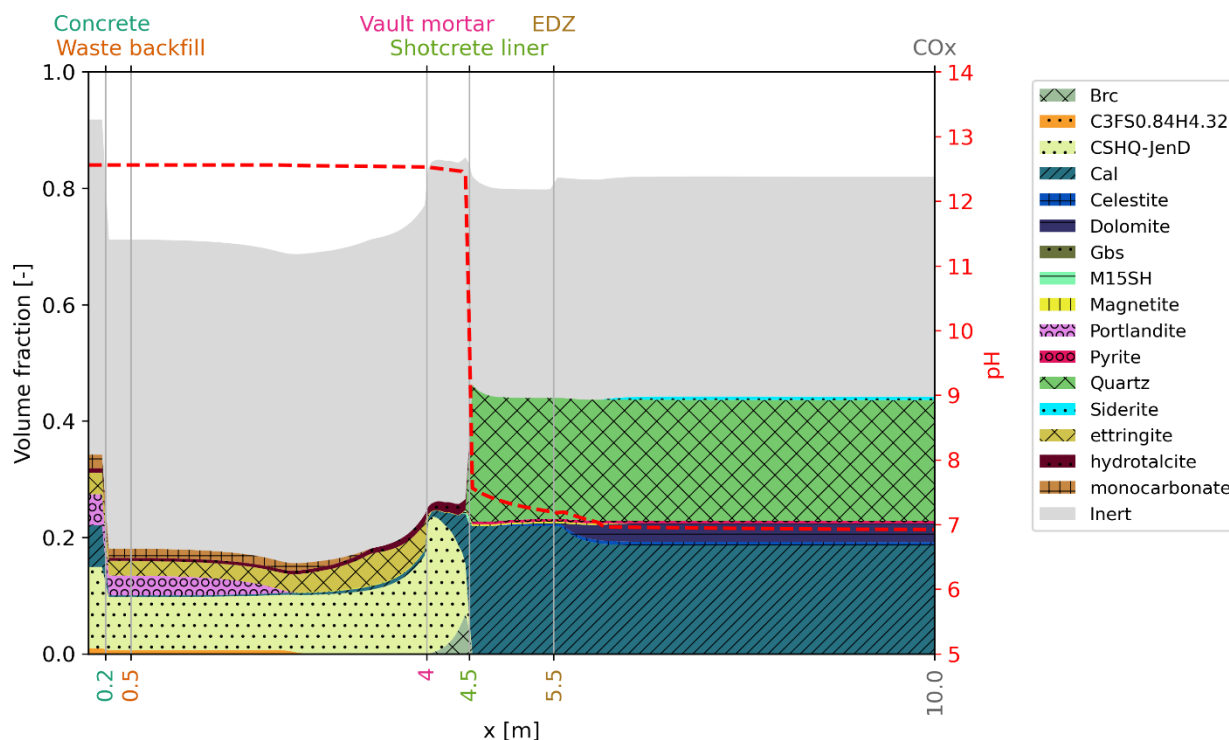


Figure 5-4. Mineral changes at 100,000 years of the ILW disposal cell in clay assuming full-water saturation (Case 1a).

The most relevant process happening is the interaction between the alkaline porewater in the cement materials and the clay porewater. This causes several changes at the interface in the cement materials, as well as the clay side. A summary of the relevant changes in the system is listed as follows:

- C-S-H phases: initially, there are two C-S-H phases with different Ca/Si ratios in the cement-based materials. CSHQ-JenD in the concrete walls and mortar (Ca/Si = 1.5) and CSHQ-TobH in the shotcrete liner (Ca/Si = 0.66). Both phases are allowed to dissolve/precipitate in the system. The main alteration occurring related to the C-S-H phases is in the liner, which is in direct contact with the clay porewater. The dissolution of the CSH-TobH mineral in the liner starts immediately until it dissolves completely at around 50,000 years. However, the CSHQ-JenD mineral in the mortar, which is in contact with the liner, precipitates in the mortar as well as through the liner until it partially replaces the CSH-TobD mineral.
- Portlandite is only found in the mortar and the concrete walls (not the liner). The portlandite in the concrete container walls remains unaffected since the reaction front does not reach that subdomain, even after 100,000 years. However, complete dissolution of portlandite occurs up to 1.6 m towards the inside of the disposal cell (from right to left in Figure 5-4). Partial dissolution of portlandite in the rest of the mortar domain (0.2 – 4 m) occurs. This causes an increase in the pore space (2.5 %) in the mortar subdomain from 0.2 to around 3.3 m.
- Calcite precipitation occurs at the cement-clay interface from the beginning of the simulation. In the cement domain, calcite precipitation extends up to 2.5 m toward the disposal cell from the

cement-clay interface (4.5 to 2 m from right to left in Figure 5-4). Calcite also precipitates in the clay to around 2 m from the interface from left to right toward the host rock.

- Other cement minerals, such as ettringite, straetlingite, hydrotalcite, monocarbonate, CSFH, and ferrihydrite (FeOOHmic) show a complex behaviour produced by the interaction with the clay porewater and with each of the cement-based materials. Ettringite dissolves completely in the liner during the first 33,000 years. In the mortar domain, ettringite precipitates during the 100,000 years. This, along with C-S-H precipitation, compensates for the dissolution of portlandite, keeping the porosity above 29% (the initial porosity of the vault mortar). Minerals, such as ferrihydrite and straetlingite dissolve completely very early in the simulation (~100 years). CSFH (C3FS0.84H4.32) follows a similar dissolution path to portlandite. Monocarbonate completely dissolves at around 0.65 m from the vault mortar interface.
- In the clay domain (including the EDZ), the main alteration is the precipitation of calcite, as mentioned. However, the pore space alteration is not significantly affected because the calcite precipitation is offset by the dissolution of other minerals in the clay, such as dolomite and celestite. Quartz also precipitates in the clay up to around 1 m from the interface with the liner. Recall that quartz is modelled with thermodynamic dissolution/precipitation reactions. Magnetite precipitates in small quantities in the clay up to 7 m (2.5 m from the cement-clay interface). Further, pyrite also precipitates at around that length in the clay. Siderite completely dissolves to around 6 m (1.5 m from the cement-clay interface).
- The pH alteration in the clay caused by the alkaline plume of the cement materials porewater extends to around 6 m (1.5 m from the interface). However, the alteration is not pronounced; the pH exactly at 4.5 m is around 7.6. On cement-based materials, the pH stabilizes at around 12.5 after 50,000 years.

5.1.3 Case 1b: 50% water saturation

In Figure 5-5, a second case by assuming in a simplified way 50% saturation conditions in the system is shown. A gas phase was not included in the model. Due to the lower diffusivity in the system, the extension of the left (toward the disposal cell) and right (toward the host rock) are less pronounced than in the fully-water saturated case. For instance, the precipitation of calcite in the clay does not exceed 1 m from the interface. In the fully-saturated case, precipitation was observed up to 2 m from the cement-clay interface. On the vault mortar, portlandite and CSFH dissolution are also less pronounced than in the fully-saturated scenario. In the fully-saturated case, these minerals dissolve around a length of 1 m. Important differences also occur at the liner. It can be observed that the precipitation of MSH is more pronounced in this case; in the fully-saturated case, there is only a small amount of MSH right at the cement-clay interface. On the other hand, the pH profile between these two cases remains almost the same. Furthermore, the smaller amounts of CSH and calcite precipitated at the interface resulted in a slightly larger porosity.

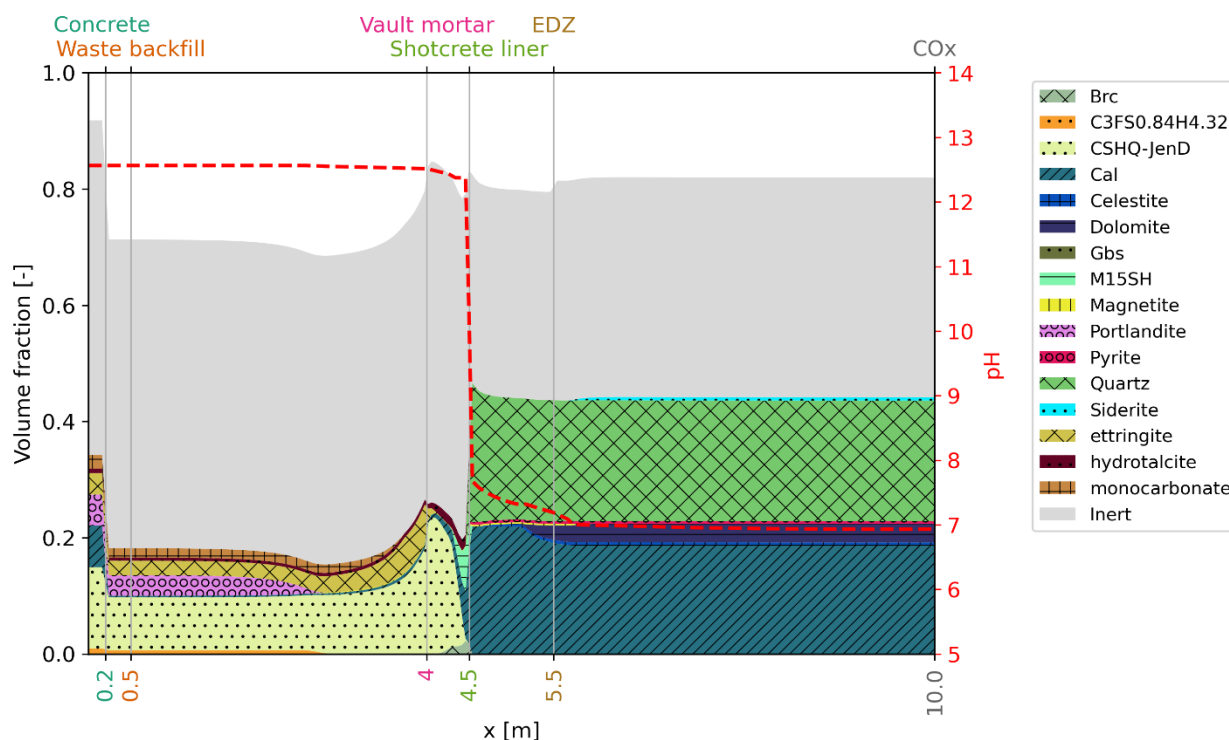


Figure 5-5. Mineral changes at 100 000 years of the ILW disposal cell in clay assuming simplified 50 % saturation conditions in the system.

5.1.4 Case 1c: 10% saturation

In Figure 5-6, a third case considering a very low saturation degree (10%) is shown. The effect of the saturation is modeled with the same procedure as in the previous case. In this case, the interactions become much slower due to a decrease of one order of magnitude of the effective diffusion coefficients. This effect causes a significant reduction in the alteration of the vault mortar. Portlandite only dissolved to around 0.7 m from the mortar-liner interface. From around 3.3 m to the inner part of the cell, there is practically no alteration produced due to the very low diffusivity. In the liner, as expected, the precipitation of calcite only occurs in small amounts. It can also be observed that the CSHQ-TobH, the CSH phase present initially in the liner, is still present after 100,000 years. Recall that in both the fully saturated and 50% saturated cases, this phase completely dissolves. On the other hand, the precipitation length of calcite in the clay only extends up to 0.5 m. The pH alteration is also slightly less pronounced in the clay, extending significantly about 0.6 m from the cement-clay interface. This shows that a very low degree of saturation would result in a less altered system.

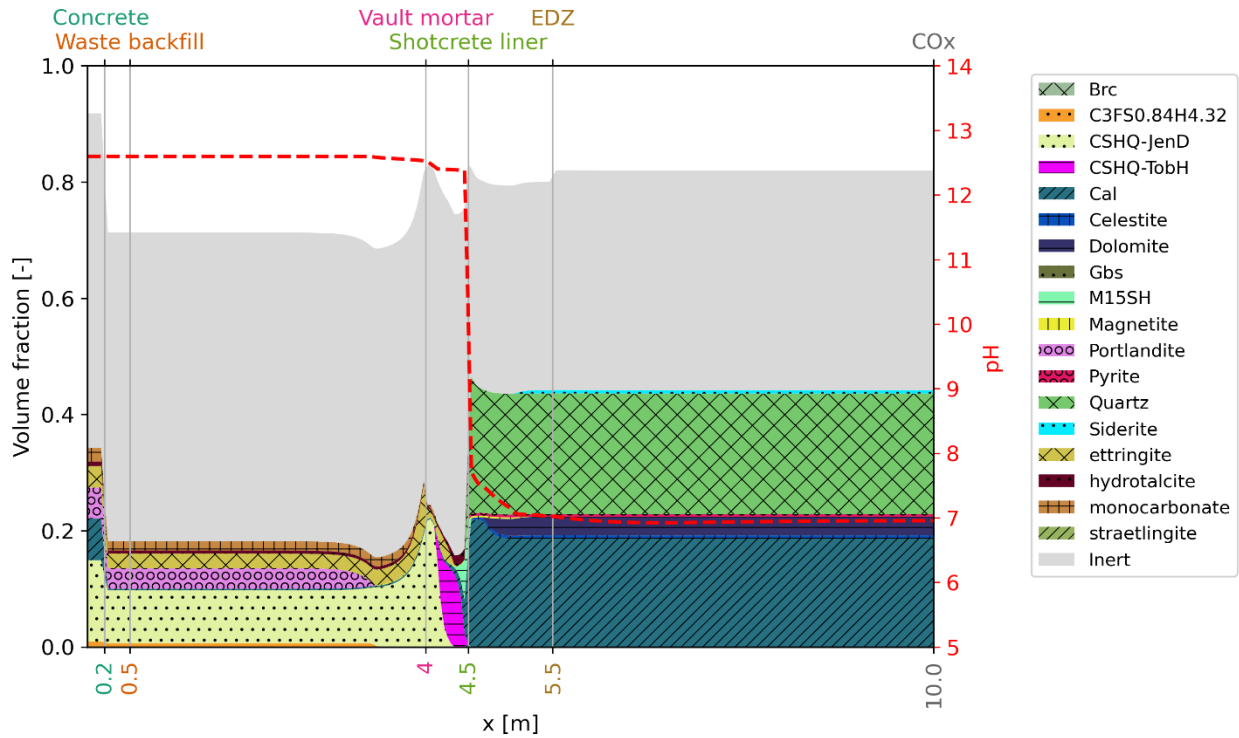


Figure 5-6. Mineral changes of the ILW in contact with clay after 100 000 years assuming 10% water saturation.

Finally, Figure 5-7 shows a comparison of the obtained porosity profiles at 100 000 years amongst the full, 50%, and 10% water saturation cases. An increasing degree of cement degradation is observed from the 10%, to the 50% and the full-saturation cases. On the other hand, however, the alteration in the clay is not significantly different in each case because, as mentioned, the calcite precipitation is offset by the dissolution of dolomite/siderite/celestite minerals. However, the precipitation of calcite in the liner does have a significant influence on the porosity profiles of the different cases, as evident.

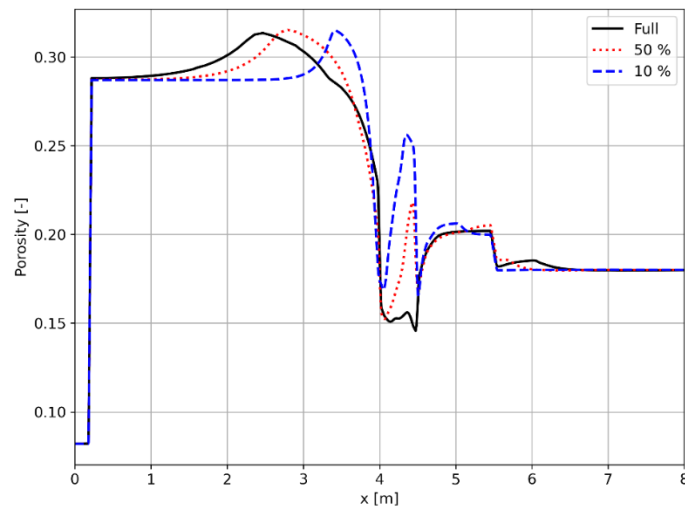


Figure 5-7. Comparison of final porosity profiles of the ILW in clay of the full, 50%, and 10% water saturation cases.

5.1.5 Case 1d: constant porosity

An additional case is presented where there is no feedback between the porosity and the mineral changes due to the dissolution/precipitation reactions. This case is solved assuming full-water saturation in the media (no effect on the effective diffusion coefficients). The results are shown in Figure 5-8. It can be observed that the results do not differ significantly from the ones presented in Figure 5-4 because the system does not become fully clogged even after 100,000 years. Recall that some minerals, like zeolites, that could precipitate in the clay domain causing clogging of the system, have been left out of the simulation. Furthermore, it is known that the chosen discretization plays a significant role in the speed of clogging in these types of systems.

In this case, not considering changes in porosity (and, in turn, on the effective diffusion coefficients) show small differences at the cement-clay interface, such as that the M-S-H phase completely dissolves after it stops precipitating at around 25,000 years. Furthermore, the calcite precipitation extends slightly towards the clay domain when not considering the feedback on porosity, a result of the increased diffusion (see Figure 5-9).

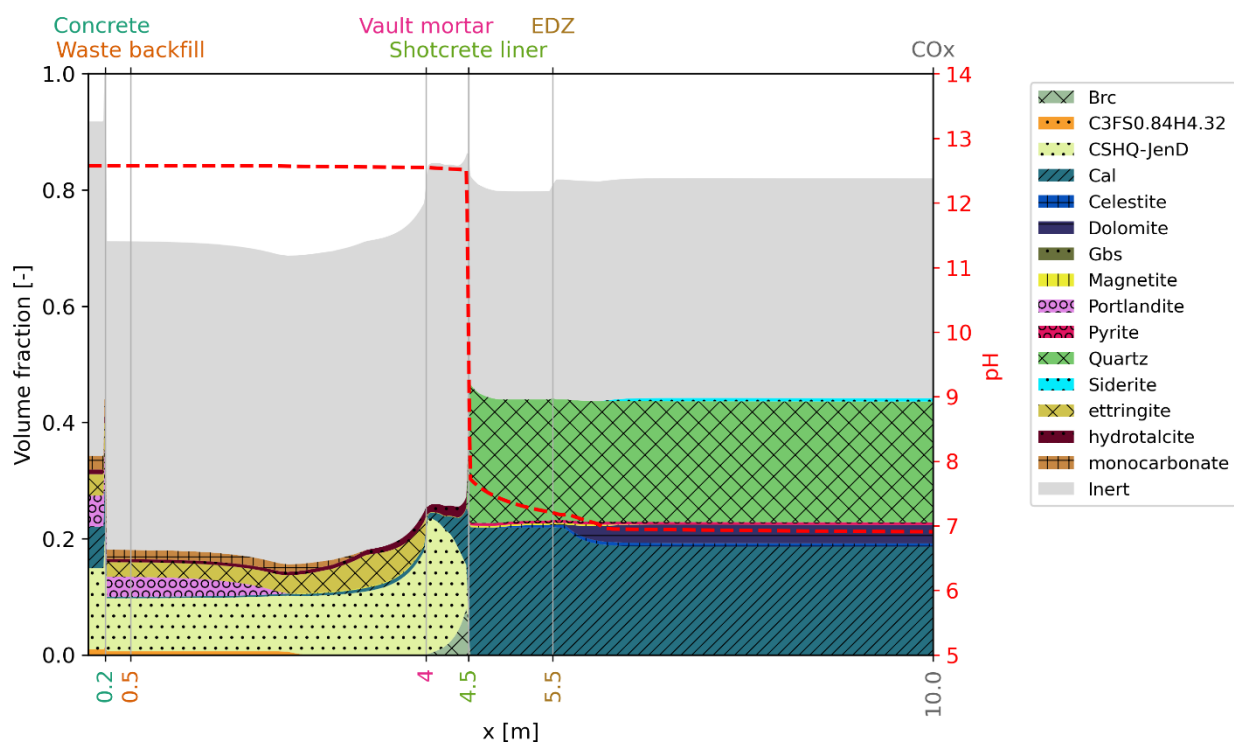


Figure 5-8. Mineral changes at 100,000 years for the ILW disposal cell in clay without considering feedback between the chemical reactions and the porosity.

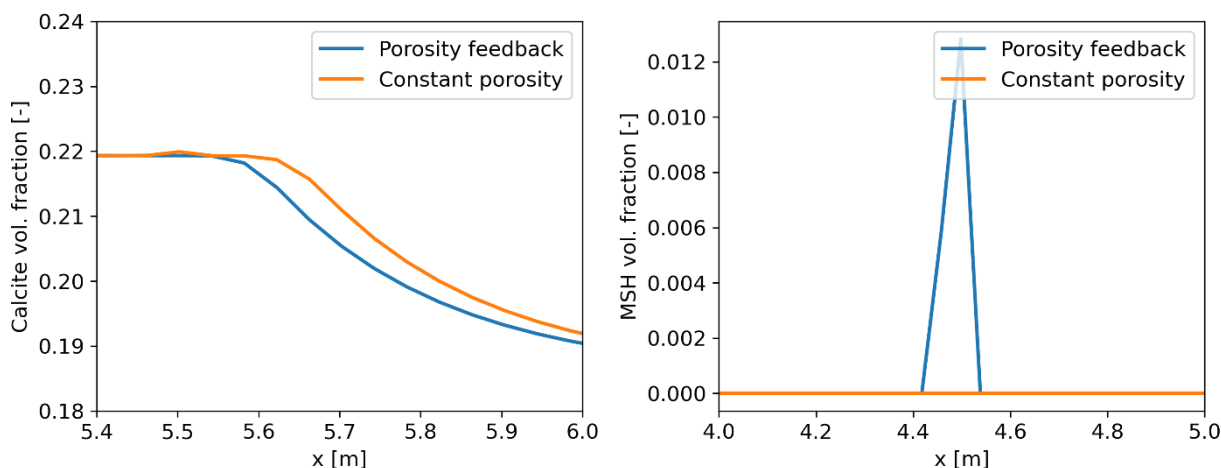


Figure 5-9. Comparison of the reactions of calcite and M-S-H between enabling porosity feedback and constant porosity for the ILW disposal cell in clay.

5.2 Simulations in two-dimensions

In this section, an upscaled version of the 1D model discussed so far is presented. Note, however, that due to computational cost, the chosen space-time discretization has been adjusted to attain reasonable computational times. The 2D mesh discretization is shown in Figure 5-10, where each colour corresponds to a different material. Note that, for simplicity, the inside of the waste packages (red) has been set with an equal composition and properties as the vault mortar. In addition, symmetry is assumed in the Y-plane to cut in half the computational cost. Special care has been put to the liner-clay interface, where refinement has been applied to mitigate numerical oscillations due to the large concentration gradient. The complete domain of the clay is shown on the right-hand side of Figure 5-10, whereas the zoomed-in portion of the disposal cell is shown on the left-hand side. The large clay domain is chosen to neglect the effect of the boundaries on the disposal cell. However, much larger mesh elements are chosen at the outer boundaries because it is expected that at this part of the domain not many changes will occur. The main processes, as shown in the 1D case, are expected to occur at the liner-clay and vault mortar-liner interfaces. The 2D unstructured mesh consists of 9789 mesh cells, which have been chosen as quadrilateral elements to reduce the computational cost.

Time discretization is also chosen as a compromise between accuracy and computational cost. In this case, fewer time steps are simulated to cover the time horizon of $1e5$ years. The time steps are in the following sequence: 100×10 years + 100×20 years + 100×40 years + 930×100 years. As mentioned for the 1D case, this discretization may not be able to capture finer processes happening at the interfaces (e.g., pore-clogging), however, to capture these processes, a much larger quantity of time steps may be needed, posing a tremendous computational cost, which could only be managed by HPC.

The 2D model has been solved using OpenGeoSys-6, with a CPU time on a single, Intel(R) Xeon(R) Gold 6148 CPU with only one core @ 2.40GHz of 230 hrs.

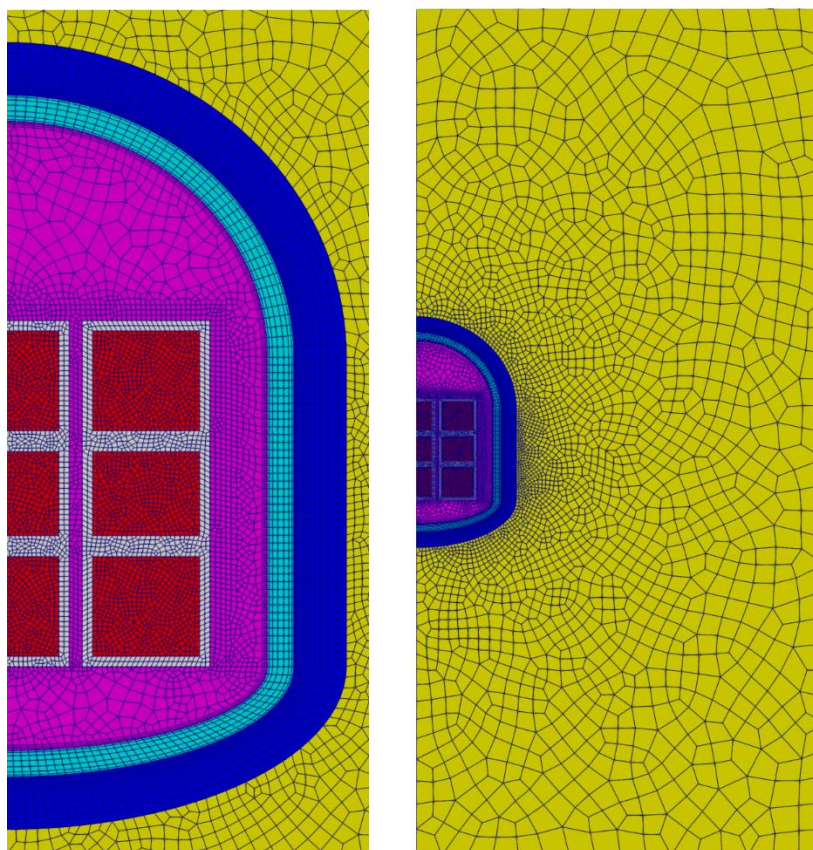


Figure 5-10. Mesh discretization of the 2D ILW disposal cell in clay.

The evolution of the volume fraction of calcite precipitation at the liner-clay interface is shown in Figure 5-11. Calcite precipitates up to around 1 m from the liner-clay interface, with a small amount of precipitate also on the liner side of the interface. Because of the difference in the space-time discretization between the 1D and 2D models, the amounts and length of alteration have some differences. However, they show a similar trend that captures the overall behaviour, as shown in Figure 5-18. In the case of calcite, as shown, there is no complex, space-dependent pattern in the evolution, i.e., the precipitation occurs to more or less the same degree around the 2D cell. This is also the case with another mineral in the clay domain, dolomite, as shown in Figure 5-12. The dissolution of dolomite shows the alteration length of the clay domain, up to 2 m from the liner-clay interface around the entire cell.

On the other hand, the dissolution of portlandite in the vault mortar does show a space-dependent pattern in the cell, as shown in Figure 5-13. This is an obvious effect of the geometry of the 2D cell, where there is a much larger quantity of portlandite at the top of the cell than at the sides. Portlandite dissolves significantly in the vault mortar, whereas only partial dissolution occurs in the concrete walls, mainly at the sides and the bottom of the cell, not at the top. The amount of portlandite inside the waste packages remains practically the same throughout the entire time frame.

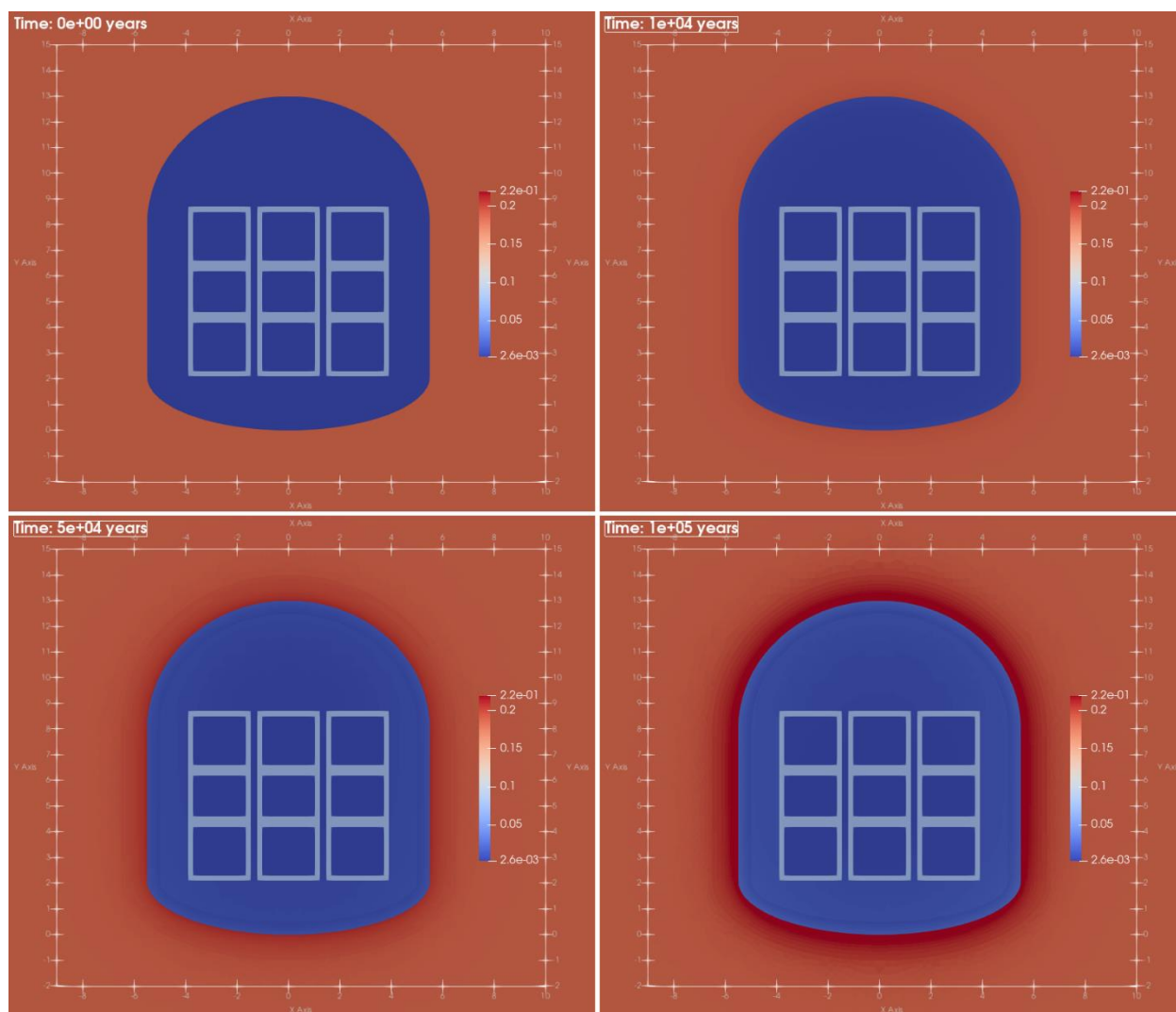


Figure 5-11. Illustration of the evolution of the volume fraction of calcite in the 2D ILW cell in clay.

In cement-based materials, the evolution of the CSHQ-JenD phase is shown in Figure 5-14. This phase shows a less pronounced precipitation pattern than in the 1D case (see Figure 5-18). This shows the influence of the finer resolution of the 1D case, where it is possible to capture a more nuanced pattern of CSH precipitation. In this case, however, it is possible to observe a space-dependent behaviour. The CSHQ-JenD phase precipitates in slightly larger amounts at the sides than at the top of the cell after 1e5 years.

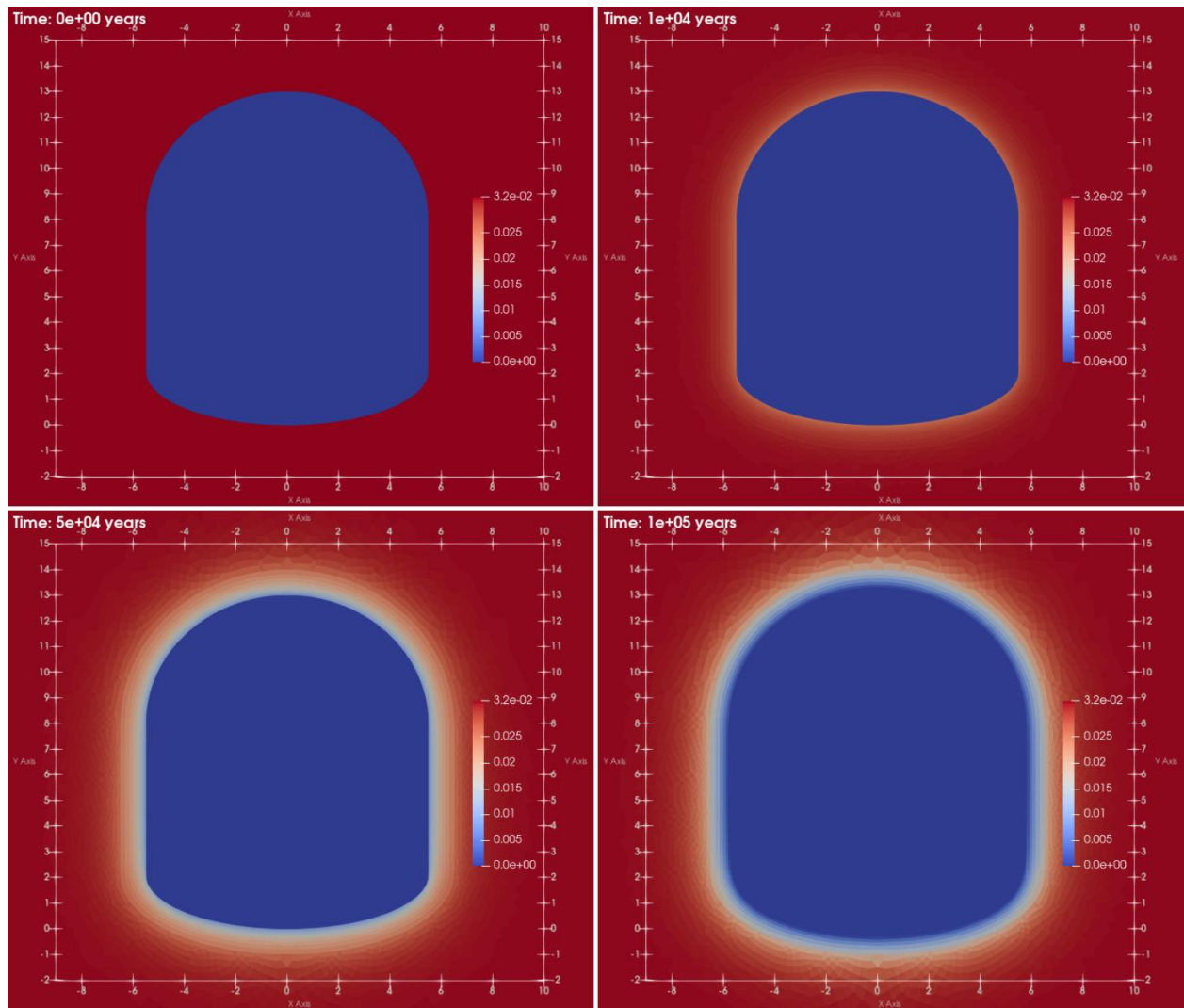


Figure 5-12. Dolomite volume fraction evolution in the 2D ILW cell in clay.

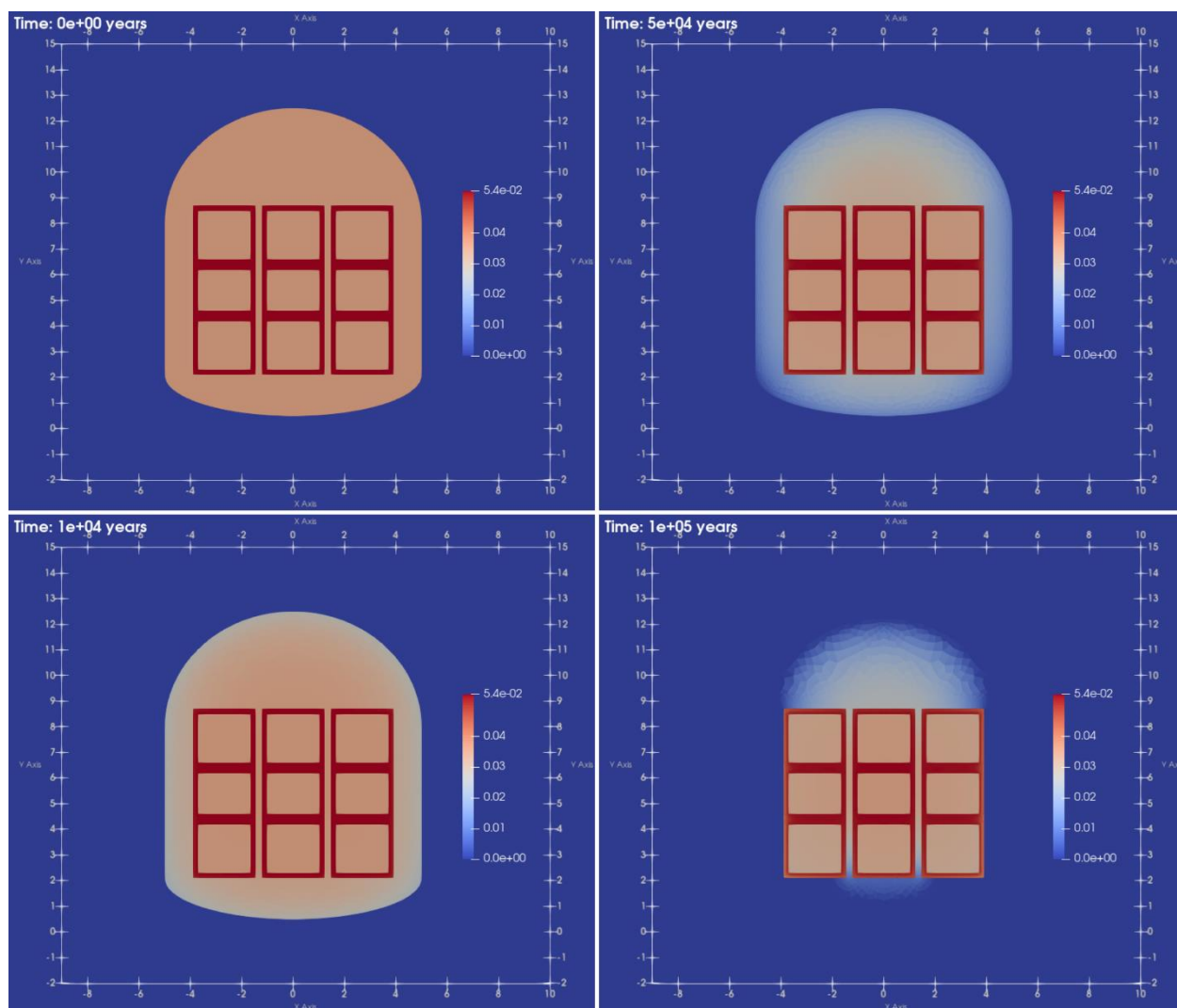


Figure 5-13. Evolution of the portlandite volume fraction in the 2D ILW cell in clay.

In Figure 5-15, the volume fraction evolution of ettringite is shown. As discussed previously, ettringite is an important mineral when measuring the degree of cement materials degradation, mainly caused by the diffusion of S(6) from the clay porewater. The dissolution/precipitation of ettringite in the 2D cell shows a strong space-dependency, which highlights the advantages of modeling the system in two dimensions. At $1e4$ years, ettringite is more or less uniformly distributed around the disposal cell, with dissolution at the liner-clay and precipitation at the vault mortar-liner interfaces, respectively. At $5e4$ years, there are significant differences in the volume fraction of ettringite inside the disposal cell. The precipitate is larger at the side walls in the vault mortar, where it follows a band of around 0.5 meters through the top arc of the cell. However, a large proportion of the top side of the vault shows a lower amount of ettringite precipitate. Finally, at $1e5$ years, ettringite shows precipitation over the entire domain, with larger quantities at the bottom, even reaching the lower corners of the concrete walls in the bottom waste packages. Also at $1e5$ years, a slight dissolution front of ettringite in the lower rounded corners of around the disposal cell can be observed.

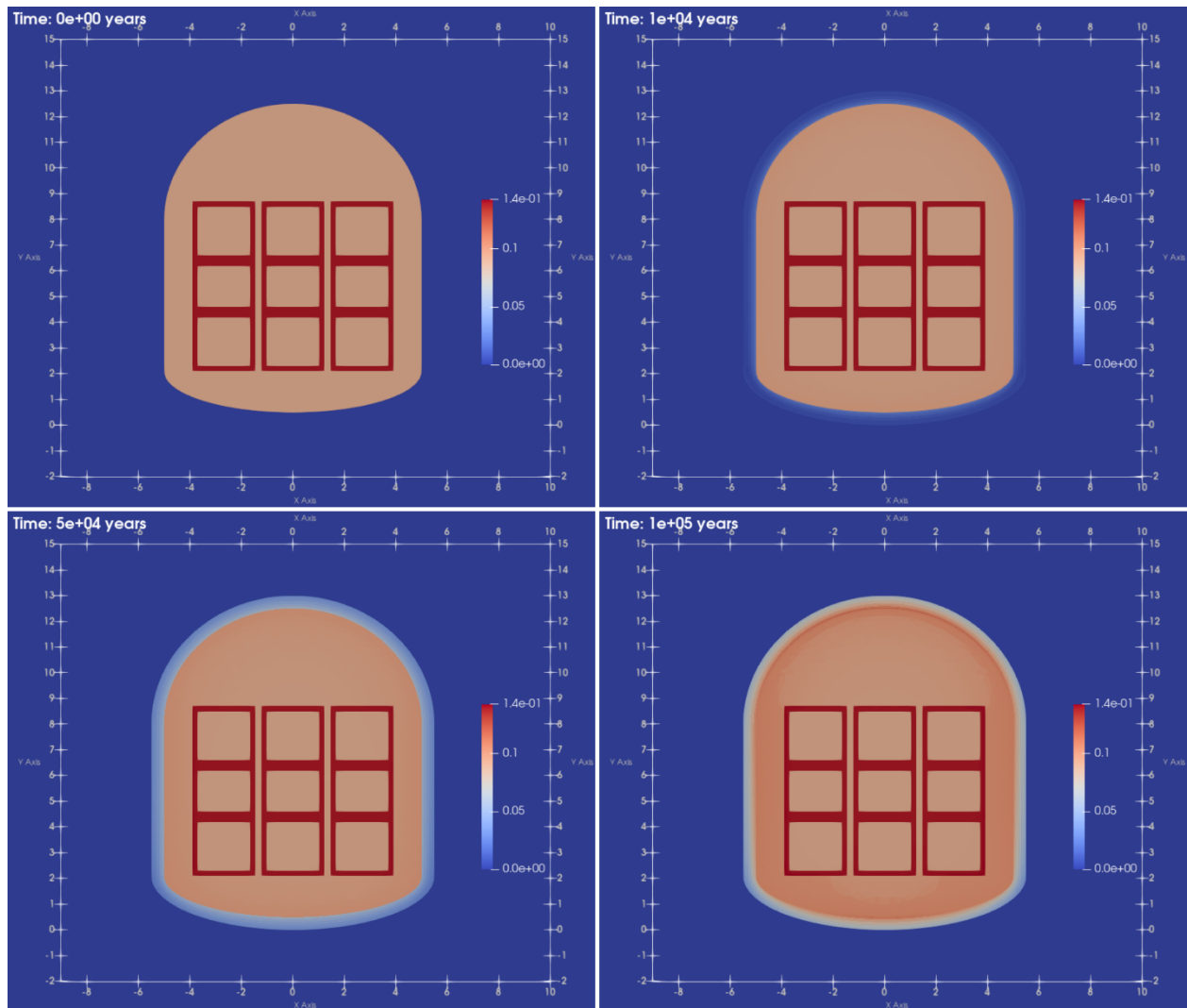


Figure 5-14. CSHQ-JenD volume fraction evolution in the 2D ILW cell in clay.

Finally, the evolution of the pH and porosity in the 2D cell is shown in Figure 5-16 and Figure 5-17, respectively. In this case, the pH alteration of the clay is less pronounced than in the 1D case, only up to around 0.5 m. Inside the disposal cell, the pH shows a similar behaviour, with values around 12.5, and a slightly increased value inside the waste package zone. Concerning the porosity evolution, the changes are not significant enough to alter the diffusion of species, mainly at the liner-clay interface. As it can be observed, the porosity slightly increases at the vault mortar-liner interface and decreases at the liner-clay interface, following a similar pattern to the 1D model.

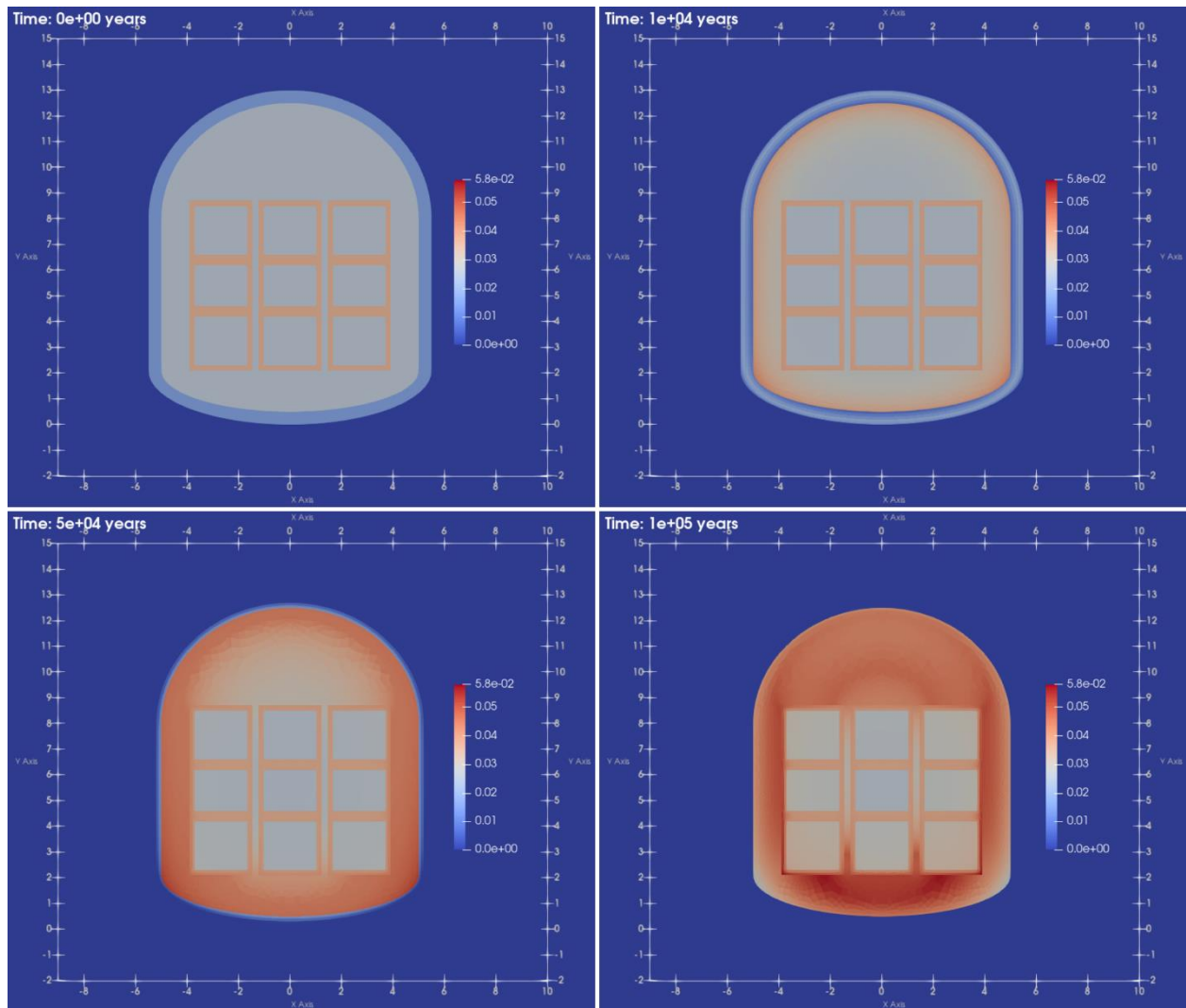


Figure 5-15. Volume fraction evolution of ettringite in the 2D ILW cell in clay.

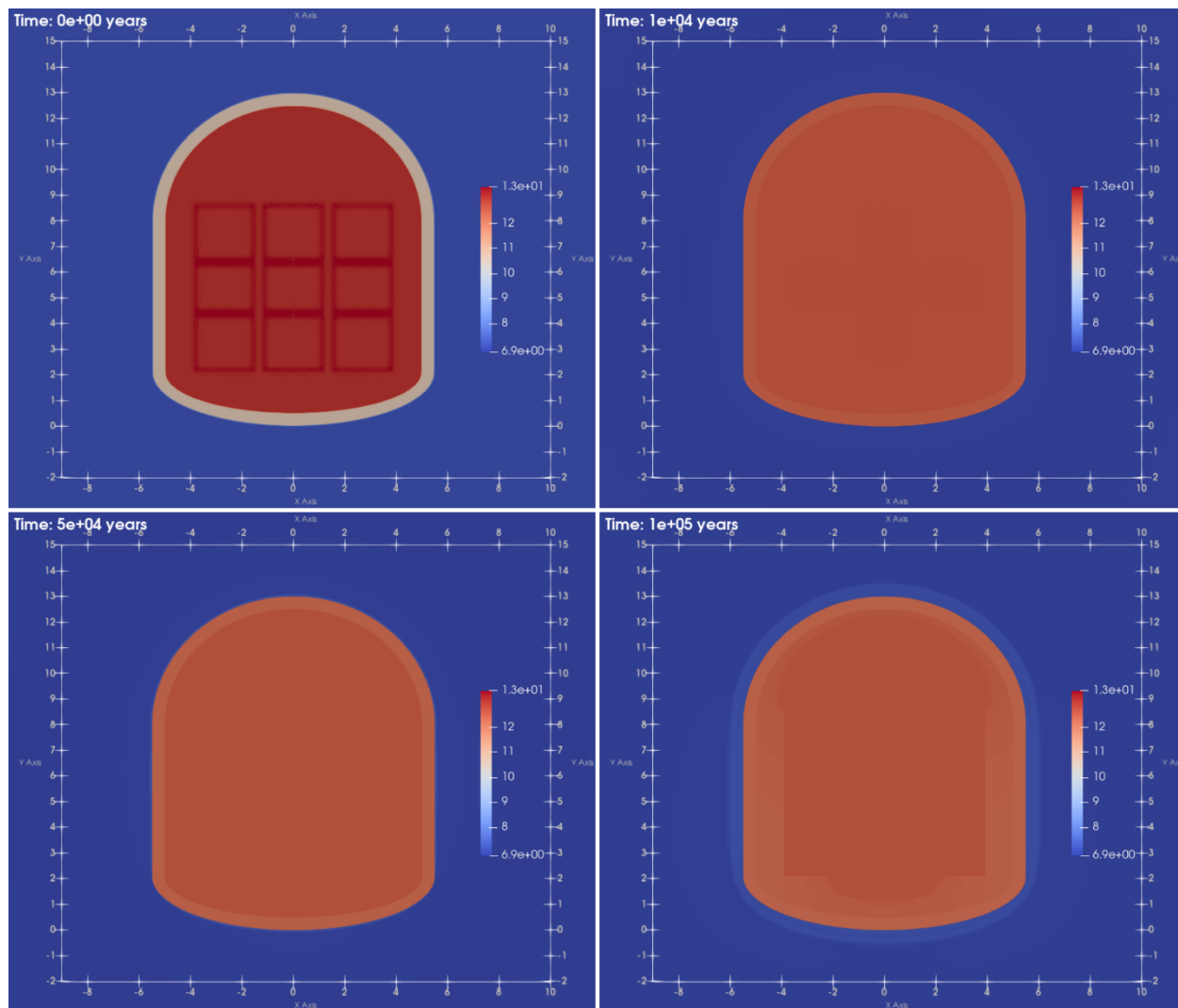


Figure 5-16. pH evolution in the 2D ILW cell in clay.

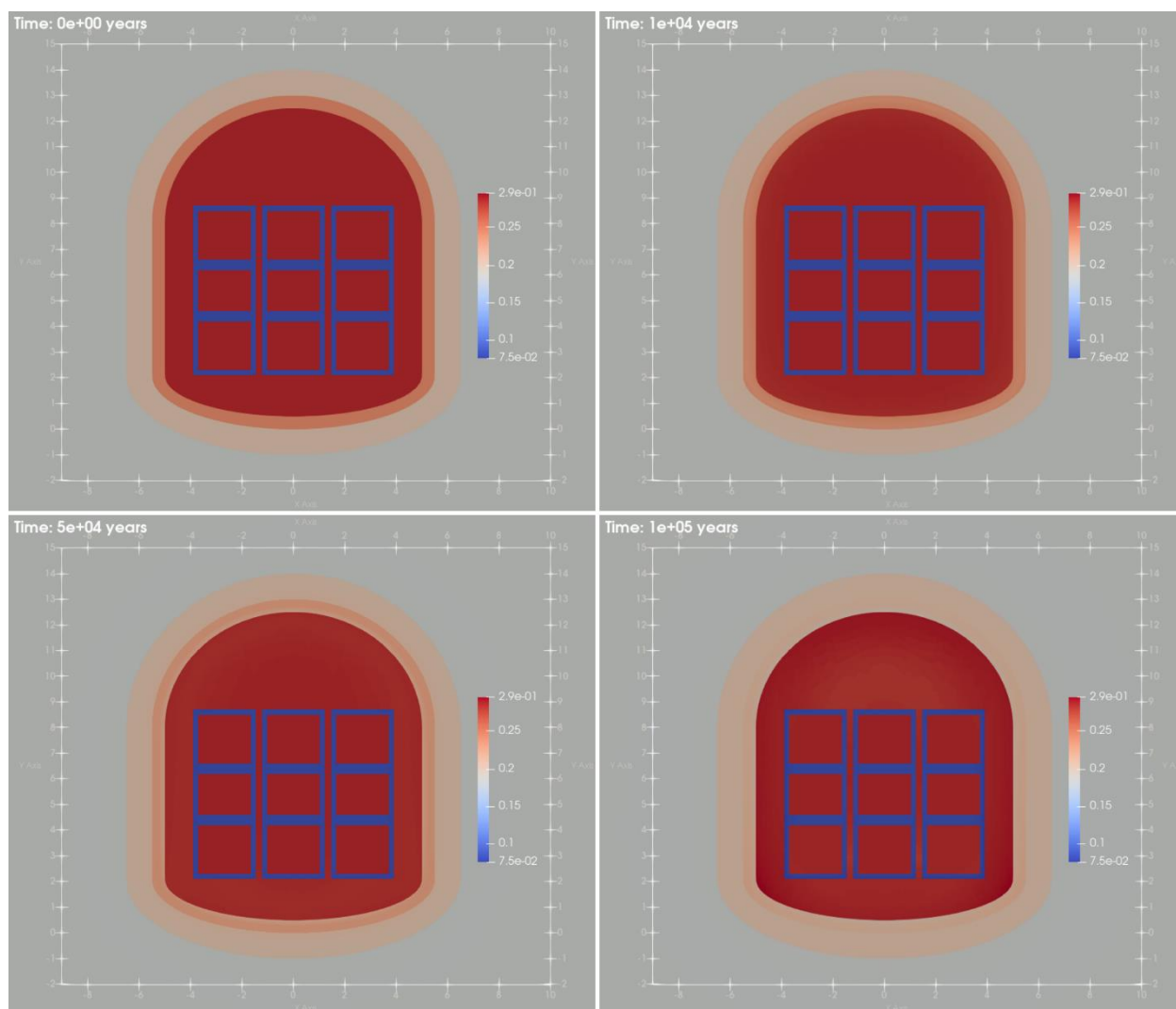


Figure 5-17. Porosity evolution in the 2D ILW cell in clay.

Finally, a comparison of the 1D and 2D models is shown in Figure 5-18. The main alteration in the clay, the precipitation of calcite, occurs in both cases with different patterns, although at the same intensity. This is a clear indication of the compromise made on the space-time resolution of the 2D model. The same occurs in the dissolution front of dolomite, which is similar between the models but occurs at larger lengths in the 1D case. On the cement-based materials, a bigger difference is observed in the behavior of the CSH-JenD phase, which shows a similar trend at much larger precipitation in the 1D case than in the 2D one. On the other hand, the evolution of ettringite results in similar amounts in the vault mortar in both cases. In contrast, the dissolution of portlandite is significantly different between the cases. In the 2D model, the dissolution front of portlandite is located at 0.8 m from the vault mortar-liner interface. In the 1D case, the dissolution front of portlandite is significantly increased, where the reaction front reaches up to 2 m from the vault mortar from the liner interface. The volume fractions of hydrotalcite are somewhat similar next to the vault mortar-liner interface in around a 0.5 m band; from that toward the inner part of the cell, hydrotalcite is found in larger amounts in the 2D case. Note that some of these differences can be caused also by the inclusion of the waste packages in the 2D model, which is not included in the 1D case; instead, a closed boundary is applied at the left-hand side of the concrete walls (see Figure 5-3).

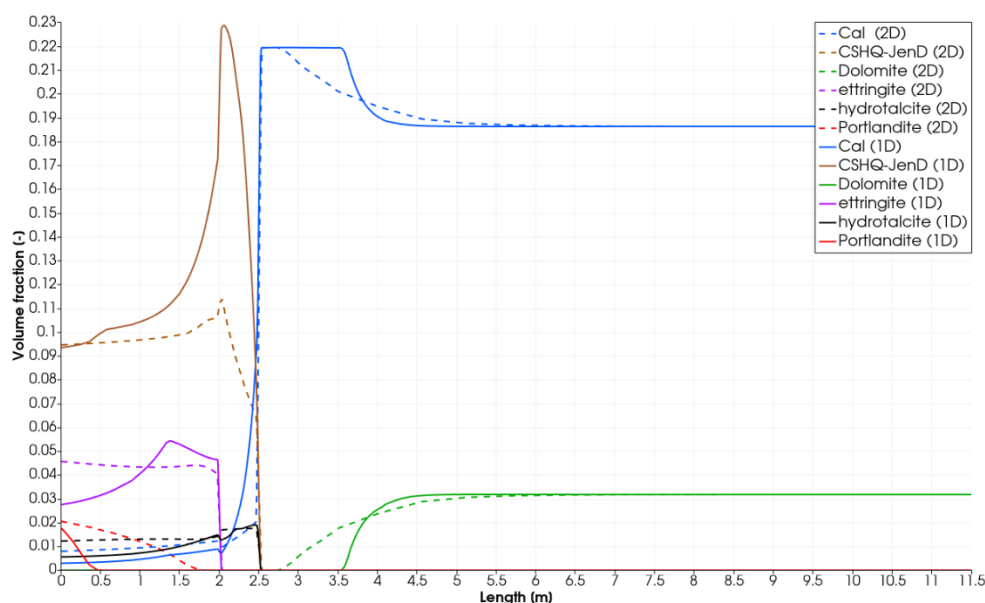


Figure 5-18. Comparison of the main minerals between the 2D and 1D disposal ILW disposal cell in clay.

5.3 Summary and conclusions

In this study, the results of simulations for an Intermediate-Level Waste (ILW) disposal cell in clay are presented. The disposal concept involves a multi-barrier system with the waste matrix, disposal container, mortar backfill, and clay host rock. The study employs a conceptual, mathematical, and numerical model described in detail in D2.16 (Samper et al. 2022).

Several simulation cases were conducted under different assumptions, varying saturation levels to create a 2D model representing a more realistic geometry. The simulations include cases with increasing chemical complexity, incorporating aqueous complexation, cation exchange, mineral dissolution/precipitation, and redox processes. The most complex chemistry, including all these processes, is presented in this deliverable.

Simulation cases in one dimension (1D) are initially explored, considering different degrees of water saturation and constant porosity. These 1D simulations provide insights into mineral changes, pH alterations, and porosity evolution over a 100,000-year period.

Results from a fully water-saturated case (1a) highlight significant interactions, including the dissolution of portlandite, calcite precipitation, and changes in C-S-H phases. Cases with reduced saturation (1b, 1c) and without porosity feedback (1d) demonstrate how different conditions affect mineral reactions and porosity evolution.

In the 2D simulations, an upscaled version of the 1D model is presented, offering a more realistic representation of the system. The spatial distribution of minerals, such as calcite, dolomite, portlandite, and ettringite, is examined over the 100,000-year period. The 2D model provides insights into the space-dependent behavior of mineral alterations, highlighting the advantages of modelling in two dimensions.

The comparison between 1D and 2D models reveals differences in the behaviour of certain minerals, emphasizing the importance of spatial considerations. The dissolution of portlandite, for instance, exhibits a space-dependent pattern in the 2D model not observed in the 1D simulations.

Given the inherent complexity of these systems, it is important to consider the sensitivity of the results to the selected discretization. Ideally, with unlimited computational resources, simulations with various

EURAD Deliverable 2.17 – Integrated reactive transport models for assessing the chemical evolution at the disposal cell scale

discretization levels could be run to test this sensitivity. However, with the current results, it is possible to identify potential signs of contrasting chemistry between adjacent nodes or cells. For example, if minerals precipitate in only a single cell in the profile, this might indicate grid dependency. The presented results do not show such contrasts, suggesting that the current grid size is sufficiently fine to represent the studied processes.

In conclusion, this comprehensive study contributes valuable insights into the long-term behaviour of ILW disposal cells in clay. The simulations consider diverse conditions and complexities, shedding light on the geochemical and mechanical evolution of the disposal system. The findings provide crucial information for assessing the performance of geological repository systems for radioactive waste, aiding in the refinement of models and predictions. The study underscores the significance of spatial considerations in accurately capturing the behavior of complex geochemical systems over extended periods, essential for the safe and effective management of radioactive waste.

6. ILW disposal cell in granite

The work has been done by Vanessa Montoya (SCK CEN) and Jaime Garibay-Rodriguez (UFZ).

In this section, the results of the ILW disposal cell in granite are presented. The conceptual, mathematical and numerical model is described in Samper et.al (2022). Contrary to the hydraulic conditions defined in Samper et.al (2022) in which advective flow has been assumed for all the simulation cases, only diffusive transport within the engineered barrier system is assumed. This is in line with the assumption of the HLW disposal cell in granite in which flow along the disposal gallery is assumed.

The effect over the diffusion coefficients of the change of porosity caused by the dissolution/precipitation reactions is modeled with the following relationship:

$$D_{eff} = \phi D_p, \quad [6.1]$$

where D_{eff} is the effective diffusion coefficient (m^2/s), ϕ is the porosity, and D_p is the pore diffusion coefficient (m^2/s).

Two cases in a 1D model are simulated, whereas only one case on a 2D setup is simulated due to computational cost. The simulation cases are shown in Table 10. Case 1a is an abstraction of the top of the 2D disposal cell. Three sections of the EBS are included, with the waste backfill and vault mortar having the same composition and properties. The system is modeled with a fixed (Dirichlet) boundary in the vault mortar side in contact with the granite porewater. The inner boundary is set as closed (Neumann). These conditions result in a purely diffusion-dominated transport. The assumption is that a flow in the Z direction (passing through the disposal cell in the XY plane) occurs in the granite host rock, and the only transport mechanism into the cell is diffusion. Other transport conditions may be also posed, i.e., advective flow in the XY plane as described in Samper et.al (2022), however in order to have more similarities with the transport processes modelled in the HLW in granite (see section 3), in this deliverable only the results considering diffusive transport have been considered

Table 11. Simulation cases for the ILW disposal cell in granite.

Case	Dimension	Description
1a	1	Diffusive transport in the Y direction
1b	1	Diffusive transport in the X direction
2	2	Diffusive transport around 2D disposal cell

On the other hand, Case 1b simulates a similar model of Case 1a but at the side of the 2D disposal cell (in the X direction). The EBS materials are the same in both cases, however, the dimensions are significantly different. The case in the Y direction has a total length of 4 m, whereas the case in the X direction has a total length of 1.3 m.

6.1 Simulations in one dimension

6.1.1 Model discretization

Y-direction. The 1D model discretization, in this case, consists of a total of 117 linear elements with non-uniform lengths through the vault mortar subdomain. The sequence of the vault mortar from left to right is $25 \times 0.02 \text{ m} + 15 \times 0.04 \text{ m} + 13 \times 0.1 \text{ m} + 15 \times 0.04 \text{ m} + 25 \times 0.02 \text{ m} = 3.5 \text{ m}$. The concrete wall and waste backfill subdomains have fix-sized elements of 0.02 m.

X-direction. In this case, since the dimensions are smaller, a uniform discretization of liner elements equal to 0.02 m is chosen, with a total of 65 elements.

Both models use the same time discretization with the following non-uniform sequence: $3000 \times 1 \text{ year} + 1000 \times 2 \text{ years} + 1000 \times 3 \text{ years} + 1000 \times 4 \text{ years} + 1000 \times 8 \text{ years} + 8000 \times 10 \text{ years} = 1\text{e}5 \text{ years}$. This time discretization has been chosen as a compromise between accuracy and computational cost. Therefore, it may not capture certain phenomena, e.g., pore-clogging, where extremely fine time steps are needed, increasing the computational cost significantly.

The CPU time on a single Intel(R) Xeon(R) Gold 6148 CPU with only one core @ 2.40GHz for the model in the X-direction is 2 hrs. on average. For the Y-direction, since the number of elements is higher, the CPU time is 6 hrs. on average.

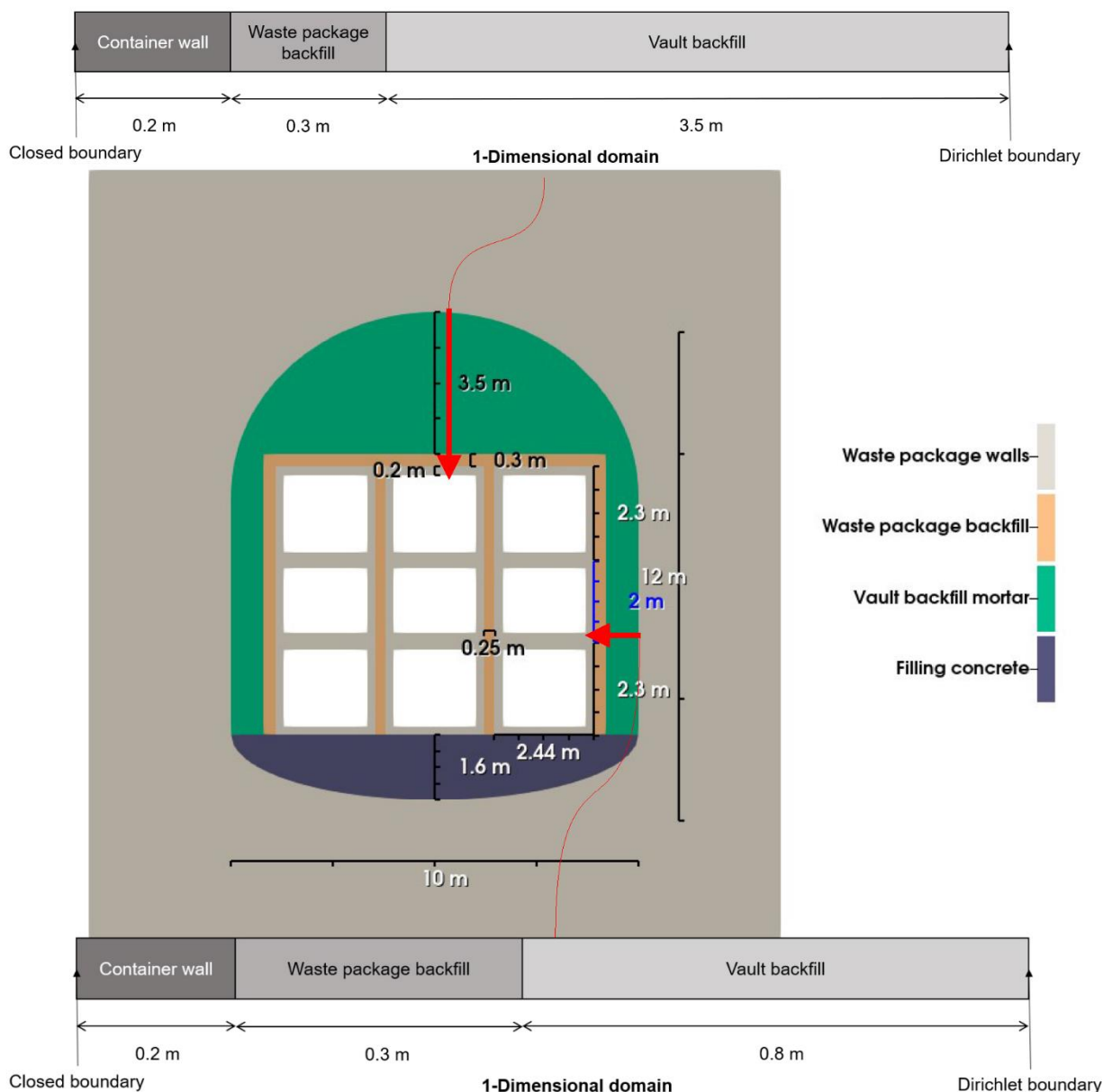


Figure 6-1. 1D abstractions of the ILW disposal cell in granite.

6.1.2 Case 1a: diffusive transport in the Y direction

In Figure 6-2, the mineral changes due to dissolution/precipitation reactions in the ILW disposal cell in granite are shown. This case considers an abstracted 1D domain from the top toward the disposal cell in the Y direction (see Figure 6-1). The main degradation indicator is the complete portlandite dissolution in both the vault mortar and the concrete after $1e5$ years. At $1e4$ years, it can be observed that the C-S-H phases also dissolve due to the in-diffusion of the granitic porewater. Initially, only the CSHQ-JenD ($Ca/Si = 1.5$) is present in both cement-based materials. The diffusion of granitic porewater causes the overall dissolution of C-S-H phases, however, the CSHQ-TobH ($Ca/Si = 0.66$) precipitates in the reaction front from the granitic porewater boundary acting as an intermediary reactant in-between the complete dissolution of C-S-H. The composition of the granitic porewater is provided in Table 2.5. Large amounts

EURAD Deliverable 2.17 – Integrated reactive transport models for assessing the chemical evolution at the disposal cell scale

of calcite precipitate can be observed for the entire time frame from the boundary in contact with the granite porewater, rich in carbonates (see Table 2.5). Initially, calcite is present in negligible amounts in the vault mortar and moderate amounts in the concrete. After 1e5 years, calcite occupies around 21 % of the volume at around 0.3 m from the granite porewater boundary. Further, calcite precipitation in the cement materials is significant up to 3 m from the boundary.

Table 6.12. Chemical composition of the granite boundary water (Samper et al., 2016).

Species (mol/L)	Granite boundary water
pH	7.825
Eh (V)	-0.188
Ca ²⁺	1.522·10 ⁻⁴
Mg ²⁺	1.604·10 ⁻⁴
Na ⁺	4.350·10 ⁻³
K ⁺	5.371·10 ⁻⁵
Fe ²⁺	1.791·10 ⁻⁸
Al ³⁺	1.85·10 ⁻⁸
Cl ⁻	3.949·10 ⁻⁴
HCO ₃ ⁻	5.049·10 ⁻³
SO ₄ ²⁻	1.561·10 ⁻⁵
SiO ₂ (aq)	3.761·10 ⁻⁴

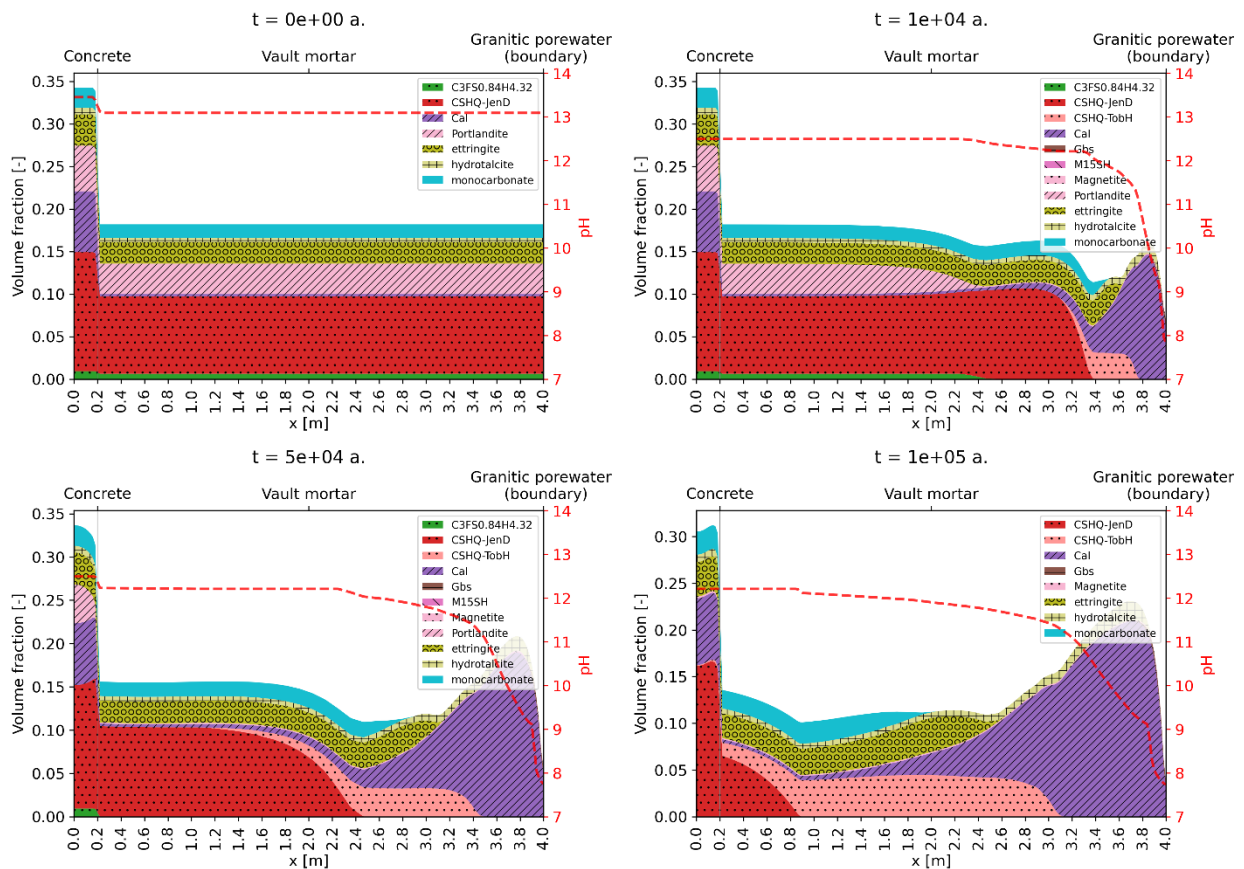


Figure 6-2. Mineral changes of the 1D ILW in granite at 0, 1e4, 5e4, and 1e5 years in the Y direction.

EURAD Deliverable 2.17 – Integrated reactive transport models for assessing the chemical evolution at the disposal cell scale

Portlandite is also present in significant amounts in the system (approx. 4.5% of volume fraction in the vault mortar). After $1e4$ years, the complete dissolution of portlandite has advanced 1.6 m from the granite boundary, and at $5e4$ years, it has completely dissolved in the vault mortar. Around this time, the reaction front reaches the concrete walls, causing the complete dissolution of portlandite in this material as well by the time frame ends. The dissolution pattern of the C3FS0.84H4.32 phase coincides with that of portlandite, which also dissolves completely in both materials after $1e5$ years. The degradation of the cement materials also shows the dissolution of additional cement minerals, such as monocarbonate and ettringite. In the case of monocarbonate, complete dissolution does not occur even after $1e5$ years. The reaction front of monocarbonate reaches around 2 m from the granite boundary. On the other hand, ettringite also dissolves up to about 1.5 m from the granite boundary. This is because the concentration of S(6) in porewater is lower than in cement-based materials. On the other hand, hydrotalcite shows a dissolution/precipitation pattern from the granite boundary; it precipitates but slowly dissolves at the boundary due to the in-diffusion of the granite porewater. In summary, the major mineral changes after $1e5$ years occur at around 3 m from the granite porewater (in the vault mortar), whereas the concrete wall does not show major alterations even after the entire time frame.

In Figure 6-3, the changes over time at different observation points in the cell are shown:

Point at 1.0 m: this point is the farthest from the granite boundary, i.e., a zone with less pronounced alterations. At this point, the system is not affected until later in the time frame, around $1.1e4$ years. Portlandite dissolves from this time until about $7.2e4$ years. Precipitation of C-S-H phases begins around the time portlandite completely dissolves. The CSHQ-JenD phase first precipitates but then dissolves completely at $1e5$ years. Before the complete dissolution of portlandite, the CSHQ-TobD phase precipitates and remains present until the end of the time frame. On the other hand, there is minor precipitation of calcite that starts very late ($9e4$ years). Ettringite and monocarbonate show a slight precipitation pattern, but, as shown, their overall behaviour is dissolution. Hydrotalcite remains unchanged throughout the time frame.

Point at 2.5 m: this point is located well within the degradation front of the vault mortar, at 1.5 m from the granite boundary. At this point, the dissolution of portlandite begins much sooner, at around $7e3$ years. The dissolution of CSHQ-JenD also occurs sooner, at about $7.7e4$ years. However, similar to the behavior at 1 m, the CSHQ-TobD phase precipitates and remains present until the end of the time frame. This point captures the overall dissolution of monocarbonate and ettringite, with a clear dissolution pattern of ettringite towards $1e5$ years and the complete dissolution of monocarbonate around $8e4$ years. At this point, it is observed that calcite precipitates strongly, occupying more than 5 % of the volume.

Point at 3.9 m: this point corresponds to the zone next to the granite boundary. Therefore, it is obvious that major alterations begin to occur very early. For instance, portlandite shows a quasi-linear dissolution behavior, where it completely dissolves at 700 years. The initial C-S-H phase, CSHQ-JenD, completely dissolves just after $1e3$ years. Furthermore, the CSHQ-TobD, which is not initially present but precipitates, dissolves completely later, at about $7e3$ years. In addition, ettringite and monocarbonate also dissolve during the first $3e3$ years completely. On the other hand, hydrotalcite shows a precipitation behavior for most of the time frame, until it begins to dissolve at later stages (around $8.5e4$ years). The degradation at this point is strong. Calcite is the only major mineral to remain present in significant amounts, occupying about 17% of the volume.

The resulting changes in porosity over time from the mineral dissolution/precipitation reactions are shown in Figure 6-4 for different observation points. In this case, an observation point at 3.65 m is also plotted. This point is where the calcite precipitation is higher at the end of the time frame. At 3.9 m, the zone next to the granite boundary, the porosity increases early due to the dissolution of cement minerals but lowers after about $1.1e3$ years due to calcite precipitation. At $1e5$ years, the resulting porosity at this point remains virtually the same as the initial porosity. At 3.65 m, the porosity change reaches a maximum at about $7e3$ years, to then steadily decrease until the end of the time frame, due to calcite

precipitation, as mentioned. Points at 1 and 2.5 m show a similar porosity change pattern at different times, with the point at 2.5 m beginning around $7e3$ years and the point at 2.5 at around $1.1e4$ years.

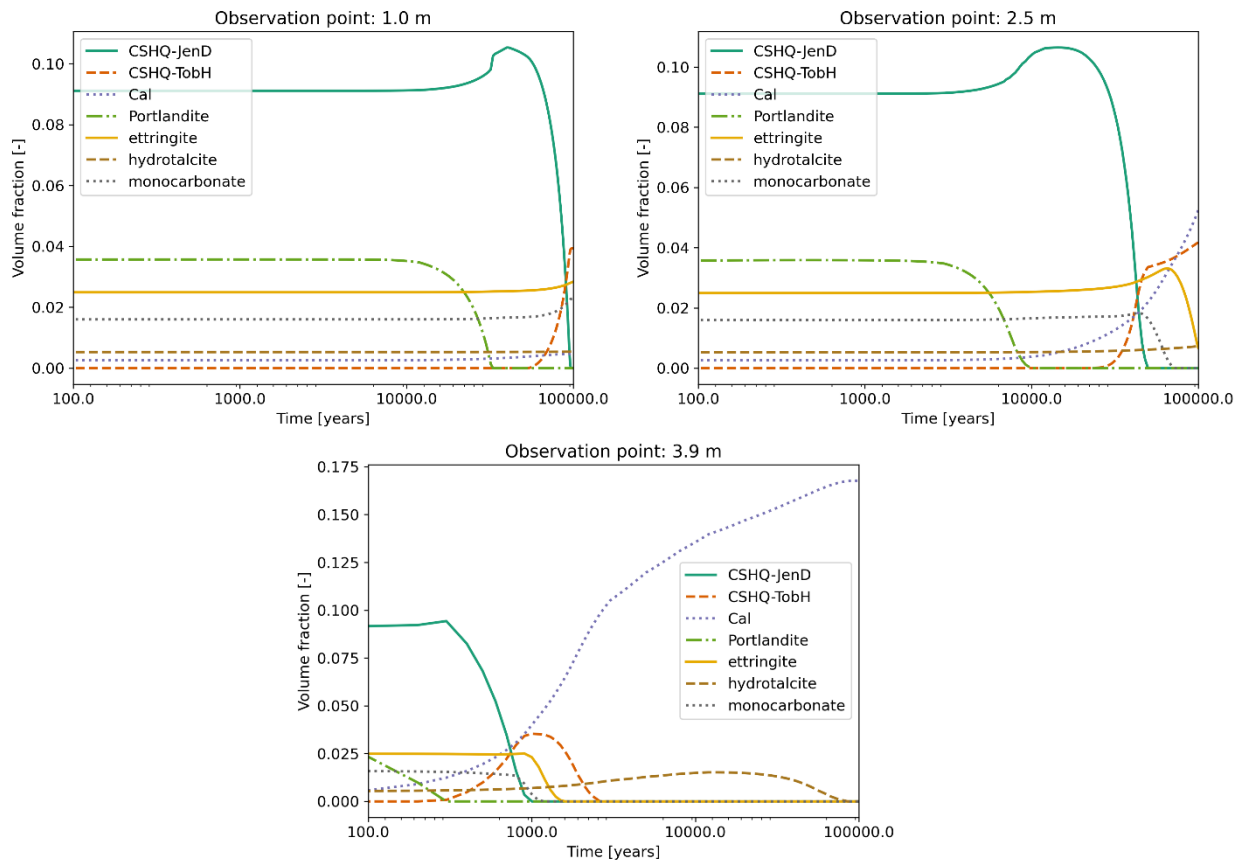


Figure 6-3. Changes in minerals over time at different observation points for the 1D ILW disposal cell in granite in the Y-direction.

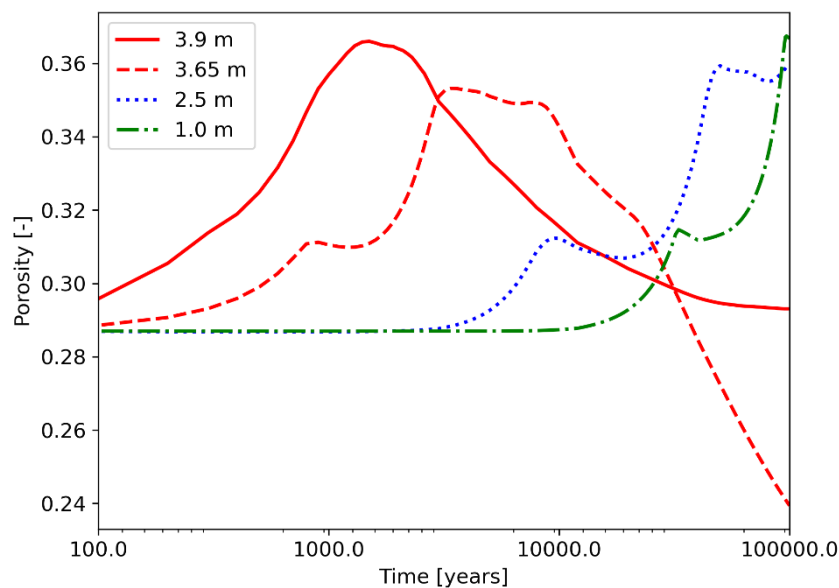


Figure 6-4. Changes in porosity over time at different observation points for the 1D ILW disposal cell in granite in the Y-direction.

In Figure 6-5, the concentration changes over time of the main species at different observation points are shown. The point at 1 m shows mainly the interaction of concrete wall and vault mortar porewater at early times since the granitic porewater does not reach this point until the later stages, at about 7×10^4 years. The major changes are due to the different K and S(6) concentrations in the cement materials. However, since both materials are of similar composition, the mixing of porewaters does not cause major alterations in their interface. After 7×10^4 years, Si release can be observed due to the C-S-H dissolution at this point. In addition, Ca release due to portlandite has a sink in the precipitation of calcite. A small decrease in the concentration of Fe can be observed also because magnetite precipitates in small quantities. At 2.5 m, there are changes in the porewater due to the mixing of the concrete and mortar similar to the one observed at 1.0 m, however, the diffusion of the granite porewater shows a much strong alteration in the system. For instance, the release of Si and consumption of Ca begins at about 9×10^3 years. The concentration of S(6) changes only around 8×10^4 years when the reaction front reaches ettringite. The concentration of Al is affected by the interplay among the dissolution/precipitation of gibbsite, hydrotalcite, and ettringite, showing an increasing value after about 9×10^3 years. Magnetite precipitation has a stronger effect on the decrease of Fe concentration at this point. Finally, at 3.9 m, the zone next to the granite porewater. Mg and C(4) strongly diffuse into the mortar from the higher concentration in the granite. At this point, the release of Al at around 1×10^3 years is noticeably larger caused by the dissolution of ettringite. On the other hand, the higher concentration of Ca coming from the vault mortar is quasi-stabilized after 7×10^3 years to about the concentration of the granite porewater.

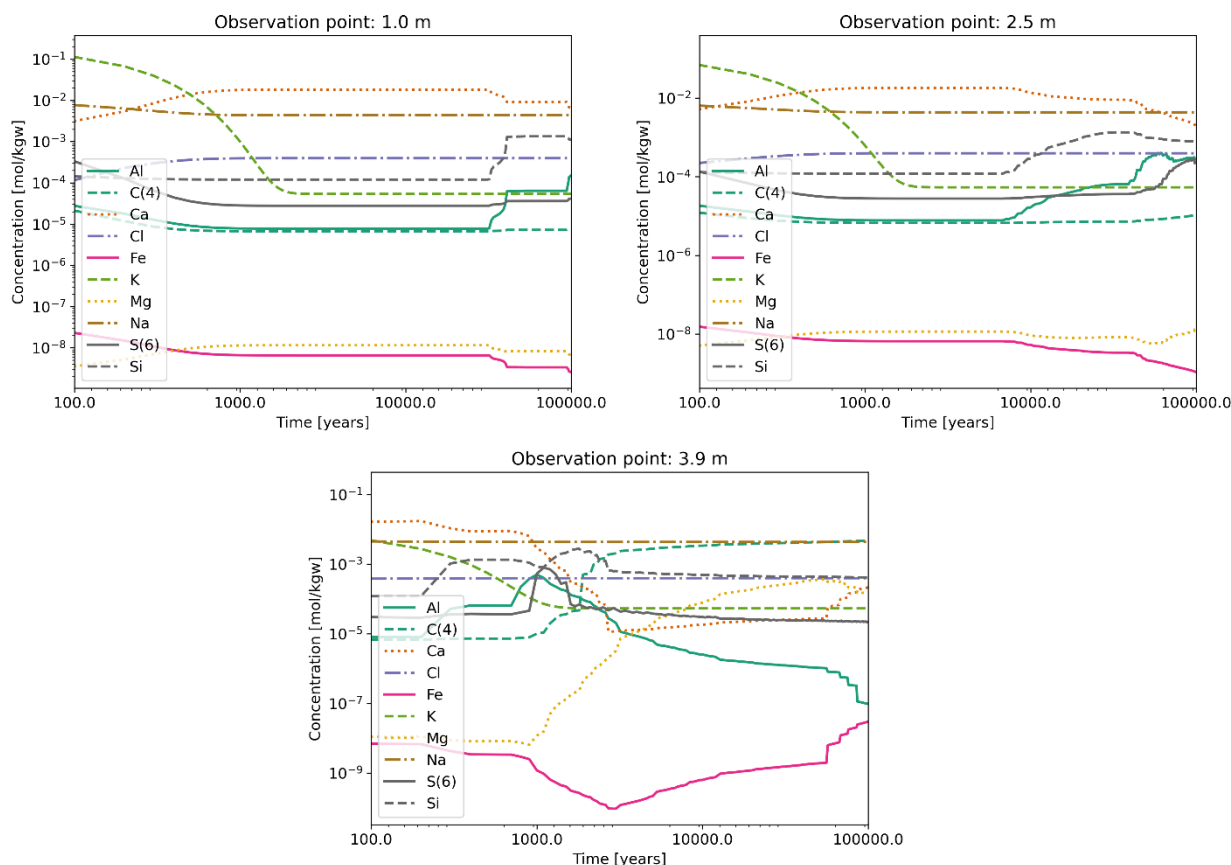


Figure 6-5. Concentration of species over time at different observation points for the 1D ILW cell in granite in the Y-direction.

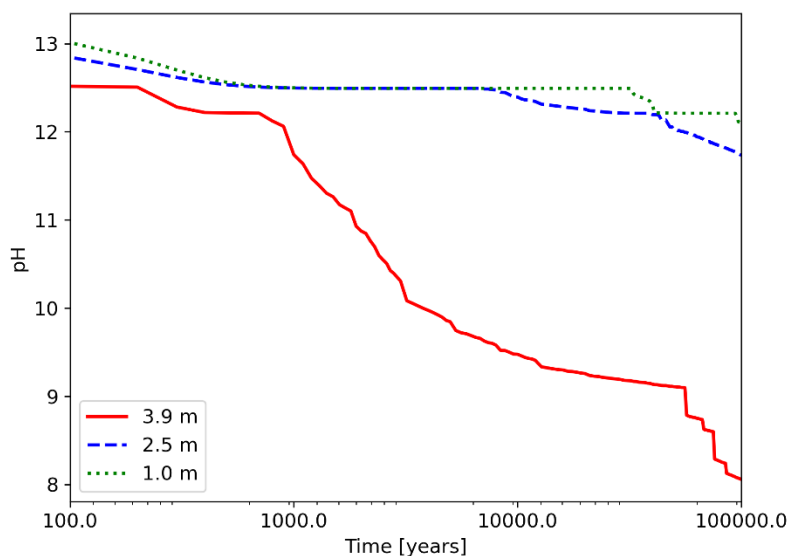


Figure 6-6. pH changes over time for the 1D ILW cell in granite in the Y-direction.

Finally, in Figure 6-6, the changes in pH over time at different observation points are shown. First, a clear decreasing pattern from the high pH in the mortar (13) to the pH of the granite porewater (7.8) is observed at 3.9 m, which is expected. This is caused by the fixed boundary in contact with the granite porewater, which creates a high chemical gradient at this point. During the first 1e3 years, the pH decreasing rate is slower. After this time, the pH decreases at a faster rate due to the complete dissolution of portlandite and CSH. At 2.5 m, the interaction is not sufficiently strong to lower the pH to that of the granite porewater, remaining still quite alkaline, just below 12. This is because there are still significant amounts of C-S-H phases at this point at 1e5 years. On the other hand, the pH evolution at 1.0 m is less significant, which is an overall change from 13 to about 12.5 even after the entire time frame.

6.1.3 Case 1b: diffusive transport in the X direction

In this case, the abstracted 1D domain of the 2D disposal cell corresponds to the right side in contact with the granite porewater (see Figure 6-1). In Figure 6-7, the mineral composition at 0, 1e4, 5e4, and 1e5 years is shown. Recall that this case has the same composition and EBS materials as the previous one, as well as the diffusive transport conditions in contact with a fixed granite porewater boundary. The only difference between this case and the previous one is the domain length of the vault mortar, which is 1.1 m, in contrast to the much larger length of the previous case of 3.8 m. Therefore, the mineral changes are expected to be similar in this case; however, there is a much larger degree of alteration due to the lower domain length, as shown. For instance, just after 1e4 years, the mineral composition, in this case, resembles the composition of the previous case but after 1e5 years. At 1e4 years, portlandite dissolves completely in the vault mortar and the reaction front reaches the concrete-mortar interface. In addition, the CSH phases completely dissolve on a 0.2 m zone from the granite porewater boundary. Monocarbonate and ettringite follow a dissolution pattern as well in the mortar, which is less significant in the concrete at 1e4 years. Calcite is the main alteration at this time, with strong precipitation in a zone of about 0.5 m from the granite boundary. At 5e4 years, the vault mortar has virtually degraded completely, with only small quantities of hydrotalcite remaining at the concrete interface. The precipitation of the M15SH is observed at this time as well. Gibbsite also precipitates in more significant amounts than in the previous case. At this time, there are still significant quantities of CSH phases in the concrete wall, as well as cement materials such as ettringite, monocarbonate, and hydrotalcite. However, at the final time, 1e5 years, the full system is completely degraded and the pH of the vault mortar stabilizes to the slightly alkaline pH of the granite porewater (7.8). In the mortar, significant amounts of gibbsite remain, while M15SH has almost dissolved completely. In the concrete domain, the

EURAD Deliverable 2.17 – Integrated reactive transport models for assessing the chemical evolution at the disposal cell scale

pH is also significantly lower, below 10. Only a small amount of CSH remains at the left-most part of the domain. In the concrete domain, significant quantities of calcite form as a precipitate. In addition, M15SH is still present in the concrete at 1e5 years. Furthermore, a small quantity of Amor-Si (amorphous silica) precipitates in the concrete.

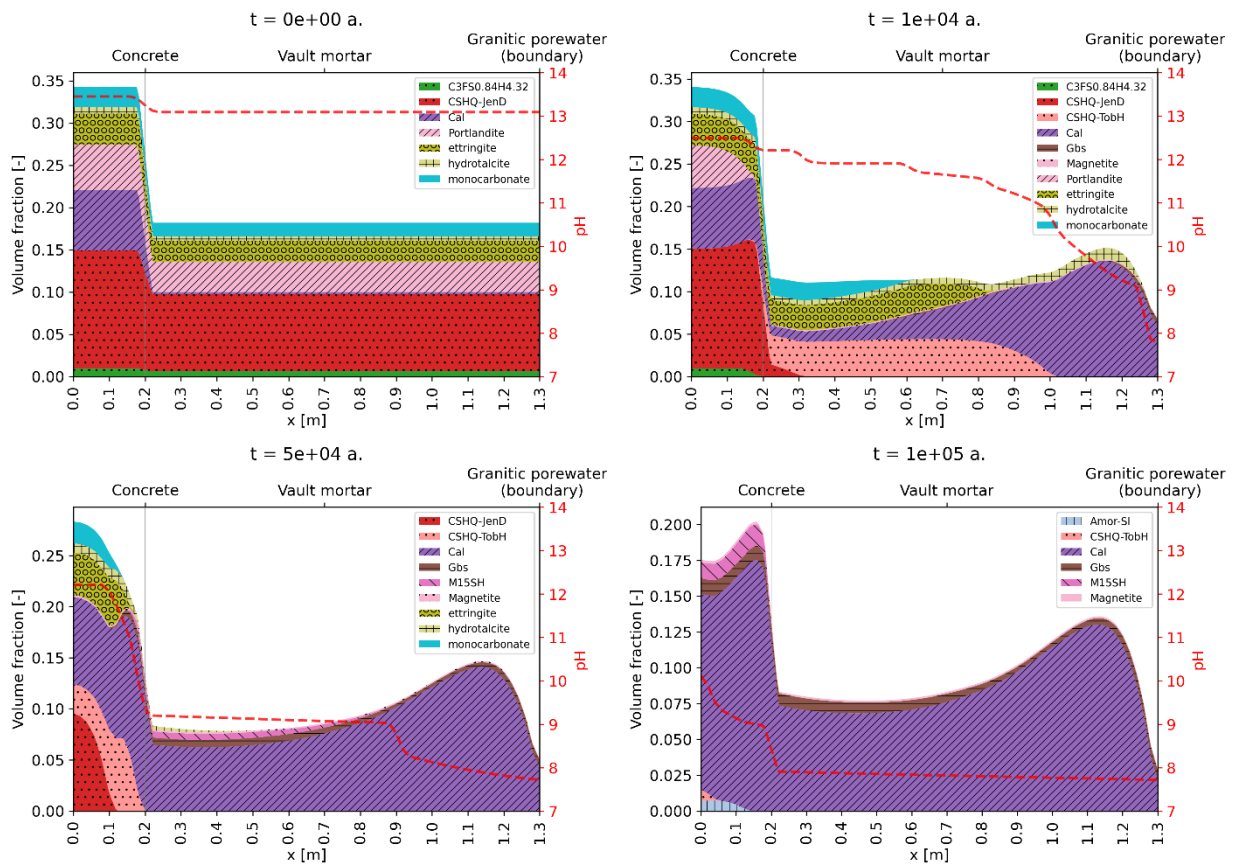


Figure 6-7. Mineral changes of the 1D ILW disposal cell in granite at 0, 1e4, 5e4, and 1e5 years in the X-direction.

In Figure 6-8, the mineral changes over time at different observation points are shown. The resulting volume fractions have similar behaviour in comparison to the case in the Y-direction, as shown in Figure 6-3. Far from the granite porewater boundary, at 0.1 m, the mineral composition remains virtually unaffected during the first 7e3 years. After this time, portlandite begins to dissolve until it completely disappears at about 5e4 years. The C-S-H phases also dissolve completely just before 1e5 years. Ettringite, hydrotoalcite, and monocarbonate also dissolve completely at different times, until only calcite precipitate remains at 1e5 years. The remaining observation points, at 0.5 and 1.2 m, also result in practically a complete dominance of calcite precipitation at the end of the time frame, with a complex dissolution/precipitation behavior of the cement-based materials at different points in time. In contrast to the case in the Y-direction, the cell degradation is larger in this case and occurs at a faster rate due to the reduced length in the domain.

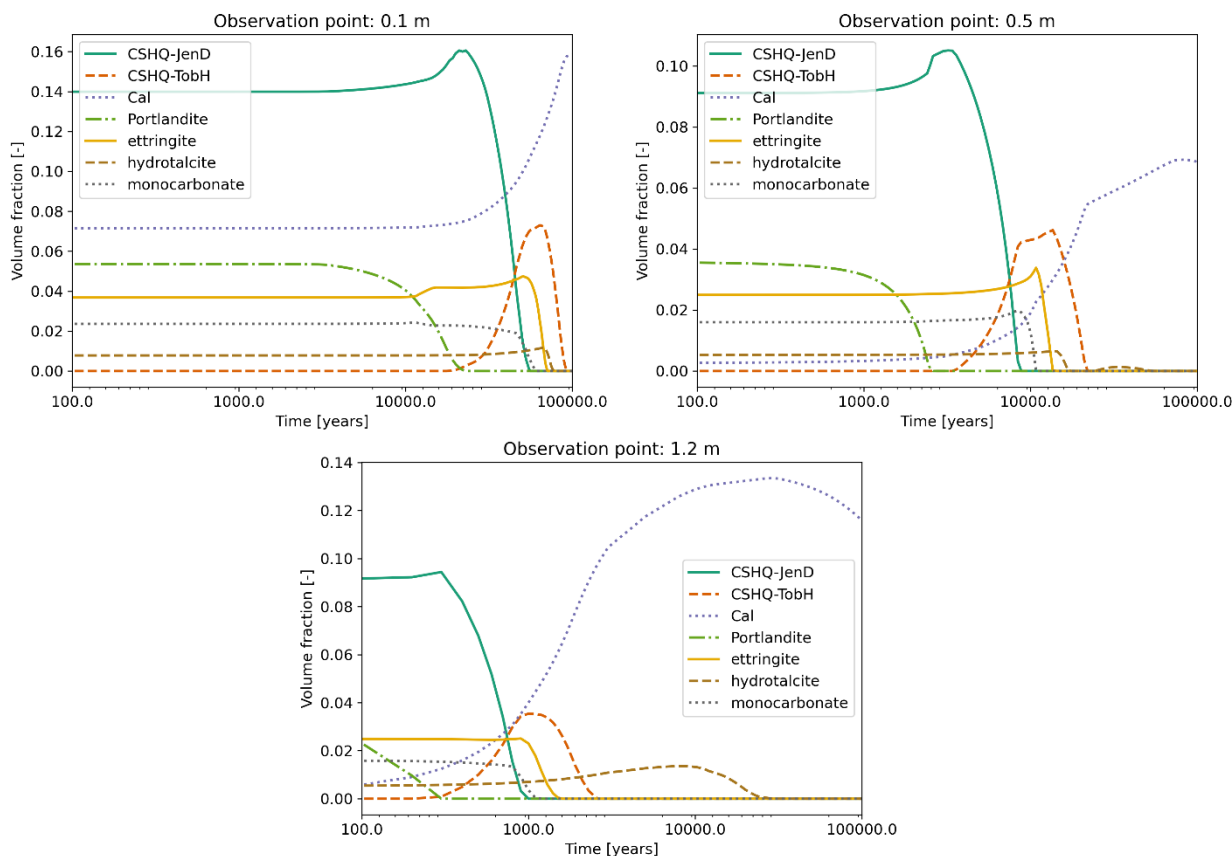


Figure 6-8. Mineral changes over time at different observation points for the 1D ILW cell in granite in the X-direction.

In Figure 6-9, the porosity changes over time at the different observation points are shown. At point 1.2, the porosity increases during approximately the first 1.2e3 years, to then decrease to around 1e4 years, mainly caused by the precipitation of calcite. After this time, calcite stops precipitating and starts to partially dissolve towards equilibration with the granitic porewater. At point 0.5 m, there is an increasing porosity pattern up to 5e4 years, where it shows a quasi-stable behaviour after this time through the remaining years. On the other hand, at 0.1 m (on the concrete domain), there is an increasing porosity behavior that does not stop, even after 1e5 years. This is because the dissolution of the cement materials dominates the precipitation of calcite, which is initially present in the concrete.

In Figure 6-10, the changes in the concentrations of the main species over time at different are shown. As discussed in the Y-direction case (see Figure 6-5), there is an interplay between the mixing of the porewater between the concrete and the mortar on the left-hand side, and the mortar and the granitic porewater on the right-hand side. As mentioned, the concentration of Al is affected by the dissolution/precipitation of ettringite, gibbsite, and hydrotalcite, with a more complex behavior at 1.2 m. At 0.1 m, the system remains practically unaffected during the first 1.2e4 years. In all three observation points, it can be observed that Mg enters the cell even far from the interface. This causes the partial precipitation of hydrotalcite (see Figure 6-8, bottom), however, it completely dissolves after 1e5 years.

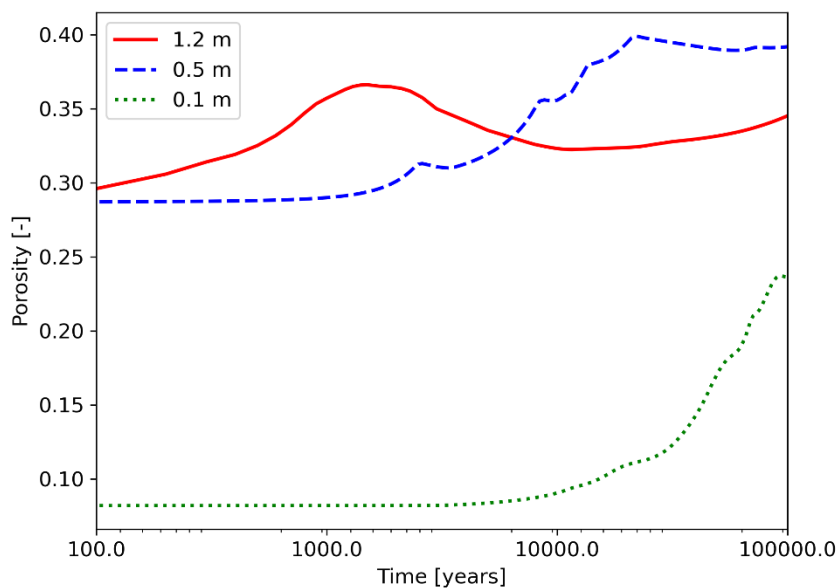


Figure 6-9. Changes in porosity over time at different observation points for the 1D ILW disposal cell in granite in the X-direction.

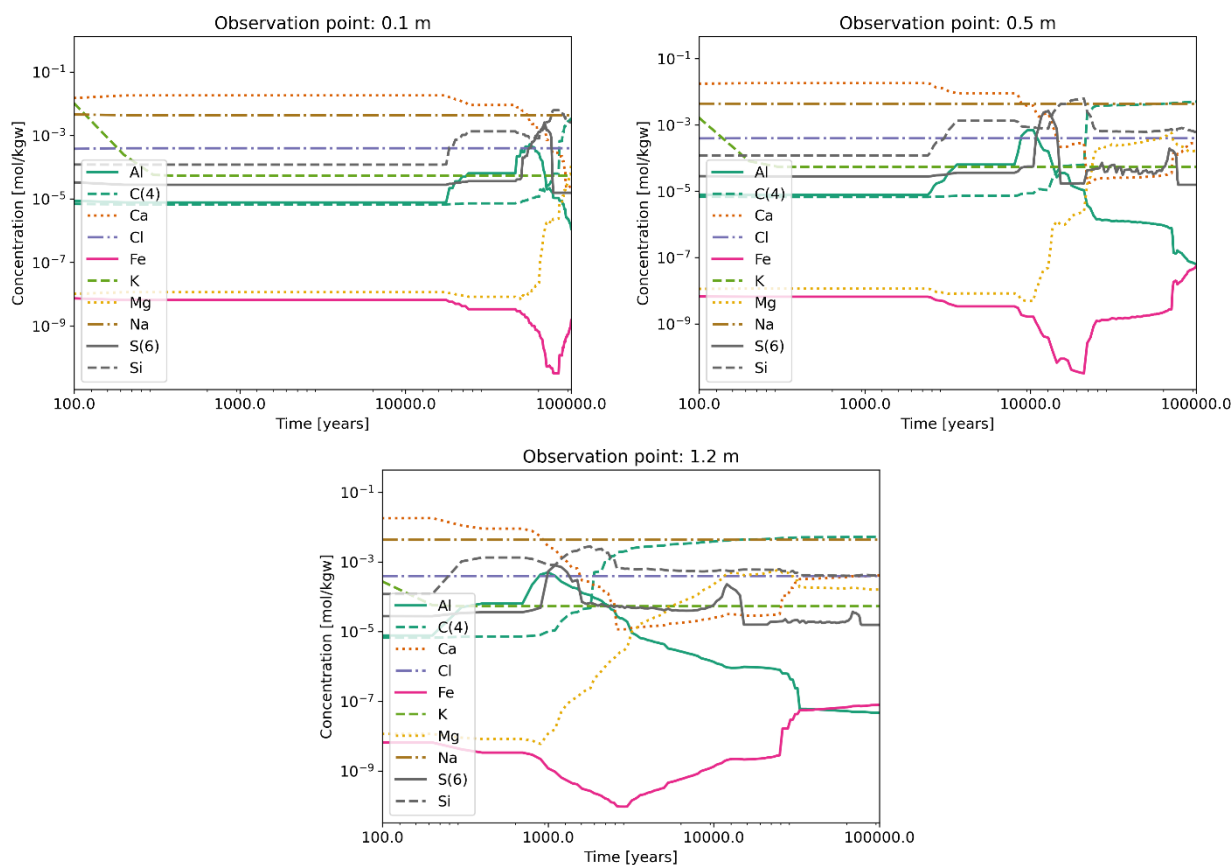


Figure 6-10. The concentration of species over time at different observation points for the 1D ILW cell in granite in the X-direction.

Finally, for the 1D case in the X-direction, the pH changes over time are shown in Figure 6-11. In contrast to the case in the Y-direction, the pH at the 3 observation points decreases dramatically well below 10

after $1e5$ years. At 1.2 m, only during the first 500 years, the pH remains unaffected. After this time, decreases at a slower rate to $1e3$ years, when portlandite and the CSHQ-JenD phase have completely dissolved. At about $7e4$ years, the pH at this point semi-stabilizes below 8, which is the pH of the granite porewater. At 0.5 m, the pH remains unaffected during the first $6e3$ years, to then follow a similar decreasing pattern to that at 1.2 m. At 0.1 m, the pH remains largely unaffected during the first $4e4$ years. Then decreases similarly to the previous points, however, it does not reach approach the pH of the granite so closely, with a final value of about 9.4.

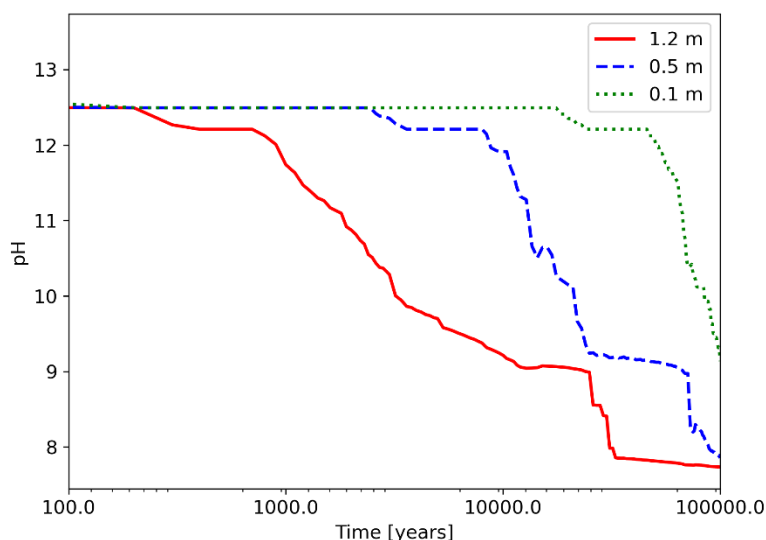


Figure 6-11. pH changes over time for the 1D ILW cell in granite in the X-direction.

6.2 Simulations in two dimensions

In this section, the upscaled 2D case of the ILW disposal cell in granite is presented. A 2D mesh of the ILW cell was constructed following an equivalent generic design to the one used in the ILW cell in clay. The main difference is that the host rock domain, in this case, granite, is not included in the model. Instead, similar to the 1D cases, a fixed boundary condition with the composition of the granite porewater is imposed around the cell. Given these considerations, the simplified boundary condition used in our study might not fully capture these complex interactions. To address this limitation, future work could explore more dynamic boundary conditions, incorporating reactive transport modeling to simulate the reciprocal effects between the cementitious disposal cell and the granite host rock. This would provide a more realistic representation of the long-term geochemical processes and allow for a more comprehensive understanding of the system's behavior. Thus, while our study provides valuable insights into the internal evolution of the disposal cell, it's important to acknowledge the limitations of the boundary conditions and the need for further research to address these complexities.

Furthermore, the 2D mesh setup does not assume symmetry; therefore, a more realistic geometry is simulated, avoiding the need to impose an impervious boundary condition in the middle of the cell. This will only affect slightly the profiles obtained, a similar case by assuming symmetry is also reasonable. The 2D mesh discretization is shown in Figure 6-12. The mesh consists of 11,994 quadrilateral cells. A uniform time-discretization, consisting of 1000 time steps of 100 years, is chosen as a compromise between accuracy and computational cost. A refined boundary layer has also been applied to the mesh due to the large concentration gradient caused by the constant boundary condition.

The CPU time on a single Intel(R) Xeon(R) Gold 6148 CPU with only one core @ 2.40GHz for the model in the 2D model is 115 hrs.

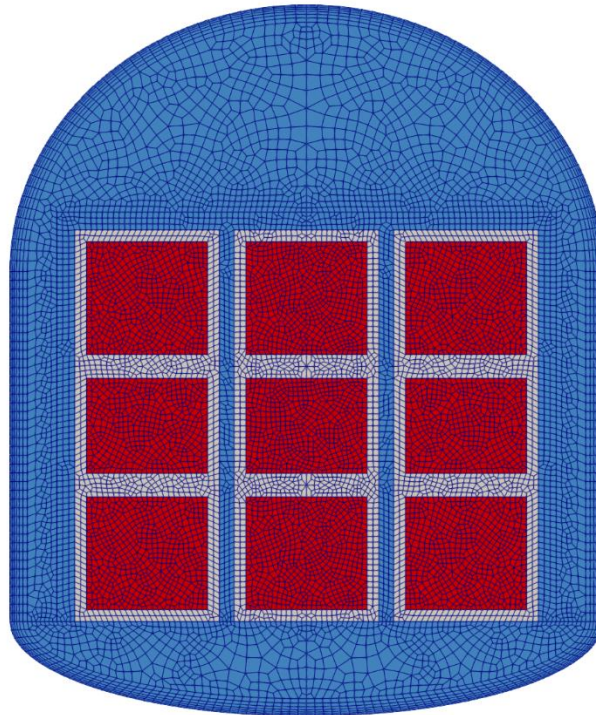


Figure 6-12. 2D mesh discretization of the ILW cell in granite.

In Figure 6-13, heatmaps of the evolution of the CSHQ-JenD phase are shown. In the 2D case, there is no visible change in the volume fraction at $1e4$ years (top-right). After $5e4$ years, CSHQ-JenD dissolves up to about 0.5 from the top of the cell (bottom-left). Also, at this time, the volume fraction of CSHQ-JenD appears to be slightly lower in a 1 m band around the cell, in comparison to the top. Moreover, there is still no visible change in the waste package zone. After $1e5$ years, CSHQ-JenD has completely dissolved from the sides of the cell. There is an approximately 1 m zone on top of the middle of the waste packages with a small amount of CSHQ-JenD. Inside the waste packages zone, CSHQ-JenD shows a minor degree of dissolution between the waste packages, in the waste package backfill. The CSHQ-JenD amount in the concrete walls remains practically unaffected, with a slight dissolution in the outer corners, most noticeable in the bottom left and right waste packages. The inside of the waste package remains virtually unaffected even after $1e5$ years.

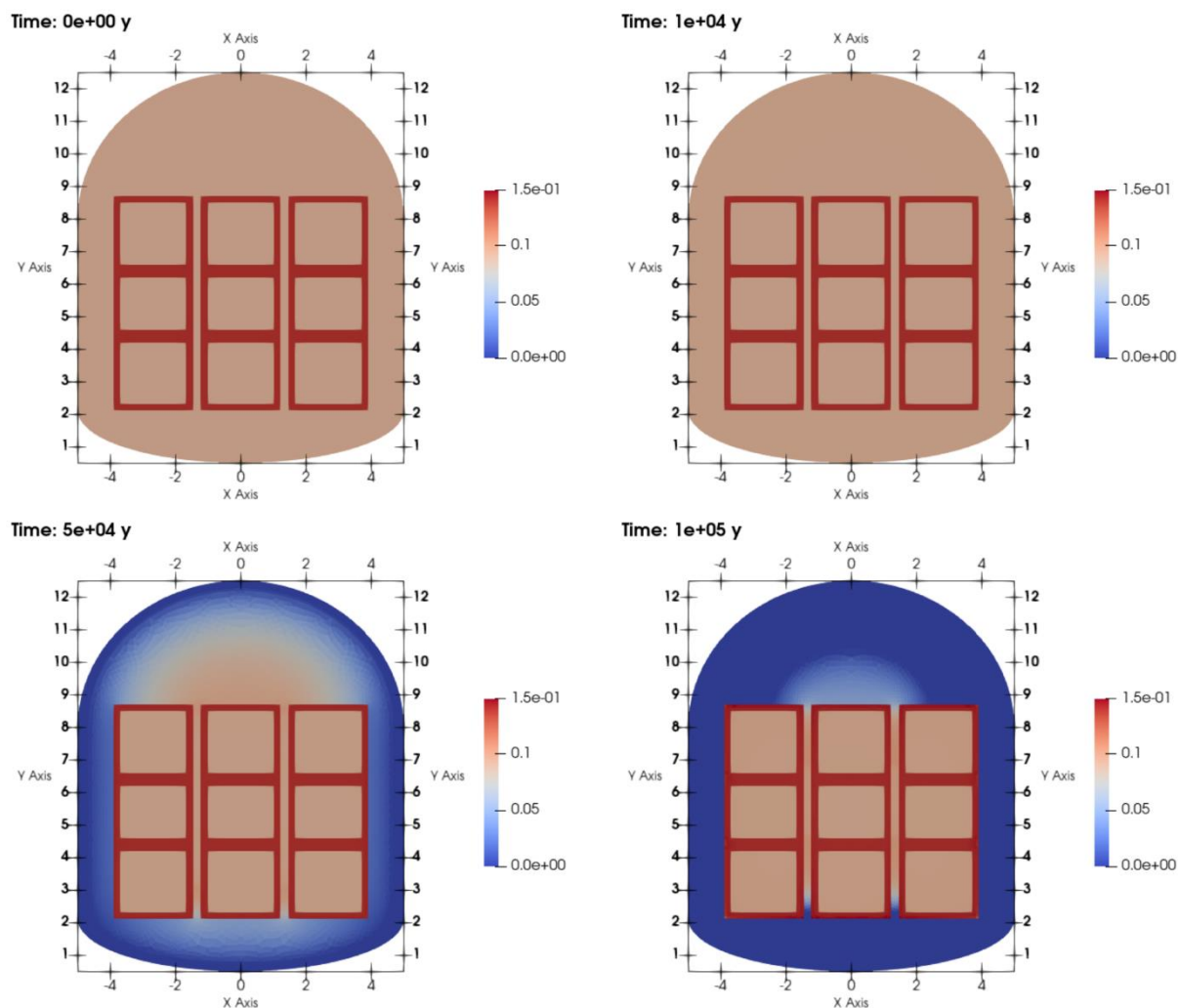


Figure 6-13. Volume fraction evolution of CSHQ-JenD in the 2D ILW cell in granite.

The other C-S-H phase that reacts in the system is the CSHQ-TobH phase. This phase is not initially present. As shown in Figure 6-14, CSHQ-TobH does not precipitate before 1e4 years. At 5e4 years, CSHQ-TobH has precipitated around the entire cell. In this case, because of the geometry, more CSHQ-TobH precipitate is accumulated on the sides of the cell. The accelerated reaction of CSHQ-TobH also causes its almost depletion on the sides of the cell at 1e5 years, where significant amounts remain in the top portion of the vault mortar.

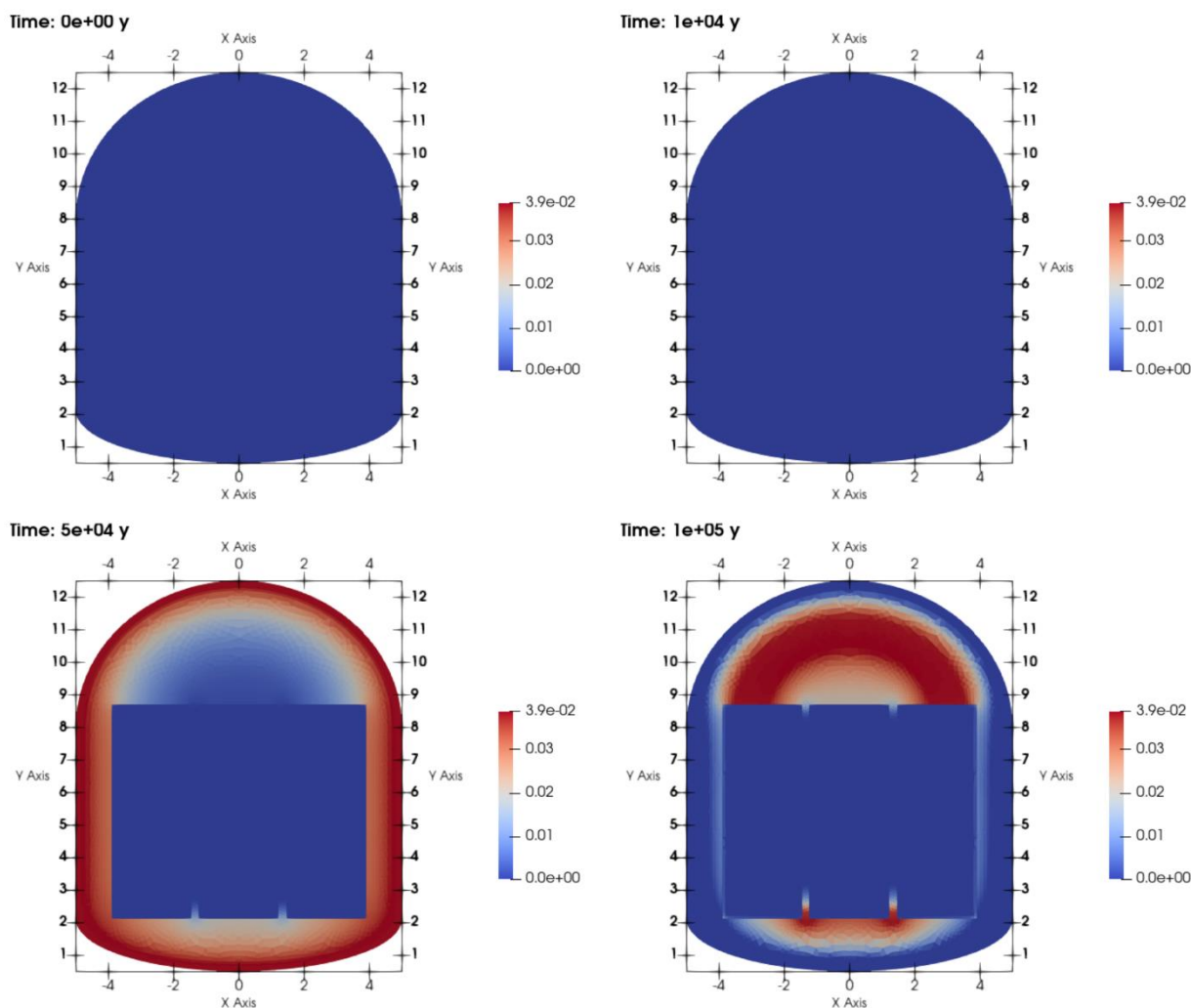


Figure 6-14. Evolution of the volume fraction of CSHQ-TobH in the 2D ILW cell in granite.

As shown in the 1D cases, calcite is a major precipitating mineral. The evolution of calcite, in this case, is shown in Figure 6-15. As in the 1D cases, calcite precipitation begins early. Even at $1e4$, it can be seen that the amount of calcite in the vault mortar has slightly increased (top-right). At this time, the waste packages are not yet affected. At $5e4$, calcite precipitation is more noticeable. The heatmap in the bottom-left shows a degree of calcite precipitation on virtually the entire vault mortar. In addition, at this time, the sides of the waste packages increase in calcite volume fraction due to precipitation. The middle section of the waste package zone is still unaffected at this time. After the entire time frame, at $5e4$ years, the calcite volume fraction increases on a band around the cell, where it shows a more uniform distribution on the sides of the mortar than at the top. The left and right columns of stacked waste packages show increased calcite precipitation almost through their entire outer concrete walls. On the other hand, even after $1e5$ years, the middle zone of the waste packages remains largely unaffected by calcite precipitation. These results are qualitatively consistent with the observation in the 1D cases for the top (see Figure 6-2) and the side (see Figure 6-7) parts of the cell.

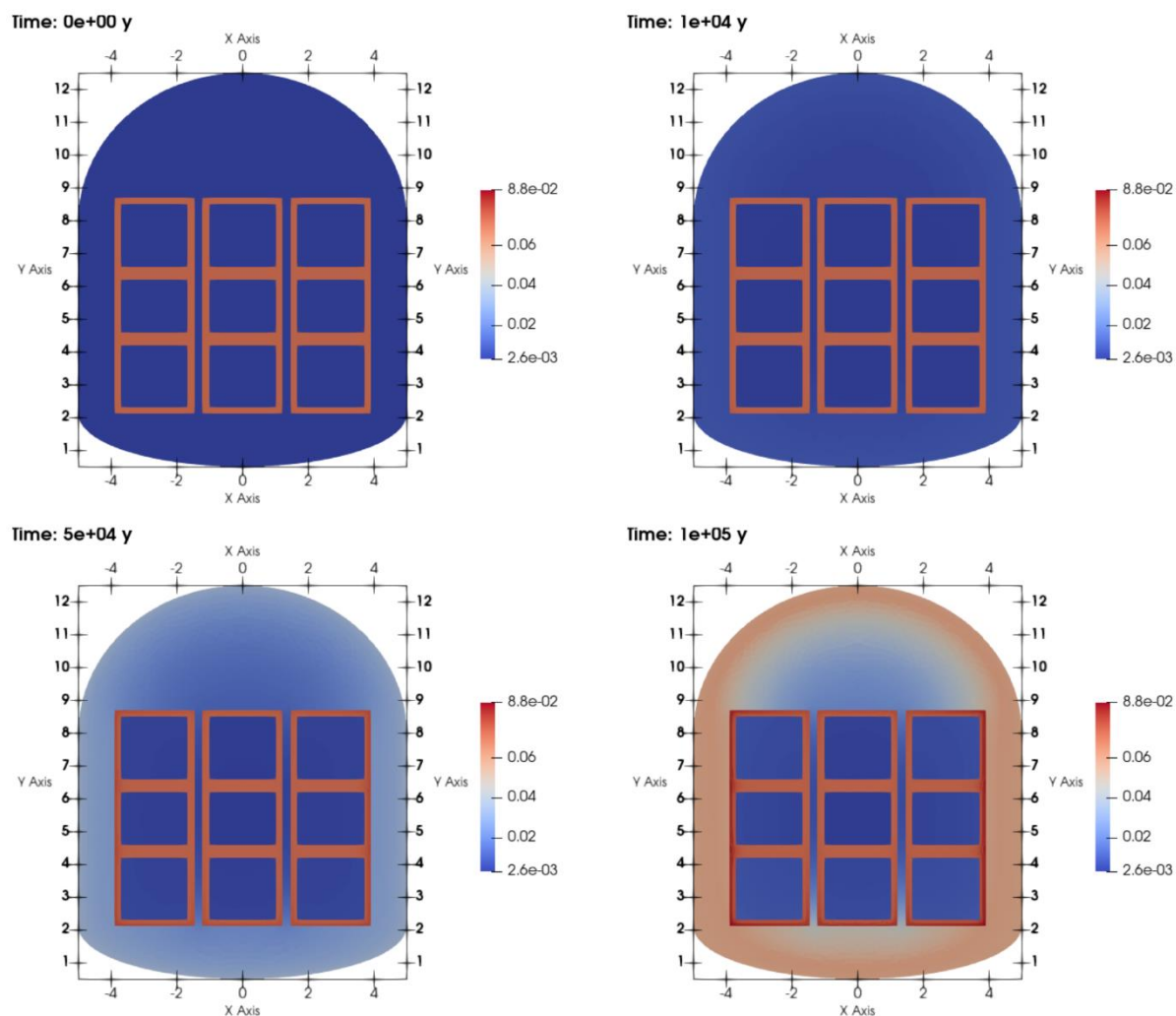


Figure 6-15. Volume fraction evolution of calcite in the 2D ILW cell in granite.

The changes in volume fraction of portlandite are shown in Figure 6-16. Initially, the volume fraction of portlandite is larger in the concrete walls. After 1e4 years, there is a strong dissolution of portlandite in the vault mortar. This dissolution follows a similar path to the other minerals; the zone of the side walls is affected sooner than the top of the cell. Additionally, the waste package zone remains unaffected. After 5e4 years, portlandite has completely dissolved from the vault mortar. A small fraction remains in the mortar between the waste packages on the sides of the middle column. Overall, the waste package zone is more altered concerning portlandite than other minerals. The outer walls of the waste packages, as well as the waste inside, show partial portlandite dissolution, whereas the waste package located in the center of the zone is largely unaltered, showing only a minor dissolution of portlandite in the concrete walls. The inside of the center waste package remains virtually intact after 1e5 years.

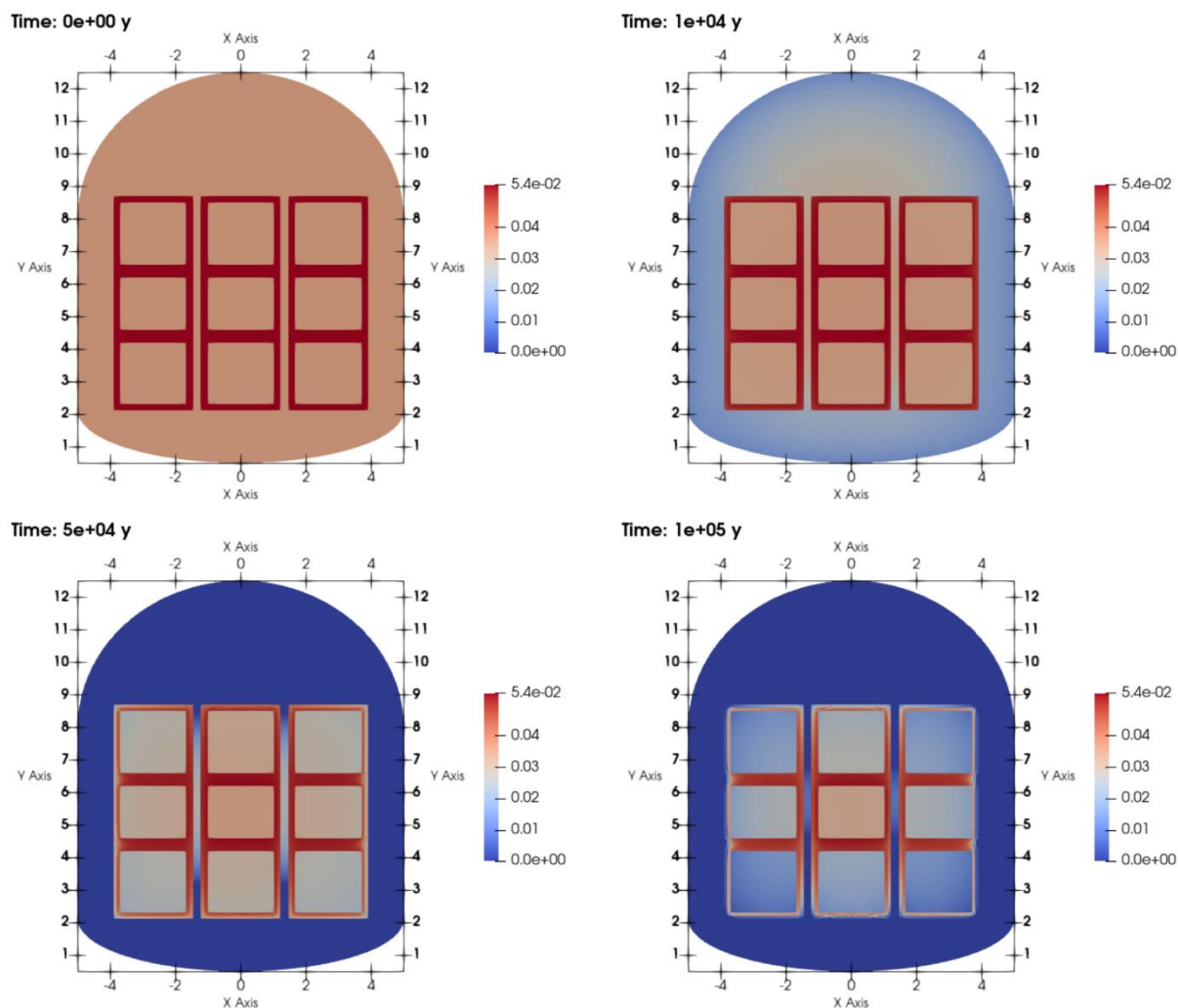


Figure 6-16. Portlandite volume fraction evolution in the 2D ILW cell in granite.

Figure 6-17 shows the pH evolution of the cell. The initial pH of the cell is about 13 throughout, with slightly more alkaline values in the concrete walls. After $1e4$ years, the pH is observed to be stable at around 12.5. Due to the continuing diffusion of the slightly alkaline granite porewater, the pH continues to lower from the vault mortar towards the inside of the cell, in the waste package zone. However, the waste package zone pH is still buffered by the remaining amount of portlandite at $5e4$ years. Finally, after $1e5$ years, the pH around the cell approaches closely the pH of the granite porewater, at about 8.8, in a 30 cm band on the top and around 1 m on the sides of the cell. Inside the waste package zone, the pH does not suffer large changes from $5e4$ to $1e5$, due to the remaining amounts of portlandite.

Note that the highly alkaline cement pore water within the disposal cell could, over time, alter the chemistry of the surrounding granite pore water. This scenario might lead to a feedback loop, affecting the boundary conditions and subsequently influencing the model outcomes. The selected boundary condition simplifies the complex interactions between the disposal cell and its surrounding geology, focusing on the diffusion of slightly alkaline granite pore water into the cell. While this provides a controlled scenario for studying the internal evolution of the disposal cell's chemistry, it's worth considering how the diffusion of reactive cement pore water into the granite could alter these dynamics. Over time, the leaching of cementitious materials and the movement of reactive ions could affect the surrounding granite's chemical properties, potentially resulting in changes to its pH and mineral composition. This could create a gradient of chemical reactions at the boundary between the disposal cell and the granite, leading to an evolving boundary condition.

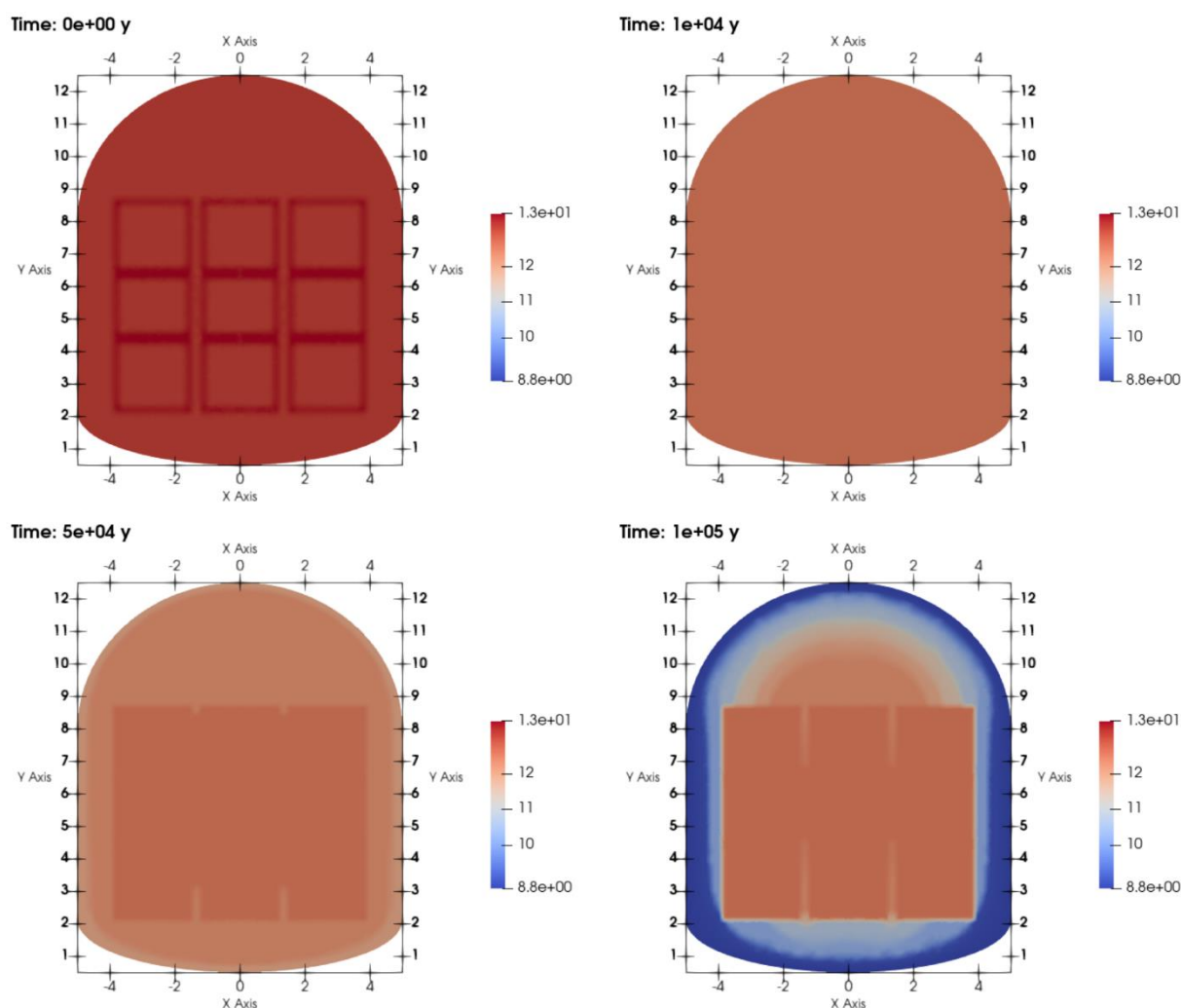


Figure 6-17. pH evolution in the 2D ILW cell in granite.

The porosity evolution of the cell is shown in Figure 6-18. As shown, the porosity is only marginally affected after $1e4$ years, with a slight increase at the boundary in contact with the granite porewater. This effect is increased at $5e4$ years, reaching the concrete walls. However, in the concrete walls, there is a slight increase in porosity instead, due to the dissolution of cement materials. The porosity in the middle section of the waste package is largely unaffected. After $1e5$ years, the porosity on most of the vault mortar has increased to around 40%. The porosity reduction effect observed in the 1D cases does not occur in the 2D case because the calcite precipitation is less pronounced. This is explained due to the differences in space-time discretization between the cases. In the 1D cases, a finer discretization was used, potentially leading to more concentrated mineral reactions, such as calcite precipitation, resulting in greater porosity reduction. The 2D case employed a coarser discretization, which may have allowed mineral reactions to be more spatially dispersed, reducing the intensity of porosity changes. Testing the 1D case with the same discretization as the 2D case would provide a more direct comparison and help to isolate the effects of dimensionality from those of discretization.

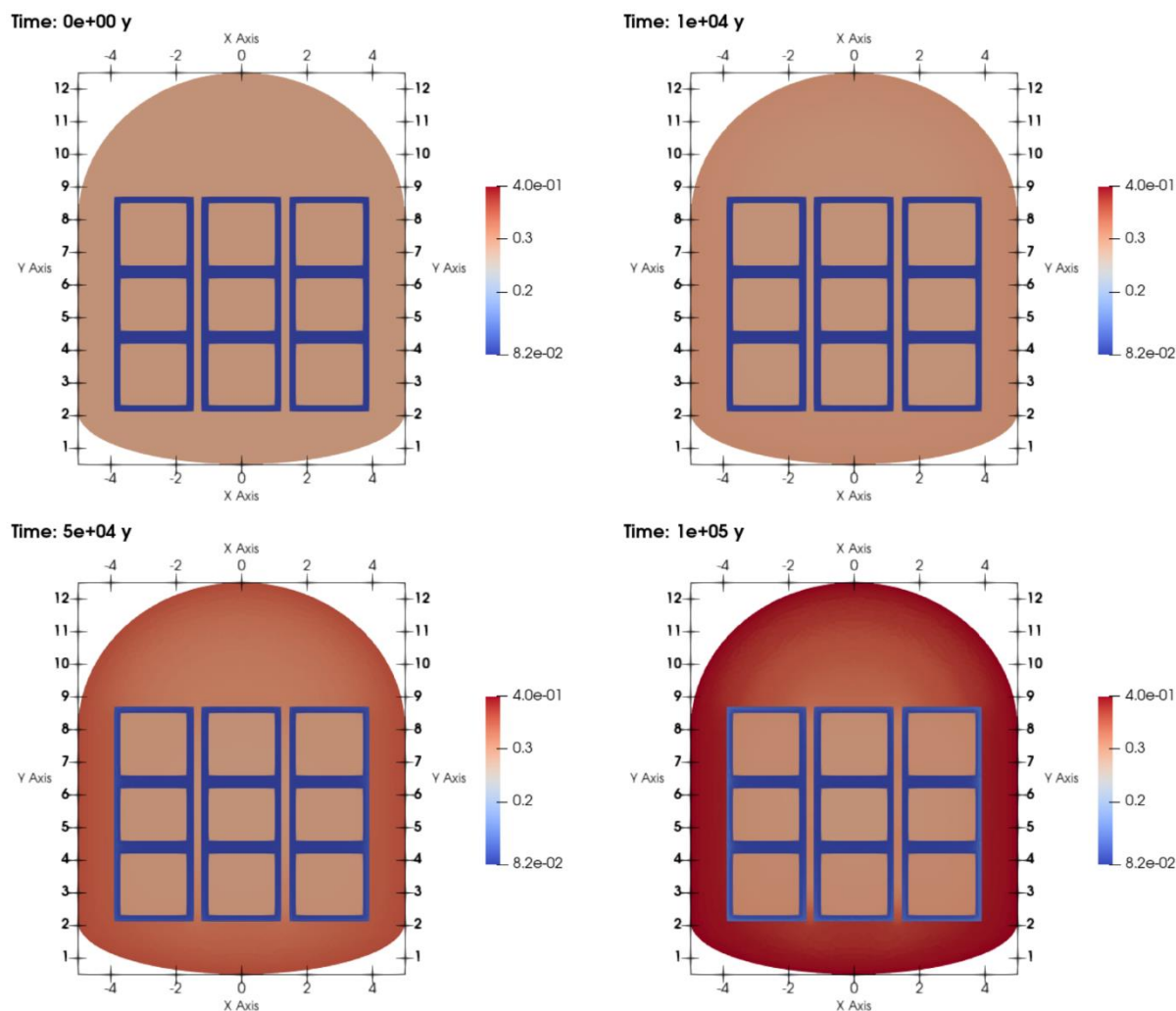


Figure 6-18. Porosity evolution in the 2D ILW cell in granite.

In Figure 6-19 and Figure 6-20, comparisons of both 1D cases (i.e., in the Y and X directions) are shown. The volume fractions are plotted using the cell information of the meshes; this is why there are linear segments in the plot lines. This also highlights the differences in spatial discretization between cases. First, in the comparison in the Y-direction (Figure 6-19), the trends of dissolution/precipitation of the main minerals are qualitatively similar, but they show significant quantitative differences due to the finer discretization in the 1D case, which is not comparable to the 2D case. Recall that the 2D case is more coarsely discretized due to the high computational cost. Furthermore, some differences may be influenced because of the more complex 2D geometry. The largest difference is in the calcite precipitation on the left side (25%). On the other hand, the C-S-H phases are more comparable, with remaining volume fractions around similar lengths in the 4 m length. Other phases such as ettringite and monocarbonate show similar trends. On the other hand, gibbsite and hydrotalcite, which have a precipitation front towards the granite boundary, show large differences. This can also be explained by the discretization differences, which induce a faster rate of porosity changes (i.e., pore-clogging), which is less pronounced with a coarser discretization. Despite this consistency in overall trends, the effect of discretization should not be underestimated. A finer discretization can lead to more detailed and precise modeling of mineral reactions, allowing for more accurate predictions of porosity changes and mineral distribution over time. Conversely, a coarser discretization might overlook critical local changes, leading to a smoother but potentially less accurate representation of the geochemical processes. In this comparison, the impact of discretization appears to primarily affect the position and sharpness of mineral fronts, rather than the broader qualitative trends. The results suggest that while the exact location of

these fronts and the rate of reactions can vary, the general patterns of dissolution and precipitation remain consistent.

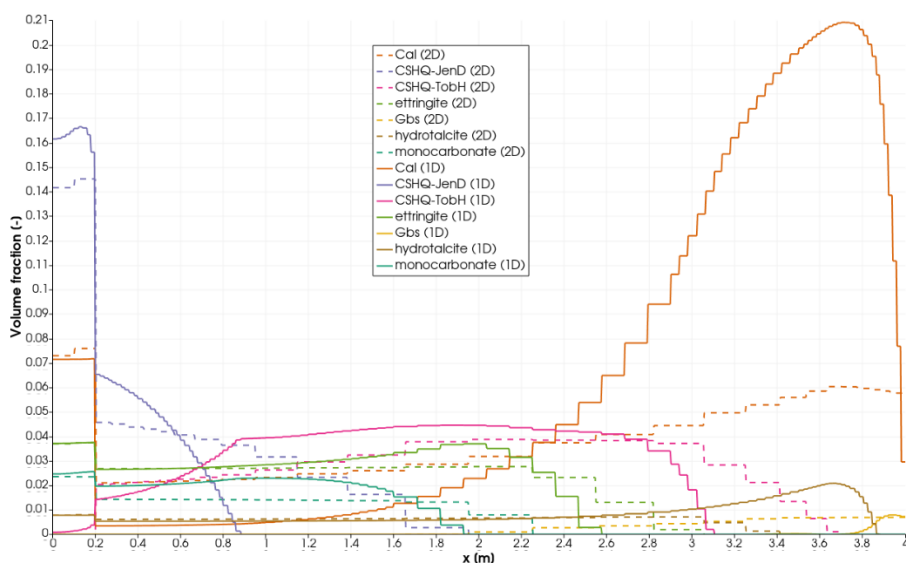


Figure 6-19. Comparison of the 1D and 2D models in the Y-direction for the ILW disposal cell in granite.

Finally, the comparison of the 1D and 2D cases in the X-direction, on the sides of the cell, is shown in Figure 6-20. In this case, the behaviour shows larger differences than in the Y-direction. For instance, the calcite precipitation profile in the 2D case cannot capture the behaviour of the 1D case. The same applies to the rest of the minerals, where the behaviour appears to be more linear in the 2D case. This could be explained by the fewer mesh elements used in this zone of the 2D cell, in comparison to the top of the cell (see Figure 6-12)..

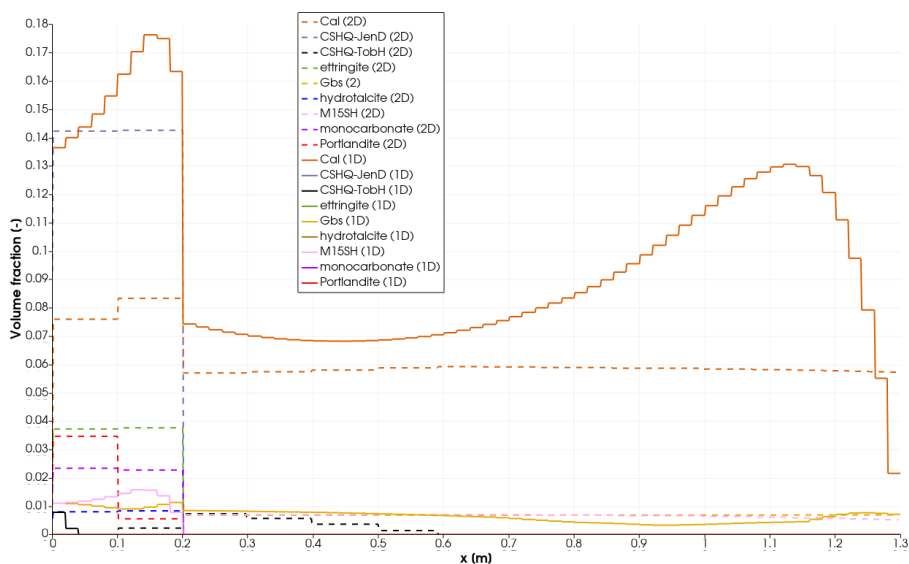


Figure 6-20. Comparison of the 1D and 2D models in the X-direction of the ILW cell in granite.

6.3 Summary and conclusions

This study significantly contributes to the understanding of the geochemical evolution of ILW disposal cells in granite rocks. The simulations of Intermediate-Level Waste (ILW) disposal cell behaviour in granite, spanning a 100,000-year period, were conducted using both 1D and 2D models. Key factors such as transport mechanisms, domain dimensions, and spatial considerations within the disposal cell emerged as crucial determinants of the system's long-term behaviour. Examining diverse transport mechanisms, mineral changes, porosity evolution, and concentration profiles, the study offers a detailed understanding of the long-term performance of the disposal cell. In 1D simulations with diffusive transport, substantial alterations were observed. These include the dissolution of portlandite, changes in C-S-H phases, and calcite precipitation, highlighting the dynamic nature of the system under different transport conditions.

Expanding the analysis to 2D models, excluding the granite host rock, revealed spatial variations in mineral changes, porosity evolution, pH levels, and concentration profiles. The complexity of these variations emphasizes the importance of specific locations within the disposal cell and the impact of transport mechanisms on the overall system.

In the comparison between the 1D and 2D cases, notable differences were observed, which can be partly attributed to the different levels of spatial discretization used in the models. The 1D case employed a finer mesh, while the 2D case used a coarser discretization due to computational constraints. These discrepancies lead to the question of how sensitive the results are to the chosen discretization. It is plausible that a finer mesh might yield more detailed and precise outcomes, potentially impacting the observed trends and the position of mineral fronts. However, broader trends appeared to remain consistent across the two cases. Further studies with consistent discretization across both 1D and 2D simulations would be required to accurately assess the sensitivity and understand the extent to which discretization might influence the results. This would help determine if finer discretization changes the outcomes dramatically or primarily affects specific details, such as the sharpness or position of reaction fronts.

The boundary condition in our model was set to a constant concentration with granitic pore water, assuming no back-diffusion of cementitious pore water into the granite or associated pH and chemical changes in the surrounding granite. This simplification raises the question of how likely it is for the pH to remain neutral at the boundary, or for the HCO_3^- concentration to remain constant over time. While this assumption allows for a more controlled simulation environment, it may not fully represent real-world conditions where diffusion can occur in both directions, leading to alterations in the chemistry of the surrounding granite. Discussing the potential effects of this boundary condition, we recognize that these simplifications may impact certain observations in our results. It would be beneficial to examine models with dynamic boundary conditions to better understand how changes in granite pore water chemistry might influence the geochemical evolution within the disposal cell. If boundary conditions are not constant, it could affect the rate of chemical reactions, mineral dissolution/precipitation, and the evolution of porosity, leading to different outcomes.

These simulations provide foundational insights for evaluating the performance of geological repository systems for radioactive waste, particularly intermediate-level nuclear waste. The findings enhance comprehension of complex interactions within the disposal cell, offering essential information to refine models and predictions. Ultimately, this research contributes to ongoing efforts for the safe and effective management of radioactive waste, advancing the design and implementation of geological repositories.

7. References

- Águila, J.F., Samper, J., Mon, A., Montenegro, L., (2020). Dynamic update of flow and transport parameters in reactive transport simulations of radioactive waste repositories. *Applied Geochemistry*, <https://doi.org/10.1016/j.apgeochem.2020.104585>.
- Andra (2016a). Safety Options Report - Operating Part (DoS-Expl). Report CG-TE-D-NTE-AMOA-SRr0000-5-0060, Andra, France.
- Andra (2016b). Safety Options Report - Operating Part (DoS-AF). Report CG-TE-D-NTE-AMOA-SR2-0000-r5-0062, Andra, France.
- Appelo, C. A. J., Postma, D., (1993). *Geochemistry, Groundwater and Pollution*, A. A. Balkema, Brookfield, Vt.
- Bildstein, O.; Trotignon, L.; Perronnet, M.; Jullien, M., (2006). Modelling iron-clay interactions in deep geological disposal conditions. *Phys. Chem. Earth Parts A/B/C*, 31, 618-625.
- Bildstein, O., Claret, F., Frugier, P. (2019). RTM for Waste Repositories. *Reviews in Mineralogy and Geochemistry* 85, 419–457.
- Blanc, P., Lassin, A., Piantone, P., Azaroual, M., Jacquemet, N., Fabbri, A., and Gaucher, E. C. (2012). Thermoddem: A geochemical database focused on low temperature water/rock interactions and waste materials. *Appl. Geochem.* 27, 2107–2116.
- Bradbury, M.H., Baeyens, B., (1997). A mechanistic description of Ni and Zn sorption on Na-montmorillonite. Part II: Modelling. *J. Contaminant Hydrology*, 27, 223-248.
- Bradbury, M.H., Baeyens, B., (2002). Porewater chemistry in compacted re-saturated MX-80 bentonite: physicochemical characterisation and geochemical modelling. PSI Bericht 02-10, Villigen PSI and NTB 01-08, Nagra, Wettingen, Switzerland.
- Bradbury, M.H., Baeyens, B., (2003). Porewater chemistry in compacted re-saturated MX-80 bentonite. *Journal of Contaminant Hydrology* 61, 329-338.
- Bradbury, M.H., Baeyens, B., (2005). Modelling the sorption of Mn(II), Co(II), Ni(II), Zn(II), Cd(II), Eu(III), Am(III), Sn(IV), Th(IV), Np(V) and U(VI) on montmorillonite: linear free energy relationships and estimates of surface binding constants for some selected heavy metals and actinides. *Geochim. Cosmochim. Acta* 69, 875-892.
- Cama, J., Ganor, J., Ayora, C., Lasaga, C.A. (2000). Smectite dissolution kinetics at 80°C and pH 8.8. *Geochim. Cosmochim. Acta* 64, 15, 2701-2717.
- Červinka, R., Klajmon, M., Zeman, J., Vencelides, T., (2018). Geochemical calculations and reactive transport modelling. SURAO Technical Report 271/2018/ENG.
- Chaparro, M.C.; Finck, N.; Metz, V.; Geckeis, H., (2021). Reactive Transport Modelling of the Long-Term Interaction between Carbon Steel and MX-80 Bentonite at 25°C. *Minerals* 11, 1272. <https://doi.org/10.3390/min11111272>.
- Cloet, V., Curti, E., Kosakowski, G., Lura, P., Lothenbach, B., Wieland, E., 2018. Cementitious backfill for a high-level waste repository: impact of repository induced effects. Nagra Arbeitsbericht NAB 18-41, Nagra, Wettingen, Schweiz.
- Dauzeres, A., Achiedo, G., Nied, D., Bernard, E., Alahrache, S., Lothenbach, B. (2016). Magnesium perturbation in low-pH concretes placed in clayey environment - Solid characterizations and modeling. *Cem. Conc. Res.*, 79, 137-150.

EURAD Deliverable 2.17 – Integrated reactive transport models for assessing the chemical evolution at the disposal cell scale

Debure, M., Frugier, P., De Windt, L., Gin, S. (2012). Borosilicate glass alteration driven by magnesium carbonates, *Journal of Nuclear Materials* 420, 347-361.

Debure, M., Linard, Y., Martin, C., Claret, F. (2019). In situ nuclear-glass corrosion under geological repository conditions. *Materials Degradation* 3, 38.

De Craen, M., Wang, L., Van Geet, M., Moors, H. (2004). Geochemistry of Boom Clay pore water at the Mol site. Report SCK•CEN-BLG-990, CSK-CEN, Belgium.

De Echave, T., Tribet, M., Jollivet, P., Marques, C., Gin, S., Jégou, C. (2018). Effect of clayey groundwater on the dissolution rate of SON68 simulated nuclear waste glass at 70 °C. *Journal of Nuclear Materials* 503, 279-289.

Deissmann, G., Haneke, K., Filby, A., Wiegers, R. (2016). Dissolution behaviour of HLW glasses under OPERA repository conditions. Report OPERA-PU-IBR511A.

Deissmann G., Ait Mouheb N., Martin C., Name N., Jacques, D., Weetjens E., Kursten B., Leivo M., Somervuori, M., Carpen, L., 2021. Experiments and numerical model studies on interfaces. Final version as of xx.xx.xxxx of deliverable D2.5 of the HORIZON 2020 project EURAD. EC Grant agreement no: 847593.

De Windt, L., Pellegrini, D., van der Lee, J. (2004). Coupled modeling of cement/ claystone interactions and radionuclides migration, *Journal of Contaminant Hydrology* 68, 165–182.

De Windt, L., Leclercq, S., van der Lee, J. (2006). Assessing the durability of nuclear glass with respect to silica controlling processes in a clayey underground disposal. *Materials Research Society Proceedings* 932, 313–320.

De Windt, L., Spycher, N. (2019). Reactive transport modeling: a key performance assessment tool for the geologic disposal of nuclear waste. *Elements* 15, 99–102.

De Windt, L., Lemmens, K., Samper, J., (2020). Definition of the materials and scenarios for HLW in Tasks 3 & 4. ACED Work Package Technical note.

De Windt, L., (2021). Personal communication.

De Windt L., Miron G. D., Fabian M., Goethals, J., Wittebroodt C. (2020): First results on the thermodynamic databases and reactive transport models for steel-cement interfaces at high temperature. Final version as of deliverable D2.8 of the HORIZON 2020 project EURAD. EC Grant agreement no: 847593.

Deissmann G., Ait Mouheb N., Martin C., Name N., Jacques, D., Weetjens E., Kursten B., Leivo M., Somervuori, M., Carpen, L. (2020): Experiments and numerical model studies on interfaces. Final version as of xx.xx.xxxx of deliverable D2.5 of the HORIZON 2020 project EURAD. EC Grant agreement no: 847593.

Duro, L., Altmaier, M., Holt, E., Mäder, U., Claret, F., Grambow, B., Idiart, A., Valls, A., Montoya, V. (2020). Contribution of the results of the CEBAMA project to decrease uncertainties in the Safety Case and Performance Assessment of radioactive waste repositories. *Applied Geochemistry* 112, 104479.

ENRESA, (2001). ENRESA 2000. Evaluación del comportamiento y de la seguridad de un almacén geológico profundo de residuos radiactivos en arcilla. ENRESA (in Spanish).

ENRESA, (2006). FEBEX: Updated final report 1994-2004. ENRESA Technical Publication PT 05-0/2006.

Fernández, A.M., Baeyens, B., Bradbury, M., Rivas, P., (2004). Analysis of the pore water chemical composition of a Spanish compacted bentonite used in an engineered barrier. *Physics and Chemistry of the Earth* 29(1), 105-118.

EURAD Deliverable 2.17 – Integrated reactive transport models for assessing the chemical evolution at the disposal cell scale

- Fernández R., Cuevas, J., Mäder, U., (2009). Modelling concrete interaction with a bentonite barrier. *Eur. J. Mineral* 21, 177-191.
- Fernández, J., (2017). Reactive Transport Models of low Permeability Structured Porous and Fractured Media. Ph.D. Dissertation. Universidad de A Coruña, Spain.
- Fleury, B., Godon, N., Ayrat, A., Perret, D., Dussossoy, J.-L., Gin, S. (2014). Development of an Experimental Design to Investigate the Effects of R7T7 Glass Composition on the Residual Rate of Alteration. *Procedia Materials Science* 7, 193 – 201.
- Frugier, P., Gin, S., Minet, Y., Chave, T., Bonin, B., Godon, N., Lartigue, J.E., Jollivet, P., Ayrat, A., De Windt, L., Santarini, G. (2008). SON68 nuclear glass dissolution kinetics: Current state of knowledge and basis of the new GRAAL model. *Journal of Nuclear Materials* 380, 8–21.
- Frugier, P., Rajmohan, N., Minet, Y., Godon, N., Gin, S., (2018). Modeling glass corrosion with GRAAL. *Materials Degradation* 2:35.
- Gaucher E., Tournassat C., Nowak C., (2005). Modelling the geochemical evolution of the multibarrier system of the Silo of the SFR repository. Final report. SKB R-05-80, Svensk Kärnbränslehantering AB.
- Gaucher E., Tournassat C., Pearson F. J., Blanc P., Crouzet C., Lerouge C., Altmann S., (2009). A robust model for pore-water chemistry of clayrock. *Geochim. Cosmochim. Acta*, 73(21), 6470–6487.
- Giffaut, E., Grivé, M., Blanc, P., Vieillard, P., Colàs, E., Gailhanou, H., Gaboreau, S., Marty, N., Madé, B., Duro, L. (2014). Andra thermodynamic database for performance assessment: ThermoChimie. *Applied Geochemistry* 49, 225–236.
- Gin, S., Abdelouas, A., Criscenti, L.J., Ebert, W.L., Ferrand, K., Geisler, T., Harrison, M.T., Inagaki, Y., Mitsui, S., Mueller, K.T., Marra, J.C., Pantano, C.G., Pierce, E.M., Ryan, J.V., Schofield, J.M., Steefel, C.I., Vienna, J.D., (2013). An international initiative on long-term behaviour of high-level nuclear waste glass. *Materials Today* 16, 243-248.
- Gin, S., Jollivet, P., Fournier, M., Berthon, C., Wang, Z., Mitroshkov, A., Zhu, Z., Ryan, J.V., (2015). The fate of silicon during glass corrosion under alkaline conditions: A mechanistic and kinetic study with the International Simple Glass, *Geochimica et Cosmochimica Acta* 15, 68-85.
- Gómez P., Turrero, M.J., Garralón, A., Peña, J., Buil, B., de la Cruz, B., Sánchez, M., Sánchez, D.M., Quejido, A., Bajos, C., Sánchez, L., (2006). Hydrogeochemical characteristics of deep groundwaters of the Hesperian Massif (Spain). *Journal of Iberian Geology* 32 (1), 113-131.
- Govaerts, J., Weetjens, E. (2010). Scoping Calculation: When and in which concentration will aggressive
- Giffaut, E., Grivé, M., Blanc, P., Vieillard, P., Colàs, E., Gailhanou, H., Gaboreau, S., Marty, N., Madé, B., Duro, L. (2014). Andra thermodynamic database for performance assessment: ThermoChimie. *Applied Geochemistry* 49, 225-236.
- Idiart, A., Laviña, M., Kosakowski, G. *et al.* (2020). Reactive transport modelling of a low-pH concrete / clay interface. *Applied Geochemistry* 115, 104562.
- Jollivet, P., Gin, S., Schumacher, S. (2012). Forward dissolution rate of silicate glasses of nuclear interest in clay-equilibrated groundwater. *Chemical Geology* 330–331, 207-217.
- Kosakowski, G. (2020). Reference document for properties of cementitious materials in ACED with GEM-Selektor and based on CEMDATA V18.1. Technical note, HORIZON 2020 project EURAD. EC Grant agreement no: 847593
- Kwon, S, Lee, C.S., Cho, S.J., Jeon, S.W., Cho, W.J., (2009). An investigation of the excavation damaged zone at the KAERI underground research tunnel. *Tunnelling and Underground Space Technology* 24(1), 1-13. ISSN 0886-7798. <https://doi.org/10.1016/j.tust.2008.01.004>.

- Liu, S., Jacques, D., Govaerts, J., Wang, L. (2014). Conceptual model analysis of interaction at a concrete–Boom Clay interface. *Physics and Chemistry of the Earth* 70–71, 150–159.
- Lu, C., Samper, J., Fritz, B., Clement, A., Montenegro, L., (2011). Interactions of corrosion products and bentonite: An extended multicomponent reactive transport model, *Physics and Chemistry of the Earth* 36, 1661-1668, doi: 10.1016/j.pce.2011.07.013.
- Marty N. M., Munier I., Gaucher E., Tournassat C., Gaboreau S., Vong C., Giffaut E., Cochevin B., Claret F., (2014). Simulation of Cement/clay interactions: feedback on the increasing complexity of modelling strategies. *Transp. Porous Med.*, 104(2), 385-405.
- Marty, N.C.M., Bildstein, O., Blanc, P. *et al.* (2015). Benchmarks for multicomponent reactive transport across a cement/clay interface. *Comput Geosci* 19, 635–653.
- Millington R. J., Quirk J. M., (1960). Transport in porous media. p. 97-106. In F.A. Van Beren, et al. (ed.) *Trans. Int. Congr. Soil Sci.*, 7th, Vol. 1, Madison, WI., Elsevier, Amsterdam. Mitchell, J K, Soga K, 2005. *Fundamentals of Soil Behavior*. 3rd Edition, Wiley 592 p.
- Martínez-Landa, L., Carrera, J., Pérez-Estaún, A., Gómez, P., Bajos, C., (2016). Structural geology and geophysics as a support to build a hydrogeologic model of granite rock. *Solid Earth* 7(3), 881-895. 10.5194/se-7-881-2016.
- Mon, A., Samper, J., Montenegro, L., Naves, A., Fernández, J., (2017). Reactive transport model of compacted bentonite, concrete and corrosion products in a HLW repository in clay. *Journal of Contaminant Hydrology* 197, 1-16.
- Neeft, E., (2020a). Personal communication.
- Neeft, E., Weetjens E., Vokal A., Leivo M., Cochevin B., Martin C., Munier I., Deissmann G., Montoya V., Poskas P., Grigaliuniene D., Narkuniene A., García E., Samper J., Montenegro L., Mon A. (2020b): Treatment of chemical evolution in National Programmes, Deliverable 2.4 of the HORIZON 2020 project EURAD. EC Grant agreement no: 847593.
- Neeft, E. (2021). HLW Callovo Oxfordian thermal evolution, internal technical note for subtask 4.1, ACED WP.
- Odorowski, M., Jégou, C., De Windt, L., Broudic, V., Jouan, G., Peugot, S., Martin, C. (2017). Effect of metallic iron on the oxidative dissolution of UO₂ doped with a radioactive alpha emitter in synthetic Callovian-Oxfordian groundwater. *Geochimica et Cosmochimica Acta* 219, 1–21.
- Ortiz, L., Volckaert, G., Mallants, D., (2002). Gas generation and migration in Boom clay, a potential host rock formation for nuclear waste storage. *Eng. Geol.* 64, 287-296.
- Pusch, R. (2001). The microstructure of MX-80 clay with respect to its bulk physical properties under different environmental conditions. SKB Technical Report TR-01-08.
- Repina, M., Renard, D., Bouyer, F., Lagneau, V. (2019). Coupling image analysis and thermo-mechanical simulation results to produce a model of the fracture network in a nuclear glass canister. *Journal of Nuclear Materials*, 522, 265 - 285.
- Samper, J., Lu, C., Montenegro, L., (2008). Coupled hydrogeochemical calculations of the interactions of corrosion products and bentonite. *Physics and Chemistry of the Earth* 33, S306-S316, doi:10.1016/j.pce.2008.10.009.
- Samper, J., Xu, T., Yang, C., (2009). A sequential partly iterative approach for multicomponent reactive transport CORE^{2D}. *Comput. Geosci.* 13, 301-316.

EURAD Deliverable 2.17 – Integrated reactive transport models for assessing the chemical evolution at the disposal cell scale

- Samper, J., Naves, A., Montenegro, L., Mon, A., (2016) Reactive transport modelling of the long-term interactions of corrosion products and compacted bentonite in a HLW repository in granite: uncertainties and relevance for performance assessment. *Applied Geochemistry* 67, 42–51.
- Samper, J., Mon, A., Montenegro, L., (2018). A revisited thermal, hydrodynamic, chemical and mechanical model of compacted bentonite for the entire duration of the FEBEX in situ test. *Applied Clay Sciences* 160, 58-70. doi.org/10.1016/j.clay.2018.02.019.
- Samper, J., L. Montenegro, L. De Windt, V. Montoya, J. Garibay-Rodríguez, D. Grigaliuniene, A. Narkuniene, & P. Poskas, (2021). Conceptual model formulation for a mechanistic based model implementing the initial SOTA knowledge (models and parameters) in existing numerical tools. Deliverable D2.16 of the EURAD Joint Project. EC Grant Agreement no: 847593.
- Samper, J. et al., (2023). Model abstraction techniques for assessing the chemical evolution at the disposal cell scale and applications for sensitivity and uncertainty. Deliverable D2.19 of the EURAD Joint Project. EC Grant Agreement no: 847593.
- Seetharam, S., Jacques, D. (2015). Potential Degradation Processes of the Cementitious EBS Components, their Potential Implications on Safety Functions and Conceptual Models for Quantitative Assessment, report OPERA-PU-SCK514, Netherlands.
- Thierry M., Baroghel-Bouny V., Bourneton N., Villain G., Stéfani C. (2007). Modélisation du séchage du béton. Analyse des différents modes de transfert hydrique. *Revue Européenne de Génie Civil*, 11, 541-577.
- Tournassat, C., (2003). Cations-clay interactions: The Fe(II) case. Application to the problematic of the French deep nuclear repository field concept. Ph.D. Dissert. Grenoble, France.
- Truche, L., Berger, G., Destrigneville, C., Pages, A., Guillaume, D., Giffaut, E., Jacquot, E., 2009. Experimental reduction of aqueous sulphate by hydrogen under hydrothermal conditions: Implication for the nuclear waste storage. *Geochim. Cosmochim. Acta* 73, 4824–4835.
- van der Lee, J., De Windt, L., Lagneau, Goblet, P., 2003. Module-oriented modeling of reactive transport with HYTEC. *Computers and Geosciences* 29, 265–275.
- Weetjens, E., Marivoet J., Govaerts, J. (2012). Preparatory Safety Assessment. Report SCK•CEN-ER-215, SCK-CEN, Belgium.
- Wittebroodt C., Goethals J., De Windt L., Fabian M., Miron G.D., Zajec B., Dettleux V. (2023): Final technical report on the steel/cement material interactions. Final version as of deliverable D2.9 of the HORIZON 2020 project EURAD. EC Grant agreement no: 847593.
- Wolery, T.J., (1992). EQ3/6, a software package for geochemical modeling of aqueous systems: package overview and installation guide (version 7.0). Technical Report UCRL-MA-110662-Pt 1. Lawrence Livermore National Laboratory, CA, USA.
- Yu, L., Weetjens, E. (2012). Estimation of the gas source term for spent fuel, vitrified high-level waste, compacted waste and MOSAIK waste. Report SCK•CEN-ER-162, SCK-CEN, Belgium.
- Zheng, L., Samper, J., (2008). A coupled THMC model of FEBEX mock-up test. *Physics and Chemistry of the Earth* 33, S486-S498.
- Zheng, L., Samper, J., Montenegro, L., (2011). A coupled THC model of the FEBEX in situ test with bentonite swelling and chemical and thermal osmosis, *Journal of Contaminant Hydrology* 126, 45-60.